THE STRUCTURE AND PROPERTIES

OF

A "MULTIPHASE" ALLOY

A thesis submitted for the degree of

DOCTOR OF PHILOSOPHY

in the

University of London

by

GEMA GONZALEZ DE ARMENGOL, B.Sc, M.Sc, D.I.C.

July 1981

Department of Metallurgy
and Materials Science
Royal School of Mines
Imperial College of Science
and Technology
London

ACKNOWLEDGEMENTS

I would like to thank very especially Dr. D.R.F. West, for his interest in this work, for his advice, helpful suggestions and constant guidance, as well as for his great kindness, patience and understanding.

My thanks also go to the technicians of the department, particularly to Mr. R. Baxter, for the preparation of innumerable amounts of specimens; to Mr. F. Higgins for the technical assistance with x-ray and S.E.M. equipments, and to Mr. G. Briers for assistance with the T.E.M. equipment.

May I also thank the photography department especially Mr. J. Rossdale, for the final printing of the photographs.

I am indebted to Dr. B.O. Weightman for contacting the company, Sulzer & Brothers Ltd., which provided the material studied in this wotk, in particular Dr. M. Semlitsch for the supply of general information about the alloy.

I acknowledge Prof. J.G. Ball and Prof. D.W. Pashley for the provision of research facilities.

Many thanks to CONICIT (Venezuelan Council for Scientific and Technological Research), for providing the grant, without which this work would not have been possible.

I am grateful to Miss A.M. de las Heras for her excellent collaboration and typing.

Very especially I would like to express my gratitude to my friends for their support and help during the writing of this thesis, particularly to Mr. and Mrs. Bond, Margarita, Gabi and Ana.

Finally, I am deeply grateful to Alberto, my dear husband, for his encouragement, great support, patience and innumerable sacrifices during the period of this work.

To my dear parents,

To Alberto and Suzanne

INDEX

		Page
ABSTRACT		1
CHAPTER I	INTRODUCTION	3
CHAPTER II	LITERATURE SURVEY	6
II.1	The allotropic transformation in cobalt	6
II.2	The effect of alloying elements on the allotropic transformation of cobalt	
	Binary systems	8
II.3	The ternary systems	
	The Co-Ni-Cr system	13
	The Co-Ni-Mo system	14
	The Co-Cr-Mo system	14
	The Ni-Cr-Mo system	15
II.4	The quaternary system	
	Co-Cr-Ni-Mo	15
II.5	MULTIPHASE Alloys - Mechanical properties and strengthening mechanism	
II.5.1	General Characteristics	19
II.5.2	Strengthening Mechanisms	19
II.5.2.a	Deformation-induced strengthening	22
II.5.2.b	Ageing-induced strengthening	24
II.5.3	Structural variables associated with the formation of hcp platelets in MULTIPHASE alloys	26
II.5.3.a	c/a ratio of the hcp phase	26
II.5.3.b	Mechanical twinning in hcp platelets	28
II.5.3.c	Mechanical twinning in fcc phase	28
II.5.4	Mechanism of hcp nucleation	29
II.5.5	Mechanical properties of MP35N and Protasul-10	31

		Page
II.6	Theoretical background to mechanical testing	34
II.6.1.a	Strain Ageing	34
II.6.1.b	Characteristics of dynamic strain ageing (DSA)	35
II.6.2	Thermally Activated Deformation Activation parameters	39
II.6.2.a	Force on a dislocation and thermal activation	39
II.6.2.b	Experimental techniques of determination of the activation parameters	40
II.6.3	Fracture Mechanisms	43
CHAPTER III	EXPERIMENTAL PROCEDURE	
III.1	Alloy Preparation	46
III.2	Specimen Preparation	46
III.3	Hardness Measurements	50
III.4	Metallography	51
III.5	X-ray Analysis	52
III.6	Transmission Electron Microscopy	53
III.7	Mechanical Properties	
III.7.a	Tensile testing	55
III.7.b	Impact testing	60
III.7.c	Compression testing Test Procedure	61 61
III.7.d	Grain Size Measurements	63
CHAPTER IV	EXPERIMENTAL RESULTS	
IV.1	Deformation	
IV.1.a	Structural features	64
IV.1.b	Hardness	65
IV.1.c	X-ray Analysis, Deformed Samples	65
IV.1.d	Transmission Electron Microscopy Analysis	72
IV.1.d.1	Introduction	72

		Page
IV.1.d.2	Electron Diffraction	81
IV.1.d.2.a	Deformation at room temperature	81
IV.1.d.2.b	Deformation at liquid nitrogen (-196°C) temperature	82
IV.2	Ageing Treatments	94
IV.2.a	Short time ageing treatments	94
IV.2.a.1	Hardness values	95
IV.2.a.2	X-ray Analysis - Rapid Heating	96
IV.2.a.3	Diffraction Analysis - Short time ageing	97
IV.2.b	Long time ageing treatments	105
IV.2.b.1	Hardness values after long ageing treatments	106
IV.2.b.2	X-ray analysis - Long time ageing treatments	108
IV.2.b.3	Results of grain size measurements	109
IV.2.b.4	Diffraction analysis for long time ageing treatments	110
IV.2.b.5	Recrystallization	111
IV.3	Tensile Test Results	131
IV.3.a	Analysis of the graphs of work hardening rate vs true plastic strain	133
IV.3.b	Summary of mechanical properties vs Temperature	134
IV.4	Impact Testing	135
IV.5	Fractographs	149
IV.5.a	Tensile fracture results	149
IV.5.b	Impact testing fractographs	152
IV.6	Compression Testing	153
IV.6.a	Description of behaviour during compression test at different temperatures	
	Room temperature	153
	360°C - 450°C	154
	550°C	155
	650°C - 680°C	157
	700°C	157
	800°C	158

		Page
IV.6.b	The temperature dependence of the 0.2% proof stress, the strain rate sensitivity, and the relaxation stress.	159
IV.6.c	Calculation of Activation Parameters	160
CHAPTER V	DISCUSSION	
V.1	Deformation Behaviour	183
V.1.a	Work strengthening at room and sub-zero temperature	
	Introduction	183
	X-ray Analysis	186
V.1.b	Structural Features	
	1. Dependence of deformation modes on temperature and amount of deformation	188
	2. Conditions for twin formation and fcc-hcp - Transformation induced by plastic deformation	196
	3. Initial stages of $\alpha \rightarrow \epsilon$ formation - The role of twinning in the $\alpha \rightarrow \epsilon$ martensitic transformation	198
	4. Kinetics of strain-induced martensitic transformation and of fcc deformation twinning	202
V.1.c	Low temperature strength	205
	- Work hardening behaviour	206
	- Tensile fracture mode analysis	213
	- Fracture Mode during impact testing	216
V.2	Annealing Behaviour	
V.2.a	Ageing Induced Strengthening	217
V.3	High Temperature Strength	225
V.3.1	General Compressive Deformation Behaviour	
V.3.1.a	Room Temperature	226
V.3.1.b	Elevated Temperatures	
V.3.1.b.1	Introduction	227

		Page
V.3.1.b.2	Discussion of observations at elevated temperature	
	360°-450°C	231
	550°-650°C	233
	700°C	236
V.3.2	The temperature dependence of the 0.2% proof stress, the strain rate sensitivity and relaxation stress	239
CHAPTER VI	CONCLUSIONS AND SUGGESTIONS FOR FUTURE WORK	
VI.1	Conclusions	242
VI.2	Suggestions for further work	245
APPENDIX I		247
APPENDIX II		249
APPENDIX III		253
APPENDIX IV		255
REFERENCES		259-265

LIST OF TABLES

Table		Page
III.1	Alloy compositions	47
IV.1	Hardness values for different amounts of deformation at different temperatures (room temperature, $-70^{o}C$, $-196^{o}C$	68
IV.2	X-ray results for deformed material	70
IV.3	Exact orientations in which electron diffraction can or cannot distinguish between twin and hcp plates	74
IV.4	Hardness values for rapid heating treatments	99
IV.5	X-ray analysis for rapid heated material	96
IV.6	Hardness values for long time ageing treatments	117
IV.7	X-ray results for long time ageing treatments	121
IV.8	X-ray diffraction analysis of possible precipitates found during ageing	122
IV.9	Values of true lattice parameter (a_o) for different alloy conditions	123
IV.10	Tensile test results	136
IV.11	Values of strain hardening exponent	143
IV.12, IV.13	Temperature dependence of 0.2% proof stress, Relaxation stress and strain rate sensitivity	165-166
IV.14	$(\Delta\sigma/\Delta T)_{\dot{\varepsilon}}^{\varepsilon}$ values	171
IV.15, IV.16	Activation parameters	172-173
V.1	Stacking fault probability values for different amounts of deformation	187
V.2	Dependence of deformation modes on temperature and amount of deformation	190

Table		Page
V.3	Stacking fault energy values for different Co-Ni alloys at room temperature	195
V.4	Results of stacking fault energy measurements on heat-treated MP35N alloy	219
A.1	2θ values for fcc and hcp planes	248
A.II.1	d values for fcc crystal structure	250
A.III.1	Work hardening rate vs strain for the solution treated material	253
A.III.2	Work hardening rate vs strain for the previously deformed material	254

LIST OF FIGURES

Page

Fig. II.1 - Effects of alloying additions on the cobalt alloy phase diagrams 10

Fig. II.2 - Change in the transformation temperature of cobalt by 1 at % of alloying addition 11

Fig. II.3 - A tentative classification of cobalt binary systems 11

Figs. II.4 to II.6 - Cobalt-rich section of the Co-Mo, Co-Cr and Co-Ni binary diagrams 12

Figs. II.7 & II.8 - Isothermal sections at 1200°C of the Co-Ni-Cr and Co-Ni-Mo ternary phase diagrams 17

Figs. II.9 to II.11 - Isothermal sections at 1200°C of the Co-Cr-Mo, Ni-Cr-Mo and Co-Cr-Ni ternary phase diagrams 18

Fig. II.12 - Tentative construction of the quaternary phase diagram Ni-Co-Cr-Mo at 1200°C 18

Fig. II.13 - Effect of cold work on yield strength and amount of hcp phase formed in various MULTIPHASE alloys 21

Fig. II.14 - Stacking fault energy in the Co-Ni-Cr system 30

Fig. II.15 - Tensile properties of MP35N 32

Fig. II.16 - Effect of ageing temperature on tensile properties of MP35N cold drawn 485% 32

Fig. II.17 - Comparison of short time elevated temperature strength/density of MP35N to several high strength and corrosion resistant alloys 32

Fig. II.18 - Ultimate tensile strength of MP159 compared to other alloys 32

Figs. II.19 & II.20 - Low temperature mechanical properties of MP35N 33

Fig. II.21 - Schematic diagrams of: a) initial yield point, b) over straining, c) strain ageing, d) strain-age hardening, e) recovery, f) serrated flow 36

Page

Fig. II.22 - Different type of serrations 36

Fig. II.23 - Determination of activation parameters from: a) change of strain rate, b) creep test, c) stress relaxation test 41

Fig. III.1 - Tensile specimens 57

Fig. III.2 - Notched impact testing specimens 57

Figs. IV.1 to IV.4 - Optical micrographs of annealed and deformed material 67

Fig. IV.5 - Hardness vs percentage of deformation for different rolling temperatures 69

Fig. IV.6 - Comparison between X-ray diffraction patterns to show shift of the peaks 71

Figs. IV.7.a, b & c - Composite diffraction patterns in which fcc - twin and hcp phases may be distinguished 75-76

Fig. IV.8 - Electron microscopy photographs of material deformed 50% at room temperature 78

Fig. IV.9 - Electron microscopy photographs of material deformed 50% at -196°C 80

Figs. IV.10 to IV.17 - Electron microscopy photographs of material deformed different % of reduction at room temperature 83-88

Figs. IV.18 to IV.25 - Electron microscopy photographs of material deformed different % of reduction at -196°C 89-93

Fig. IV.26 - Optical micrographs from rapid heating treatments 98

Figs. IV.27 & IV.28 - Hardness curves for rapid heating treatments 100-101

Figs. IV.29 to IV.32 - Electron microscopy photographs of material previously deformed and heat treated for short times (2 min to 15 min) at different temperatures 102-104

Figs. IV.33 to IV.35 - Optical micrographs of material previously deformed and aged for long times (5 h to 100 h) at different temperatures (600°C/700°C) 112-113

Page

Figs. IV.36 to IV.37 - Scanning electron micrographs of material previously deformed at room temperature and -196°C and heat treated for long times at different temperatures 114-115

Figs. IV.38 & IV.39 - Micrographs of recrystallized material showing precipitates 116

Fig. IV.40 - Hardness vs deformation for different ageing times and temperatures 118

Fig. IV.41 - Hardness vs ageing time for constant ageing temperature 119

Fig. IV.42 - Hardness vs ageing temperature for constant ageing time 120

Figs. IV.43 to IV.49 - Electron microscopy photographs of material previously deformed at room temperature and -196°C and aged for long times (5 h , 100 h) at different temperatures (600°C - 700°C) 124-128

Figs. IV.50 & IV.51 - Electron microscopy photographs of recrystallized material 129-130

Fig. IV.52 - True stress vs true strain curves of solution treated material tested at room temperature and -196°C 137

Fig. IV.53 - True stress vs true strain curves of material solution treated and deformed tested at room temperature 138

Fig. IV.54 - True stress vs true strain curves of material solution treated tested at sub-zero temperatures 139

Fig. IV.55 - True stress vs true strain curves of material previously deformed 45% tested at sub-zero temperatures 140

Fig. IV.56 - Log true stress - log true strain graphs of solution treated material tested from room temperature to -196°C 141

Fig. IV.57 - Log true stress - log true strain of material previously deformed tested from room temperature to -196°C 142

Fig. IV.58 - Work hardening rate vs plastic strain for solution treated material tested from room temperature to -196°C 144

Page

Fig. IV.59 - Work hardening rate vs plastic strain for previously deformed material tested from room temperature to -196°C 145

Figs. IV.60 & IV.61 - Variation of 0.2% true stress, tensile stress at instability, fracture stress and elongation with temperature for solution treated and deformed material respectively 146-147

Fig. IV.62 - Energy absorbed vs temperature 148

Figs. IV.63 to IV.66 - Schematic representation of compression test for:
IV.63 solution treated material 161
IV.64 solution treated and aged material 162
IV.65 previously deformed 45% material 163
IV.66 previously deformed 45% and aged material 164

Fig. IV.67 - 0.2% proof stress vs temperature for materials: a) solution treated, solution treated and aged; b) deformed; c) deformed and aged 167

Fig. IV.68 - Strain rate sensitivity vs temperature for the solution treated material 168

Fig. IV.69 - Strain rate sensitivity vs temperature for material deformed and deformed and aged 169

Fig. IV.70 - Relaxation stress vs temperature 170

Figs. IV.71 to IV.81 - Scanning electron micrographs of fracture surfaces of the material solution treated, tested in tension from room temperature to -196°C 174-176

Figs. IV.82 to IV.86 - Scanning electron micrographs of fracture surfaces of the material previously deformed, tested in tension from room temperature to -196°C 177-178

Fig. IV.87 - Low magnification S.E.M. photographs of fracture surfaces of solution treated material, tested from room temperature to -196°C 179

Fig. IV.88 - Low magnification S.E.M. photographs of fracture surfaces of material previously deformed, tested from room temperature to -196°C 180

Page

Fig. IV.89 - Fracture surfaces at low magnifications. Impact testing. S.E.M. micrographs 181

Fig. IV.90 - Fracture surfaces at higher magnifications. Impact testing. S.E.M. micrographs 182

Fig. V.1 - Structural diagram for MULTIPHASE alloys 184

Fig. V.2 - Shift of X-ray peaks due to stacking faults 188

Fig. V.3 - Deformation structures as a function of composition and temperature 192

Fig. V.4 - Volume fraction of ϵ martensite as a function of temperature 192

Fig. V.5 - Deformation structures observed near room temperature as a function of stacking fault energy at room temperature 193

Figs. V.6 & V.7 - Variation of stacking fault energy with temperature for Co-30wt%Ni - 15wt%Cr and Co-35 at % Ni 194

Fig. V.8 - Schematic drawing of a dislocation distribution near the twin source 197

Fig. V.9 - Effect of test temperature on the tensile properties and the strain hardening exponent in Fe-15%Cr13%Ni 212

Fig. V.10 - Variation of stacking fault energy with temperature for Co and Co-Ni alloys 219

Fig. V.11 - Schematic free energy vs composition curves for a Co-35%W alloy 221

Figs. V.12.a & b - TTT curves for Co-20wt%Cr and Co-25wt%W alloys 223

Fig. V.13 - Hardness vs ageing time for a Co-35wt%W alloy aged at 800°C 223

Fig. V.14 - Serrated flow shown on sections of flow curves of nickel and nickel-cobalt alloys 238

ABSTRACT

An investigation was carried out on a "MULTIPHASE" type alloy, designated PROTASUL10; this contains 35wt%Co - 35wt%Ni - 20wt%Cr - 10wt%Mo, and small Ti additions. Two levels of Ti were studied, i.e. wt%, 0.15 and 0.745. This type of alloys when solution treated consist of a metastable fcc solid solution. High strength can be produced by deformation.

Studies were made by means of X-rays and transmission electron microscopy on the work-strengthening due to deformation at room and sub-zero temperatures, observing the transformations (fcc → hcp and twinning) taking place during these deformations and on further annealing between 425°C and 650°C. The precipitation and recrystallization processes taking place between 700°C and 850°C were also analysed.

An extensive study was performed on the mechanical properties from room temperature to -196°C, using tensile testing and impact testing, for materials in the solution treated condition and previously deformed 45% by rolling at room temperature. The strength at elevated temperatures was studied using compression testing for materials in the solution treated, solution treated and aged (600°C/5 hrs), 45% deformed and 45% deformed and aged (600°C/5 hrs), conditions. The relationship of mechanical properties to the microstructure was also analysed.

The alloy in the solution treated condition has a metastable fcc structure. Deformation causes profuse deformation twinning and some ε martensite formation, which increases in amount with decreasing temperature. Both are responsible for the strengthening effects observed. Further strengthening is obtained by ageing the material in the range of temperature 474°C-650°C. This was attributed to ε formation and to diffusion of molybdenum atoms towards stacking faults and ε platelets.

Dynamic strain ageing effects occur within the temperature range 360°C-700°C and are attributed to the interaction of solute atoms, mainly molybdenum atoms, with dislocations. The strongest D.S.A. effect was observed at 550°C.

Tensile testing from room temperature to -196°C showed high ductility values, which indicated similarities with the TRIP steels. The modes of fracture were analysed by scanning electron microscopy. Ductile failure was observed from room temperature to -111°C and intergranular separation at -196°C.

CHAPTER I

INTRODUCTION

MULTIPHASE alloys form a family of cobalt-nickel base alloys which contain 20pct Cr, and 10pct Mo. The cobalt-nickel proportions vary from 60Co:10Ni to 30Co:40Ni. These alloys possess a very useful combination of properties namely, high strength, ductility, and excellent corrosion resistance.

The alloy under consideration (PROTASUL 10)* belongs to the family of the MULTIPHASE alloys. It is a wrought alloy which has developed from MP35N** alloy by adding different Ti contents (0.15-0.745) to enhance forgeability. These alloys are used for hip joints endoprostheses. Therefore the requirements of properties for its selection is rather demanding. The material must have high strength, good ductility, high fatigue strength, since the implant is subjected to a series of fluctuating stresses, good wear resistance and from the point of view of inertness the ideal implant should be capable of dissolution only in the passive mode when immersed in body fluids. It should be compatible with other alloys without provoking galvanic corrosion and should be resistant to

* Registered trademark of Sulzer Brothers Ltd, Switzerland
** Trademark of Standard Pressed Steel Company, USA

micromechanical corrosion.

Its use has also been extended to the aerospace industries, for high strength fastening elements, and to the marine industry for valves, shafts and other highly loaded parts where long lasting corrosion resistance to salt water is a key requirement.

Unlike most cobalt base alloys which are hardened by precipitation of intermetallic compounds or stable carbides, the MULTIPHASE alloys derive their strength mainly from mechanical deformation which induces phase transformation in the material.

In the solution treated condition these alloys are single-phased and possess a face centred cubic structure which is stable above $\sim 480^{\circ}C$-$980^{\circ}C$ depending on the alloy composition. Below $\sim 270^{\circ}C$-$740^{\circ}C$ the hcp is the stable structure. However the high temperature fcc structure persists on cooling to room temperature and below because transformation is sluggish. In the case of MP35N the fcc structure is stable above $650^{\circ}C$ and the hcp structure is stable below $425^{\circ}C$.

Transformation is induced by deformation, the amount of the transformed product being a function of the temperature and amount of deformation.

In the past, the high strength of the worked material has been entirely attributed to the strain induced hcp phase. A more recent study attributes the strength only to deformation twinning.

These controversies existent in the literature have led the present research in a direction to try to throw some light on this matter. Also detailed studies on the mechanical properties at low and at high temperatures had not been reported prior to the present work. Therefore, it was thought that would be interesting to cover the whole range of temperatures from sub-zero temperatures, i.e., -196°C, to elevated temperatures, i.e., 950°C. Special reference to the temperature transformation ranges of the fcc → hcp was given, trying to obtain a relationship between mechanical properties, phase transformations occurring and microstructure.

In order to fulfil this programme of work, plastic deformation at room and sub-zero temperatures (from ∿ 2% to ∿ 80%) was carried out to study the transformations that occur, in particular the formation of ε phase and/or twins. The annealing characteristics of such plastically deformed material and of the undeformed solution treated material were also studied. Recovery, precipitation and recrystallization were analysed for the higher temperature treatments.

X-ray analysis, optical and electron microscopy techniques were used to try to follow the changes occurring during the various treatments.

CHAPTER II

LITERATURE SURVEY

In order to understand the transformations undergone during deformation and on annealing, in the particular cobalt-based alloy considered in the present study, a general background is given on cobalt, its crystal structure and allotropic transformation and the role of alloying additions.

The phase diagrams that relate to the alloy studied, binaries, ternaries and quaternary are very briefly reviewed.

The work done on MULTIPHASE alloys, with particular attention to MP35N strengthening mechanisms and mechanical properties is also summarised. Finally, the basic theory of dynamic strain ageing and general fracture processes is briefly summarised.

II.1 The allotropic transformation in cobalt

Pure cobalt undergoes an allotropic transformation upon heating, from hexagonal closed packed (ε) to face centred cubic (α) ([1]). The ε phase is stable at temperatures below 417^{o}C and the α form is stable at higher temperatures up to the melting point. The lattice parameters (Å) for both allotropes are given below:

ε cobalt (h.c.p.)			α cobalt (f.c.c.)
a	c	c/a	a
2.5071	4.0686	1.6228	3.5441

The $\varepsilon \rightleftarrows \alpha$ transformation is sluggish; the fundamental reason is to be found in the very low free energy change associated with the transformation. Much of the high temperature phase (α) is retained on cooling through the transformation temperature. However, the retained α may be transformed at room temperature by plastic deformation ([2]) ([3]) ([4]).

The $\alpha \rightarrow \varepsilon$ transformation is martensitic, and is characterised by the following features:

1. The transformation is essentially athermal in nature.

2. In a thermal cycle of cooling and re-heating, the transformation is found to be reversible with, however, hysteresis being observed in the transformation temperatures. The temperatures at which the transformation begins on heating ($430^{o}C$) or cooling ($390^{o}C$) are independent of the heating rates.

3. The amount of the hcp ε cobalt which forms from the α cobalt is independent of grain size of the starting material.

4. The transformation occurs by shear with surface tilts being commonly observed. The crystallographic relationship between fcc and hcp phases are

$$\{111\}_{\alpha} \; // \{0001\}_{\varepsilon} \; : \; \langle 110 \rangle_{\alpha} \; // \; \langle 11\bar{2}0 \rangle_{\varepsilon}$$

II.2 The effect of alloying elements on the allotropic transformation of cobalt

Binary systems

The temperature at which the transformation from hcp to the fcc occurs is influenced by alloying elements. Therefore, alloying elements can be classified into two categories ([5]): i) ε stabilisers, ii) α stabilisers.

Giamei et al ([5]) proposed two types of equilibrium diagrams for the effect of alloying additions to cobalt (Fig. II.1). The full lines represent equilibrium phase boundaries and the dashed lines represent martensitic transformation temperatures. The mode of allotropic transformation characterized by the Ms and As temperature lines is a shear type diffusionless martensitic reaction. In Fig. II.1.a (type 1), the transformation will probably occur by a nucleation and growth mechanism, whereas in (type 2), the reaction temperatures are so low at higher solute concentrations that the only mode of transformation observed is the martensitic mode.

If the transformation temperature is raised, the fcc phase field is said to be constricted, while depression of the transformation leads to an enlarged α -field.

Fig. II.2 summarizes the change in transformation temperature produced by 1 atomic per cent of solute

metal, in terms of the atomic number of the solute ([6]).

Fig. II.3 ([1]) ([7]) summarizes the types of cobalt-rich equilibrium diagram produced by the solution of various solutes. In class I, the transformation temperatures are lowered.These are divided into class I.A, when there is a completely "open" α field where continuous solid solution between the terminal elements exists, and class I.B, where there is an "expanded" but "limited" α field, if continuous solid solution formation is prevented by one or more intermediate phases.

The alloying additions which tend to stabilise the α phase are iron, nickel, carbon, manganese, etc. While chromium, molybdenum, tungsten, etc. tend to stabilise the ε phase.

Fig. II.1.c, is a schematic representation of the type of phase diagram expected for cobalt alloyed with the refractory metals. Depending on the particular cobalt-refractory metal system, the Ms temperature may fall to below room temperature with increasing solute concentration. In alloys where the Ms lies below room temperature, the fcc α phase may occur at room temperature as a metastable phase due to suppression of the perictectoid reaction by rapid cooling. In such alloys deformation of this metastable fcc α phase may result in the transformation to the hcp ε phase.

It can be seen in Fig. II.4 ([7]) that the addition of molybdenum causes the temperature of the martensitic fcc→hcp transformation to fall and that of

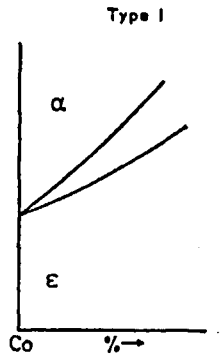


Fig. II.1.a - Type 1 Constricted $\mathcal{L}$ field

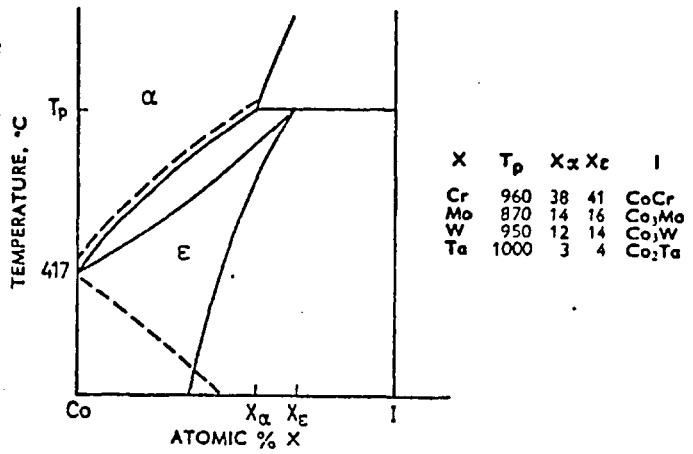


Fig. II.1.c Schematic equilibrium diagrams for cobalt alloyed with the refractory metals. Solid lines are equilibrium boundaries; dotted lines represent martensitic transformation temperatures

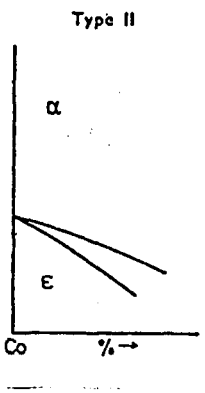


Fig. II.1.b - Type 2 Enlarged $\mathcal{L}$ field

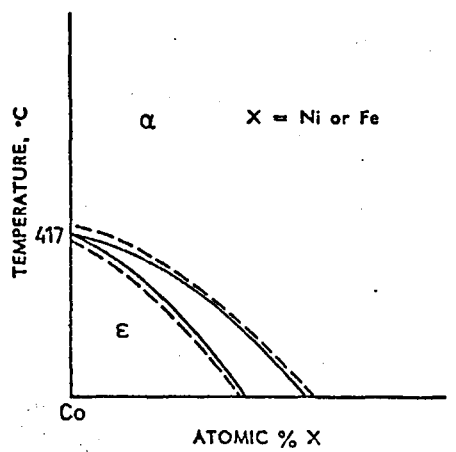


Fig. II.1.d - Schematic equilibrium diagrams for cobalt-base alloys containing nickel or iron. Solid lines are equilibrium boundaries; dotted lines represen martensitic transformation temperatures.

Fig. II.1 - Effects of alloying additions on the cobalt alloy phase diagrams (5)

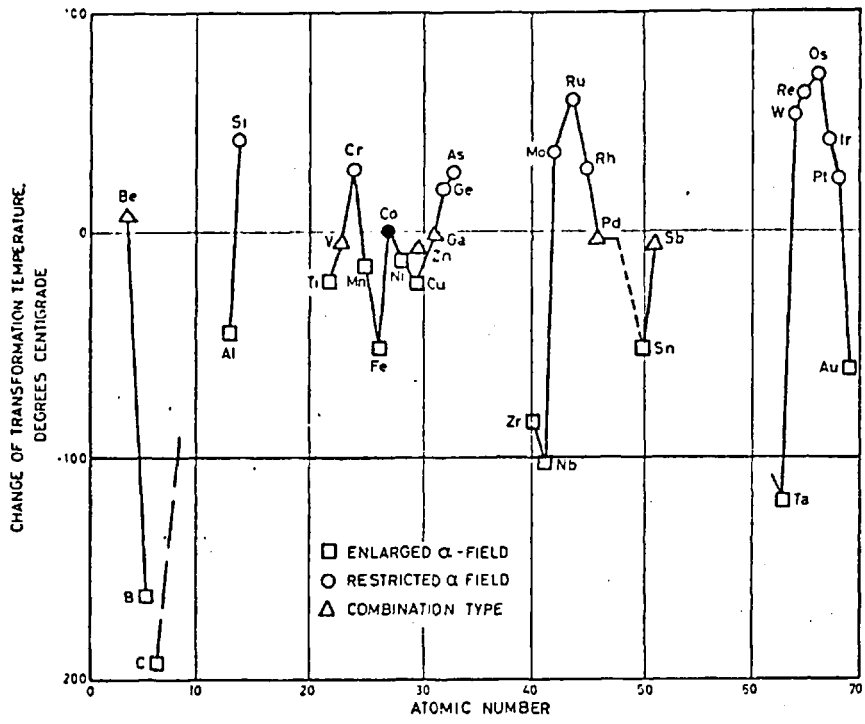


Fig. II.2 - Change in the transformation temperature of cobalt by 1 atomic per cent of alloying addition, in terms of the atomic numbers of the elements (6)

Li	Be ○											B □	C	N	O
Na	Mg											Al □	Si ○	P	S
K	Ca	Sc	Ti □	V ○	Cr ○	Mn ■	Fe ■	Co —	Ni ■	Cu □	Zn □	Ga	Ge ○	As ○	Se
Rb	Sr	Y	Zr □	Nb □	Mo ○	Tc	Ru ●	Rh ♂	Pd ■	Ag	Cd	In	Sn □	Sb ○	Te
Cs	Ba	Ce	Hf	Ta ○	W ○	Re ●	Or ●	Ir ♂	Pt ♂	Au	Hg	Tl	Pb	Bi	Po
1a	2a	3a	4a	5a	6a	7a	8_1	8_2	8_3	1b	2b	3b	4b	5b	6b

■ CLASS I A, OPEN α-FIELD

□ CLASS I B, EXPANDED α-FIELD

● CLASS II A, CLOSED α-FIELD

○ CLASS II B, CONTRACTED α-FIELD

♂ TRANSITION TEMPERATURE RAISED, BUT CONTINUOUS α SOLID SOLUTION.

Fig. II.3 - A tentative classification of cobalt binary systems (6)

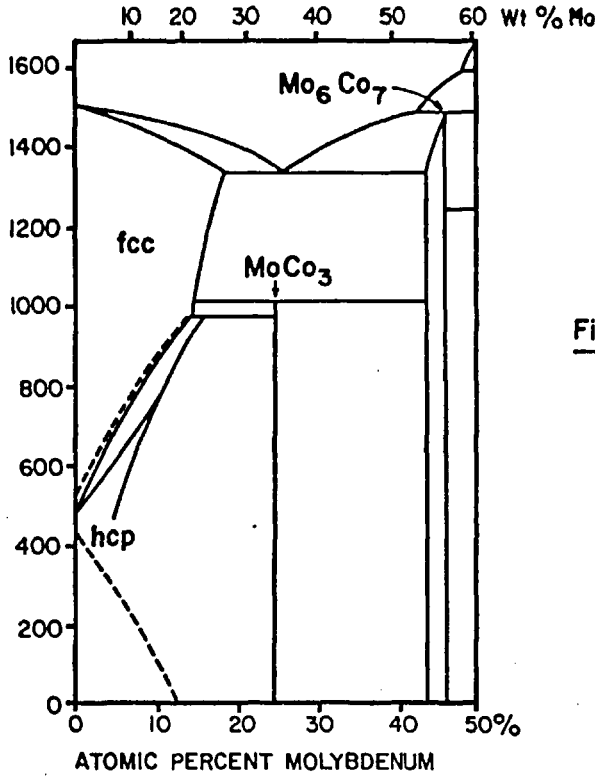


Fig.II.4. Cobalt rich section Co-Mo binary diagram (10) showing the martensitic---, and equilibrium modes——, of transformation of hcp/ fcc cobalt.

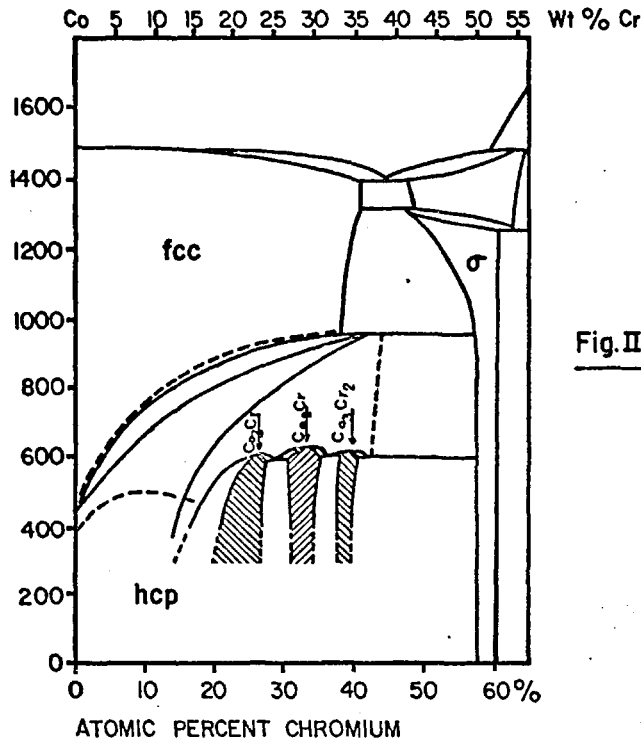


Fig.II.5. Cobalt rich section Co-Cr binary diagram (8),(10) showing the equilibrium mode of transformation and that the martensitic fcc/hcp is always above room temperature for less than 40% Cr.

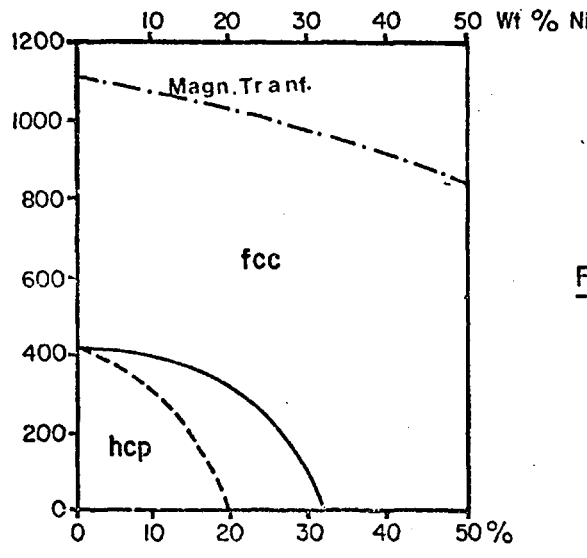


Fig.II.6. Co.Ni Binary System

the reverse transformation to rise. In alloys containing more than 12at% Mo the temperature of the martensitic fcc →hcp transformation falls to below room temperature which can cause the fcc phase to occur as a metastable phase at room temperature. In this system it appears that the equilibrium constitution is represented by $\alpha + Co_3Mo \rightleftharpoons \varepsilon$

Fig. II.5 shows the Co-Cr phase diagram. This provides an example of a system where the martensitic fcc to hcp temperature lies above room temperature even for high alloy additions (up to 40%wtCr). Apparently the allotropic transformation proceeds sufficiently rapidly in the alloys containing more than 15wt%Cr so that the reaction goes to completion before the Ms temperature is reached ([9]). This can be seen by looking at the TTT curve for the Co-Cr ([7]) (Fig. V.12.a).

The Co-Ni system is shown in Fig. II.6. Nickel forms a series of solid solutions with fcc cobalt. The ε and α two-phase region is shown in this figure, although its width is in dispute.

II.3 The ternary systems

The Co-Ni-Cr system

The isothermal section at 1200°C of this system is shown in Fig. II.7 ([11]) ([12]). At this temperature there is a very extensive face-centred cubic (α) solid solution representing solution of chromium in the cobalt-nickel alloys. The bcc solid solution of

cobalt and nickel in chromium (β) is less extensive. The cobalt-chromium σ-phase dissolves appreciable quantities of nickel and a small three-phase triangle exists as shown.

The Co-Ni-Mo system

This system as investigated by Beck (12) (Fig. II.8) at 1200°C is shown in Fig. II.8. At this temperature the face-centred cubic ternary solid solution is extensive; it may enter into equilibrium either with MoNi containing a relatively small amount of cobalt (δ) or with Mo_6Co_7 containing more than 20% nickel (μ). The fcc solid solution based on the cobalt-nickel α phase extends to 36% molybdenum on the nickel-molybdenum side and to 22.5% on the cobalt-molybdenum side of the diagram. The corner of the three-phase field on the α boundary is placed at 10% cobalt, 35% molybdenum, 55% nickel.

The Co-Cr-Mo system (Fig. II.9)

Fig. II.9 is an isothermal section at 1200°C of the Co-Cr-Mo (12) (13). The Cr-Mo σ-phase extends approximately half-way across the isothermal section in a field roughly parallel to the chromium-molybdenum side of the diagram. It will be recalled that the Co-Mo system contains a σ phase stable between 1620°C and 1250°C, while there is a similar phase stable from 1470°C to room temperature in the Co-Cr system. A ternary phase, designated R, is observed between the ends of the σ and

μ phases. At 1300°C the solid solution between the two σ phases arises.

The Ni-Cr-Mo system (Fig. II.10)

Fig. II.10 shows the isothermal section at 1200°C as determined by Beck (14). About three-quarters of the area of the diagram is covered by solid solutions of the α phase in the nickel corner and by the two-phase and three-phase fields in which α coexists with ε, σ, ρ, and δ phases. α, ε and σ coexist in a three-phase field whose boundaries are as follows: α corner 43%Cr, 53.5%Ni and 3.5 Mo; σ corner 49% Cr, 28% Ni and 23% Mo, and ε corner 60%Cr, 29.5% Ni and 10.5% Mo (wt%). The σ phase field is approximately parallel to the chromium-molybdenum side of the diagram, comprising a range of about 23 to 45% Cr. As molybdenum replace chromium in the σ structure, the lattice parameter expands.

II.4 The Quaternary system (Co-Cr-Ni-Mo)

This system has been investigated by Beck et al (14). At constant temperature a quaternary phase diagram is represented by a tetrahedron, each corner point of which corresponds to 100% of one component, the four faces of the tetrahedron, then, are isothermal sections of the four ternary systems and the six edges are isothermal binary systems. Fig. II.12 is a tentative construction of part of the quaternary Co-Ni-Cr-Mo system, at 1200°C (15).

In the quaternary Co-Ni-Cr-Mo at 1200°C, sections of constant molybdenum content are triangular sections through the tetrahedron parallel to the Cr-Ni-Co face. As the amount of molybdenum increases, the size of the equilateral triangle becomes smaller. Fig. II.11 shows an isothermal diagram at 1200°C in which the α phase boundary for the 5% Mo section through the Co-Ni-Cr-Mo system is plotted.

To identify the phases which coexist with the alpha phase in the quaternary system (14) some general statements can be made from observations of the Cr-Co-Mo and Cr-Ni-Mo ternary systems at 1200°C (Figs. II.9 and II.10). In the Co-Cr rich region of the diagram, the Mo content of α phase coexisting with σ phase ranges from 0 to approximately 12.5% Mo. The Mo content coexisting with R phase ranges from 12.5 to ~16% Mo. Above 16% Mo, the μ phase coexists with α . On the chromium-nickel side of the diagram, the α phase coexists with ε from 0 to 5% Mo, and with the ternary σ phase between 5 and 19%. The ternary P phase coexists with α on the chromium-nickel side between 19 and 33% Mo. The δ and quaternary α phases coexist over very limited compositional ranges, above 33% Mo. As the cobalt content increases, the solubility of molybdenum in the α phase decreases from 36% in the nickel-molybdenum binary system at 1200°C to 22.5% Mo in the cobalt-molybdenum system. Both the δ and μ phases, which coexist with α in the Co-Ni-Mo system

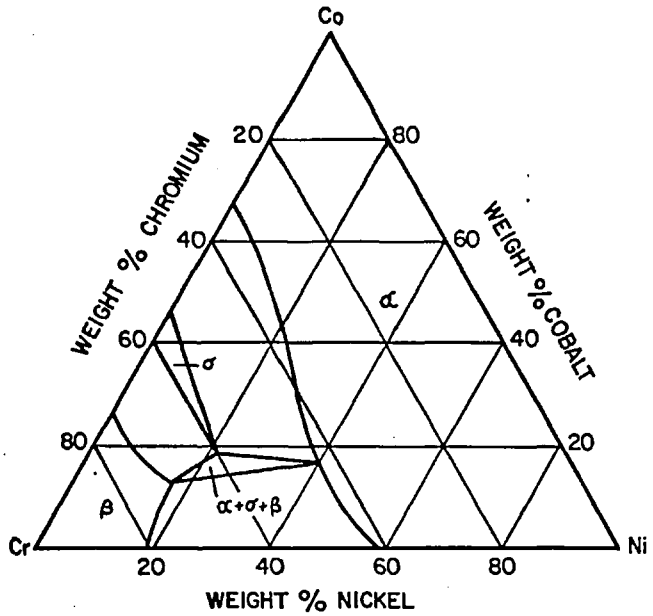


Fig.II.7. Isothermal section at 1200°C of the cobalt-chromium-nickel ternary phase diagram (after Rideout, Manly, Kamen, Lement and Beck.12).

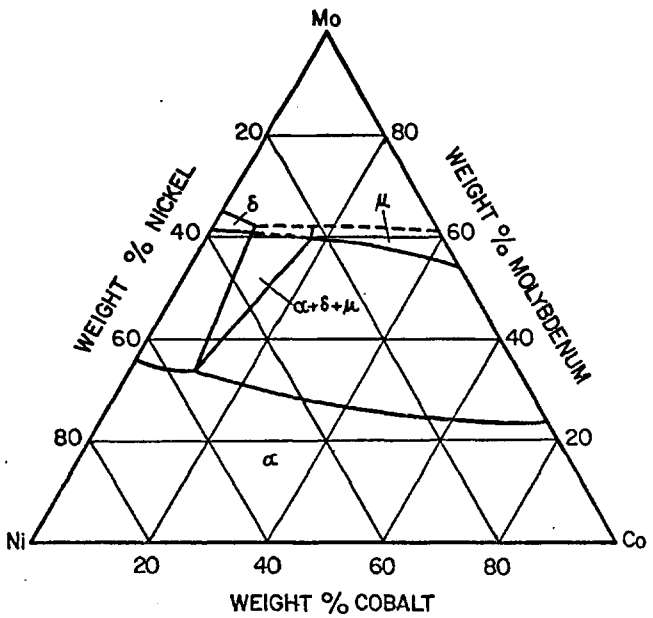


Fig.II.8. Isothermal section at 1200°C of the cobalt-nickel-molybdenum system (after Das, Rideout, and Beck.11).

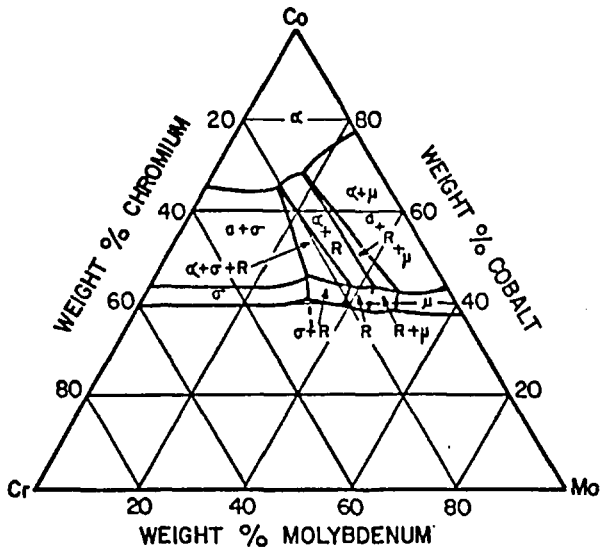


Fig.II. 9. Co-Cr-Mo ternary diagram at 2200°F(1200°C)

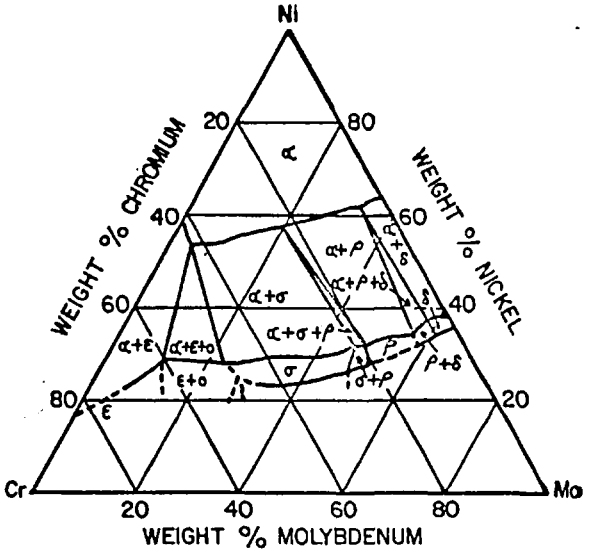


Fig.II.10. Ni-Cr-Mo ternary diagram at 2200°F (1200°C)

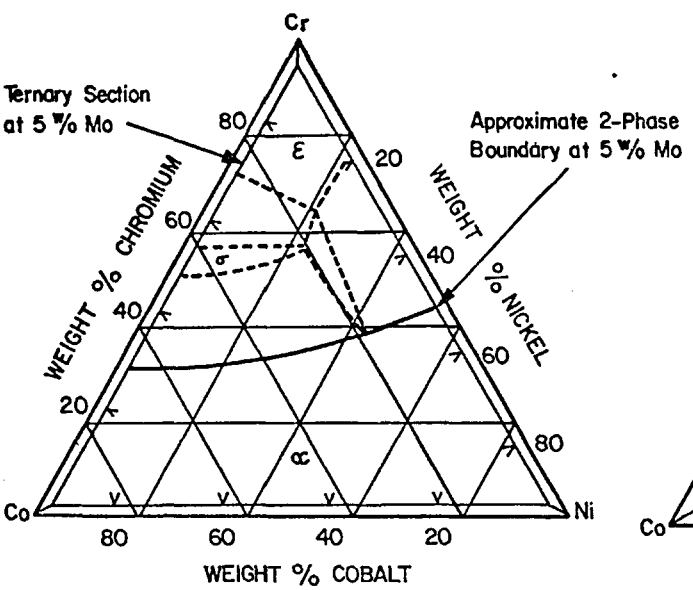


Fig.II.11. Co-Cr-Ni ternary diagram at 1200°C

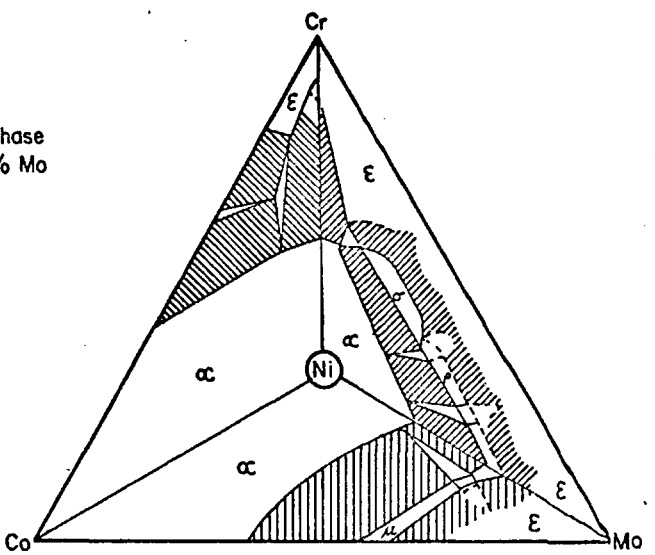


Fig.II.12. Tentative construction of the quaternary phase diagram Ni-Co-Cr-Mo at 1200°C

at 1200°C (Fig.II.8) are very hard, although their presence in α alloys does not appear to have nearly so drastic an effect on toughness as that of the sigma phase. The occurrence of the brittle inter-metallic σ phase in alloy systems involving the transition elements is interesting. The presence of σ , even in small amounts, in high temperature alloys is undesirable because of the brittleness which it imparts. The composition ranges over which sigma (σ) exists are, therefore, important. In the Cr-Ni-Mo ternary system at 1200°C, the σ phase coexists with α in alloys containing from 3.5 to 19% Mo. However, solid solutions of the cobalt-chromium σ phase penetrate deep into the 1200°C isothermal section of the Co-Cr-Mo ternary system, in this system σ coexists with α below 13% Mo.

The overall effect of molybdenum additions to the Cr-Co-Ni ternary system, is to decrease the extent of fcc (α) solid solution, e.g. in the 10% Mo section. σ phase coexists with the α solid solution at both chromium-cobalt and chromium-nickel extremes of the α -phase boundary. The α phase also coexists with ε and σ in a three-phase field near the chromium-nickel side of the diagram.

II.5 MULTIPHASE alloys - Mechanical properties and strengthening mechanisms

II.5.1 General Characteristics

The strengthening mechanisms in the MULTIPHASE

alloys have been studied by a number of workers ([16-19]). For example, Graham and Youngblood ([18]) studied the effect of swaging to about 20 pct at temperatures where the hcp phase is thermally stable (e.g. from 400°C to 900°C depending on composition). They observed an increase in the yield strength by more than a factor of two, compared to that of specimens swaged where the fcc polymorph is the only stable phase. The increase in strength is caused by deformation of the alloys and not a precipitation phenomenon, because the yield strength of the solution treated specimens which were not swaged did not increase.

Summarising, MULTIPHASE alloys consist of a single phase with a fcc structure. Working at room temperature by swaging, drawing, rolling or other cold forming techniques increases the yield strength to about three- to five-fold compared with the fully annealed condition, while maintaining a good ductility. There is a significant change in the microstructure that accompanies the pronounced increase in yield strength, which has been associated with the formation of hcp platelets in the fcc grains ([16,17,18]) or twinning ([20]). It has also been observed that the increase in yield strength depends upon composition. As shown in Fig. II.13 as the nickel content increases the yield strength decreases, for MULTIPHASE alloys, for the same amount of deformation.

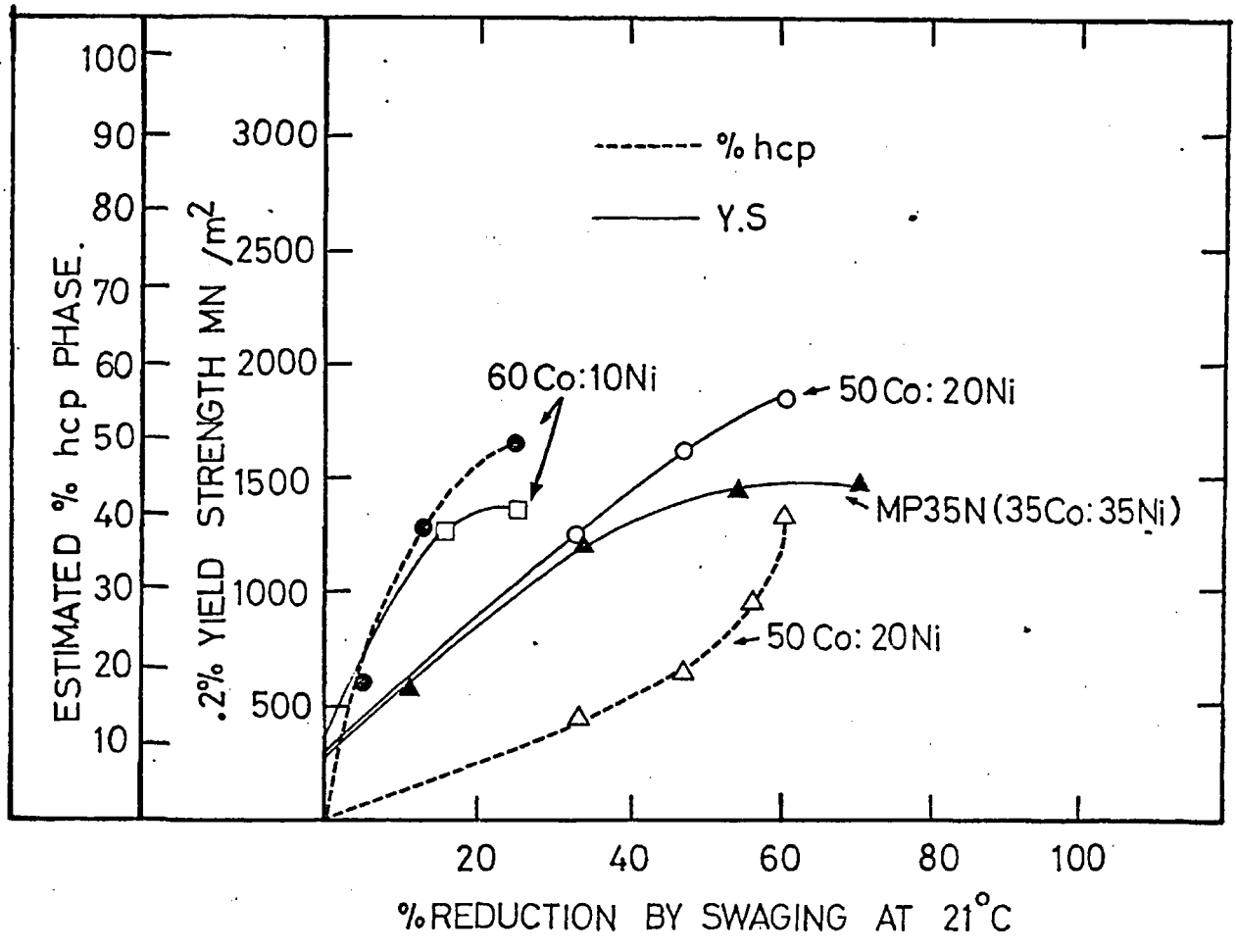


FIG. II.13 Effect of cold work on yield strength and amount of hcp phase formed in various MULTIPHASE alloys (16)(18).

II.5.2 Strengthening Mechanisms

II.5.2.a Deformation-induced Strengthening

Several authors ([16-19]) have related the deformation induced strengthening of MULTIPHASE alloys to the formation of fine ε hcp platelets in the fcc grains, which depends on the relative stability of the α and ε phases at room temperature. Although the ε phase is stable up to 425°C in MP35N, under equilibrium conditions (Fig. V.1), air cooling from the annealing temperature makes it possible to obtain an essentially fcc metastable structure at room temperature. The room temperature stacking-fault energy, γ, is rather low (25 mJ/m^2), and the Ms temperature for the martensitic-type $\alpha \rightarrow \varepsilon$ transformation is somewhat below room temperature. The martensitic transformation from the metastable fcc structure to the stable hcp structure can be achieved by mechanical deformation at room temperature. The extent of the $\alpha \rightarrow \varepsilon$ transformation increases with the amount of cold work and depends on the original grain size.

The $\alpha \rightarrow \varepsilon$ transformation occurs on the close-packed {111} planes of the fcc structure and results in the formation of thin hcp platelets which are coherent with the matrix ([16]). The coherency strains promote the formation, in each grain, of networks of ε platelets on intersecting sets of {111} planes. The presence of these networks leads to an increase in the material's strength, since the mobility of imperfections in the fcc matrix is considerably decreased.

The 0.2% offset yield strength is given by the relation

$$\sigma_y = \sigma_0 + K_y d^{-1/n} \quad (i)$$

where n=2 or 3, and d is the ε platelet interspacing which decreases as the amount of cold work increases.

This relationship is similar to the Hall-Petch type; it has been concluded (16) that the ε platelet interspacing, d, is the parameter that controls the deformation-induced strengthening of MP35N (35Co-35Ni-20Cr-10Mo). However, Viatour et al (21) have shown that the phase transformation does not begin until a certain deformation near to 18% has been exceeded. Above this, the amount of phase transformed rises linearly (10% increase in plastic deformation leads to a 5% volume increase of the hcp phase). These authors made an attempt to investigate the mechanism responsible for the alloy hardening by means of microplasticity and density measurements. They found the microplasticity curves show three distinct zones: (i) The first is linear and is characterized by $\sigma = E.\varepsilon$, Hooke's Law (σ= stress, ε = strain); (ii) In the second, microstrains start to occur when the stress exceeds a certain value, σ_0, and increase linearly with deformation according to a law of the $\sigma = E.\varepsilon$ type; this zone corresponds to the displacement of existing dislocations; (iii) The third is characterized by a parabolic increase of the microstrains; it extends beyond a certain stress σ_1, and it corresponds to the coming into play of the dislocation sources.

They found a relationship of the same type as the Petch law, except for the exponent.

The reasoning considers the operation of dislocation sources located at a grain boundary, and it is supposed that the first of them becomes active at stress σ_1, corresponding to a shear stress made up of the following components:(i) The stress required to move the generated dislocations. (ii) The stress which balances the opposing shear stress to the dislocations already generated, and to the grain boundary towards which the generated dislocation is moving.

In addition, to calculate the microplastic deformation, use is made of the equation: $\varepsilon_p = \frac{1}{2}bLu$

b = Burgers' vector; L = length of free dislocations per unit volume which contribute to the strain; u = mean distance crossed by each dislocation.

All this eventually leads to a relationship between the microstrain ε_p and the applied stress σ of the form:

(1) $$\varepsilon_p = K_3 d^{3/4}(\sigma - \sigma_1)^{9/4}$$

K_3 = a constant which depends on the material and on the law according to which the length of active source increases with increasing applied stress.

If $\sigma_{0.2}$ designates the 0.2%-offset yield strength, substitution in equation (1) gives:

(2) $$\sigma_{0.2} = \sigma_1 + \left(\frac{0.002}{K_3}\right)^{4/9} d^{-1/3}$$

The comparison of this theoretical expression with the experimental results showed slight differences. Therefore, since the theoretical model was based on a deformation mechanism in which the distance between hcp platelets is the only parameter involved, it is likely that other mechanisms contribute to the material's plastic deformation.

II.5.2.b Ageing-induced Strengthening

The structural changes observed on holding the MP35N alloy in the $\alpha + \varepsilon$ field (425°C - 650°C) have been attributed ([16]) to segregation of solute atoms on preferred sites. Depending on the time the cold-worked material is held in this temperature range, the following reactions have been reported to take place at the interfaces between the α matrix and the deformation-induced ε lamellae: i) segregation of Mo atoms; ii) formation of an fcc compound (a=3.54Å), possibly a metastable allotrope of Co_3Mo; iii) formation of the Co_3Mo equilibrium compound (ordered hexagonal DO_{19}, a = 5.13Å, c = 4.12Å)

Localisation of the segregated Mo atoms, at the interfaces between α matrix and the primary ε platelets retards the intervention of the dislocation sources; this accounts for the improved strength. The decrease in the lattice parameter of the α matrix during ageing agrees with this mechanism, since the atomic diameter of Mo is distinctly greater than that of cobalt, nickel and chromium;

the decreased parameter also indicates that it is the Mo atoms that diffuse towards the ε platelets (19).

II.5.3 Structural variables associated with the formation of hcp platelets in MULTIPHASE alloys

Some of the structural variables which have been associated (18) with the work strengthening and the stress-induced formation of the hcp platelets in MULTIPHASE alloys are:

a) c/a ratio of the hcp phase,

b) mechanical twinning of the hcp platelets,

c) mechanical twinning of the fcc phase

II.5.3.a c/a ratio of the hcp phase

The c/a ratio of 1.67 measured (18) for the hcp phase in cold worked 50Co:20Ni (20Cr10Mo) alloy is significantly greater than the ideal ratio 1.633 for the close-packed spheres. The high c/a ratio could account for the thinness of the hcp platelets and the high yield strength of MULTIPHASE alloys. Calculations based on X-ray data indicate that the interatomic spacing a on the close-packed {0001} hcp plane is the same as that on the {111} plane of the parent fcc phase. Therefore, the high c/a ratio is the result of an expansion in the c axis or the [0001] hcp direction. As a result of this expansion, the fcc phase between the first set of parallel hcp platelets formed would be in compression. The thicker a platelet

becomes, the greater is the compressive stress. The magnitude of the compressive stress on the fcc phase due to the high c/a ratio of two parallel hcp platelets can be estimated from the equation:

$$\sigma_c \doteq E \frac{[(c/a)\ \text{actual} - (c/a)\ \text{ideal}]\ t}{[(c/a)\ \text{ideal}]\ S}$$

E = Young's modulus, 233.2×10^3 MN/m^2 for MULTI-PHASE alloys

t = the thickness of the hcp platelets

S = the average platelet spacing

This compressive stress would tend to inhibit the formation of additional hcp platelets on {111} fcc planes parallel to the initial platelets. However, it would promote the formation of hcp platelets on an intersecting set of {111} fcc planes on which it has a high shear component. Because of the closely-spaced, intersecting network of hcp platelets developed in this manner within each grain, the movement of dislocations over large distances would become extremely difficult. It appears that the initial and major mode of deformation involves the formation of the hcp platelets. After severe deformation, the build-up of high internal stresses, locked in by the platelet network, should make further formation of additional hcp phase extremely difficult. Additional plastic strain could occur by twinning and ordinary slip, which do not increase the amount of hcp phase.

II.5.3.b Mechanical twinning in hcp platelets

A compressive stress perpendicular to the {0001} planes of a hcp platelet would favour the formation of mechanical $(10\bar{1}2)$ twins. In cold worked MULTIPHASE alloys, those mechanical twins could prevent an increase in the thickness of an existing hcp platelet by a stress-induced transformation. This transformation in pure cobalt and cobalt-rich alloys occurs by the passage of partial dislocations on the {111} planes of the parent fcc that are parallel to the {0001} plane of the existing hcp platelet. This parallel alignment ({0001} hcp// {111} fcc) is a necessary requirement for the easy movement of these partial dislocations. A $(10\bar{1}2)$ mechanical twin would be a barrier to the passage of the dislocations because the {0001} plane of the twin is almost perpendicular to the {111} fcc habit plane.

II.5.3.c Mechanical twinning in fcc phase

These mechanical twins are easily distinguished from annealing twins which are much wider than the area of a grain selected for electron diffraction. Graham and Youngblood (18) reported evidence of their existence.

Remy and Pineau (22) studied the influence of the SFE on plastic deformation modes in binary Co-33/35Ni, ternary Co-(30/35/40/45)Ni-14Cr and quaternary Co-(20/30)Ni - 14Cr - 5Mo. They found a relationship between SFE values and the prevailing mode of deformation

(slip, twinning and/or $\alpha \rightarrow \varepsilon$ martensitic transformation). This is discussed in Chapter V in relation to the results of the present work.

Measurements of the stacking fault energy values in the Co-Ni-Cr system have been made by several workers (23) (24) (25) (26); this is shown in Fig. II.14.

The transformation-induced product has also been studied (22) in relation to nickel content, temperature and amount of deformation.In the quaternary alloy Co-Ni-15Cr-5Mo twins and hcp platelets, co-existed in some temperature range below Md such that the domains of twinning and hcp martensite overlapped.

II.5.4 Mechanism of hcp nucleation

A nucleation mechanism for the transformation in Co-Ni alloy has been proposed (55). Cold-work enhances the nucleation process of the phase by introducing glissile a/2 <110> dislocations which may dissociate into a/6 <211> partial dislocations which bound a stacking fault, as suggested by Cohen and Weertman (24). The motion of the primary partial dislocation distorts the close-packed plane. The strain at the dislocation core and the change in lattice parameter help to nucleate a second partial dislocation two close-packed planes away. This creates two additional planes of product phase that will grow since the stacking fault energy is negative during the phase change.

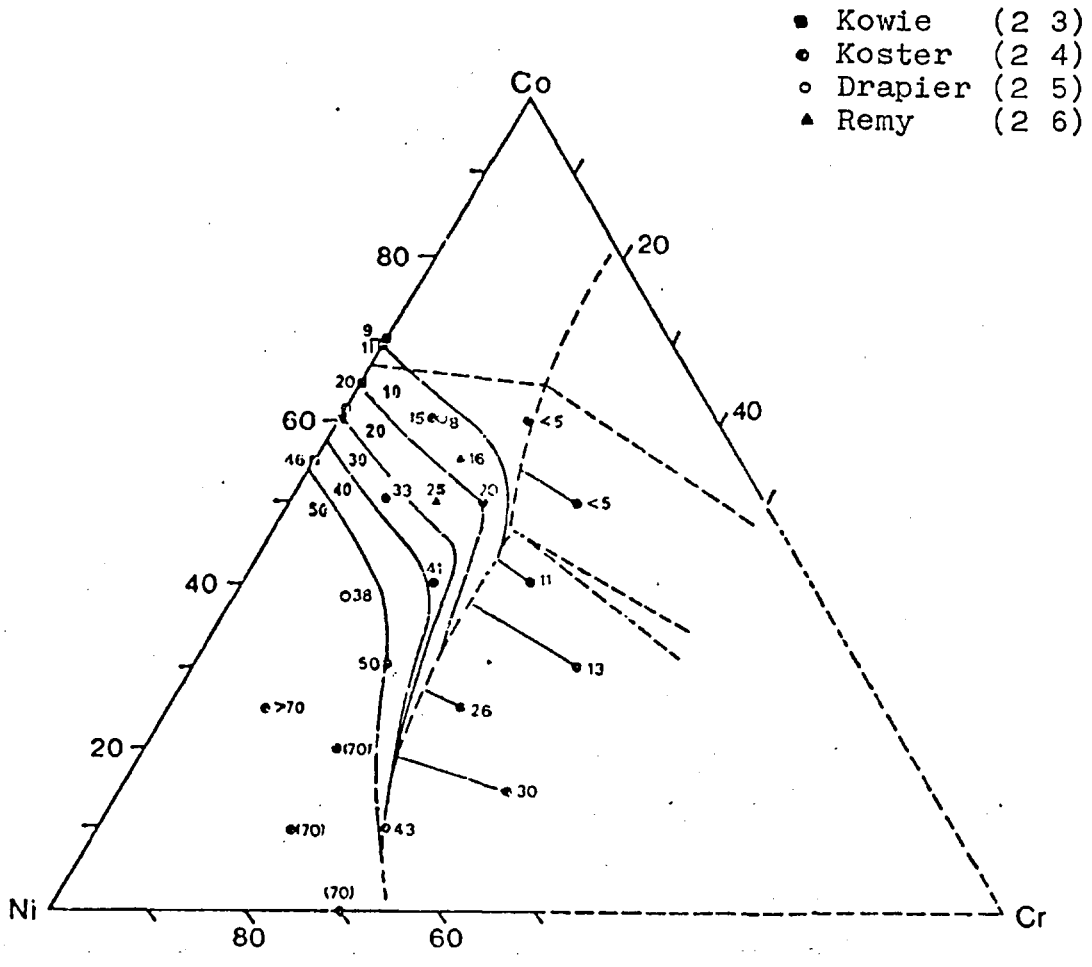


Fig. II.14 - Stacking fault energy in the Co-Ni-Cr system (mJ/m^2)

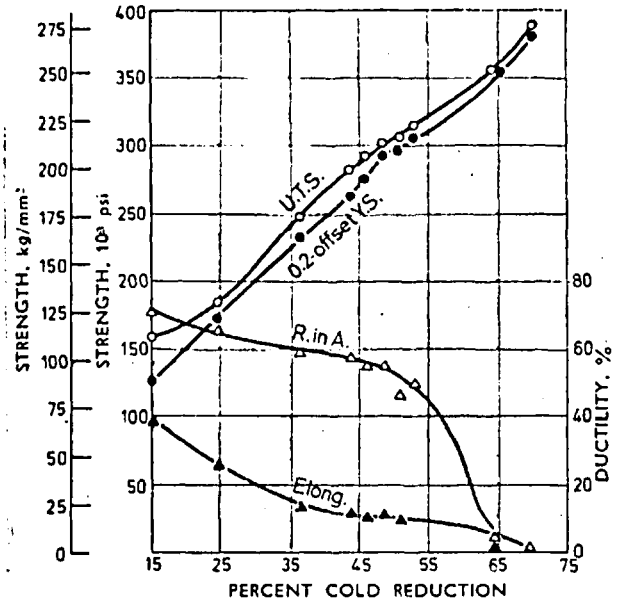
II.5.5 Mechanical properties of MP35N and Protasul-10

The mechanical properties of the quaternary 35Co-35Ni-20Cr-10Mo alloy (MP35N) and Protasul-10 (the same composition but with approximately 1% Ti added) have been investigated by several authors (16-19) and (27 - 40).

Figs. II.15 and II.16 show the strength and ductility for the cold-drawn MP35N as a function of the percentage of reduction and the effect of ageing respectively.

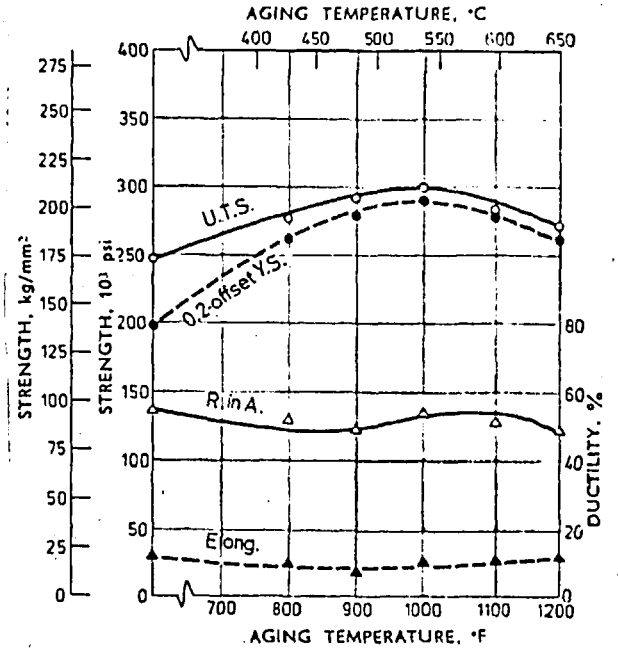
Figs. II.17 and II.18 compare MP35N and MP159 (another MULTIPHASE alloy: 36Co-25Ni-19Cr-9Fe-7Mo-3Ti) with some commercial alloys to show the comparison in properties.

MP35N can be strengthened to above 1,793 MN/m^2 (40) tensile strength with good ductility, by combining a phase transformation that is induced by cold work and an ageing reaction. Although the low temperature deformation has not been extensively studied, Montana has reported (40) the mechanical properties of MP35N cold worked 49% and aged. These results are given in Figs.II.19 and II.20. In these figures can be observed the relatively high ductility and notch toughness at sub-zero temperatures. Similar results have been found in a study of the deformation characteristics of metastable β-phase in a Ti-15wt%Mo (44) alloy, in which enhanced ductility and strengthening at low temperatures were attributed to twin formation.



Tensile properties of cold-drawn MP35N aged at 1100 °F for 4 hours.

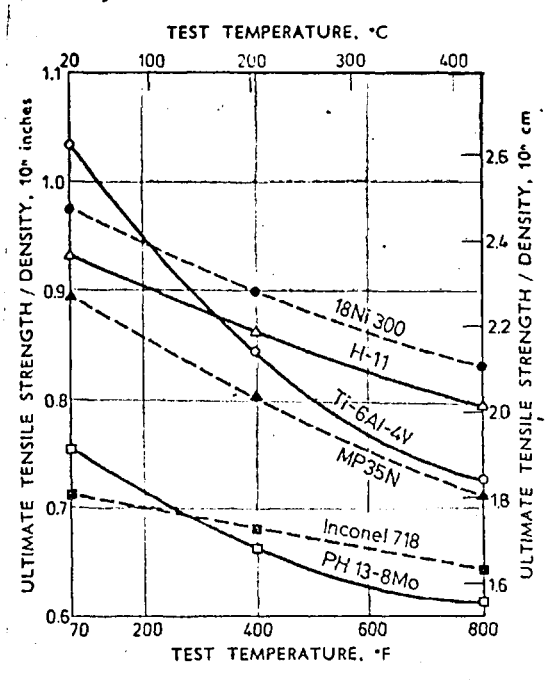
Fig. II.15 (43)



Effect of aging temperature on tensile properties of MP35N cold drawn 48·5%. Aging time : 4 hours. Points on the Y axis are for alloy in as-drawn condition.

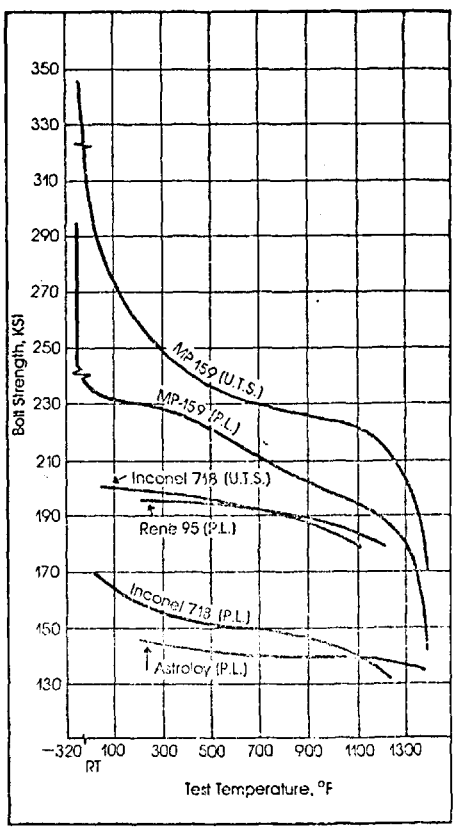
Fig. II. 16 (43)

Fig. II.17(43)



Comparison of short-time elevated-temperature strength / density of MP35N to several high-strength and corrosion-resistant alloys.

Fig. II.18(38)



Ultimate tensile strength (U.T.S.) and proportional limits (P.L.) of MP159 and Inconel 718 bolts and proportional limits of René 95 and Astroloy bolts.

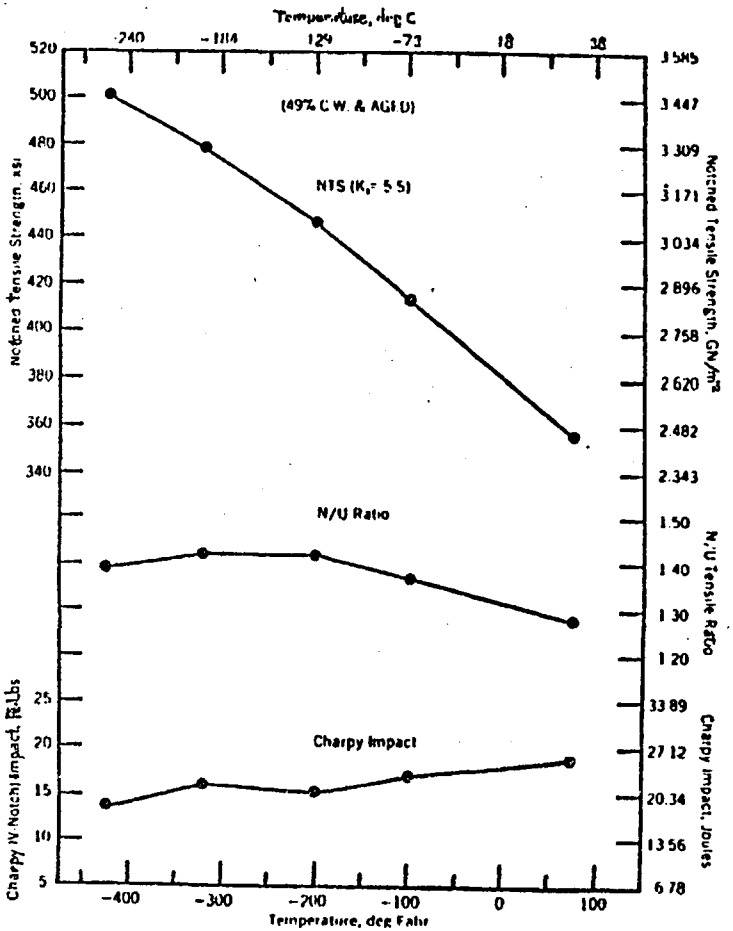


Fig. II.19 LOW TEMPERATURE NOTCHED PROPERTIES OF MP35N MULTIPHASE ALLOY LONGITUDINAL TENSILE SPECIMENS AND CHARPY IMPACT SPECIMENS (40)

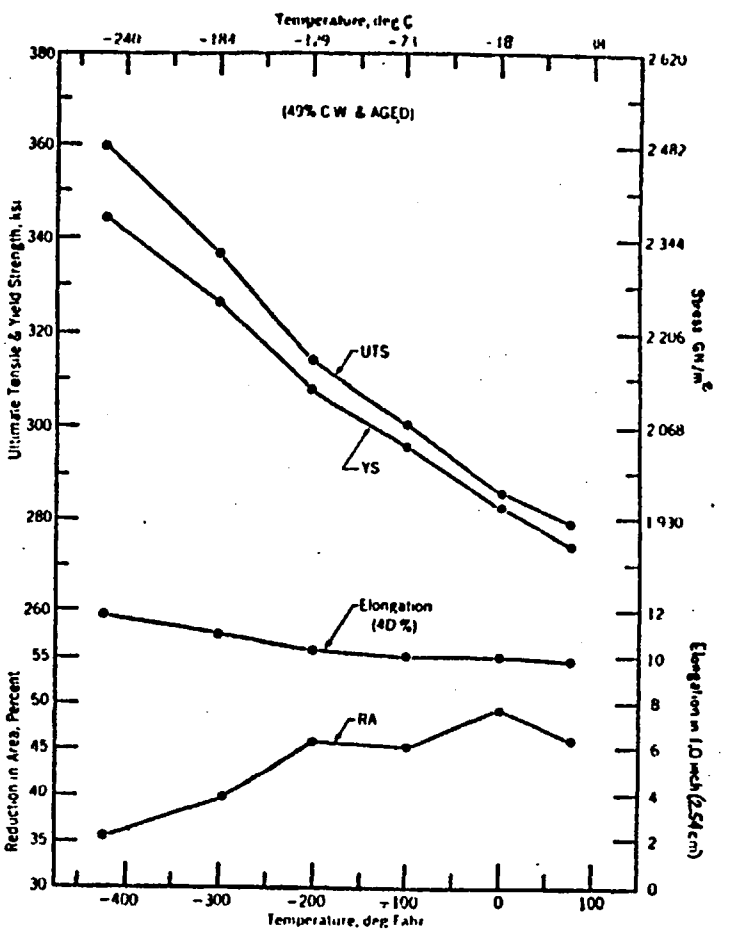


Fig. II.20 LOW TEMPERATURE MECHANICAL PROPERTIES OF MP35N MULTIPHASE ALLOY LONGITUDINAL TENSILE SPECIMENS .250 INCH (6.35 CM) DIAMETER (40)

II.6 Theoretical background to mechanical testing

II.6.1.a Strain Ageing

When solute atoms are sufficiently mobile to be able to diffuse to dislocations, they can slow down the freely moving dislocations by forming an 'atmosphere' around them. An increase in yield stress occurs, on ageing or during straining, being classified as 'static strain ageing' and 'dynamic strain ageing' respectively.

Numerous detailed studies of strain ageing caused by interstitial and substitutional atoms have been conducted in different materials having different crystal structures. The effects of substitutional solutes were fully reviewed by Brindley and Worthington (45) and interstitial atom effects were reviewed by Baird (46). In both cases the general characteristics are: a) increase in yield stress, b) rise in the ductile/brittle fracture temperature, c) high work hardening rate, d) serrated flow (The Portevin le Chatelier effect), e) plateaux or peaks in the temperature dependence of flow or proof stress curve, f) very low (or negative) strain-rate sensitivity, g) very low relaxation stresses, h) very low creep rate. Most of these effects can be explained as arising from the segregation of solute atoms to dislocations, producing pinning of the dislocations (46).

Some of these effects are summarized in Fig. II.21 (45), where a constant temperature is employed.

No yield point is observed on re-loading after resting the material under stress for short times, (Fig.II.21.b); over-straining removes the yield effects. However, when the test is stopped for longer times, the yield point returns on restarting the test (static strain-ageing), and the yield discontinuity is purely transient (Fig. II.21.c).

If precipitation or recovery occur during this period, then the level of the stress/strain curve will be raised (Fig. II.21.d) or lowered (Fig. II.21.e) respectively. If the test is performed at temperatures where solute diffusion can occur, the interaction of solute atoms with moving dislocations will produce repeated fluctuations in stress, and a serrated flow on the stress-strain curve will appear (Fig. II.21.f). This is termed dynamic strain ageing (DSA).

II.6.1.b Characteristics of dynamic strain ageing (DSA)

Dynamic strain-ageing effects occurring during the test can increase the tensile properties, fatigue strength and creep strength at moderately high temperatures (46). As has been mentioned above, DSA is characterized by the appearance of serrations in the stress/strain curve. It has been proposed that the onset of serrations coincides with the point at which effectively all mobile dislocations become locked by strain ageing at stages during the test, so that the stress increases until deformation is nucleated locally, with a sudden drop in stress when dislocation multiplication occurs. The fresh dislocations

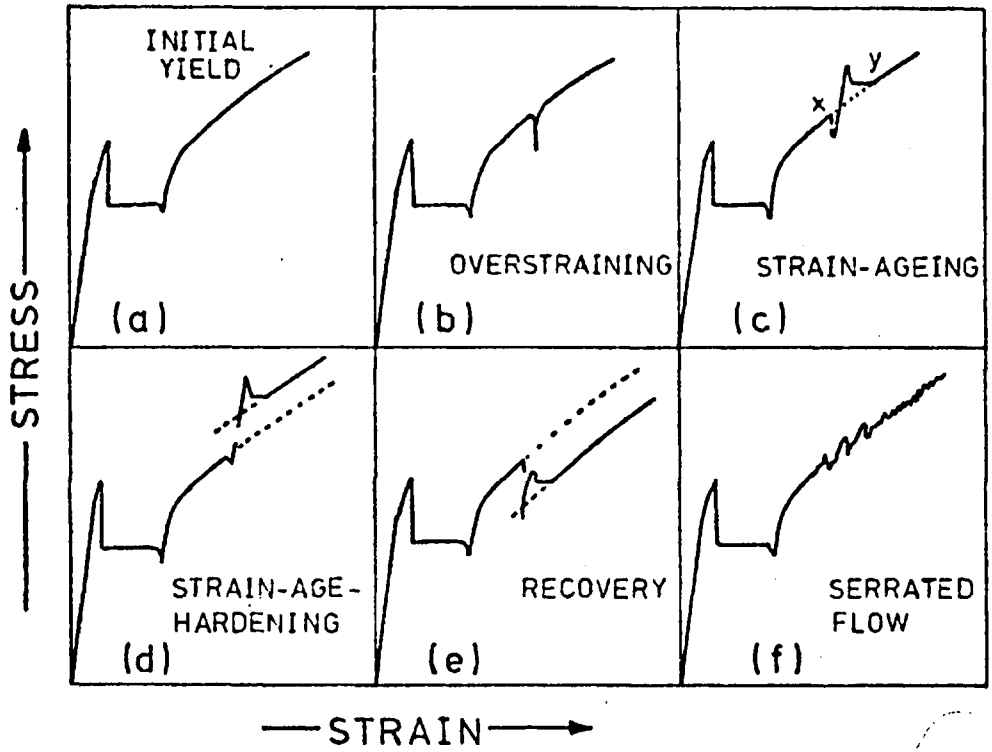
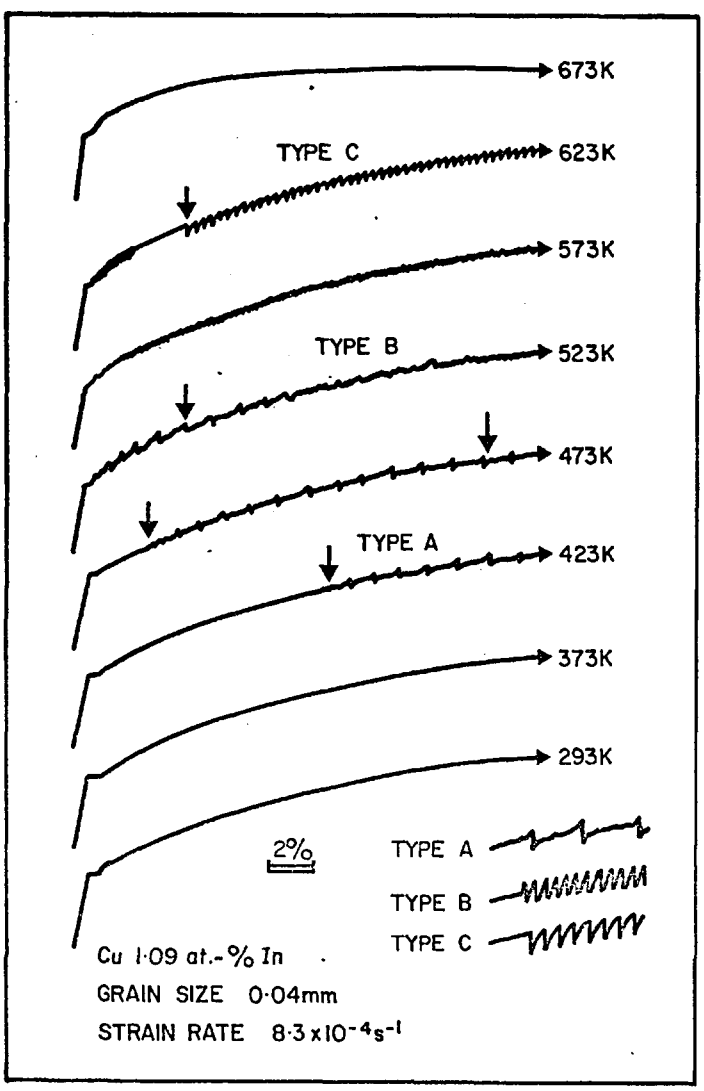


Figure II.21 Schematic diagrams of; (a) initial yield point, (b) Over straining, (c) strain ageing, (d) strain-age hardening, (e) Recovery, (f) Serrated flow.



are then pinned by diffusion of solute atoms and the process is repeated. At high temperatures the atmospheres become sufficiently mobile to move with dislocations so that they are never fully locked.

Three different types of serrations have been reported (45). Type A serrations rise above the general level of the stress/strain curve and are periodic in nature. Type B serrations, oscillate about the general level of the stress/strain curve and occur in rapid succession. Type C serrations fall below the general level of the stress/strain curve. All these different serrations appear in the alloys studied in the present work for certain temperatures and certain alloy conditions. Fig. II.22 (45) shows schematically the different types of serrations; the mechanisms by which they arise with different test conditions are dealt with in the Discussion Chapter. Therefore, only a very brief summary of the theoretical basis behind these effects is given here.

The solute atmospheres exert maximum drag on the dislocations when they move at some critical speed, v_c, given by (45) $\quad v_c = \frac{4D}{h}$

D = diffusion coefficient of the solute

h = effective radius of the solute atmosphere.

A critical strain rate exists, given by

$$\dot{\varepsilon}_c = b\rho v_c = \left[\frac{4b\rho}{h}\right] D$$

ρ = mobile dislocation density

If the moving dislocation density is considered to be strain dependent then a modified equation is given as: $\dot{\varepsilon}_c = K \cdot \varepsilon_c^{(m+\beta)}$

where, K, β and m are constants given by the variation of vacancy concentration with strain $C_v = B.\varepsilon^m$ and the variation of dislocation density with strain $\rho = N\varepsilon^{\beta}$

As indicated above DSA effects can arise from the presence of interstitial or substitutional atoms. The main difference is the high diffusion coefficients and high interaction energies with dislocations, presented by interstitial solutes compared with substitutional solutes. Thus, interstitial atoms produce marked strain-ageing effects in shorter times and at comparatively lower temperatures.

Dynamic strain-ageing due to interstitial atoms can occur at around room temperature in slow tensile deformation (46) at very high interstitial solute levels. However, at very high strain rates such as obtained in impact deformation, the effects appear at 400-670°C. Carbon and nitrogen are the main interstitial elements for DSA.

In substitutional alloys, it is found that a certain strain is required for the onset of serrations and this depends on the composition and the grain size. The higher the solute content the smaller the minimum strain to the onset of serrations. This minimum strain increases

with increasing grain size. At high temperatures the serrations disappear. The dislocation atmospheres are sufficiently mobile to exert little drag on the dislocations at the velocity involved.

II.6.2 Thermally Activated Deformation - Activation Parameters

Plastic deformation may be thermally assisted depending on time, temperature and strain rate. The determination of the possible rate controlling mechanisms involved has been extensively reviewed by Evans and Rawlings (47). The most relevant points will be briefly outlined below.

II.6.2.a Force on a dislocation and thermal activation

The maximum force required to move a dislocation through a slip plane corresponds to the sum of long-range forces (Fu) due to obstacles like dislocations on parallel slip planes or second phase particles, plus short-range forces (F*), which act over a few atomic distances only, e.g. motion of jogs on a screw dislocation or overcoming interstitial atoms. More energy is generally required to overcome a long range obstacle than a short range one.

The applied stress at $0^{o}K$ is given by

$$\tau = \frac{\bar{F}u + \bar{F}^*}{\rho.b}$$

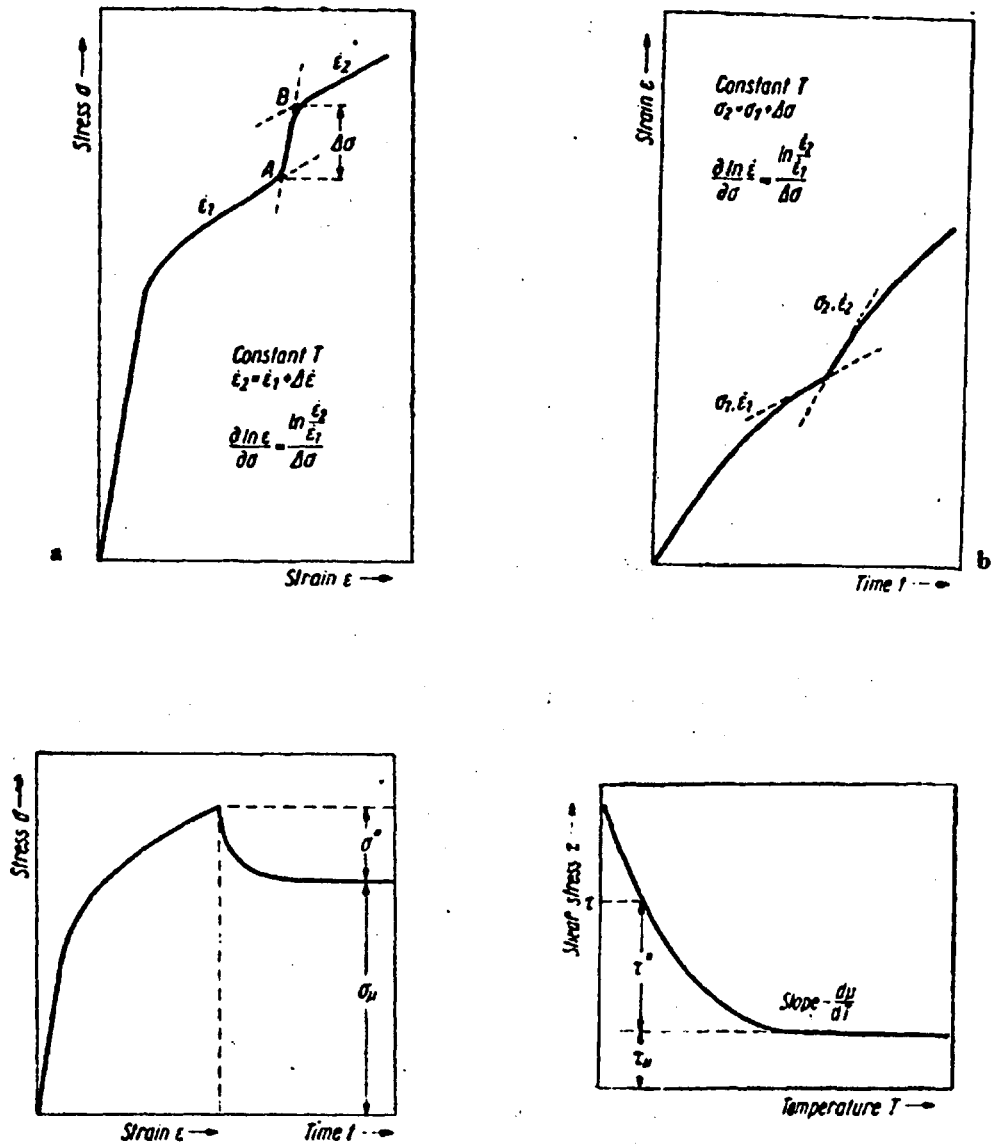
At any temperature above $0^{o}K$ atomic thermal fluctuations can assist the applied stress in overcoming obstacles and at sufficiently high temperatures all short-range obstacles can be overcome by thermal fluctuations, and the applied stress equals the stress to overcome long range obstacles, τ_u. Because of this temperature dependence τ^* is called (47) the thermal stress and τ_u is termed the athermal stress.

On this basis the activation parameters are calculated (47). The most important of these parameters are activation volume (V^*), activation area (A^*) and activation enthalpy (ΔH) and the total activation enthalpy, ΔH_o. Depending on the value of these parameters it is possible to identify the rate controlling deformation mechanisms.

II.6.2.b Experimental techniques of determination of the activation parameters

Evans and Rawlings (47) converted their activated parameters equations so that they contained only experimentally measurable quantities, i.e., temperature, strain rate and tensile stress.

Thus, activation volume and activation enthalpy can be determined from differential creep, differential constant strain rate tests and from stress relaxation experiments. These are shown schematically in Fig. II.23.



a

b

c. Determination of the athermal and thermal components of stress by the extrapolation procedure

Fig. II.23 - Determination of activation parameters(47) from:
a) change of strain rate
b) creep test
c) stress relaxation test

However, some requirements have to be met for the validity of the experimentally determined parameters, i.e., in a constant strain rate test, the equations are only valid if the applied stress is a unique function of temperature and strain rate.

The values for the thermal and athermal components of stress can be evaluated from the stress relaxation tests (Fig. II.23.c). However, relaxation can never be complete in a finite time, so, over the long relaxation period required, either recovery or dislocation pinning is likely to occur providing erroneous values of the athermal stress. On the other hand, the thermal stresses can only be determined unambiguously if the mobile dislocation density is stress independent.

The activation parameters are only significant if one type of obstacles controls the deformation rate. In general there are several types of obstacles in existence in a lattice and these may or may not contribute to the stress. If ΔH_o is found to be stress-dependent, positive identification of the rate-controlling obstacles is not possible.

The variation of the thermal stress with strain and the possible variations of activation volume and enthalpy, is important because it indicates whether the thermal mechanism depends in any way upon the dislocation density, point defect density, etc., or whether the mechanism itself changes with strain.

Most workers have assumed that the mobile dislocation density is stress independent and that the stress is a unique function of strain-rate and temperature. However, Evans and Rawlings (47) have conducted careful experiments to verify the various parts of the theory they proposed and they found close agreement between both.

II.6.3 Fracture Mechanisms

The macroscopic and microscopic features of the fracture surfaces give an insight into the ductility of a material and the mechanisms operating during fracture. This subject has been widely studied and reviewed by many authors (48)-(51). Therefore only a brief summary of the types of fracture is given here. The type of fracture relates to its mechanics, that is, how the loads are applied to the structure and how they are redistributed during the fracturing process. The kinds of fracture are: ductile, brittle, creep, fatigue and adiabatic shear.

Ductile fracture means the fracture proceeds slowly as the external loads supply energy to extend the crack. This process involves considerable plastic flow of the material adjacent to the crack.

Brittle fracture means the crack spreads rapidly and there is little plastic deformation during crack propagation. In creep fracture the crack is produced by applying the loads for a very long time and

in fatigue fracture it is formed by the repeated fluctuations of the load. Adiabatic shear fracture is produced by very rapid loading such that the heat generated by plastic straining has no time to flow throughout the crystal.

In a ductile material by altering the temperature, state of stresses or rate of loading, a brittle kind of fracture may be induced.

In bcc materials there is a strong temperature dependence of the modes of fracture. This is not so in fcc materials which fracture mainly in a ductile mode. However, phase transformations can notably influence the fracture mode. Very high elongation values and high strength may accompany phase transformations during plastic straining, and this has been studied extensively in TRIP steels (53) - (55). Suppression of necking and suppression of the initiation and propagation of micro-cracks by relaxation of stress concentrations due to the formation of the strain-induced martensites are characteristic of this effect. Fatigue crack propagation has also been studied in austenitic stainless steel (57), and crack growth rate was found to be relatively low when martensite was produced at the crack tip.

Maxwell (52) in a fractographic analysis in TRIP steels found that failure was strongly dependent on the presence of both strain-induced and stress-assisted martensite, and suggested that the mechanisms of failure

were: a) cleavage across the stress-assisted martensite plates, and b) decohesion at the interfaces between austenite and strain-induced martensite with subsequent void formation. Monteiro and Fonseca ([58]) observed ductile failure in 310 type alloy and an intergranular mode of fracture related to inclusions at the grain boundaries. However, in type 302 alloy, three different types of fracture were observed, at necking for each temperature. At 77°K fracture took place in a ductile manner with the martensite helping in the nucleation and propagation of cracks. At 193°K and above, strain-induced martensite relates to an effective blocking of necking and the fracture surface appears brittle. At higher temperatures 273 and 298°K, the fracture surface showed cleavage facets. In spite of the apparently brittle fracture, the uniform elongation was high, which indicates the large effect of the phase transformation on the ductility of this material.

CHAPTER III

EXPERIMENTAL PROCEDURE

III.1 Alloy Preparation

Table III.1 lists the alloys compositions. These alloys were provided by SULZER BROTHERS LTD., Winterthur, Switzerland, in the form of 25.4 mm diameter bars, one metre long. The chemical analyses given in Table III.1 were provided by SULZER. The main difference in composition between the two alloys was in the titanium content. Sulzer obtained the alloys as wrought material from the Latrobe Steel Company (U.S.A.), then subjected them to a special forging process; such bars are finally processed by Sulzer into an implant material known under the name PROTASUL-10 (registered trademark of the Sulzer-treated and finish-machined MP35N material). Since about 1975, Sulzer has been using only the alloy with 0.7% Ti, because the material can be consequently processed much better without the risk of cracks ([113]).

III.2 Specimen Preparation

The material was received in the recrystallized-annealed (1050±10°C) condition; this is a totally austenitic structure with low hardness. The as-received bars were cut in small pieces of about 7 cm length, and each piece was hot-rolled at 1100°C, with a reduction of 2 mm in each pass, to a final thickness of 5 mm. After this hot-rolling,

TABLE III.1

ALLOYS COMPOSITIONS

wt. %	C	Si	Mn	Cr	Ni	Mo	W	Ti	Co
Alloy B	0.026	0.066	0.036	20.0	35.68	10.0	0.1	0.15	Bal.
Alloy A	0.01	0.05	0.024	20.5	35.5	9.5	0.09	0.745	Bal.

the long strips were cut to about 5 cm long and 1.5 cm wide. Each small piece was ground to remove the oxide layer and surface irregularities and to make it flat and of uniform thickness (∿ 3 mm).

These specimens were homogenized at 1100°C for one hour in a furnace with an argon atmosphere, and water quenched. A cross section of a specimen heat treated in this way was examined to observe the thickness of the oxide layer, and microhardness tests were also carried out. It was found that the oxide layer was very small, easily removed by simple grinding in silicon carbide waterproof grinding paper. It was decided therefore that there was no necessity to seal these specimens in evacuated silica capsules for heat treatment annealing at 1100°C (½ hr).

After homogenization, these strips of an initial 3 mm thickness were rolled at room temperature, with interstage annealing, for 30 min at 1100°C in an argon atmosphere, to obtain samples to be subsequently given various degrees of deformation (0 to 87%), rolling at room temperature and at sub-zero temperatures, and to finish with a standard thickness of 0.5 mm strip. This time all the samples were sealed in silica tubes.

The samples were finally rolled at different temperatures: 20°C, -70°C, -196°C, with reductions of 5%, 10%, 20%, 30%, 40%, 50%, 65%, 80% and 87%, respectively, to give strips 0.5 mm thick. Sub-zero temperatures were achieved using different mixtures of acetone or methanol

and liquid nitrogen. The reductions during each rolling pass were quite small (e.g. 0.070 mm each pass) in order to minimize the increase in temperature. In the interval between passes, specimens were kept in the liquid medium which was held at the required temperature.

Hardness measurements, optical microscopy, X-ray analysis and electron microscopy were carried out on a sample of each strip of each different pct of deformation of each alloy. Since the compositions of both alloys were closely similar, except for Ti content, it was decided to perform further heat treatments and structural studies on only one of them; alloy A was selected. However, for mechanical properties tests specimens from both alloys were prepared and tested to observe the effect of Ti on the mechanical properties.

Reversion treatments of the deformed alloy (using times between 2 min and 30 min) were carried out in a salt bath at temperatures between 464°C and 700°C. These temperatures were chosen to take account of the fact that the transformation temperature (fcc ⇌ hcp) for MP35N lies in the range 425°C to 650°C.

The salt bath used was a mixture of sodium nitrate ($NaNO_3$) and potassium nitrate (KNO_3). One specimen for each pct of deformation at room temperature and one specimen of 50% deformed at -70°C were taken. The whole batch of deformed samples was introduced together into the salt bath for each time-temperature treatment, in

order to keep the same conditions for all the specimens. After the treatments, the specimens were quenched in water as rapidly as possible. For treatments of 2 minutes, specimens rolled at -196°C (liquid nitrogen temp.) 65% and 80% were also included in the batch.

Hardness measurements, X-ray analysis and optical microscopy examination were carried out on each of these samples.

After rolling, the strips were cut into small samples (5 mm x 10 mm x 0.5 mm), using a Macrotome 2 precision cutting machine. Each required sample was surface ground on water-cooled emery wheels down to 600 grade paper.

Further heat treatments of duration from 5 hrs to 100 hrs were carried out on samples from each degree of deformation for specimens previously rolled at room temperature and at -196°C. The specimens were wrapped in molybdenum foil and sealed in argon filled silica capsules. The molybdenum foil was used for preventing specimens from sticking together. After heat treatments the capsules were broken under water to ensure a rapid quench.

Optical and electron microscopy, X-ray diffraction analysis and hardness measurements were used to study each of these samples.

III.3 Hardness Measurements

The specimens were ground to remove the thin

oxide layer formed on quenching, on a water cooled rotary grinding wheel, using waterproof silicon carbide paper 600 grade.

Hardness measurements were made on each deformed sample, using a Vickers' testing machine with a 20 Kg load. For each specimen, the mean value of 10 readings was taken. The standard deviation was assessed using the relationship:

$$D = \frac{5 \Sigma d}{4n \sqrt{n-1}}$$

D = standard deviation
d = deviation from mean value
n = number of measurements

The standard deviations calculated from the results obtained were of the order of ± 1 to ± 3 units.

III.4 Metallography

Samples from each different deformation were examined by optical microscopy. The final polishing was done on horizontal wheels with "selvyt cloth" impregnated with 3 and 1 μ diamond paste. The specimens were very difficult indeed, to attack. Several solutions were tried, chemically and electrolytically. Finally one solution was found which gave good results for revealing the general structure. This was [HCl(8 ml), HNO_3(0.5 ml), glycerin (2 ml), cupric chloride (50-150 mg)] chemical etching solution $\sim 2\frac{1}{2}$ minutes.

Photo-micrography was carried out for the most relevant microstructures.

III.5 X-ray Analysis

X-ray analysis was carried out for each sample from each different deformation from each ageing temperature.

The instrument used was a Phillips p w 1050/25 diffractometer with a monochromator attached in order to select the wavelength diffracted from the sample rather than the primary beam, to improve resolution and to eliminate unwanted x-rays from the tube target. The output goes to a fast-acting automatic recorder. The paper chart on the recorder moves at a constant speed so that the distances along the length of the chart are proportional to 2θ.

The "d" values are determined from each reflection by measuring the Bragg angle θ and using the Bragg Law: $\lambda = 2d \sin\theta$ (63)

Copper K_{α_2} and cobalt radiation were used; the values of $\lambda_{CuK\alpha_2} = 1.542$, and λ Co = $K\alpha = 1.79021$, $K\alpha_1 = 1.78092$ $K\alpha_2 = 1.79278$. An anode voltage of 40 KV and a current of 35 mA were used for all the analyses. The relative intensities were estimated by chart inspection. The "d" values for the fcc matrix were calculated by:

$$d = \frac{a}{\sqrt{h^2+K^2+1^2}} = \frac{\lambda}{2\sin\theta}$$

$$\frac{1}{d^2} = \frac{4}{3}\left\{\frac{h^2+h^k+k^2}{a^2}\right\} + \frac{l^2}{c^2}$$

Cobalt radiation was used to compare with previous analysis done using copper radiation. Precise lattice parameter measurements ([3]) were calculated for each condition, by computing "a" for each peak on the pattern and plotting against $\left(\frac{\cos^2\theta}{\sin\theta} + \frac{\cos^2\theta}{\theta}\right)$; a straight line results and a_o, the true lattice parameter value is found by extrapolating the line to zero values. This expression holds quite accurately down to very low values of θ.

III.6 Transmission Electron Microscopy

Samples of $\sim$ 0.5 mm thick were thinned to 0.2 mm by grinding on water-cooled emery wheels down to 800 grade paper. 3 mm diameter discs were prepared by spark cutting from the thinned material. Electropolishing was carried out by a two stage technique. The first polishing stage was made using a vertical jet of about 1.2 mm diameter. The electrolyte was supplied through a vertical inlet tube by gravity feed from a reservoir. The electrolyte was recirculated by the use of a minipump.

The electrolyte used in the first stage was 1 $HClO_4$ + 10 acetic acid, maintained at about 15°C; the applied potential was 80 volts and the current was controlled at 20 mA. The polishing rate was calculated to be about 20μm/min. The profile was made on both sides of the specimen to have a thickness in the centre of the disc of approximately 10 μm. The second stage of the

electropolishing was made by holding the disc with a pair of tweezers in a beaker containing the electrolyte (with a stainless steel strip serving as the cathode). The second stage electrolyte was 80 ml methanol, 20 ml concentrated H_2SO_4 and 5 ml of 85% H_3PO_4;[64] maintained at about 10°C; the applied potential was 4 ± 1 volts and the current was kept at 0.08 A. A light was held behind the beaker. Electropolishing in these conditions was carried out until the moment of perforation, signalled by a flash of light. At this point, the polishing current was interrupted and the sample was removed, throroughly rinsed and dried. Subsequently, foils were prepared using a Struers automatic apparatus. A thin foil is produced by electrolytical removal of metal from both sides. When a hole is produced, it is detected by a photocell and the process is interrupted and at the same time an "alarm" is activated. The specimen was then removed very quickly and immediately immersed in a clean solution of ethanol. The foils were passed through three sets of clean ethanol to ensure absolute removal of the electrolyte, before being allowed to dry. The electrolyte used was 1 part of perchloric acid + 10 parts of acetic acid at room temperature.

The foils were examined using a Philips EM301, 100KV transmission electron microscope.

In order to identify some of the particles present in some foils an extraction replica technique was applied and the replicas were examined in the Philips TEM.

III.7 Mechanical Properties

III.7.a Tensile testing

Initially small flat tensile specimens were made of the dimensions shown in Fig. III.1.a. These specimens after stamping were annealed for 30 min at 1100°C in an argon atmosphere, and water quenched. The edges of the specimens were ground to avoid crack initiation sites and the surfaces along the gauge length were electro-polished to obtain a good surface finish.

Tensile tests on these specimens were unsatisfactory, giving considerable scatter in the tensile properties. After testing up to fracture, the 'grip' portions of the specimens were very deformed and the holes elongated, therefore, these specimens were discarded for tensile test. However, they were used to give relatively small percentages of deformation (2%, 5%, 10%, 17%, 20%, 25% and 30%) at room temperature and -196°C to compare with the samples rolled approximately the same amounts, by transmission electron microscopy. A 3 mm disc was cut in the spark machine from the centre of the gauge length and examined by transmission electron microscopy and optical microscopy to see the appearance of the slip lines on the surface.

Round tensile specimens British Standards No. 12, dimensions given in Fig. III.1.b were made and tested. To prepare these specimens the original bars were hot rolled at 1100°C to a final thickness of 1 cm and then

homogenized for 30 min to 1100°C in an argon atmosphere. The specimens were machined so that the gauge length was parallel to the rolling direction. These specimens when tested at low temperatures proved to be too strong for the stainless steel grips available and the grips cracked before the specimen fractured.

Accordingly a third choice of specimens was selected, the British Standards No. 11 double headed round tensile specimens, dimensions shown in Fig. III.1.c. These specimens were machined from the same bars as the previous ones. Since these specimens proved to be satisfactory, in order to compare deformed and undeformed material, other set of specimens were prepared. The hot rolled plus annealed at 1100°C bars were cold rolled 45%; 0.2 mm was taken off in each rolling pass. Care was taken that the temperature did not rise above room temperature. This was done by immersing the specimens in cold water. In this case, as in the previous ones, the specimens were machined so that the gauge length was parallel to the rolling direction. Impact test specimens and compression specimen were also prepared from these bars so that the larger dimension was parallel to the rolling direction.

Both materials deformed 45% and undeformed solution treated from both alloys A and B were tested at various temperatures from room temperature to -196°C (i.e., 20°C, 2°C, -12°C, -35°C, -50°C, -70°C, -80°C, -105°C, -111°C, -196°C). A sample from the received material

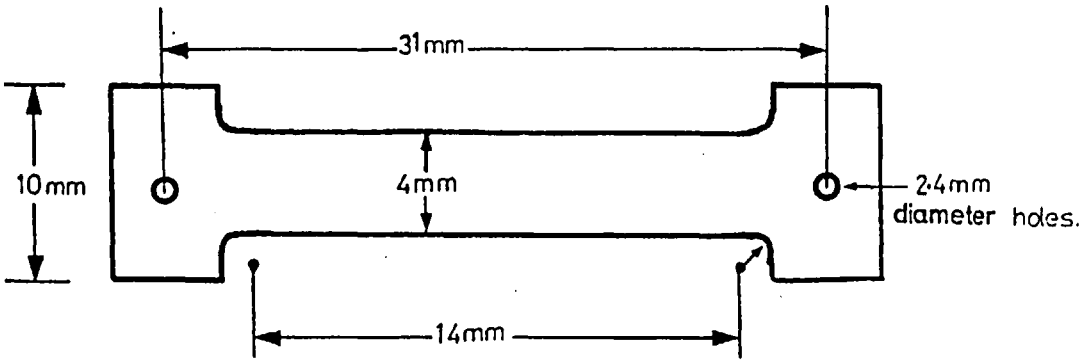


FIG III.1a. Flat tensile specimen.

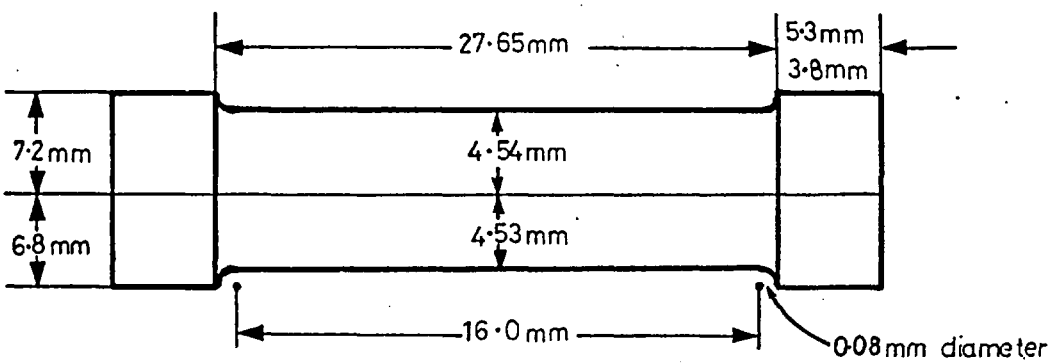


FIG.III.1b Round tensile specimen. No.12

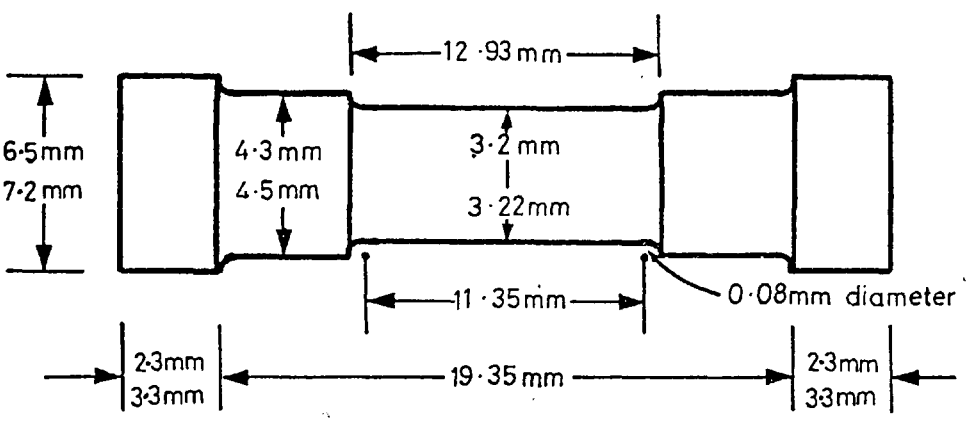


FIG. III.1c Round tensile specimen No.11

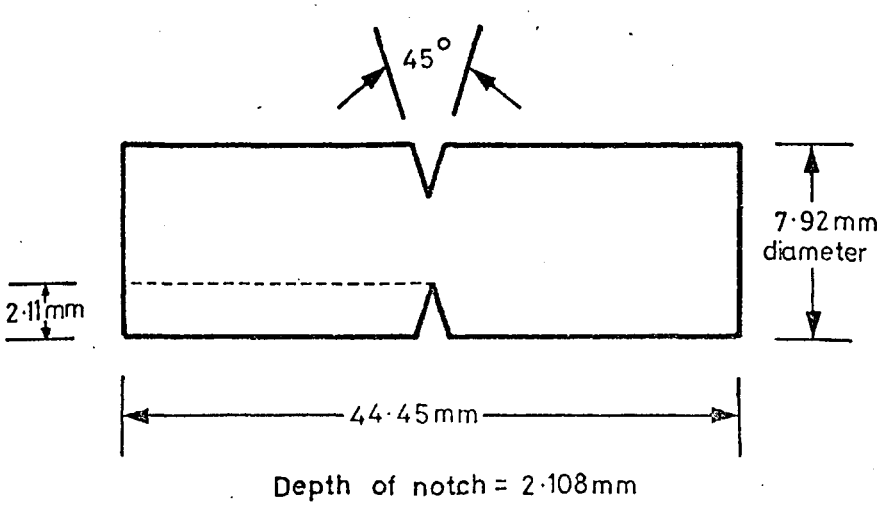


FIG.III.2 Notched impact testing specimens.

was also tested at these temperatures. Most of the tests were duplicated for checking, and good agreements were obtained most of the times.

The fracture surfaces of both alloys from each test temperature were examined under a Cambridge scanning electron microscope. In order to determine the composition of certain particles and features observed in the fractured samples, the Jeol 35 scanning electron microscope was used, which by means of a wavelength dispersive X-ray spectrometer permits micro-area X-ray analysis. This provides only qualitative information of the chemical elements present but not quantitative. Different degrees of deformation were also performed in the specimens (from 10% to 50%) at room temperature and from 10% to 30% at -196°C. Discs were prepared from the centres of the gauge length cut at 45° to the tensile axis, in a slitting wheel machine; these discs were ground to about 300 μm thickness. 3 mm diameter discs were cut from them, to prepare specimens to be examined by transmission electron microscopy. This aimed to study deformation processes in the plane of maximum shear stress. Also it was intended to compare the effects of these deformations with those resulting from rolling to the same percentage deformations.

All the specimens were tested in an Instron machine, at a cross-head speed of 0.05 cm/min, i.e., an initial strain rate $\dot{\varepsilon} = 4.34 \times 10^{-3}$ sec $^{-1}$, where strain rate, $\dot{\varepsilon}$ = crosshead speed/gauge length. For the specimens

tested at low temperatures the whole jig was immersed in a flask filled with different mixtures depending on the required temperature, i.e. for temperatures down to -20°C a "cardice" mixture was used (CO_2) and for temperatures down to -120°C, mixtures of liquid nitrogen and acetone and liquid nitrogen and methanol were used.

True stress - true strain curves were plotted from the load-elongation charts. A computer program was written (Appendix IV) to calculate these values directly from the load-elongation graphs. The program makes corrections for the elastic contribution of the machine and calculates the values of true stress and true strain, elongation and reduction of area, as follows:

$$\text{True} = \frac{L}{A_o}(e + 1) \; ; \; \varepsilon_{true} = \text{Ln}\,(e+1)$$

L = Load

A_o = initial area of the specimen

e = conventional linear strain or engineering strain

$$e = \frac{d \times XS}{CS \times Lo}$$

d = distance from the chart

XS = cross-head speed

CS = chart speed

Lo = initial gauge length

The true stress and true strain at fracture are calculated from $\sigma_f = \frac{L_f}{A_f}$; $\varepsilon_f = \frac{\text{Ln}A_o}{A_f} = 2\text{Ln}\frac{D_o}{D_f}$

where Lf = load at fracture

Do = initial diameter

Df = final diameter - diameter of the neck after fracture

q = reduction of area $= \frac{A_o - A_f}{A_o}$

Af = area after fracture

these values of q were checked with the relationship of true strain at fracture, i.e., $\varepsilon_f = \text{Ln}\frac{1}{1-q}$ and were in good agreement.

Elongation values were calculated by $\frac{lf - lo}{lo}$

lf = final gauge length, and these values were checked with the values obtained from the load-elongation charts, giving also good agreement.

III.7.b Impact Testing

Impact testing using notched specimens described in Fig. III.2, was carried out on both alloys, homogenized and 45% previously deformed. The tests were made at different temperatures ranging from room temperature to -196°C. A Hounsfield balance impact machine was used. The specimens were immersed in different mixtures for about 15 min or until the desired temperature was reached and then they were immediately placed in the machine and the test was performed.

The fracture surfaces of several specimens tested at different temperatures were examined in a

Cambridge scanning electron microscope.

III.7.c Compression Testing

Compression specimens of dimension 2.5 x 2.5 x 6 mm were prepared from the homogenized bar and from the 45% cold work material; for both alloys the specimens were prepared so that the longer dimension (6 mm) was in the rolling direction. One set of specimens from each of the conditions for both alloys was chosen to be aged at 600°C for 5 hrs. These specimens were sealed in evacuated silica capsules containing a third of an atmosphere of argon and water quenched after the treatment. The specimens were tested in the range from room temperature to 800°C, at intervals of 50°C from 350°C to 700°C. Each specimen was ground at both ends using an "adapted grinding jig" to assure flat opposite parallel sites, before the test.

Test Procedure

This test was performed following the same procedure of previous works ([106]). The compression specimens were tested in a 5 Ton Instron Universal testing machine fitted with a special rig and furnace attachment on the underside of the crosshead. The specimens were positioned between the main alumina rams of the machine separated from them by hot pressed silicon nitride spacing blocks. They were left in the furnace for 20 min

to obtain a stable temperature. The temperature was measured using a thermocouple attached to one of the alumina rams with the tip at the same level as the specimen. For tests above 550°C a continuous slow stream of high purity argon was passed through the specimen chamber.

Once the specimen reached the required temperature, the crosshead was started at a speed of 5×10^{-3} cm/min, ($\dot{\varepsilon}$ approx. 1.4×10^{-4} sec $^{-1}$). A full scale deflection of 100 Kg was used and the test trace was kept on the chart, by using the stepped zero suppression facility of the machine (in 100 Kg steps).

In the post-yield region the cross-head and chart speeds were simultaneously increased by a factor of 10. After about 6 cm in the chart, both cross-head and chart speeds were returned to the original settings, (to determine the strain rate dependence of the flow stress). The chart was left to run for 2 cm and stress relaxation tests were carried out by stopping the cross-head for a period of 10 min, at the end of which the initial strain rate was again applied and the entire cycle was performed once more. See Figs. IV.63 to IV.66 for a diagrammatic representation of the test.

Including the heating up period the entire test took about an hour for each sample. At least 2 specimens were tested at most of the temperatures for each alloy, for each condition.

III.7.d Grain Size Measurements

Grain size measurements were done by means of a fully automated device, Bausch & Lomb Omnicon 3000, which consists of a microscope and a TV video scan, controlled by a minicomputer Nova/4c. Software determines feature boundaries, areas and perimeters, makes an statistical calculation and gives the standard deviation values for grain size area.

Errors can arise in machine counting, e.g. - the machine could take twin boundaries as grain boundaries, and/or could fail to count some grain boundaries intersections from areas of low contrast. In order to avoid these errors drawings of the micrographs were made on tracing paper, taking only the grain boundaries features; to account for the thickness of lines drawn, the area was calculated as $A = Am + Pm \times \frac{1}{2}\ gbt$

gbt = grain boundary thickness
Am = area of grain
Pm = perimeter of grain

The method used gives the percentage of error, according to the number of grains intercepted, and to the total number of grains in the whole field observed.

CHAPTER IV

EXPERIMENTAL RESULTS

IV.1. Deformation

IV.1.a Structural Features

The specimens were deformed by rolling, giving different amounts of deformation, from 2% to 87%, at room temperature and sub-zero temperatures (-70°C & -196°C). Figs. IV.1 to IV.4 show optical micrographs for different deformations at -196°C. Figs. IV.3 & IV.4 are micrographs of specimens very heavily deformed (50% & 80% at -196°C and room temperature, respectively). Specimens rolled to the same amount of deformation, but at different temperatures, (-70°C, -196°C) showed very similar structures. Fig. IV.1 shows the annealed material 1 hr at 1050°C; the structure contains a large number of annealing twins. Slip lines appear inside the grains with small amounts of deformation (Fig. IV.2, 10% deformation at -196°C). As the amount of deformation increases, the grains become elongated in the rolling direction, and various features are observed inside the grains, i.e., slip lines, very fine striations and deformation twins. Figs. IV.2. to IV.4, show these features quite clearly. At very high deformations (80%, 87%) the structure becomes extremely complex (Fig. IV.4.).

IV.1.b Hardness

Table IV.1 gives the hardness values, corresponding to the different rolling schedules. These values have been plotted in Fig. IV.5. It is observed that the hardness increases as the amount of deformation increases. The values for rolling at room temperature and at -70°C are very similar; while rolling at -196°C gives higher values. Alloy B (0.75 Ti) shows slightly higher values than Alloy A (0.15 Ti).

IV.1.c X-ray Analysis. Deformed Samples

X-ray analysis were performed on the samples deformed at -196°C and room temperature, looking for the formation of hcp ε-phase and possible changes in lattice parameter with deformation.

In the deformed samples no new peaks were observed in either alloy for any of the deformation temperatures. There was however a large broadening of the peaks with deformation, due to strain effects. Shift of peak positions were also observed, with deformation. All peaks shifted towards smaller angles with respect to the only annealed (undeformed) material; (Fig. IV.6). In the annealed material peak doublets were observed but not in the deformed samples. The peak positions (200) and (311) presented the most marked broadening.

In the very heavily deformed material, (65% & 80% at -(196°C) the position (200) disappears completely.

X-ray results were repeated using cobalt radiation since this has been reported to give better results in detecting the hcp phase. However no difference was found either in relative peak positions or in detection of any new peaks.

Table IV.2 shows a summary of these results. The arrows indicate the peak shift direction relative to the annealed sample. No definitive conclusion can be taken from X-ray analysis about the presence of hcp phase, since the peak broadening makes it very difficult to detect any hcp positions, which would be very close to, or overlap the fcc positions. The peak broadening is very irregular; and for the heavily deformed samples (65% & 80%) there is a slight change in the peak slope at the 2θ hcp positions, which could be taken as a peak. Therefore, X-rays alone cannot confirm the presence or absence of ε-phase. Lattice parameter values were also calculated. Accurate values were obtained by plotting 'a' against $\left(\frac{\cos^2\theta}{\sin^2\theta} + \frac{\cos^2\theta}{\theta}\right)$ which approaches zero as θ approaches 90°. These values are shown in Table IV.2 and Table IV.9. The lattice parameter does not change with amount of deformation and has a value of 3.585 ± 0.005 Å which is the same as the homogenized material, which consists of a single phase fcc structure. The material deformed at room temperature presents the same lattice parameter values as the material deformed at $-196^{\circ}C$.

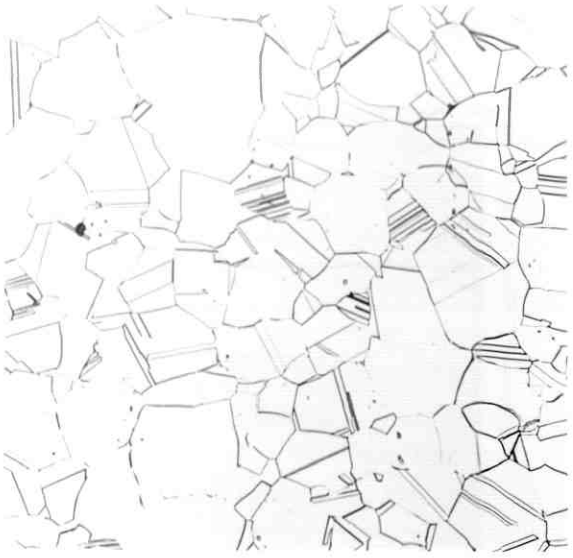


Fig. IV.1 - Microstructure of Co-Ni-Cr-Mo wrought alloy in recrystallized condition after annealing in value at 1050°C/1hr X 200

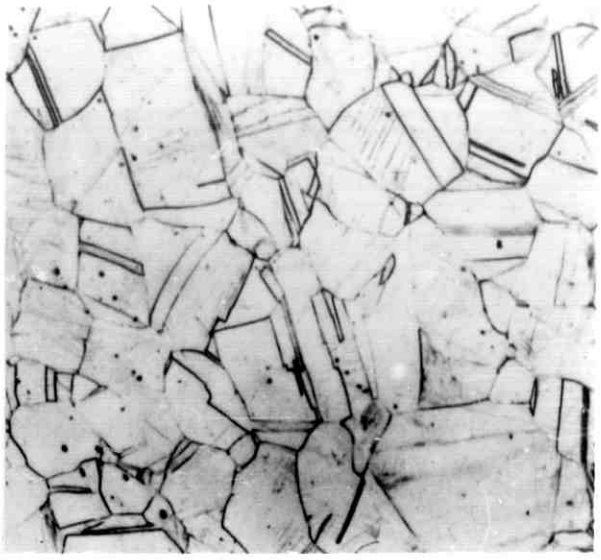


Fig. IV.2 - Alloy deformed 10% at -196°C X 375

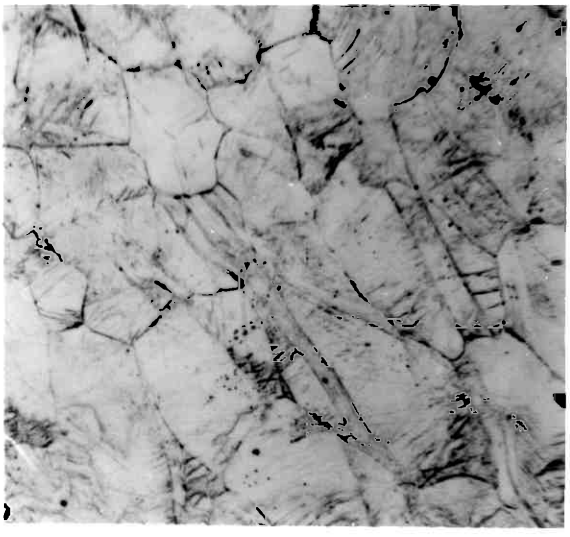


Fig. IV.3 - Alloy deformed 50% at -196°C X 345

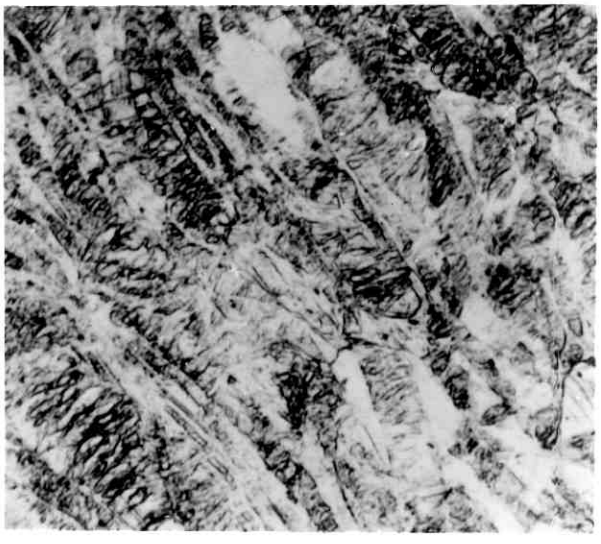


Fig. IV.4 - Alloy deformed 80% at room temperature X 125

TABLE IV.I

VICKERS HARDNESS HV

% deformation	RT rolling		-70 °C rolling		liquid nitrogen (-196 °C) rolling	
	Alloy B	Alloy A	Alloy B	Alloy A	Alloy B	Alloy A
2%	200		-		206	-
5%	230		-		216	-
10%	265	270	-	271	282	288
20%	315	320	-	325	351	353
30%	341	359	354	381	397	420
50%	391	443	402	450	465	490
65%	412	466	424	469	493	535
80%	427	473	430	480	520	549
87.5%	439		-		-	

Annealed sample (1100 °C) 1 hour: Alloy A: 177 HV - Alloy B: 188 HV

As received material (fully homogenized and hot forged): 453 HV (in the form of hip joint from Alloy A)

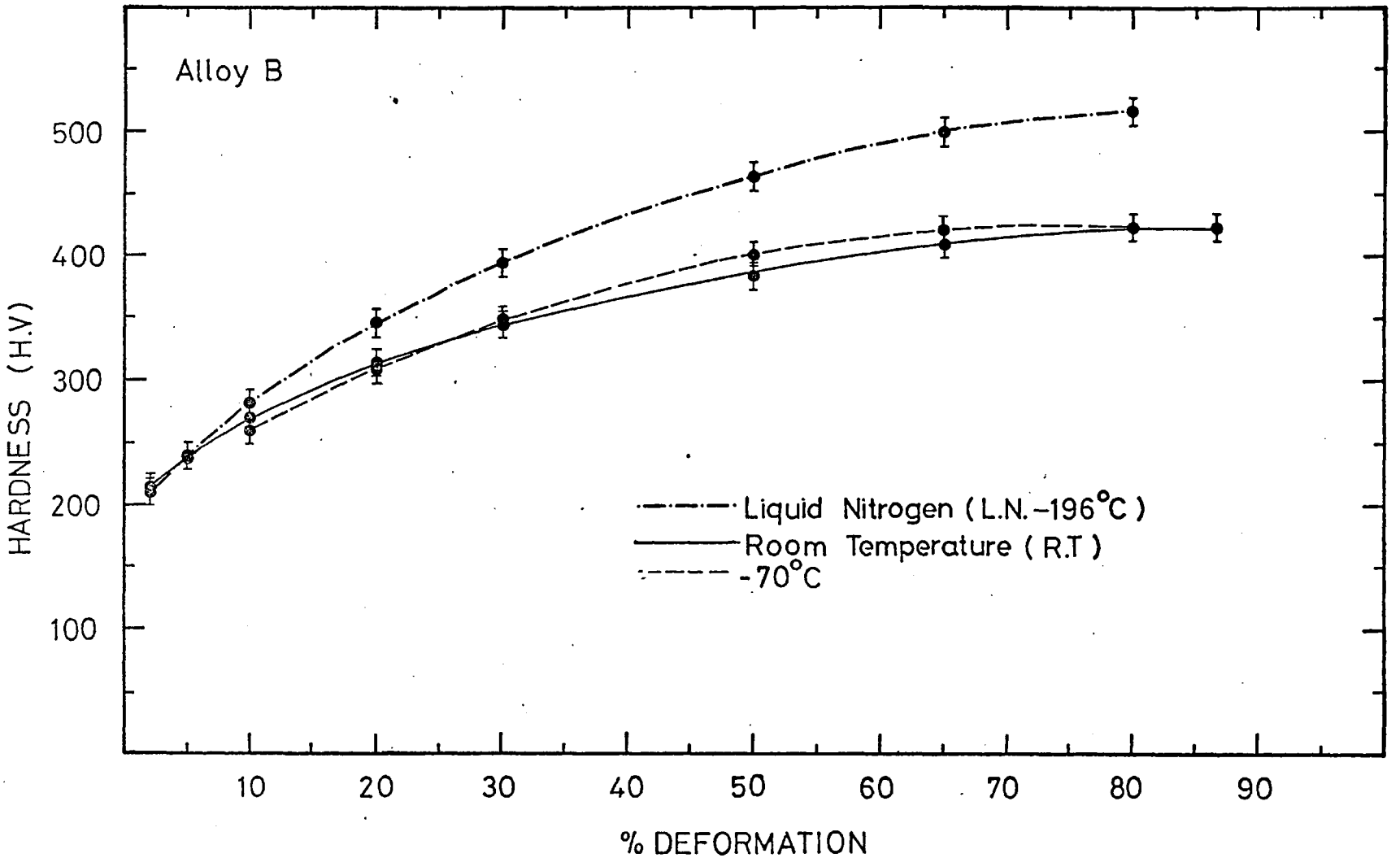


FIG. IV.5 Hardness vs. deformation for different rolling temperatures.

TABLE IV.2

X-RAY RESULTS - DEFORMED MATERIAL

Cobalt radiation $K\alpha_1 = 1.79021$
$K\alpha_2 = 1.79028$

hkl	2θ	d	I/I₁	I	a	2θ	d	I/I₁	I	a	2θ	d	I/I₁	I	a	2θ	d	I/I₁	I	a
	ANNEALED					10% DEFORMATION AT L N					20% DEFORMATION AT L N					30% DEFORMATION AT L N				
111	51.7	2.05	100	100	3.556	$\overleftarrow{51.4}$	2.06	74	37	3.568	$\overleftarrow{51.1}$	2.07	100	85	3.585	$\overleftarrow{51.2}$	2.07	34	22	3.585
200	60.3	1.78	65	65	3.564	$\overleftarrow{60.1}$	1.787	40	20	3.574	$\overleftarrow{59.8}$	1.795	29	25	3.59	$\overleftarrow{59.8}$	1.795	7	5	3.59
220	90.4	1.26	27	17	3.568	$\overleftarrow{90}$	1.265	100	50	3.578	$\overleftarrow{89.7}$	1.27	29	25	3.59	$\overleftarrow{89.75}$	1.27	100	65	3.59
311	112.4	1.08	42	42	3.57	$\overleftarrow{112}$	1.08	50	25	3.58	$\overleftarrow{112.4}$	1.08	29	25	3.58	$\overleftarrow{111.8}$	1.08	30	20	3.58
222	119.8	1.04	17	12	3.58	$\overleftarrow{119}$	1.04	10	5	3.6										
	50% DEFORMATION AT L N					65% DEFORMATION AT L N					80% DEFORMATION AT L N									
111	$\overleftarrow{51.5}$	2.06	38	25	3.568	$\overleftarrow{51.4}$	2.06	100	85	3.568	$\overleftarrow{51.4}$	2.06	100	90	3.568					
200																				
220	$\overleftarrow{90.1}$	1.265	100	65	3.577	$\overleftarrow{90}$	1.266	70	60	3.58	$\overleftarrow{89.9}$	1.267	39	35	3.58					
311	$\overleftarrow{112}$	1.08	15	10	3.58	$\overleftarrow{112}$	1.08	2	2	3.58										
	30% DEFORMATION AT R T					50% DEFORMATION AT R T					65% DEFORMATION AT R T					80% DEFORMATION AT R T				
111	$\overleftarrow{51.4}$	2.06	15	10	3.568	$\overleftarrow{51.5}$	2.06	30	30	3.568	$\overleftarrow{51.5}$	2.06	39	35	3.568	$\overleftarrow{51.45}$	2.06	35	30	3.572
200	$\overleftarrow{59.8}$	1.795	7	5	3.59	$\overleftarrow{59.95}$	1.792	10	10	3.583	$\overleftarrow{60}$	1.79	10	10	3.58	$\overleftarrow{59.95}$	1.792	5	5	3.583
220	$\overleftarrow{90}$	1.266	100	70	3.58	$\overleftarrow{90.1}$	1.265	100	97	3.577	$\overleftarrow{90.1}$	1.26	100	85	3.577	$\overleftarrow{90}$	1.266	100	80	3.58

← = peak shift direction

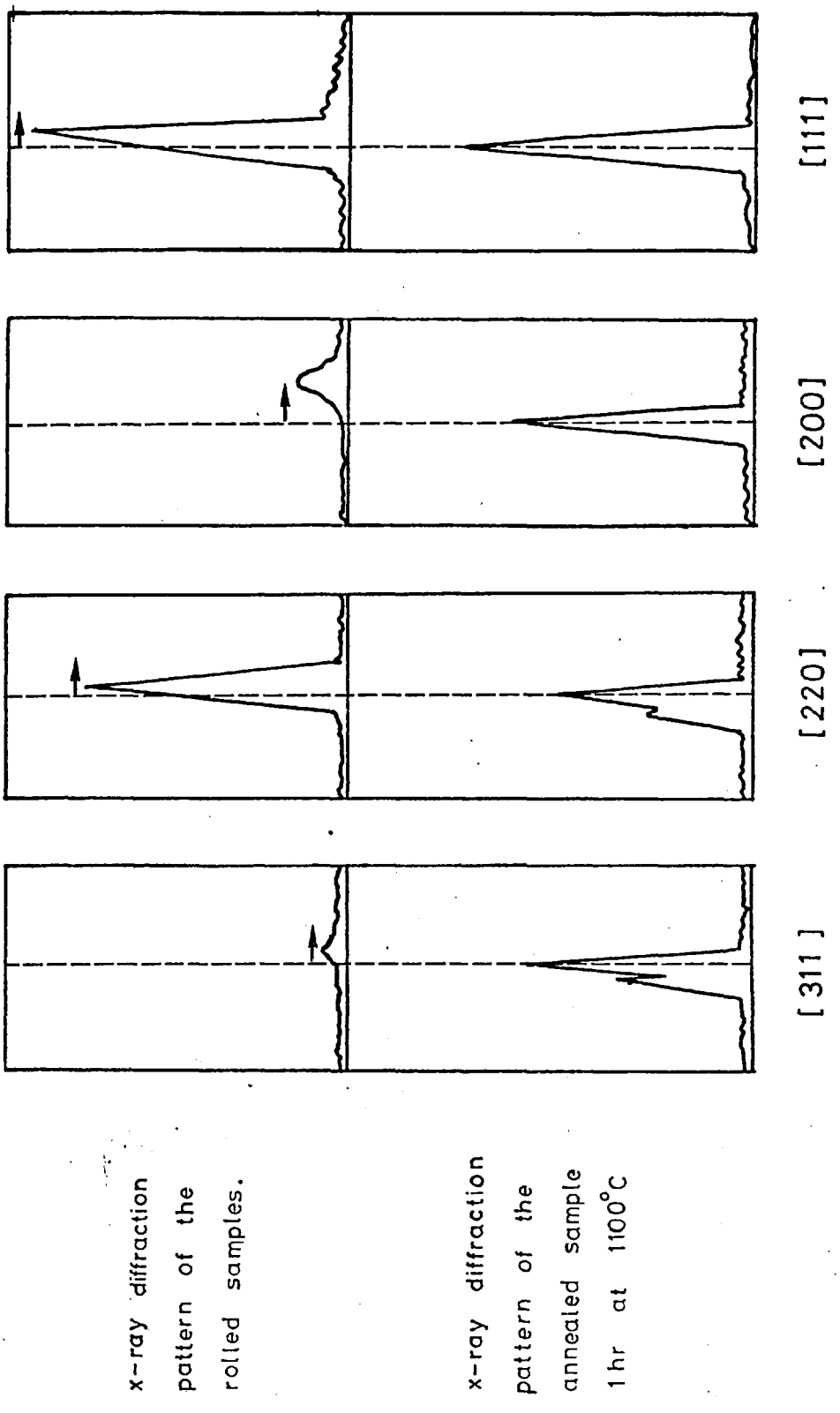


FIG. IV. 6 Comparison between x-ray diffraction patterns to show shift of the peaks.

IV.1.d Transmission Electron Microscopy Analysis

IV.1.d.1 Introduction

Very many difficulties are encountered in the analysis of the diffraction patterns for positive identification of mechanical twins from hcp-ε -phase; this is due to the fact that deformation structures involving microtwins or thin ε -platelets or both, show very similar morphologies, and in some cases identical diffraction patterns.

In the case of thin hcp platelets and microtwins, the diffracted intensity distribution in reciprocal space is extended into streaks perpendicular to their habit planes, causing the diffraction spots to be analyzed to change position continuously during a specimen tilt. In practice because of intensity streaking combined with double diffraction, or because more than one platelet habit may contribute to the diffraction pattern, it may be difficult to recognize the exact orientation.

Kestenbach ([59]) has constructed composite diffraction patterns for analysis of thin twin or/and hcp plates in a fcc matrix. He surveys the orientations in which twins and hcp plates may or may not be distinguished. Table IV.3 is a summary of his work. It is seen that no distinction is possible if the beam enters the matrix along<100>,<211>, or<310> directions. In these cases, twin and hcp electron diffraction patterns are identical and overlap with the matrix spots. Thus, the composite

diffraction patterns are the same as the matrix patterns alone. For all the other cases in which twin and hcp may be distinguished, the composite diffraction patterns are reproduced in Figs. IV.7.a, b and c.

The electron diffraction pattern from the material deformed 50% at (-196°C) temperature (Fig. IV.8) is a good example of a composite fcc - twin - hcp and the beam direction fits Kestenbach's model; however, double diffraction is present and even though the spots were indexed in agreement with Fig. IV.7, an ambiguity due to double diffraction is present; this happens for matrix orientations of the <123> and <012> types. In these orientations double diffraction may produce all hcp spots from twin spots and viceversa; therefore, spots 3 and 4 in Fig. IV.8 could either be twins or ε-phase. Due to the large inclination of the plates with respect to the electron beam in these orientations, double diffraction from the regions adjacent to the interfaces is difficult to distinguish even by dark field techniques. Fig. IV.9 is a 50% deformed material at room temperature and shows another good example of a composite fcc - hcp-twin with an [012] matrix orientation; in this case, however, it was possible to distinguish between the twins and the hcp ε-phase.

It is important to realise that the diffraction patterns of twins or ε plates may in many cases be identical, and the apparent identification of one may not

TABLE IV.3

Exact Orientations in which Election Diffraction can or cannot distinguish between twin and hcp plates of (111) - Habit in fcc matrix [59].

Beam direction ⟨hkl⟩ in Matrix	Total Number of Variants	Variant hkl in which distinction is possible	Number of Variants in which distinction is possible
110	6	$1\bar{1}0$, $10\bar{1}$, $01\bar{1}$	3
100	3	-	0
211	12	-	0
310	12	-	0
111	4	111	3
321	24	321, 312, 231 213, 132, 123 $\bar{3}21$, $\bar{3}12$, $2\bar{3}1$ $21\bar{3}$, $1\bar{3}2$, $12\bar{3}$	12
411	12	411, 141, 114	9
210	12	210, 201, 120 102, 021, 012	6
221	12	$22\bar{1}$, $2\bar{1}2$, $\bar{1}22$	9
511	12	$5\bar{1}\bar{1}$, $\bar{1}5\bar{1}$, $\bar{1}\bar{1}5$	Not determined
521	24	$2\bar{1}5$, $\bar{1}52$, $\bar{1}25$ $52\bar{1}$, $5\bar{1}2$, $25\bar{1}$	Not determined
741	24	741, 714, 471 417, 174, 147	Not determined

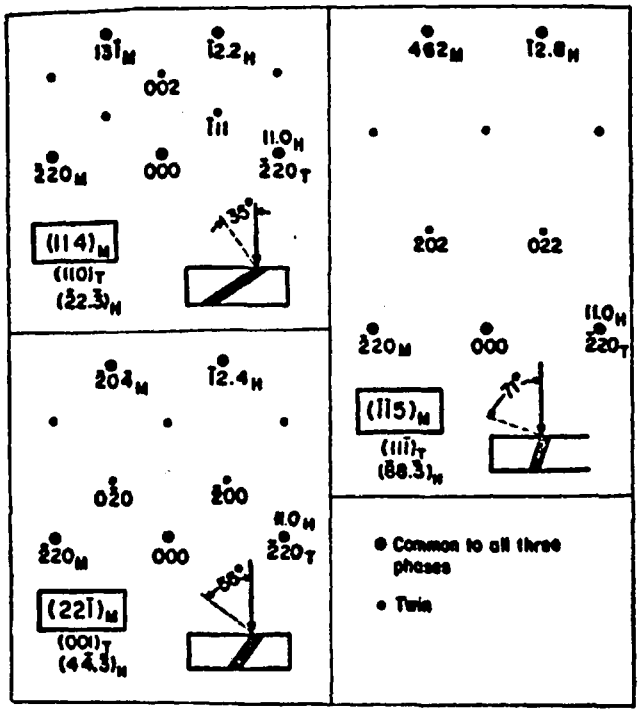


Fig. IV.7.a - Composite FCC-twin-HCP electron diffraction patterns with extra spots due to twinning on (111) matrix planes. Indices in parentheses refer to reciprocal lattice planes. Plate orientation in foil indicated by angle between incident beam and plate normal (59)

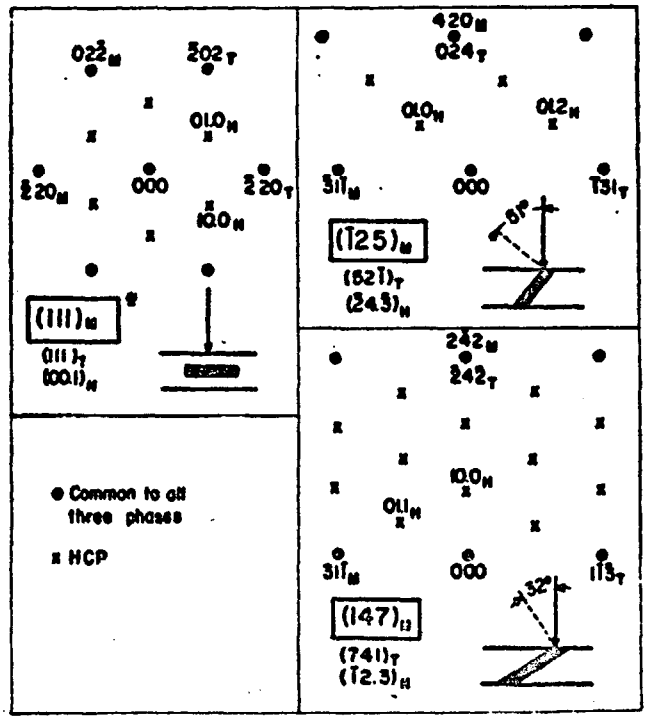


Fig. IV.7.b - Composite FCC-twin-HCP electron diffraction patterns with extra spots due to HCP plates on (111) matrix planes. Plane indces and plate orientation as in Fig. IV.7.a (59)

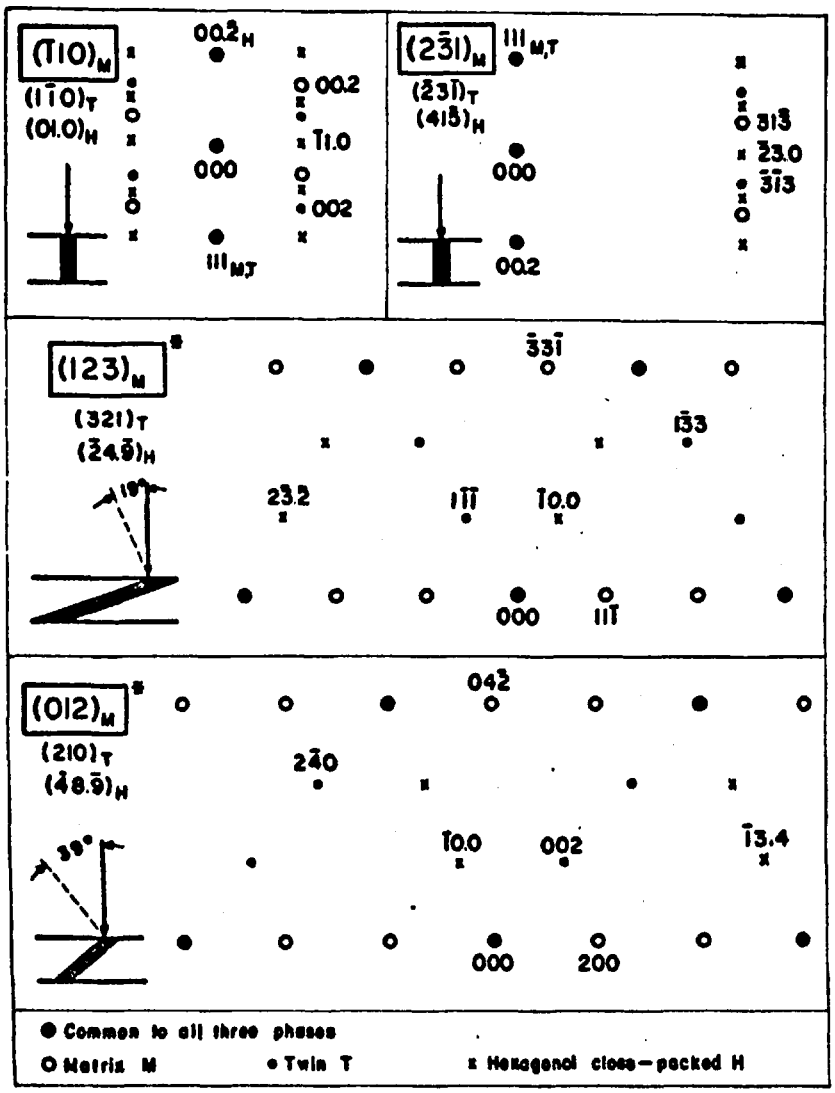


Fig. IV.7.c – Composite FCC-twin-HCP electron diffraction patterns with extra spots due to twinning and HCP plates on (111) matrix planes. Plane indices and plate orientation as in Fig.a . Double diffraction effects not included (59)

Fig. IV.8 - Material deformed 50% at -196°C

Fig. IV.8.1 - Bright field 30 K

Fig. IV.8.2 - HRDF from spots 5 and 7, showing matrix 30 K

Fig. IV.8.3 - HRDF from spots 1 and 2, showing twins 30 K

Fig. IV.8.4 - HRDF from spots 3 and 4, showing HCP bands 30 K

Fig. IV.8.5 - HRDF from spot 6, reflection from a different grain 30 K

Fig. IV.8.6 - Diffraction Pattern

Fig. IV.8.7 - Key of interpretation of D.P.

m = matrix

h = hcp phase

t = twins

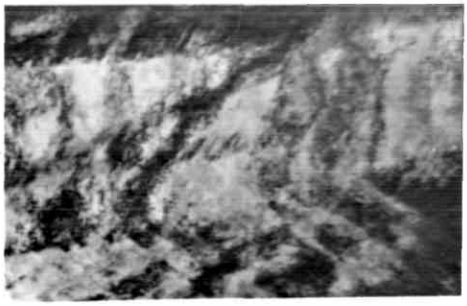


Fig. IV.8.1

↑ B F

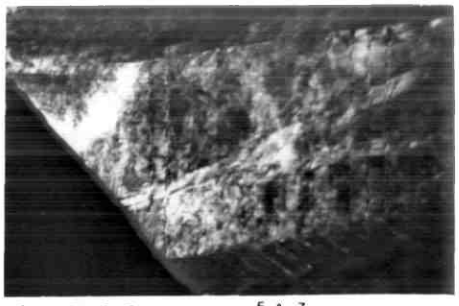


Fig. IV.8.2

5 & 7 ↑

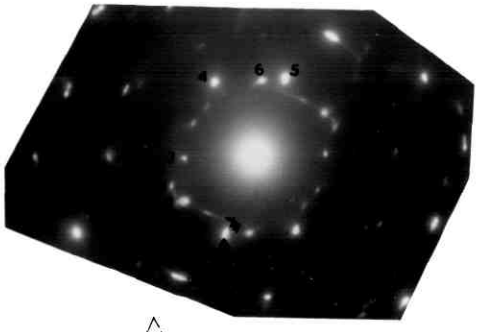


Fig. IV.8.6

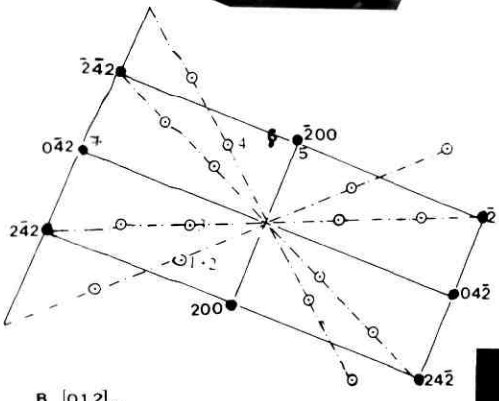


Fig. IV.8.7



Fig. IV.8.5

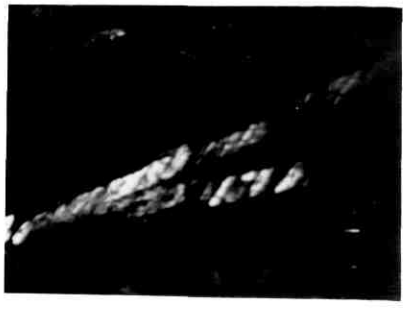


Fig. IV.8.3



Fig. IV.8.4

Fig. IV.9 - Material 50% deformed at room temperature

Fig. IV.9.a - Bright field 30 K

Fig. IV.9.b - HRDF from spot 6 in D P, showing twins 30 K

Fig. IV.9.c - HRDF from spot 4 in D P, showing ε-hcp bands 30 K

Fig. IV.9.d - HRDF from spot 5 showing twins 30 K

Fig. IV.9.e - HRDF from spot 2, HCP reflexion 30 K

Fig. IV.9.f - HRDF from spot 1, showing twin bands, the same as from spot 3

Fig. IV.9.g - HRDF from spot 7, showing matrix 30 K

Fig. IV.9.h - Key of interpretation for Diffraction Pattern

m = matrix

t = twin

h = hcp phase

* = common to all phases

o = double diffraction spots



Fig. IV.9.f



Fig. IV.9.g



Fig. IV.9.a



Fig. IV.9.g



Fig. IV.9.b

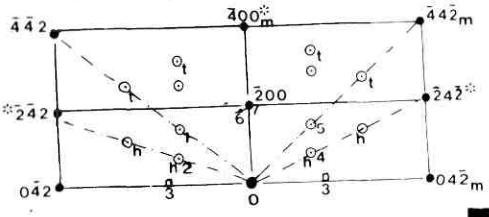
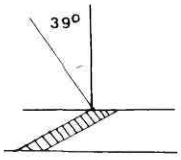




Fig. IV.9.e



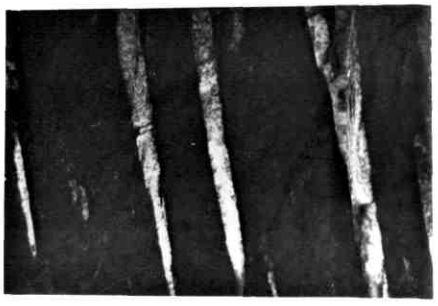


Fig. IV.9.c



Fig. IV.9.d

exclude the presence of the other.

In the present work examples have been carefully selected to avoid ambiguity and they are shown in further sections (2.a and 2.b).

IV.1.d.2 Electron Diffraction

IV.1.d.2.a Deformation at room temperature (Figs. IV.10 to IV.17)

For very small amounts of deformation (5%) the material shows dislocations (Fig. IV.10); as the amount of deformation increases (i.e. 10%) the matrix becomes faulted and dislocation networks and stacking faults can be observed (Fig. IV.11). Figs. IV.12 and IV.13 show the material deformed 30% and 50% respectively, the matrix is very faulted with twins. For higher deformations the structure becomes extremely complex. The effect of stacking faults, dislocations, twins and other features produces very complicated structures which, of course, are manifested in the diffraction patterns, showing streaks and satellite spots. Fig. IV.17 is an example of this; it shows a very streaky pattern, presenting a matrix twinned in two axes and satellite spots. This corresponds to a material deformed 80% by tension at room temperature.

Very few examples of hcp ε -phase were found with deformation at room temperature, and these were only after 50% deformation. Fig. IV.14 shows one of these examples in a material deformed 65%. The typical

orientation relationship fcc/hcp (111)//(0001), shown in the diffraction patterns, and ε -platelets can be seen in the HRDF taken from the hcp spots.

Figs. IV.15 and IV.16 show examples of twins in 65% and 80% deformed samples at room temperature.

IV.1.d.2.b Deformation at liquid nitrogen (-196°C) temperature (Figs. IV.18 to IV.25)

For deformation at subzero temperatures, a similar process happens; dislocations, stacking faults and deformation twins increase in number as the amount of deformation increases. However, comparing deformation at this temperature with deformation at room temperature, for smaller deformations the structures show greater numbers of dislocations and stacking faults. Fig. IV.18 is a material deformed to a very small strain (about 2% at -196°C). However, quite a number of dislocations are shown. At 20% deformation the structure, already, looks very complex, with dislocation networks and twins in two directions crossing each other (Fig. IV.20). Even at deformations as small as 10%, mechanical twins are seen (Fig. IV.19). The material deformed by tension did not present a structure as complex as the material deformed the same amount by rolling, the dislocations seemed to get aligned. It has to be noted that these foils were prepared from sections cut at 45° to the tensile axes. Figs. IV.21 and IV.22 show samples deformed by tension

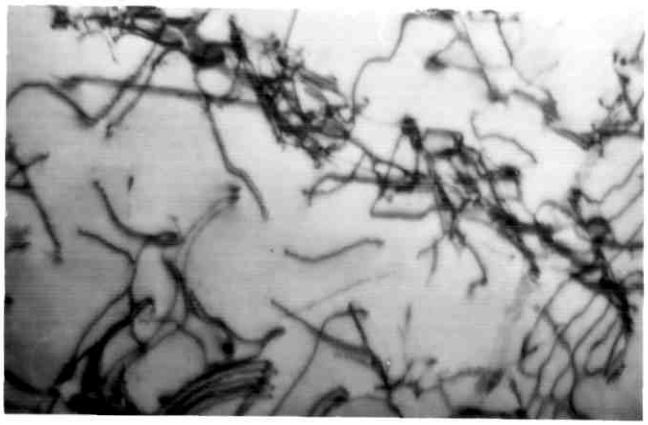


Fig. IV.10 - Bright field image of a sample deformed approx. 5% at room temperature showing dislocations

Mag. 58 K

Fig. IV.11 - Bright field images from a sample deformed 10% at room temperature

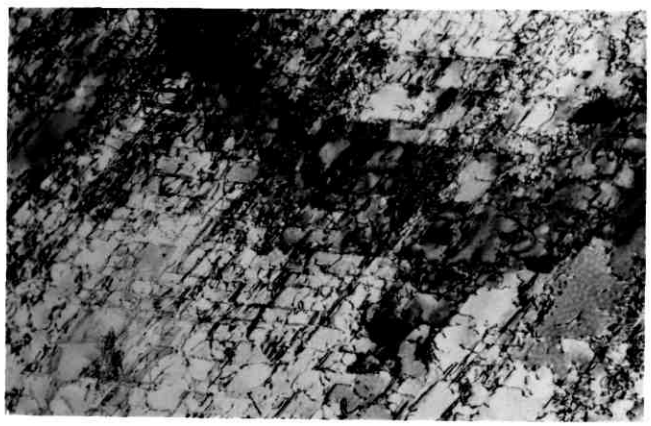


Fig. IV.11.a - 24 K



Fig. IV.11.b - is same area as 'a' but at higher magnification 80 K, showing stacking faults and dislocations lying on (111) plane

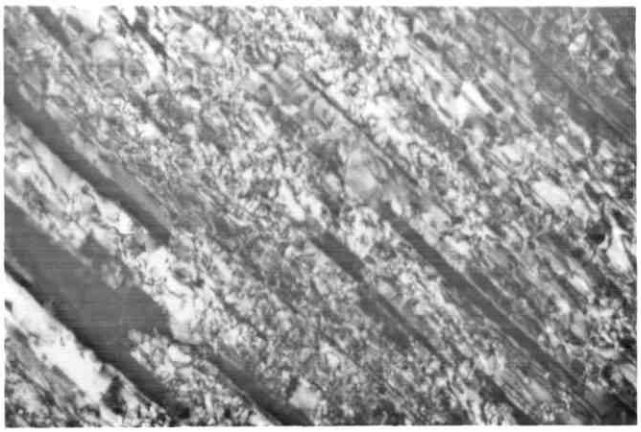


Fig. IV.12.a - HRDF showing a very faulty matrix. Mag. 80 K

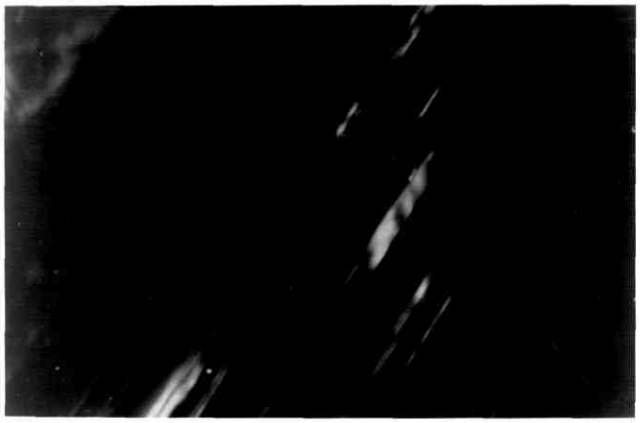


Fig. IV.12.b - CDF showing twins
Mag. 100 K

Fig. IV.12 - Material deformed 30% by rolling at room temperature

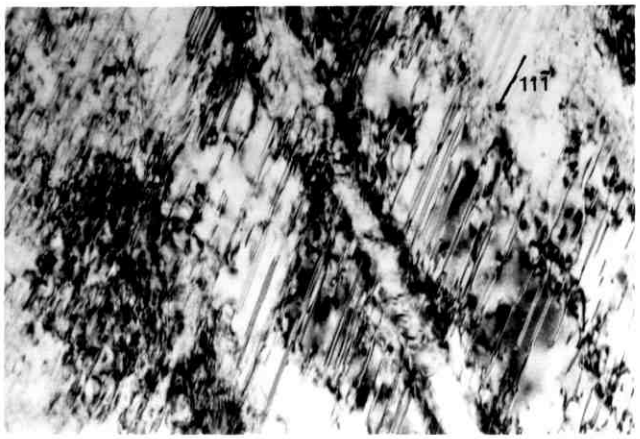
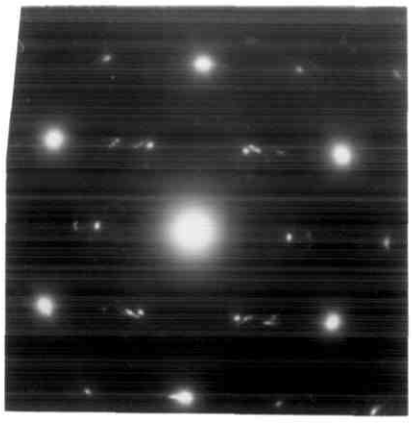


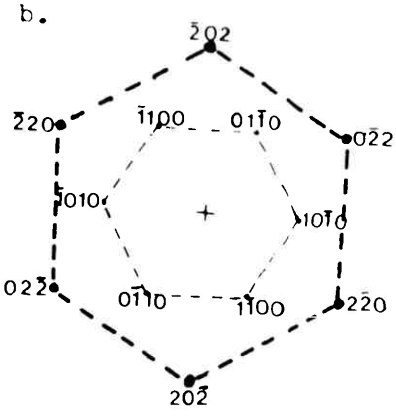
Fig. IV.13 - Bright field from material deformed 50% by tension at room temperature, showing twins lying on (111) plane.
Mag. 130 K



Fig. IV.14.a - HRDF from faint hcp spots in diffraction pattern showing ε- plates Mag. 27 K



b.



c. ● matrix
· ε phase

Fig. IV.14.b - Diffraction Pattern

Fig. IV.14.c - Key of D.P. showing typical orientation relationship fcc/hcp (111)//(0001)



Fig. IV.15.a - HRDF showing twins. 3 8 K

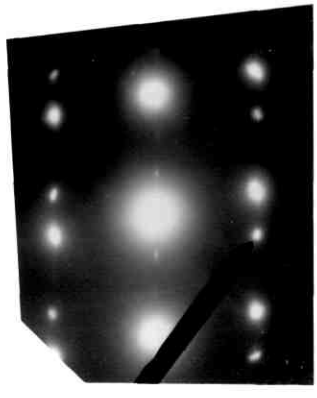


Fig. IV.15.b - Diffraction Pattern indicating spot for a

Material deformed 65% by rolling at room temperature

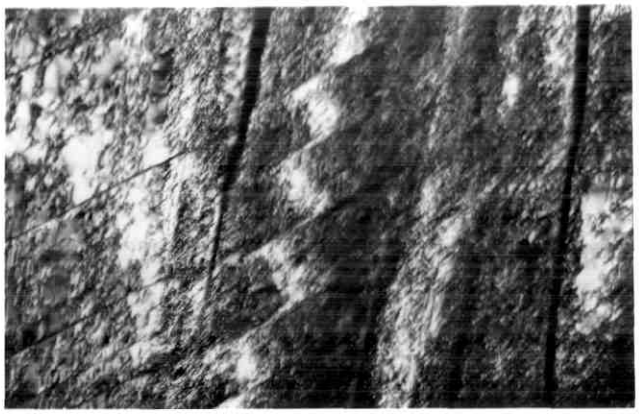


Fig. IV.16.a - H.R.D.F. shows matrix (spot 1)

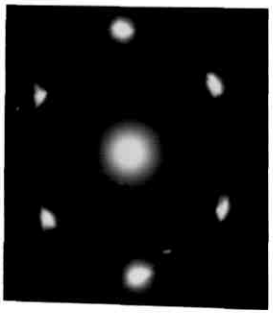


Fig. IV.16.b - Diffraction Pattern

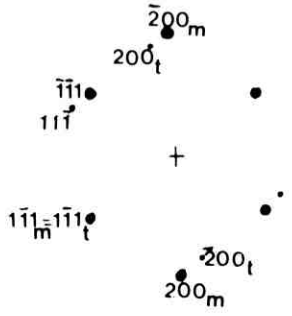


Fig. IV.16.c - Key of Diffraction Pattern



Fig. IV.16.d – HRDF from spot 2 showing twins lying on $(1\bar{1}1)$ plane

Material deformed 80% in tension at room temperature.

Fig. IV.17 - Material deformed by tension 80% at room temperature

a - BrightField 38 K

b - HRDF from spot 3, showing matrix

c - Diffraction Pattern, showing twins (t) satellites spots and streaking B [110]

d - Key of diffraction pattern

e - HRDF from spot 1

f - HRDF from spot 2

g - HRDF from spots 1 and 2 together

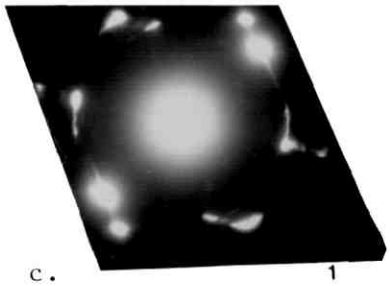
a.



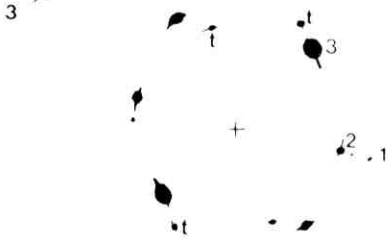
b.



c.



d.



e.





2 + 1 f.

g.

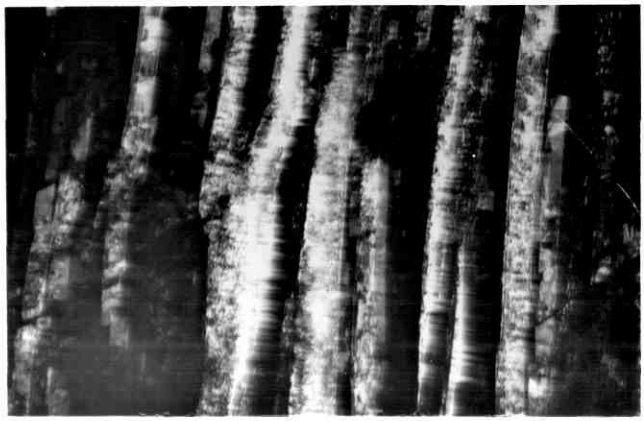




Fig. IV.18.a - Bright field showing aligned dislocations and stacking faults
Mag. 18 K

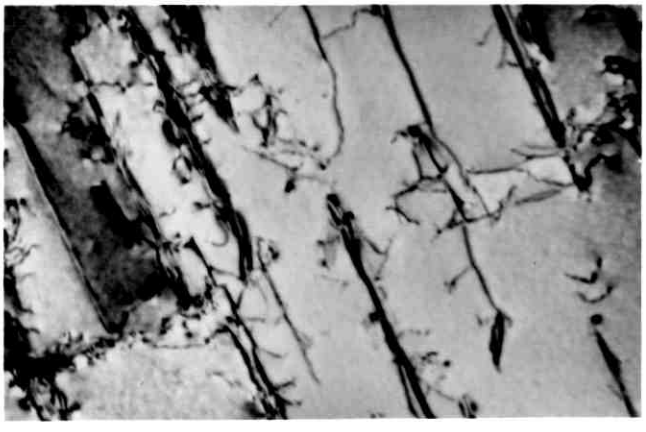


Fig. IV.18.b - Bright field showing dislocations at higher magnifications Mag. 48 K

Fig. IV.18 - Material deformed 2% at -196°C

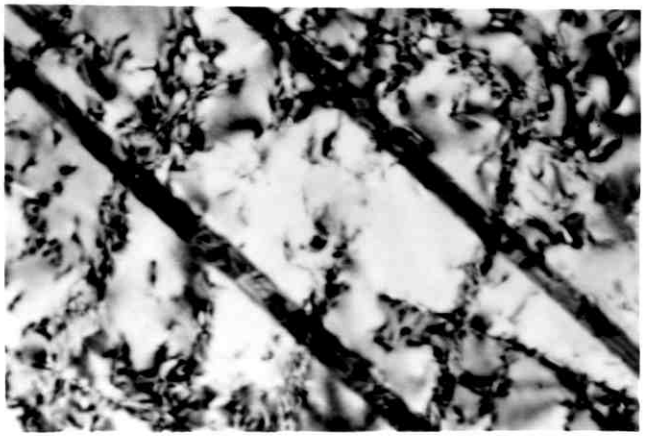


Fig. IV.19 - Material deformed 10% at -196°C. Showing dislocations and twins. Mag. 80 K

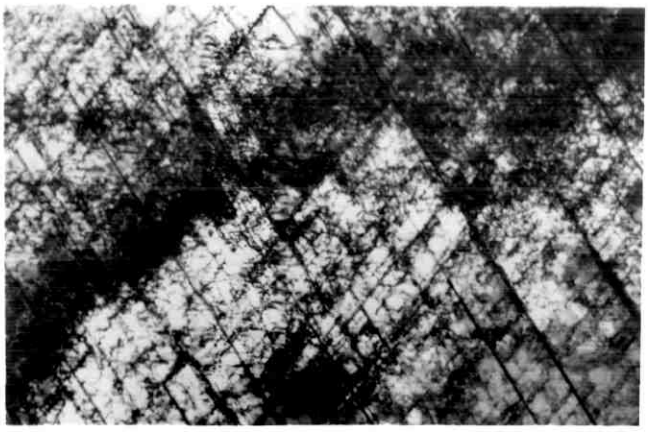


Fig. IV.20.a - Bright field showing twins crossing each other Mag. 24 K

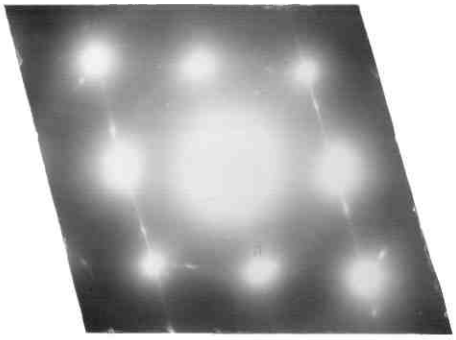


Fig. IV.20.b - Diffraction Pattern

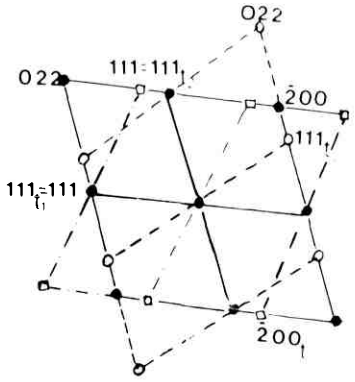


Fig. IV.20.c - Key of Diffraction Pattern

- ● matrix
- □ t_1
- ○ t_2

Fig. IV.21 - Material deformed 17% by tension at -196°C

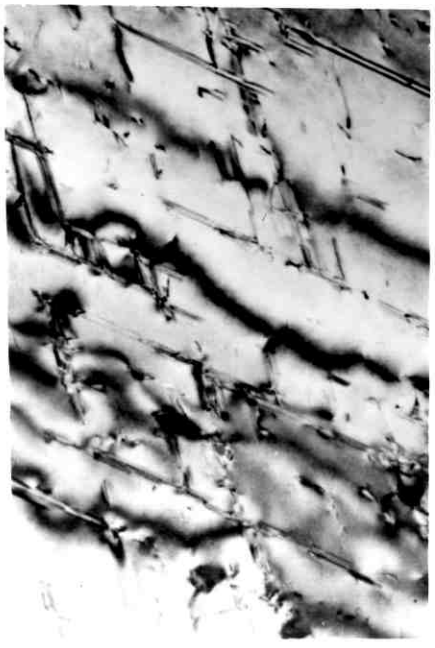


Fig. IV.21.a - Bright field 100 K

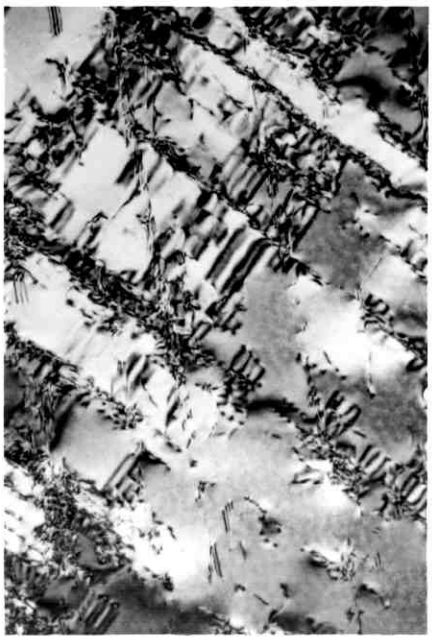


Fig. IV.21.b - Bright field showing dislocations and stacking faults Mag. 48 K

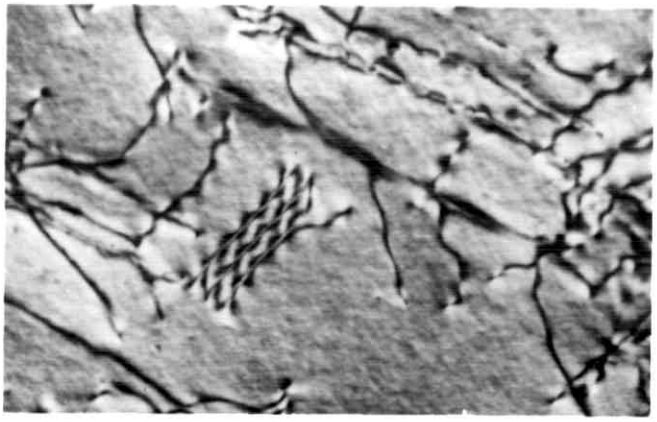


Fig. IV.22.1 - Bright field, material deformed 27% by tension at -196°C, showing dislocations Mag. 100 K

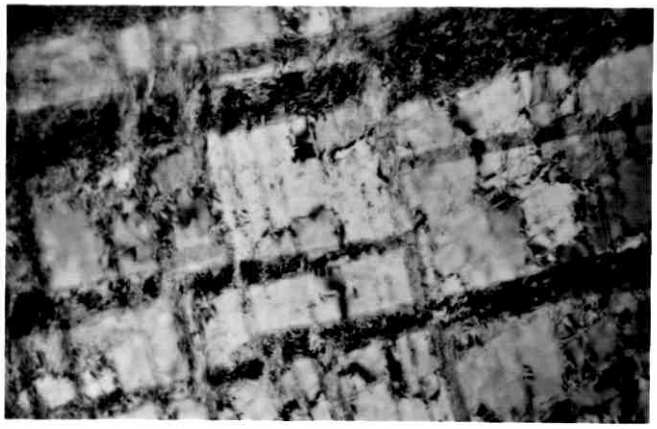


Fig. IV.22.2.a - Bright field, material deformed 30% by tension at -196°C Mag. 43 K



Fig. IV.22.2.b

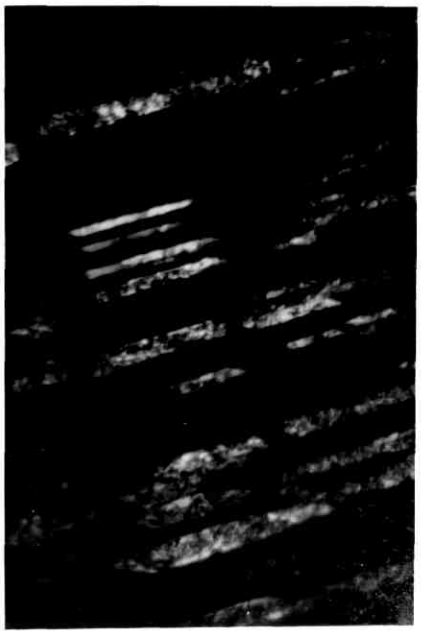


Fig. IV.22.2.c

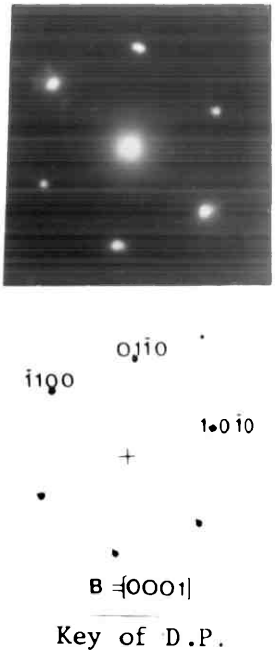
Figs. IV.22.2.b & IV.22.2.c - HRDF showing twins in different (111) planes Mag. 58 K



Fig. IV.23.a - Bright field 58 K



Fig. IV.23.b - HRDF from small area indicated in a. Mag. 180 K - using g spot not shown in D P



Key of D.P.



Fig. IV.24.c - HRDF showing twins Mag. 24 K



Fig. IV.24.a - Bright field showing phase and a coarse precipitate Mag. 24 K



Fig. IV.24.b - HRDF from a showing ε - phase Mag. 24 K



Fig. IV.25.a – HRDF from spot 1 showing the matrix Mag. 30 K

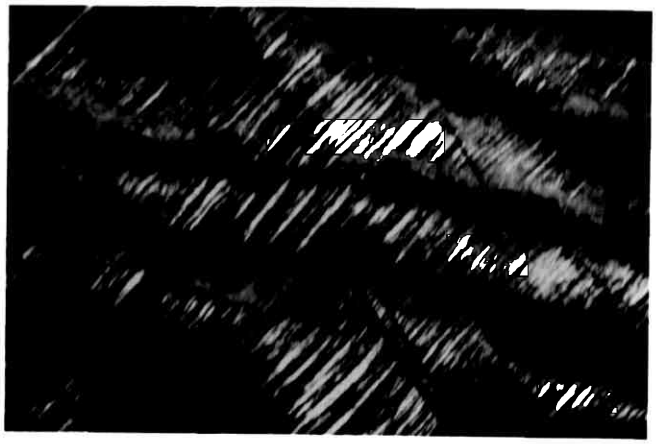


Fig. IV.25.b – HRDF from spot 2 showing ε-phase Mag. 30 K

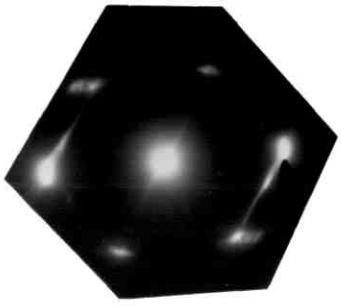


Fig. IV.25.c - Diffraction Pattern

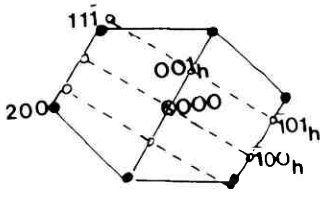


Fig. IV.25.d - Key of Diffraction Pattern $(\bar{1}2\bar{1}0)//(110)$

Fig. IV.25 - Material deformed 65% by rolling at $-196^{o}C$

different amounts in liquid nitrogen.

At 50% deformation by rolling at -196°C there is clear evidence of the presence of hcp phase formed as platelets. Fig. IV.23.b shows an hcp platelet taken from a very small section shown in the bright field photograph giving an hcp (0001) diffraction pattern. Fig. IV.24.b is another example of an hcp pattern, beam direction $[1\bar{2}1\bar{3}]$ with satellite spots, showing a very fine hcp phase. Fig.IV.24.c shows the presence of twins in the same material, and a particle surrounded by a high dislocation density. At higher deformation the structure becomes extremely complex and a great number of twins are present to accommodate the stresses of the matrix. Fig. IV.25 shows the presence of ε at this deformation; as fine platelets. The similarities with twin morphology may be noted.

IV.2. Ageing Treatments

Ageing treatments were carried out for short times (2 min, 5 min, 30min) at different temperatures, and long time ageing treatments for 5 hrs, 30 hrs, up to 150 hrs at the same temperatures (464°C, 555°C, 640°C and 700°C). For treatments at higher temperatures (i.e. 850°C, 950°C only long time ageing was performed (2 hrs to 95 hrs).

IV.2.a Short Time Ageing Treatments

The materials previously deformed from 10%

up to 80% were aged in a salt bath.

Figs. IV.26.b and c show optical micrographs from a 50% previously deformed sample at room temperature and aged for short times at 555°C, 640°C and 700°C. The grains appear elongated due to the previous deformation. All the structures look quite similar. However, at 640°C after holding the material for 30 min, some of the slip lines have disappeared; some recovery is taking place, which agrees with the slight drop in hardness shown at these temperatures (600°C, 640°C) (Fig. IV.28). Fig. IV.26.a shows the homogenized sample aged at 555°C for 2 minutes. No change is observed in this sample compared to the annealed (not aged) material.

IV.2.a.1 Hardness Values

Table IV.4 gives the hardness values for the material previously deformed by different amounts and aged for short times at different temperatures. Figs. IV.27 and IV.28 show the graphs of hardness vs ageing time and hardness vs temperature, respectively.

The material hardens very rapidly after holding for very short times, even for small amounts of deformation, these values remain fairly constant or slightly increase (up to 30 min for 464°C). However, on ageing at 555°C and 640°C, the heavily deformed material seems to show a hardness peak between 2 and 10 min and then the hardness decreases (up to 30 min). Comparing hardness vs

temperature for different ageing treatments (2', 15', 30') Fig. IV.28, for low deformations, the hardness decreases with increase in temperature for the different times; however, the more heavily deformed material presents a hardness peak between 550° and 600°C and decreases at 700°C for all the ageing times.

The hardness values for the homogenized sample did not change with ageing time and temperature.

IV.2.a.2 X-ray Analysis - Rapid Heating

Two samples were examined in the rapidly heated condition; these were both 65% deformed at room temperature and aged for 2 min at 464°C and at 700°C. The X-ray analysis results for these samples are shown in Table IV.5 below (for cupper radiation).

TABLE IV.5

X-ray analysis for rapidly heated material (copper radiation) Å

Annealed material			65% deformed at -196°C + aged 2' at 464°C			65% deformed at -196°C + aged 2' at 700°C		
hkl	2θ	a	2θ	I/I1	a	2θ	I/I1	a
111	44	3.565	43.8	100	3.580	43.8	90	3.580
200	51.2	3.569	50.6	5	3.608	50.5	5	3.61
220	75.1 75.3	3.574	75	60	3.582	75	50	3.582
311	91.2 91.42	3.576	91	5	3.585	90.8	5	3.591
222	96.47 96.8	3.576	96.5	5	3.580	96.5	5	3.58

In the aged material there was a shift towards smaller angles with respect to the annealed material. (Shown by an arrow in Table IV.5). And the lattice parameter values are the same as those of the material deformed but not aged. (Table IV.2), probably the short ageing treatment (2 min) is not affecting the lattice parameter values.

IV.2.a.3 Diffraction Analysis

Short time ageing (rapid heating 2 min to 30 min)

Holding the material previously heavily deformed (50% and higher), even for a short time 15 min at 464°C, showed the presence of hcp phase. At this temperature it is expected from the Multiphase alloys diagram (Fig. V.1.)that the hexagonal phase will be stable (below transformation region). Fig. IV.29 shows a sample treated at this temperature, twins are present as well as ε , and both effects cause streaking in the diffraction pattern. At 640°C, within the fcc + hcp region some hexagonal phase is present. Fig. IV.30 is a sample previously very heavily deformed 65% at room temperature. Fig. IV.31 shows the hcp platelets formed in a sample previously deformed 50% at (-196°C) and aged at 640° 15 minutes. The platelets showed large numbers of dislocations (Fig.IV.31.b).

In the material aged at 700°C even for very short time 2 min, twins were observed but not the hcp phase (Fig. IV.32).

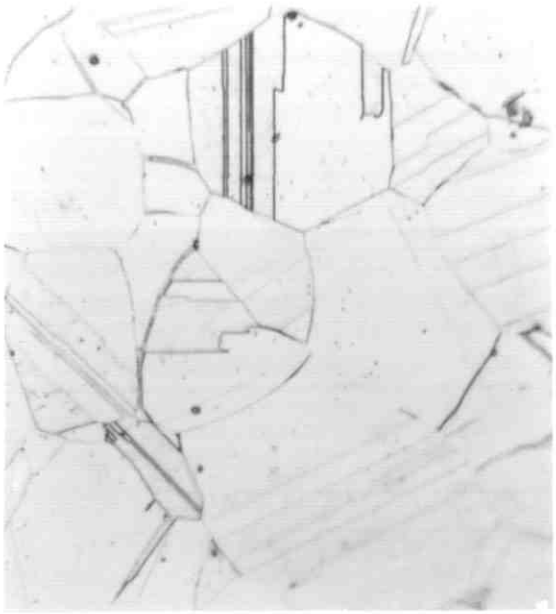


Fig. IV.26.a - Material homogenized and aged 2 min at 555°C X 470

Fig. IV.26 - Short time ageing treatments.

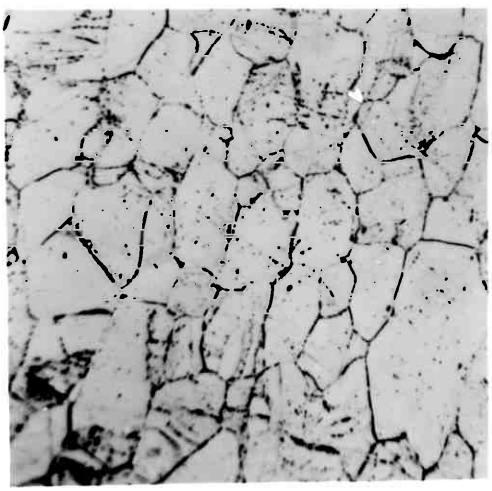


Fig. IV.26.b - Material previously deformed 50% at room temperature and aged 30 min at 640°C X 345

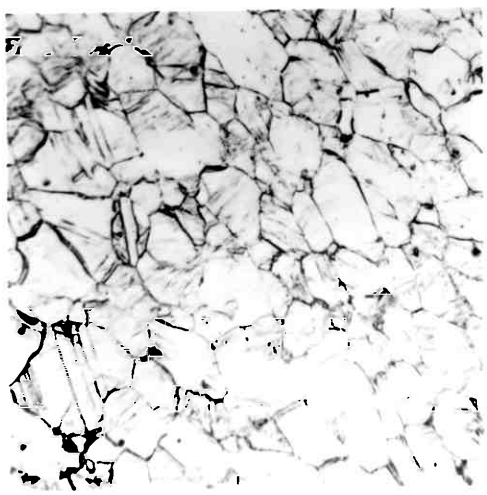


Fig. IV.26.c - Material previously deformed 50% at room temperature and aged 2 min at 700°C X 345

TABLE IV.4

HARDNESS VALUES FOR SPECIMENS RAPID HEATED IN A SALT BATH AT DIFFERENT TEMPERATURES

H T % Deformation	Deformed not heat treated	464°C			555°C			640°C			700°C
		2 min	15 min	30 min	2 min	15 min	30 min	2 min	15 min	30 min	2 min
2%	200			241	251	-	241				210
5%	230	271	273	243	253	-	243	239	230	251	210
10%	265	337	337	339	323	331	339	-	296	-	300
20%	315		420	425	408	444	454	413	430	418	421
30%	341		463	470	496	487	501	475	471	466	455
50%	391	509	493	513	526	505	520	532	504	502	490
65%	412	509	513	520	557	538	513	530	534	498	483
80%	427	513	544	549	562	560	569	542	518	528	513
50% (rolled at -70°C)		470	444	463	476	485	492	485	471	483	476
65% (rolled at LN)		603	-	-	600	-	-	593	-	-	588
80% (rolled at LN)		605	-	-	612	-	-	613	-	-	590

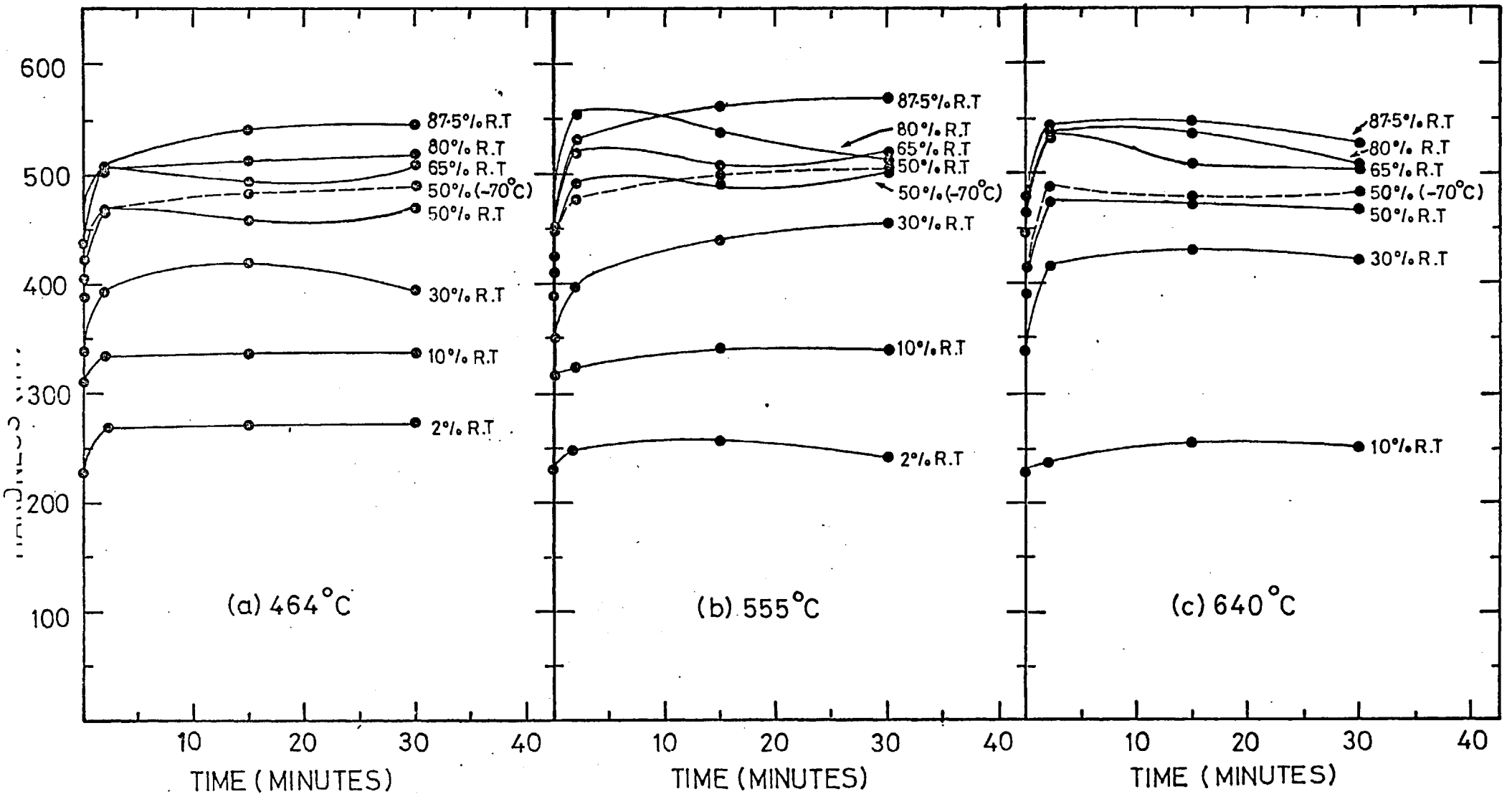


FIG. IV. 27 Hardness vs. heating time for different deformations.

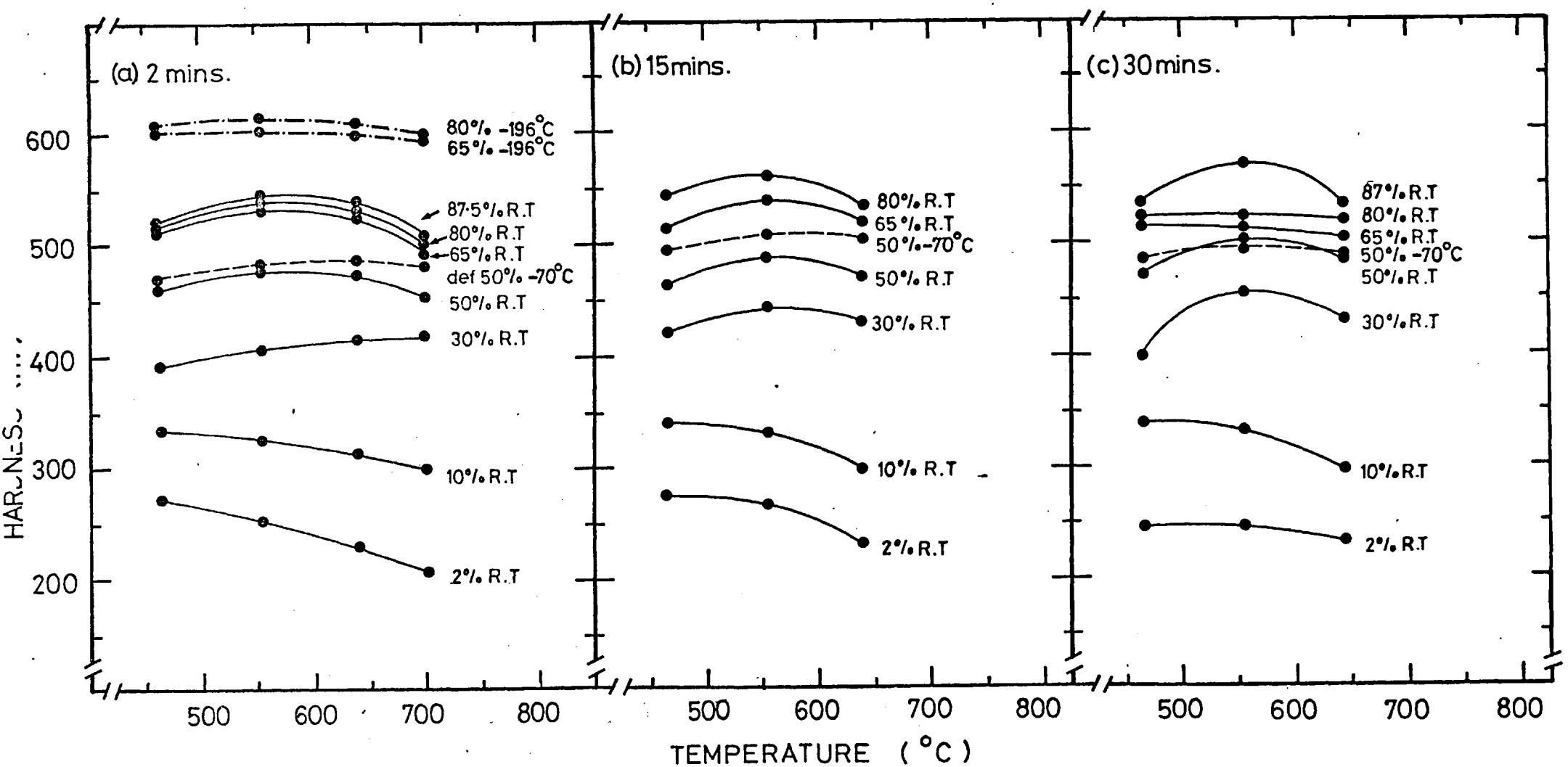


FIG. IV. 28 Short time ageing treatments.

Fig. IV.29 - Material 50% deformed at room temperature and heat treated at 464°C 15 min

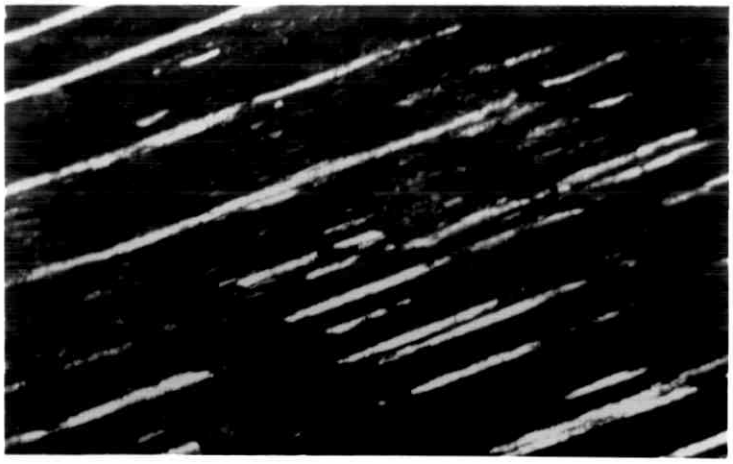


Fig. IV.29.a - HRDF from spot 2, showing hcp phase
Mag. 30 K



Fig. IV.29.b - HRDF from spot 1 showing twins

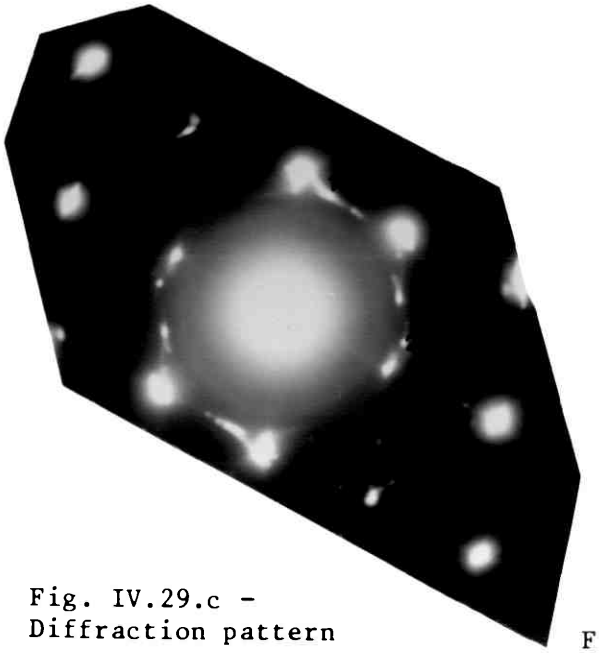


Fig. IV.29.c -
Diffraction pattern

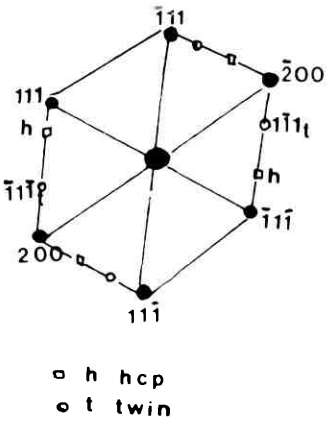


Fig.IV.29.d. Key of Diffraction Pattern
$(\bar{1}10)_M // (\bar{1}\bar{2}.0)_H$



Fig. IV.30.1.a - Bright field.
Mag. 58 K

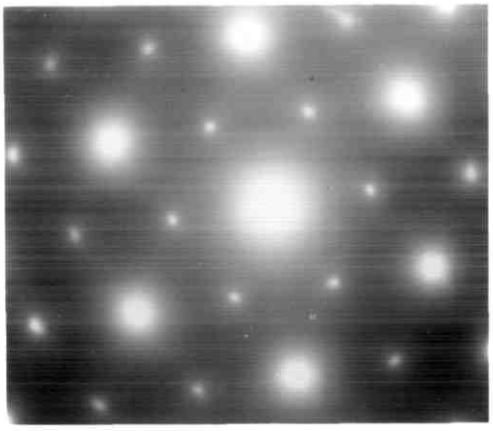


Fig. IV.30.1.b - Diffraction pattern
(111)//(0001)

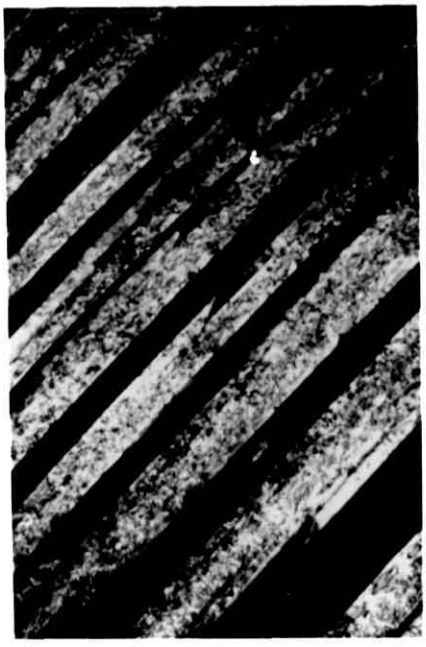


Fig. IV.30.2.a - HRDF showing
twins



Fig. IV.30.2.b - HRDF showing
hcp phase

Fig. IV.30 - Material previously deformed 65% at room temperature.
Heat treated at 640°C 15 min



Fig. IV.31.a - Bright field
Mag. 18 K



Fig. IV.31.b - HRDF from spot indicated in D.P., showing hcp platelets. Area from central part of Fig. a
Mag. 48 K

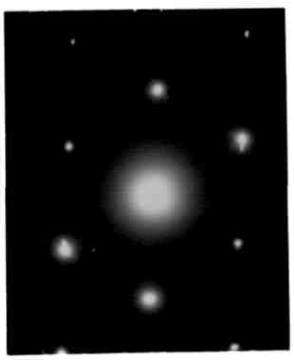
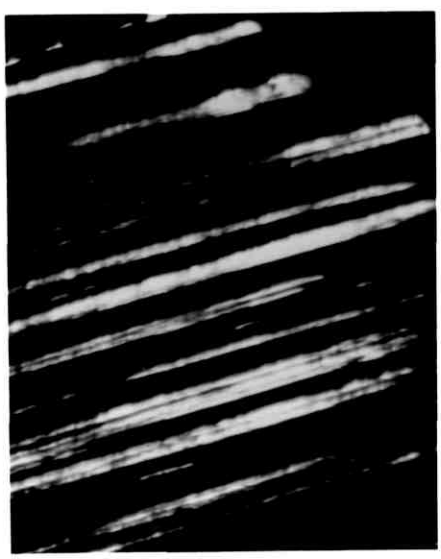


Fig. IV.31.c - Diffraction pattern B [0001]

Fig. IV.31 - Material deformed 50% at -196°C. Heat treatment at 640°C 15 min



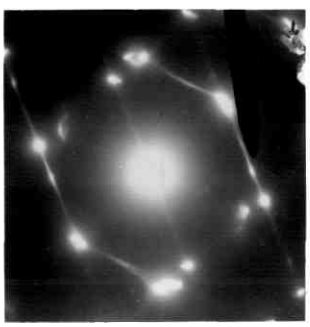


Fig. IV.32 - same deformation as above. Heat treatment at 700°C 2 min. Showing twins
Mag. 80 K

IV.2.b Long time ageing treatments

Figs. IV.33 to IV.35 show optical micrographs of the deformed material ; aged at different temperatures for different times.

For the heavily deformed material (50%) ageing at 600°C, after long times (100 and 150 hrs) does not show very marked differences from the samples given shorter ageing (5 hrs); some striation mark disappear, but very few. Fig. IV.36.d shows a scanning electron micrograph from a sample 50% deformed at room temperature and aged at 600°C for 147 hrs. Very deep striation marks can be observed, the same effect is seen in Fig. IV.36.c, which shows a scanning electron micrograph from a sample previously deformed 50% at liquid nitrogen temperature and aged at 600°C for 100 hrs. At this deformation temperature the effect is much more marked, and these deep striations will act as sites for precipitates as can be seen in Fig. IV.37, which shows the same deformation treatment but ageing at 700°C for 100 hrs. On ageing at 700°C recovery in most of the grains has occurred, and some recrystallized grains can be observed. Little difference in the structure is seen with ageing time. It is only after 100 hrs that some precipitate is present. On ageing at 850°C for 95 hrs the material completely recrystallizes. A very small recrystallized grain size and

the presence of a Cr, Mo rich precipitate along the grain boundaries, are observed. Figs. IV.38 and IV.39 are optical and scanning micrographs for the material aged at this temperature. The precipitate particle size is about 70 μm .

Grain growth is observed after ageing for 2 hrs at 950°C (Fig. IV.39).

IV.2.b.1 Hardness values after long ageing treatments

Long time ageing treatments were performed on the material previously deformed from 2% to 80% at room and liquid nitrogen temperatures. Table IV.6 gives a summary of the hardness values for the different samples, and Figs. IV.40 to IV.42 show the variation of hardness with deformation, ageing time and temperature respectively.

The specimens previously deformed at room temperature and aged, showed lower hardness values than those deformed at liquid nitrogen temperature and aged. However, in general, the ageing behaviour for both types of deformation treatments was very similar. The hardness values increase with ageing for all temperatures, the specimens with higher deformations have the higher hardness values for all the ageing times and temperatures (Fig. IV.40).

Specimens given prolonged ageing showed lower hardness values than those given short ageing treatments.

Comparing hardness changes as a function of ageing time for constant temperatures (Fig. IV.41). It is observed that at 470°C for deformation from 50% upwards the hardness increases with ageing time. At 600°C, there are scatter and fluctuations of hardness values with ageing time; this effect was observed as well for rapid heating treatments at 555°C. For the room temperature deformed material the hardness either remains constant or decreases slightly up to 30 hrs, and then remains fairly constant up to 100 hrs ageing time. For the liquid nitrogen temperature deformed material the hardness increases slightly up to 30 hrs after 30% deformation and then remains fairly constant or slightly decreases up to 100 hrs. On ageing at 700°C the hardness decreases with ageing time for the material deformed up to 20% at liquid nitrogen temperature; however it increases with ageing time for the heavily deformed material (50% and 65%). For the material previously deformed at room temperature the hardness slightly increases or remains almost constant for small deformations (up to 20%) decreases up 50% and again increases for the heavily deformed material (65% and 80%). Comparing changes in hardness with temperature for constant ageing times it is observed that hardness decreases with increase in temperatures, this effect being quite marked at 850°C, in which the material shows just slightly higher values than the original homogenized sample. After 5 hours ageing treatment the hardness values are fairly similar for the different ageing temperatures

(470°C, 600°C, 700°C).

No change is observed in the homogenized material either with ageing temperature or time.

IV.2.b.2 X-ray analysis - Long time ageing treatments

X-ray analysis was carried out on samples deformed and aged for long times, as well as on the annealed plus aged material. Special attention was given to those samples in which precipitation was observed by means of optical and scanning electron microscopy, (such as the ageing treatments 700°C/100 hrs and 850°C/95 hrs), in order to identify the precipitate and observe the changes in lattice parameter with ageing time.

Table IV.7 shows a summary of the values obtained. The peaks in these samples were fairly symmetrical and the broadening disappears with higher temperatures; as an indication of recovery and recrystallization at 850°C, the peaks were very narrow and symmetric at 950°C, at which temperature the material is completely recrystallized. On ageing at 700°C for 100 hrs new peaks are observed as an indication of some precipitation, and for higher deformations at the same temperature more peaks are present; the same effect is observed for higher temperatures and higher deformations (i.e. the number of peaks present increases at 850°C/950°C). The peak positions for the deformed plus aged material shift towards larger angles with respect to the deformed

material; but in most samples they remain at about the same position as in the annealed material. The chemical composition of the precipitates was also studied by means of the Jeol 35 scanning electron microscope. This apparatus gives qualitative but not quantitative analysis.

The chromium content of the matrix varied from one site to another, especially near grain boundaries. Particles rich in Cr and Mo were found, and some Ti rich particles. Using data from the ASTM index cards, the possible precipitate types are listed in Table IV.8.

The lattice parameter decreases with ageing time (Table IV.9). This effect is more marked in the samples previously deformed at -196°C, than in the samples previously deformed at room temperature. No change is observed in the homogenized material with ageing time.

IV.2.b.3 Results of grain size measurements

Grain size measurements were made in the annealed material and also in deformed and deformed plus aged material. For the deformed material the grains elongated in the rolling direction with the increasing amounts of deformation. The measurements were made to compare with the grains after ageing, for the material deformed, from -10% to 50% at -196°C. The results are given on the next page.

Amount of Def.	Grain size in μm^2 (area)					
	Not Aged	Ageing Treatments				
		600°C		700°C	850°C	1050°C
		5 h.	100h.	100h.	95 h.	1 h
50% LN	1941	2041	4021*	2067	219.8	
30% LN	1025				251.6	
10% LN	839.2				271.6	
Annealed						1268

* this value does not follow the general behaviour

As can be seen, as the amount of deformation increases the recrystallized grain size (after 850°C/95 hs ageing) decreases. Even after 10% deformation, the material recrystallizes. It is apparent that at 700°C some part of the material has started to recrystallize since the average grain size is smaller than the material aged at 600°C/100 hs.

IV.2.b.4 Diffraction analysis for long time ageing treatments (5hs to 147 hs)

For samples previously deformed by small amounts (i.e. up to 20% at room temperature and liquid nitrogen) after heating for 30 hours and 100 hours at 470°C no presence of hcp phase was detected by means of transmission electron microscopy. Fig. IV.43 shows a bright field of a sample deformed 20% at -196°C and aged

at 470°C for 30 hs. Stacking faults and dislocations are observed. However, for the material deformed 20% at liquid nitrogen and aged at 600°C for 100 h the presence of hcp phase was observed (Fig. IV.47). Only after long time ageing the hcp phase was found, for prior 20% deformations at -196°C. After 5 hours at 600°C only twins were observed, with internal dislocations Fig. IV.44. The matrix from this material presents many stacking faults (Fig. IV.44.c).

In the material heavily deformed in liquid nitrogen (50% and 65%) hcp phase was observed after ageing at 600°C for 5 hrs and 30 hrs (Fig. IV.45). Some recovery is observed in the long time treatments (100 h) at 600°C, Fig. IV.46 .

At 700°C, after long time ageing treatment, (30 h and 100 h), some recovery has taken place, but still twins are observed (Figs. IV.48 and IV.49).

IV.2.b.5 Recrystallization

On ageing at 850°C the material presents complete recrystallization, and the presence of a precipitate a chromium molybdenun compound (Figs. IV.50 and IV.51); the matrix presents stacking faults and some dislocations Figs.IV.50.1.b and IV.50.2.

The precipitates are observed along grain boundaries (Fig. IV.51.b) and probably along an old grain boundary Fig. IV.51.a. The diffraction pattern from one particle is shown in Fig. IV.51.c.



Fig. IV.33.a - Material previously deformed 50% at -196°C and aged 5 hrs at 600°C X 345

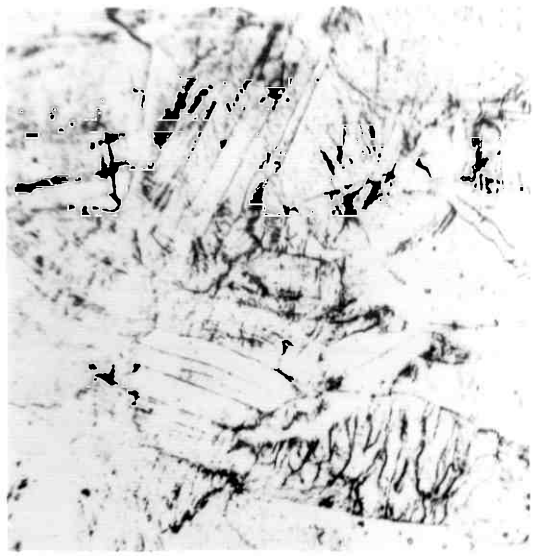


Fig. IV.33.b - Material previously deformed 50% at -196°C and aged 100 hrs at 600°C X345

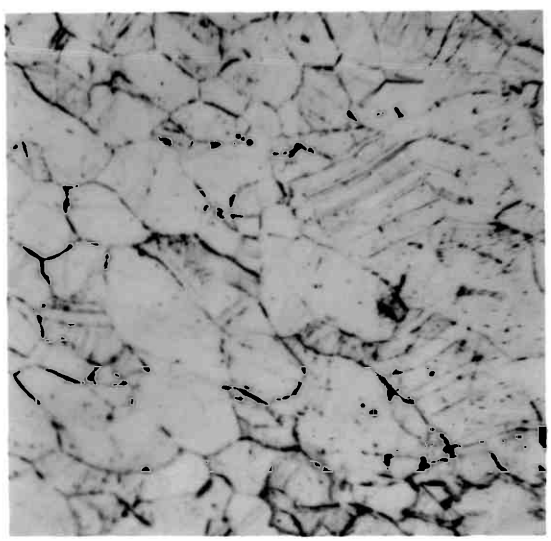


Fig. IV.33.c - Material previously deformed 50% at room temperature and aged 30 hrs at 600°C X 345

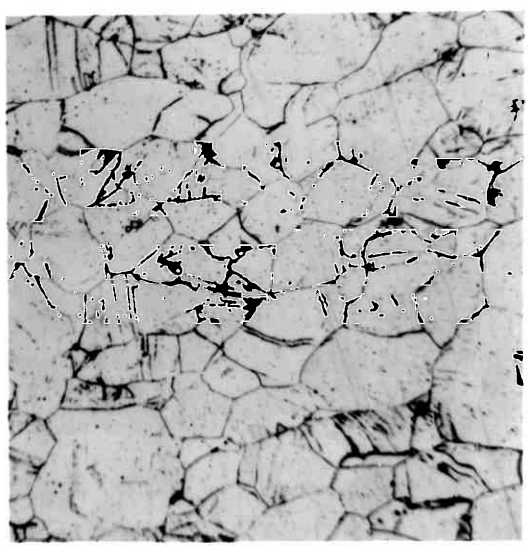


Fig. IV.33.d - Material previously deformed 50% at room temperature and aged 147 hrs at 600°C X 345

Fig. IV.33 - Long time ageing treatments at 600°C

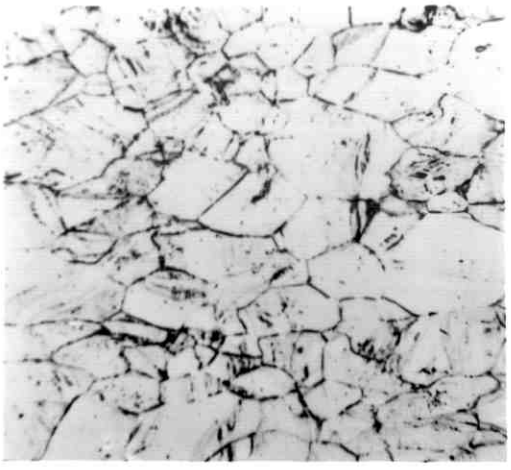


Fig. IV.35.a - Material previously deformed 50% at room temperature and aged 5 hrs at 700°C X 345

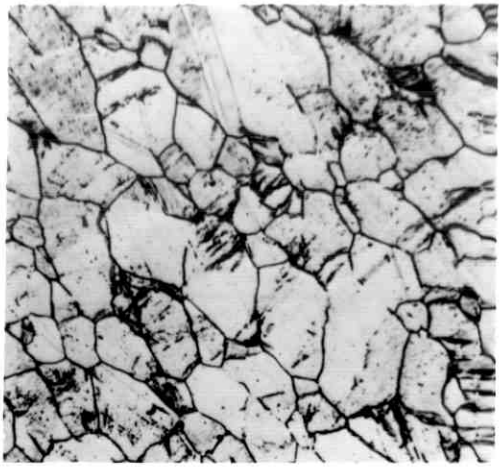


Fig. IV.35.b - Material previously deformed 50% at room temperature and aged 30 hrs at 700°C X 345



Fig. IV.35.c - Material previously deformed 50% at -196°C and aged 100 hrs at 700°C X 345

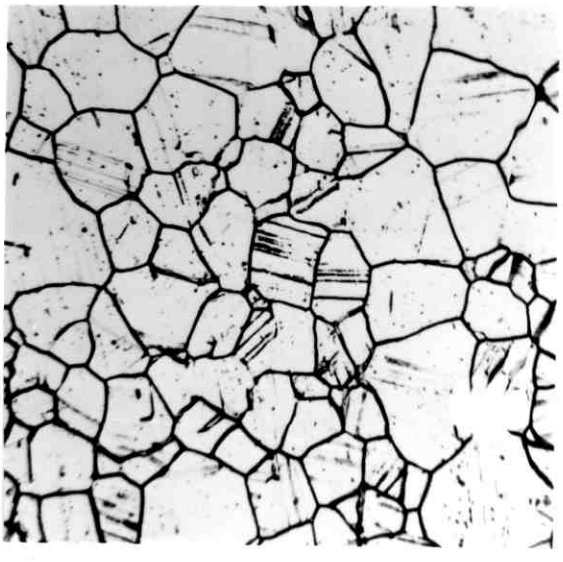


Fig. IV.35.d - Material previously deformed 20% at room temperature and aged 30 hrs at 700°C . X 345

Fig. IV.35 - Long time ageing treatments at 700°C



Fig. IV.36.a X 500

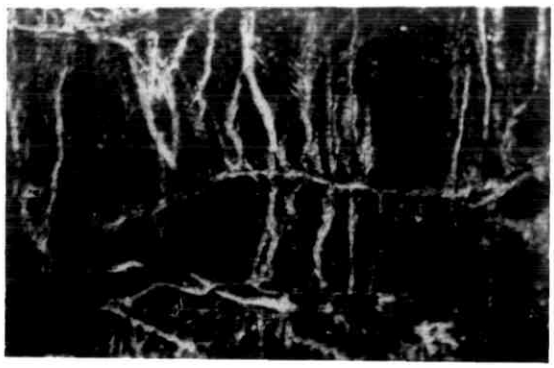


Fig. IV.36.b 1K

Figs. IV.36.a, b and c - Material previously deformed 50% at -196°C and aged 100 hrs at 600°C

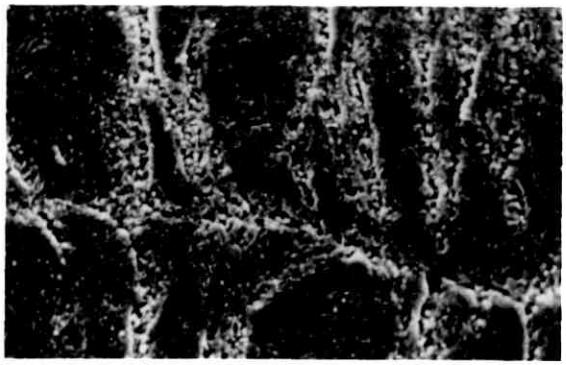


Fig. IV.36.c 5 K



Fig. IV.36.d - Material previously deformed 50% at room temperature and aged 147 hrs at 600°C

2 K

Fig. IV.36 - Scanning electron micrographs

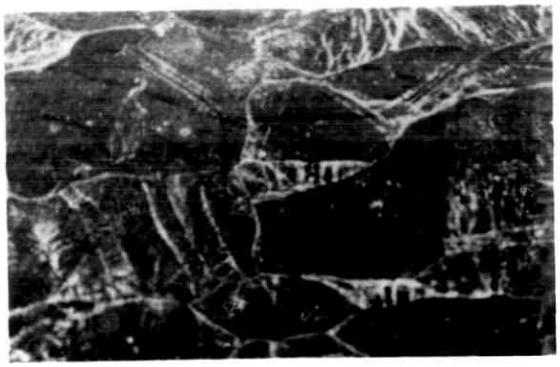


Fig. IV.37.a - X 500



Fig. IV.37.b - X 2 K

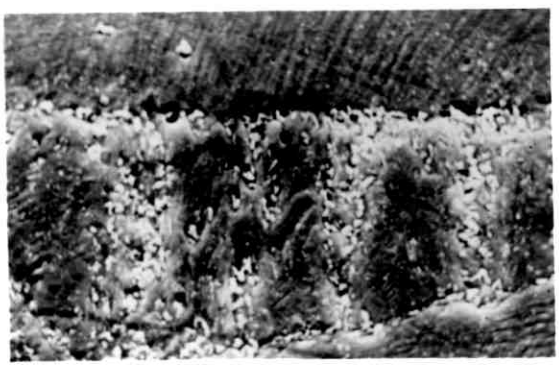


Fig. IV.37.c - 5K

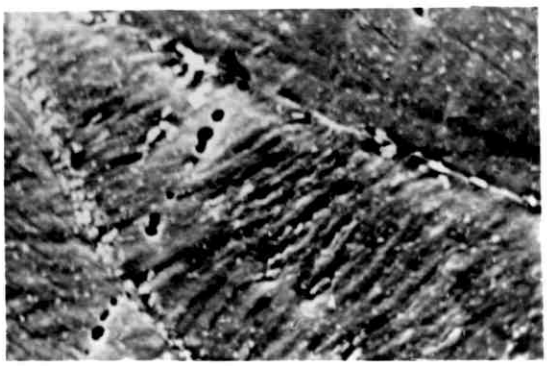


Fig. IV.37.d - 10 K

Fig. IV.37 - Scanning electron micrographs

Material previously deformed 50% at -196°C and aged 100 hrs at 700°C. Showing precipitates lying on grain boundaries and striations inside the grains.

Fig. IV.38 - Recrystallization

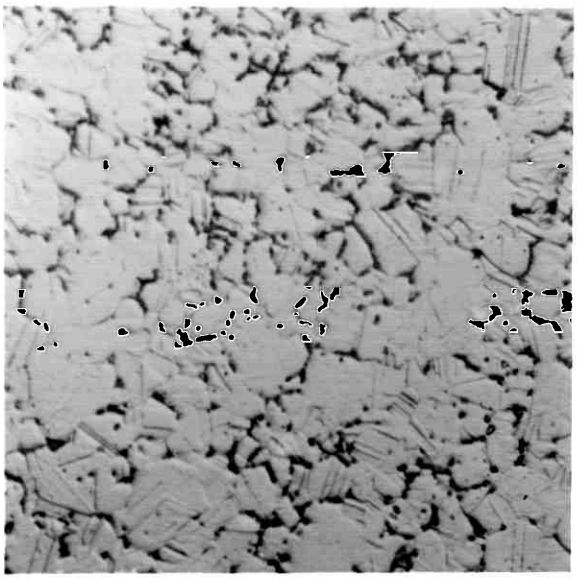


Fig. IV.38.1.a - Material previously deformed 2% at room temperature X 375

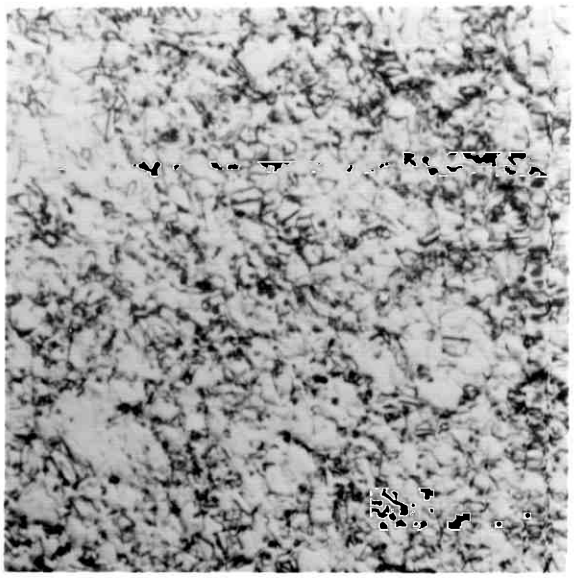


Fig. IV.38.1.b - Material previously deformed 50% at room temperature X 375

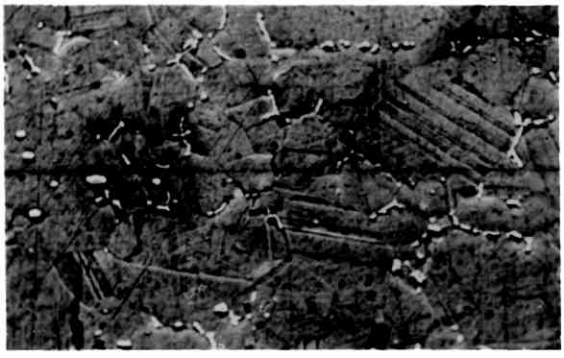


Fig. IV.38.2.a - Material previously deformed 2% at -196°C S.E.M. X 2 K



Fig. IV.38.2.b - Material previously deformed 50% at -196°C S.E.M. X 2 K

Fig. IV.38 - Material aged at 850°C 95 hrs

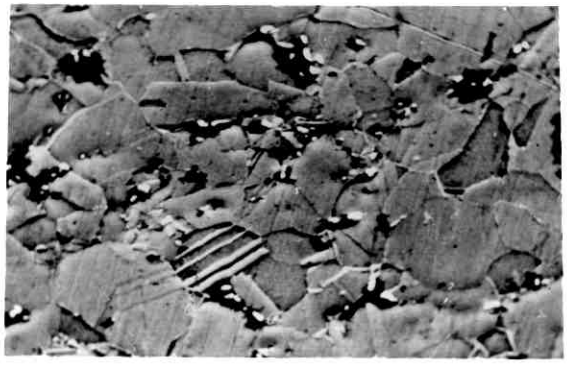


Fig. IV.39 - Material previously deformed 50% at -196°C. Aged 2 hrs at 850°C + 2 hrs at 950°C S.E.M. X 2 K

TABLE IV.6

HARDNESS VALUES FOR LONGER TIMES HEAT TREATMENTS AT DIFFERENT TEMPERATURES

		T = 470°C*						T = 700°C						T = 600°C						
		Material Rolled at R T			Material Rolled at -196°C			Material Rolled at R T			Mater. Rolled at -196°C			Material Rolled at R T				Material Rolled at -196°C		
		5h	30h*	116h*	5h	26h*	116h*	5h	30h	100h	23h	30h	100h	5h	30h	112h	147h	5h	30h	100hr
Undeformed S.T.		-	-	-	171	172	170	169	-	172	166	-	-	-	-	180	175	174	-	166
	2%	-	-	-	221	213	211	-	-	-	194	-	206	-	-	-	-	192	200	213
1	5%	-	-	244	-	-	-	-	229	212	-	214	226	216	235	238	-	-	212	212
2	10%	-	296	-	-	299	285	277	248	268	286	294	280	298	286	315	-	322	315	293
3	20%	-	367	381	394	381	426	387	358	343	362	369	374	399	404	400	376	379	374	386
4	30%	460	466	456	-	-	-	450	407	388	-	-	-	447	466	463	445	-	-	-
5	50%	450	470	516	532	549	577	463	435	412	490	490	501	498	466	480	476	505	532	532
6	65%	466	509	520	509	593	618	453	457	457	532	528	516	494	501	498	490	557	575	566
7	80%	-	505	536	575	618	628	505	463	460	549	549	520	509	503	-	498	-	613	615

850°/95h 263 (10% & 20% RT def)//238 (80% & 50% RT def)

950°/1h 273 (50% del RT)

1000°/2h 200 (80% def RT)

S.T. Solution treated

* age cooling to R T

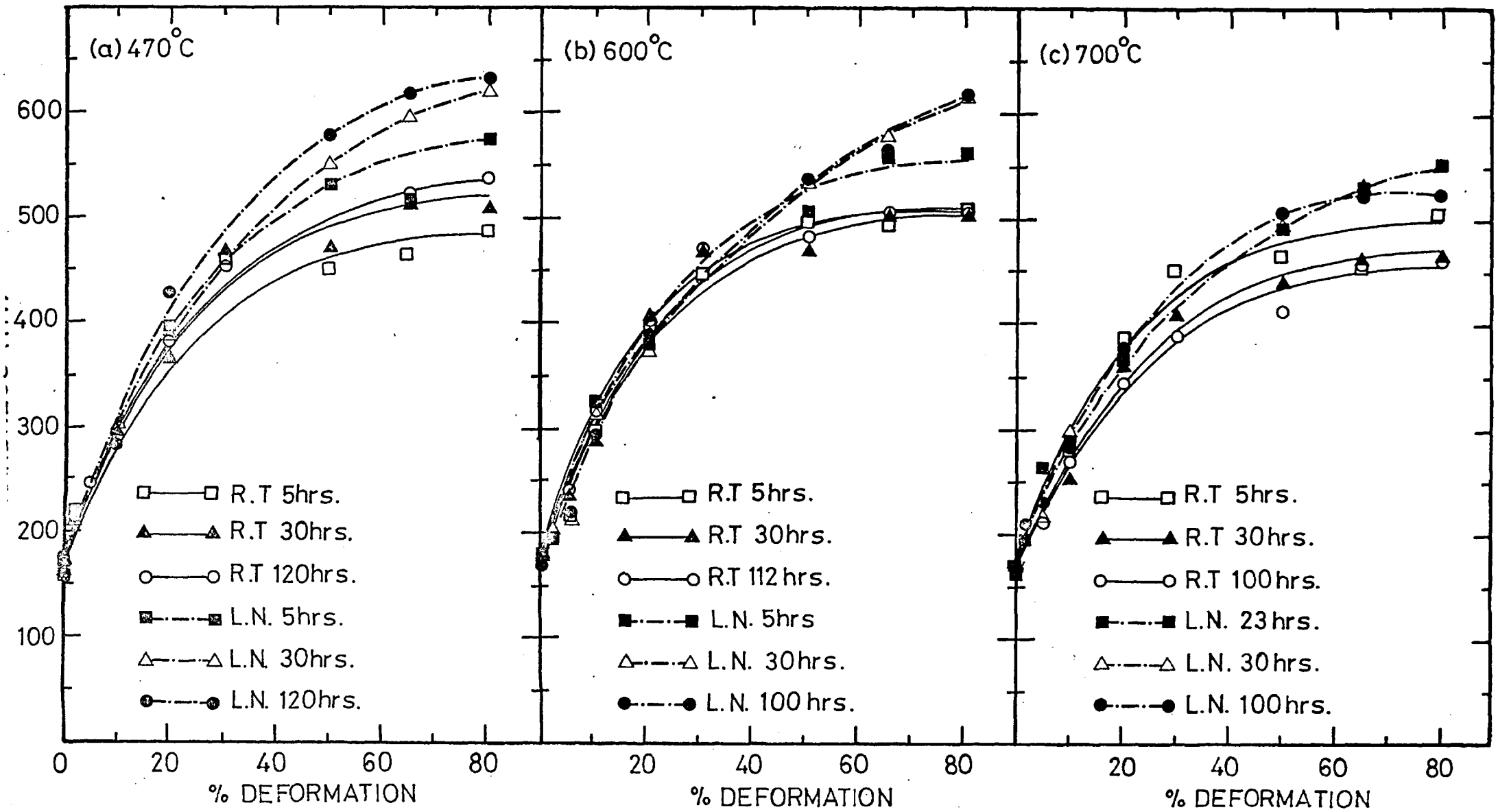


FIG. IV.40 Hardness vs. deformation for different ageing times and temperatures.

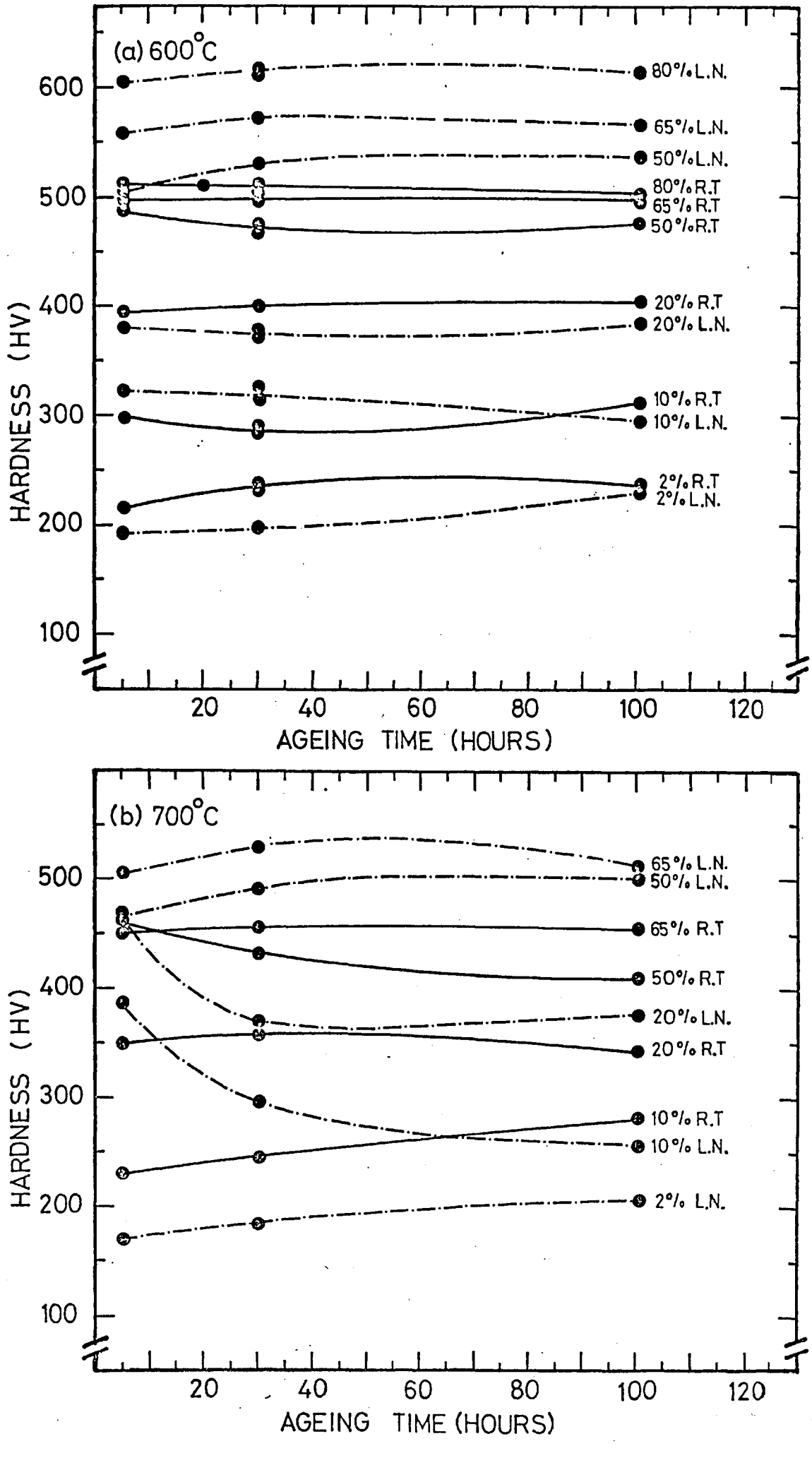
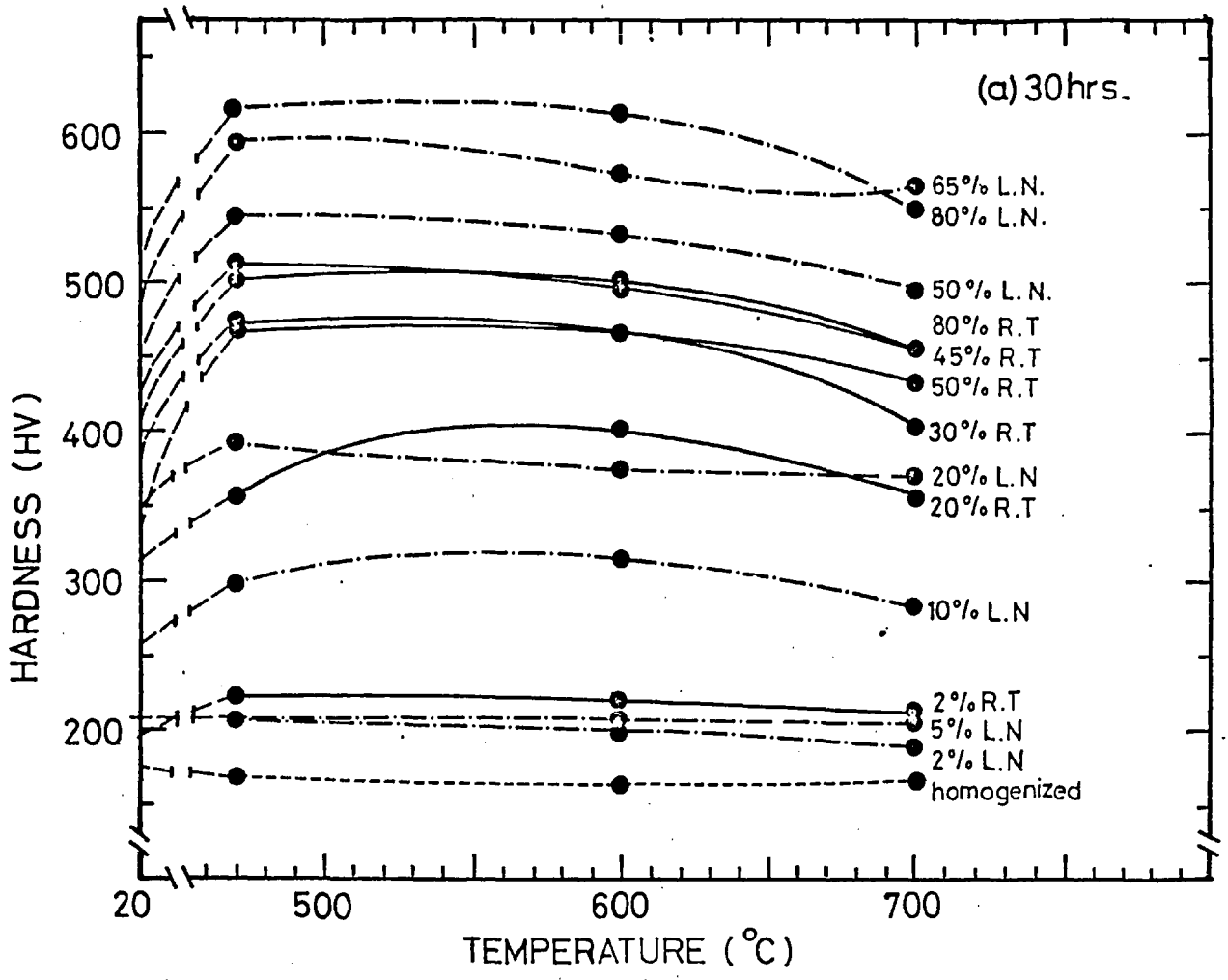


FIG. IV.41 Hardness vs. ageing time for constant ageing temperature.



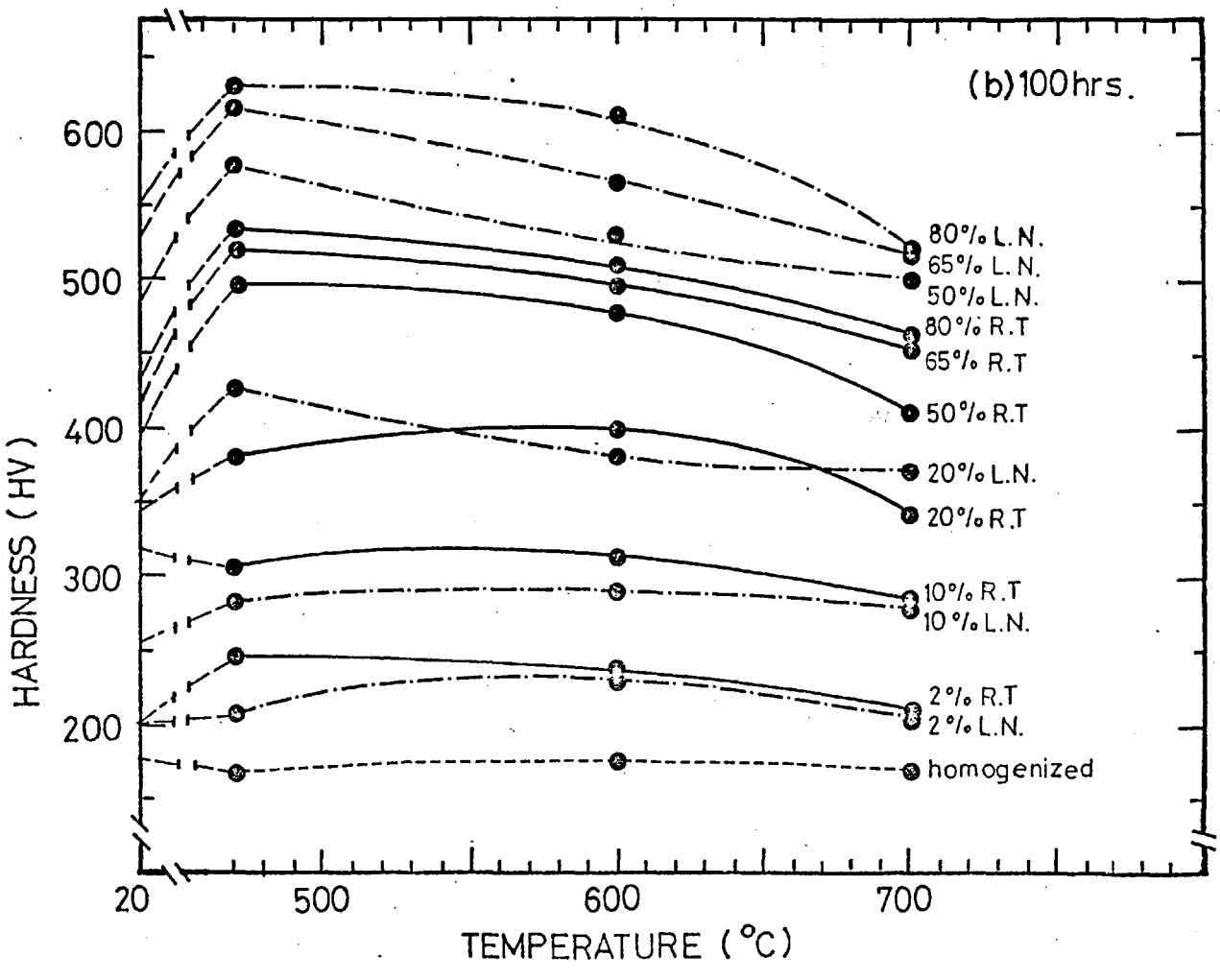


FIG. Ⅳ. 42 Hardness vs. ageing temperature.

TABLE IV.7

X-ray Analysis Long Ageing Treatments (cobalt radiation)

	Ageing at 600°C									Ageing at 700°C/100hrs								
hkl	2θ	d	a	2θ	d	a	2θ	d	a	2θ	d	a	2θ	d	a	2θ	d	a
	Annealed + Aged 700°C/100h			30% def L N + Aged 600°C/30h			50% def at L N + Aged 600°C/100hr			2% def L N			50% def L N			50% def RT		
	27.2*	3.8067								34*	3.062		45.6*	2.31		44.7*	2.35	
	28.2*	3.6743											50.5*	2.106				
111	51.4	2.064	3.575	51.8	2.049	3.549	51.6	2.057	3.563	51.4	2.064	3.575	52.2	2.035	3.524	51.6	2.057	3.562
200	59.95	1.7935	3.587	60.2	1.785	3.57				59.95	1.792	3.584				60	1.79	3.580
220	90	1.266	3.580	90.1	1.265	3.578	90.2	1.264	3.575	89.95	1.266	3.581	90.8	1.257	3.555	90.2	1.26	3.571
	80% def L N + Aged 700°C/100hr			2% def R T + Aged 850°C/95hr			80% def R T + Aged 850°C/95hr			50% def RT + 850°C/95h+950°C/2h			2% def R T + 850°C/95h+950°C/2h					
	27.6*	3.753		34*	3.062													
	44.8*	2.35																
	50.6*	2.09																
111	51.55	2.06	3.568	51.5	2.06	3.568	51.5	2.06	3.568	51.4	2.06	3.568	51.6	2.057	3.563			
							53*	2.006		53*	2.006							
							54.6*	1.95		54.5*	1.95							
										56.8*	1.88							
										57.4*	1.86							
200	60.2	1.78	3.57	60	1.79	3.580	60.1	1.79	3.580	60	1.79	3.580	60.2	1.785	3.57			
220	90.2	1.264	3.575	90.05	1.265	3.578	90.2 90.4	1.26	3.572	90	1.266	3.581	90.2	1.264	3.575			

* new peaks

TABLE IV.8

X-ray Diffraction Analysis of possible Precipitates found during Ageing

Ageing temp. at which PPT was observed	d Å	FCC Matrix	*Co_3Mo a=5.13Å c=4.12Å	$M_{23}C_6$ a=10.62Å	M_6C a_o=11.02Å	$(Mo,Cr)_4C$ a_o=2.982 c_o=28.81	Co_2Mo_3 Tetrag. a_o=9.23/Co=4.83	Cr-Ni-Mo** phase Tetr(σ)	
700°/100hrs	3.8067						111	d values	
700°/100hrs	3.753			022					
700°/100hrs	3.6743								
700°/100hrs									
850°/95hrs	3.062		10.1	222					
	2.35		20.2	024	422	015		2.32	311
	2.106		11.1		333	018	212		
	2057	111	00.2	333 115			411	2.056	330
850°/95hrs	2.006						311	2.004	202
850°/95hrs	1.95		20.1		440	10$\underline{10}$,00$\underline{15}$	222	1.964	411
950°/2hrs	1.88		10.2	044	442		312	1.864	331
	1.79	200		135				1.789	312
	1.26	220				024	551	1.263	631

* Drapier et al (6)
** Rideout and beck (5)

TABLE IV.9

Values of true lattice parameter (a_o) for different alloy conditions and different ageing temperatures

Material treatment		No Aged	AGED				
			600°C		700°C	850°C	950°C
			30hrs	100 hrs	100 hrs	95hrs	2 hrs
Annealed (1100°C/1hr)		3.585					
Deformed at -196°C	2%	3.585			3.573		
	10%	3.585					
	20%	3.585					
	30%	3.585	3.584				
	50%	3.585		3.583	3.565		
	65%	3.585					
	80%	3.585			3.566		
Deformed at R T	2%					3.578	3.577
	30%	3.585					
	50%	3.586			3.563		3.578
	65%	3.584					
	80%	3.585				3.576	

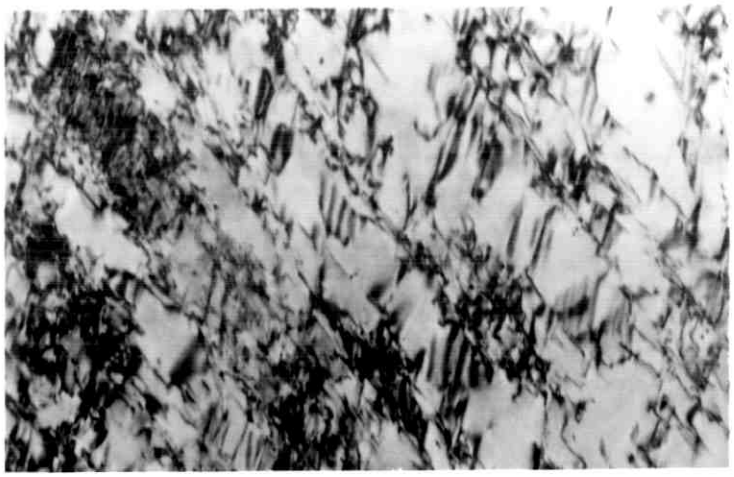


Fig. IV.43 - Material previously deformed 20% at -196°C and aged 30 hrs at 470°C
Mag. 100 K

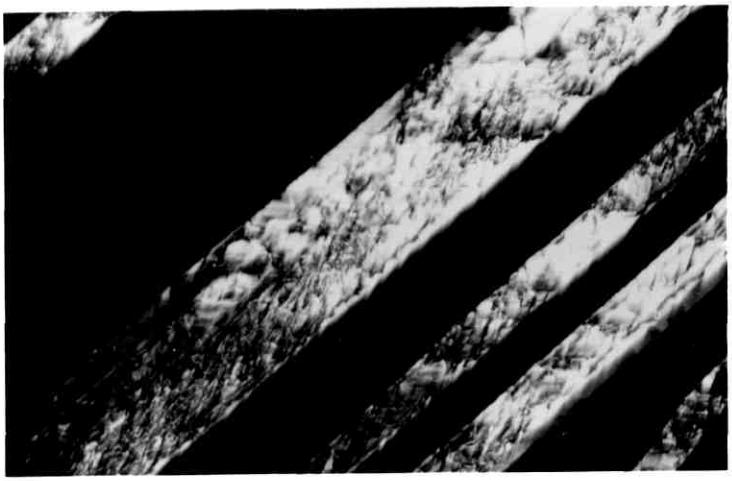


Fig. IV.44.a - HRDF showing very faulty twins lying on $(1\bar{1}1)$ plane Mag. 48 K

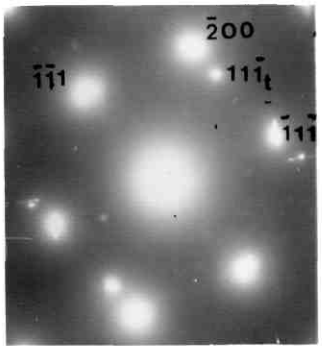


Fig. IV.44.b - Diffraction Pattern

B [0 1 1]

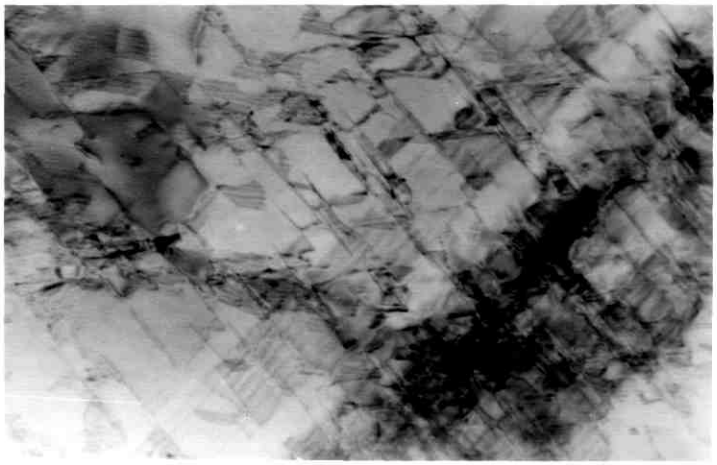


Fig. IV.44.c - Structure showing stacking faults
Mag. 80 K

Fig. IV.44 - Material previously deformed 20% at -196°C and aged 5 hrs at 600°C



Fig. IV.45.a - HRDF from spots 5 & 3 showing matrix Mag. 38 K

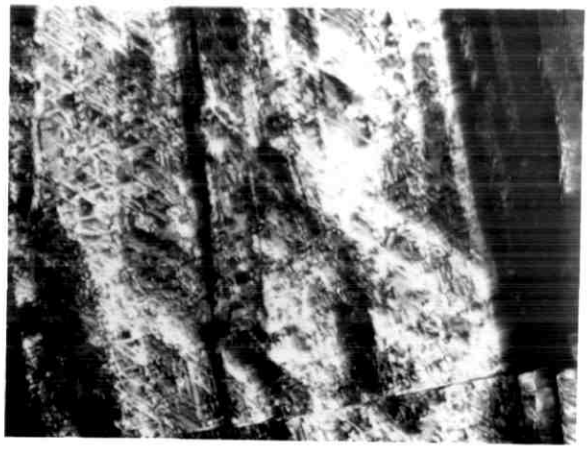


Fig. IV.45.b - HRDF from spots 1,2 & 4, showing hcp phase Mag. 38 K

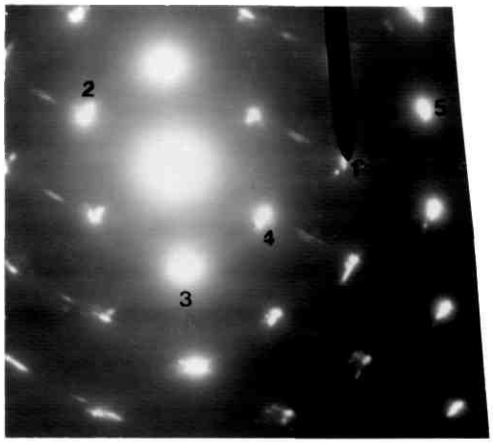


Fig. IV.45.c - Diffraction Pattern for a and b

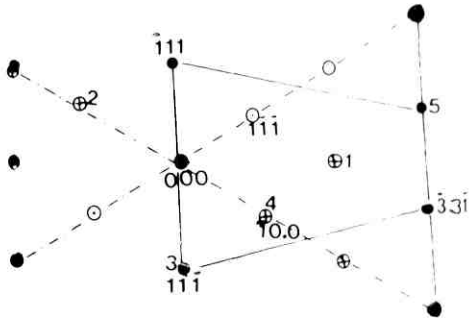


Fig. IV.45.d - Key of D.P.c

● common to all three
e twin
hcp
(123)m
(321)t
(24.9)h

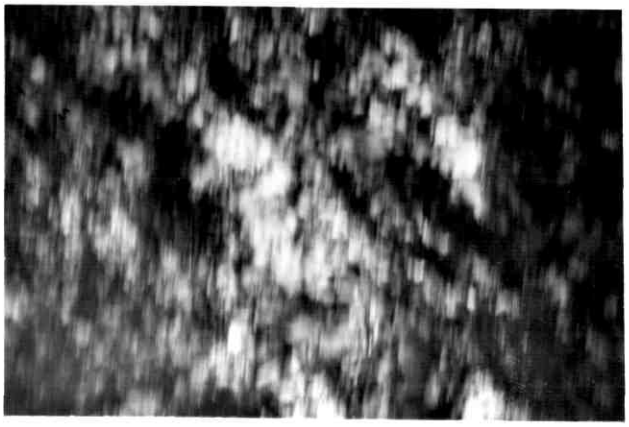


Fig. IV.45.e - HRDF from inner spots showing hcp phase Mag. 48 K

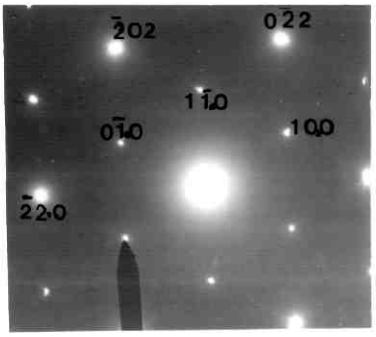


Fig. IV.45.f - Diffraction Pattern (111)//(0001)

Fig. IV.45. - Material previously deformed 65% at -196°C and aged 5 hrs at 600°C

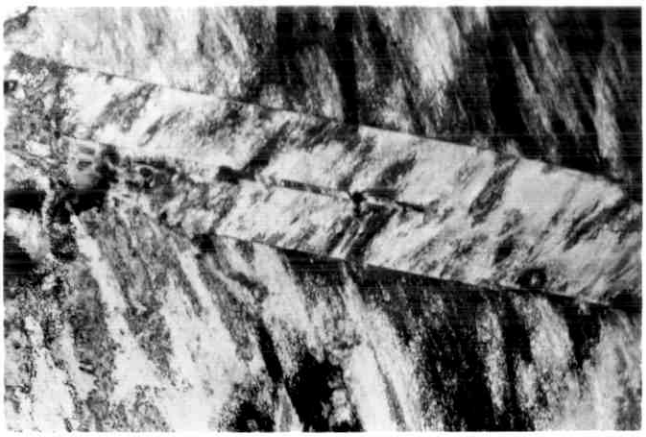


Fig. IV.46.a 8 K

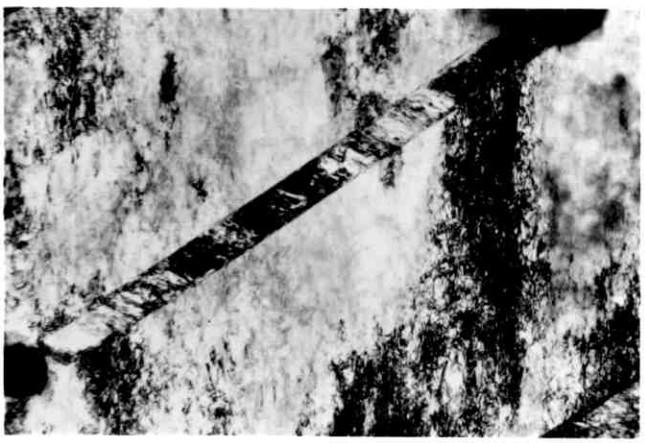
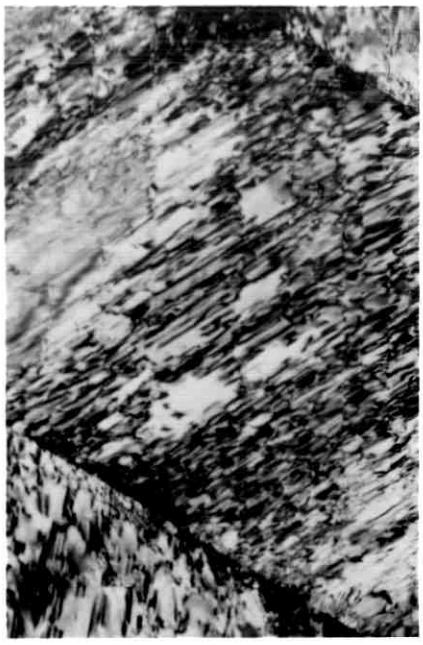


Fig. IV.46.b - 38K



Fig. IV.46.c - 80 K

Fig. IV.46 - Material previously deformed 50% at -196°C and aged 100 hrs at 600°C. a, b, and c are bright field views from the same area at different magnifications, showing a twin within a twin





Figs. IV.47.a & b - Are different magnifications from the same area; showing matrix with stacking faults
a) 58 K b) 80 K

Fig. IV.47 - Material previously deformed 20% at -196°C and aged 100 hrs at 600°C



Fig. IV.48.a - Bright field 58 K

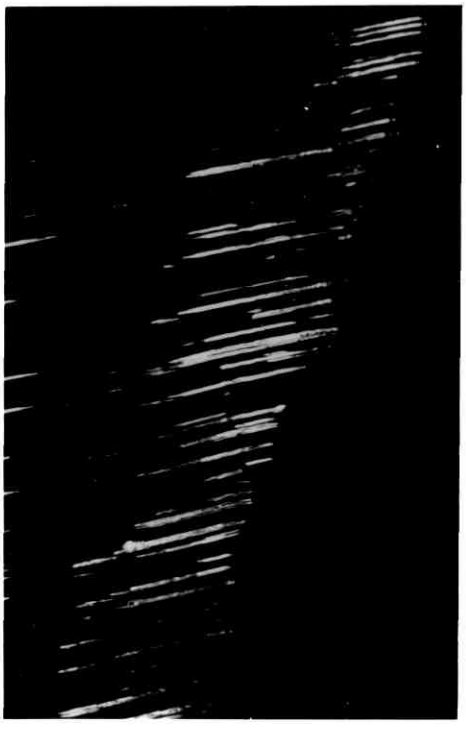


Fig. IV.48.b - HRDF showing twins on $(1\bar{1}1)$ 48 K

Fig. IV.48 - Material previously deformed 20% at -196°C and aged 30 hrs at 700°C

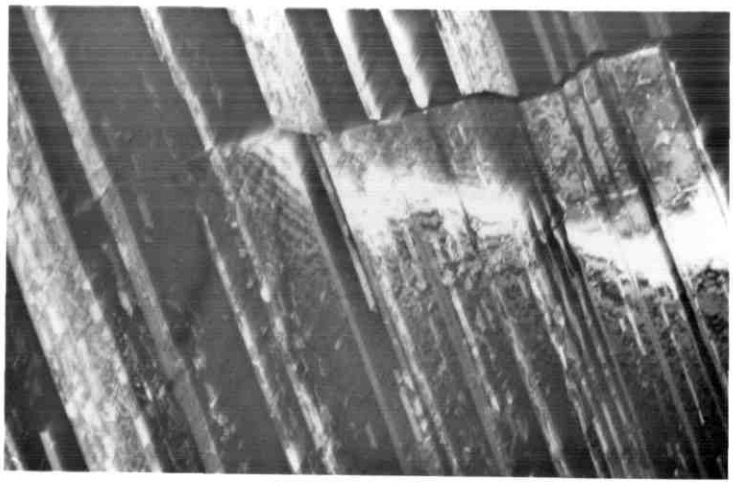


Fig. IV.49.a - HRDF showing twins Mag. 30 K

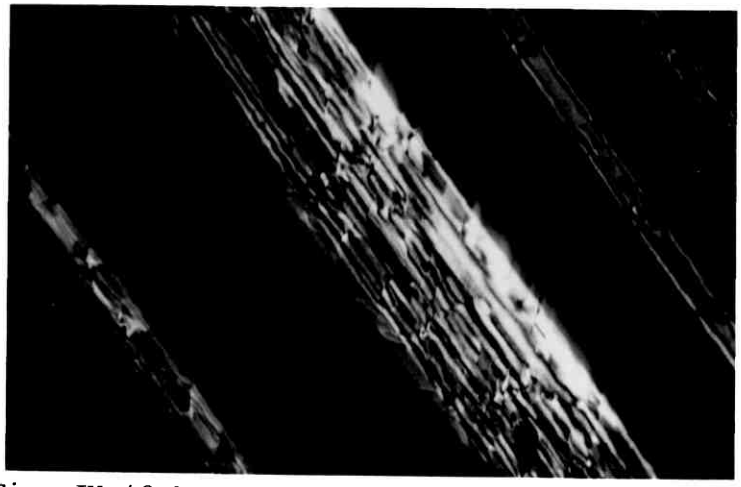


Fig. IV.49.b - HRDF showing a faulted twin at higher magnification Mag. 80 K

Fig. IV.49 - Material previously deformed 50% at -196°C, aged 100 hrs at 700°C

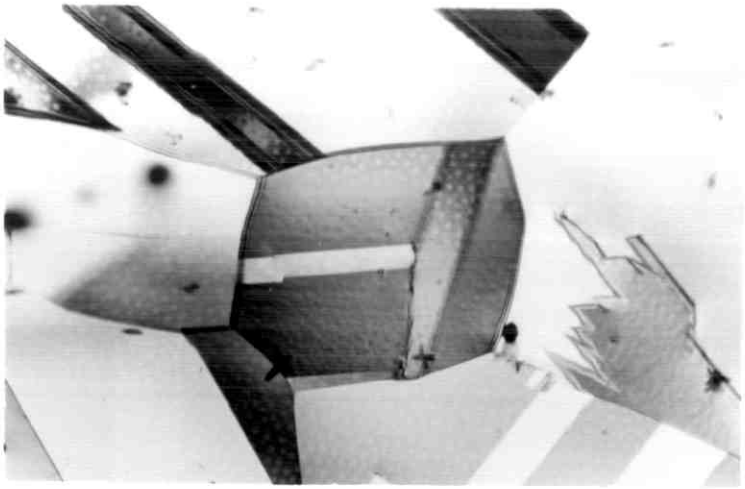


Fig. IV.50.1.a - Bright field showing matrix recrystallized 8 K

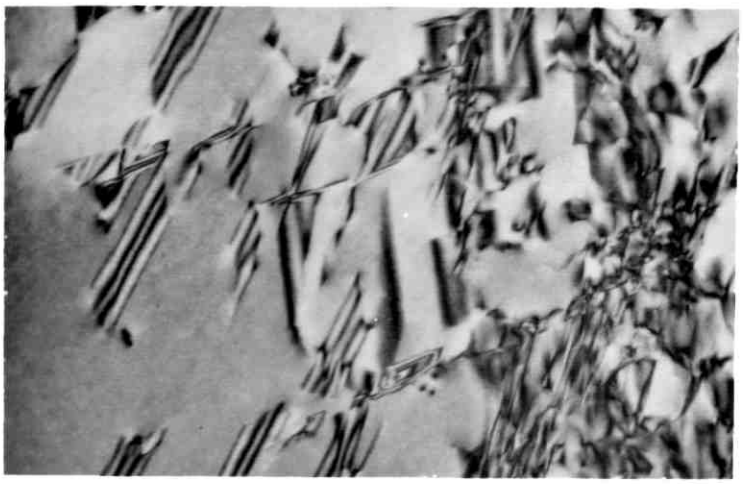


Fig. IV.50.1.b - Bright field from a different area of the same sample showing stacking faults and dislocations 8 K

Fig. IV.50.1 - Material previously deformed 30% at room temperature

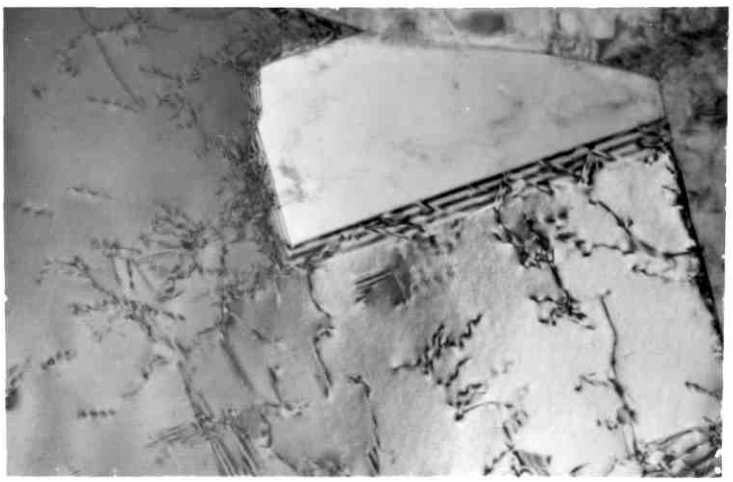


Fig. IV.50.2 - Material previously deformed 80% at room temperature; bright field showing a more faulty matrix than above. Some stacking faults and dislocations are seen. Mag. 58 K

Fig. IV.50 - Ageing Treatments at 850°C - 95 hrs.

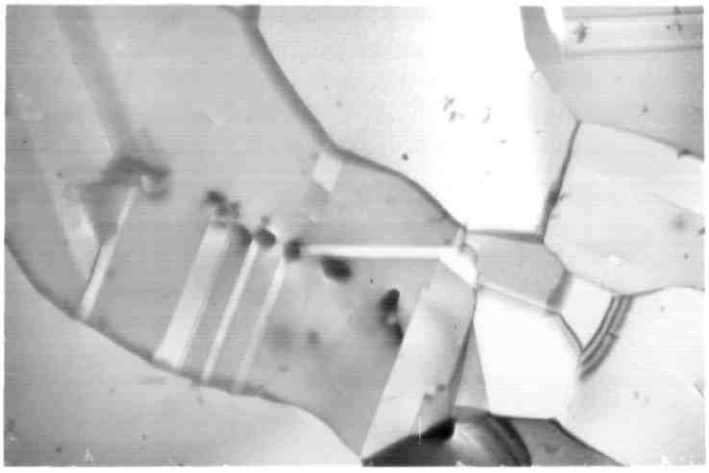


Fig. IV.51.a - 8K

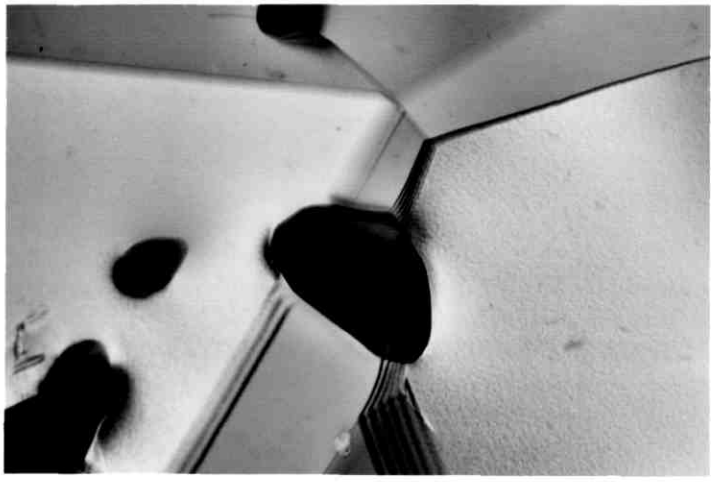


Fig. IV.51.b - 24 K



Fig. IV.51.c - 58 K

Fig. IV.51 - Ageing treatments at 950°C 2 hrs. Material completely recrystallized, showing precipitate particles lying probably along an old grain boundary and on the new ones

IV.3 Tensile Test Results

Table IV.10 shows the results for the two alloys A and B in the solution treated and deformed conditions tested from room temperature to -196°C.

The behaviour of both alloys is very similar at all temperatures except for alloy B which when tested at room temperature, in the deformed condition, showed lower values of proof stress and strain hardening; however, this was the only case in which this behaviour was observed. In all the other cases the behaviour of both alloys is very similar, the values of proof stress, tensile stress at instability and fracture stress increase with decreasing temperature, while the reduction of area and elongation values remain fairly constant with temperature for the solution treated condition. For the deformed condition the elongation increases from 25% to 35% for alloy A tested at 111°C and to 30% for alloy B tested at -196°C.

Alloy A (higher Ti content) shows slightly higher values of proof stress, tensile stress at instability and fracture stress than alloy B, for all conditions.

As is expected the deformed material shows much higher values of stress and lower values of ductility than the solution treated material. For most of the cases duplicate tests were performed and these

showed very good agreement. Figs. IV.52 - IV.55 show the true stress - true strain graphs for both alloys (solution treated and deformed), tested from room temperature to -196°C. The strain hardening exponent was calculated from the slopes of the graphs log true stress - log true strain (Figs. IV.56 and IV.57). These graphs did not show a straight line, but there was only a small difference in the slope for the solution treated material tested from room temperature to -196°C. However, the mean value of all points was in good agreement with the values of n calculated at instability, which are showed in Table IV.11. This behaviour was not observed in the previously deformed material, which show a straight line at all test temperatures with the same value of strain hardening exponent, which is in very good agreement with the values of n showed in Table IV.11 for the same conditions. Table IV.11 shows the values of n obtained from the graphs; n_A is the slope of a mean line through all the points.

The solution treated material shows almost the same value of strain hardening exponent as measured from the strain to instability for all the test temperatures; the variation is between 0.55-0.46, and the slopes obtained from the graphs for just one average line through all the points have approximately these values. The deformed material presents slightly greater differences in the n values, as measured from the strain

at instability, however they vary between 0.10-0.21. The values from the graphs agree fairly well with these values; they are 0.12-0.13. The value of the strain hardening exponent of alloy B deformed and tested at R T, of 0.35 can be considered as an anomalous value, since it does not agree at all with the general behaviour, in any case this test is not to be considered since it presented rather low values of general level of stress, only for this condition. A duplicate of this test was not available, therefore it can be considered as an anomalous test.

IV.3.a Analysis of the graphs of work hardening rate vs True plastic strain

Work hardening rate values were calculated over very short intervals of the curve true stress - true strain. These values were plotted in log-log graph for the solution treated material (Fig. IV.58), tested at room temperature, -4°C, -80°C and -196°C. The data for the deformed material tested at room temperature, -50°C, -111°C and -196°C were also plotted (Fig. IV.59). Appendix III shows tables A.III.1 to 3 with the values of work hardening rate vs true plastic strain.

Observing Fig. IV.59, very little change is obtained in the slope of the work hardening rate vs strain graph, for the deformed material at any temperature, moreover the rate of change

$d(d\sigma/d\varepsilon)/d\varepsilon$ is approximately the same for the different test temperatures; this behaviour is observed in both alloys A and B, although the data shown is only for B. This observation could be deduced as well from Fig. IV.57.

The solution treated material shows a rather different situation; as was observed in Fig. IV.56 the log true stress - log true strain graph did not show a straight line, plotting the work hardening rate vs true strain, it is also observed in Fig. IV.58 that a "multiple stage" work hardening occurs. The work hardening rate decreases at all temperatures with increasing strain, up to approximately a common value of strain about 0.14; thereafter, the $\left(\frac{d\sigma/d\varepsilon}{d\varepsilon}\right)$ value changes to a lower value; this is so for all temperatures except for -196°C which presents a sharp increase in work hardening rate after 0.4 plastic strain. The material tested at room temperature presented only two different stages, while in the material tested at subzero temperatures three stages were observed, except the test at -196°C which showed a fourth stage. For the subzero temperature tests, the first change in the slope of the work hardening rate vs true plastic strain plot is at about 0.03 plastic strain and the second at about 0.14 plastic strain, as was mentioned before.

IV.3.b Summary of Mechanical Properties vs temperature

Figs. IV.60 and IV.61 show the variation of

strength (i.e.0.2% proof stress tensile stress at instability and fracture stress) and ductility with temperature for the solution treated material (Fig. IV.60) and for the deformed material (Fig. IV.61). For the solution treated condition for both alloys it is observed that the strength increases as the temperature decreases. However the values of reduction of area, and elongation remain fairly constant with decreasing temperature.

For the deformed material the tensile stress and proof stress increase as the temperature decreases, however, the fracture stress seems to reach a maximum and then decrease for very low temperatures (-196°C and -111°C) the reduction of area follows a behaviour similar to the solution treated material, remaining fairly constant with decreasing temperature. However, the elongation values increase slightly (about 10% increase) for the very low temperatures (-111°C and -196°C). Both alloys show similar behaviour.

IV.4 Impact Testing

Fig. IV.62 shows the energy absorbed at fracture vs temperature for both alloys in the solution treated and deformed conditions. The energy absorbed remains almost constant for alloy B, solution treated from room temperature down to -196°C. Alloy A shows a slight decrease beginning at about -80° C.

For the deformed material the values decrease

TABLE IV.10

TENSILE TEST RESULTS

Alloy Condition	Test Temper	0.2% Proof stress (MN/m^2)	Tensile stress at instability (MN/m^2)	True Strain at instability (M)	Fracture Stress (MN/m^2)	Reduction of Area (%)	Elongation (%)
As received	R T	503	2042	0.80	2035	47	70
Alloy A-ST	R T	408	1 548	0.54	2 154	47	79
Alloy B-ST	R T	399	1352	0.51	1388	38	76
Alloy A-Def	R T	1206	1367	0.11	2025	44.4	24
*Alloy B-Def	R T	653*	928*	0.35*	1114	38.3	23
Alloy B-ST	- 4°C	407	1423	0.50	1800	44	75
Alloy B-Def	- 2°C	1198	1389	0.10	2628	38	25
Alloy A-Def	- 2°C	1212	1422	0.13	2500	43.8	25
Alloy B-ST	- 12°C	314	1271	0.55	1660	47	82
Alloy A-Def	- 12°C	1152	1305	0.10	2243	41	24
Alloy B-Def	- 18°C	1011	1217	0.16	2214	40.6	29
As received	- 23°C	423	1250	0.47	2000	37.9	67
Alloy B-ST	- 30°C	456	1429	0.51	1900	43.8	75
Alloy A-ST	- 35°C	490	1466	0.49	2402	44.1	72
Alloy A-Def	- 27°C	1163	1428	0.16	2500	38	29
Alloy B-Def	- 27°C	1161	1391	0.12	2571	37.5	25
Alloy B-ST	- 50°C	414	1394	0.50	1750	37.5	74
Alloy B-Def	- 50°C	1294	1458	0.10	2750	38.3	24
Alloy A-Def	- 50°C	1158	1436	0.13	2642	37.5	26
Alloy A-ST	- 70°C	430	1494	0.49	2143	37.9	71
Alloy B-Def	- 70°C	1172	1527	0.102	2857	43.8	20
Alloy B-ST	- 80°C	449	1606	0.575	2143	43.8	79
Alloy A-ST	-105°C	487	1607	0.50	2442	44.1	73
Alloy A-Def	-111°C	1200	1607	0.21	2314	37.9	35
Alloy B-ST	-196°C	572	1963	0.46	2487	37.9	74
Alloy B-Def	-196°C	1339	1850	0.20	3008	35.4	30

ST = material solution treated
Def= material previously deformed
RT = Test at room temperature
* = This test showed anomalous behaviour

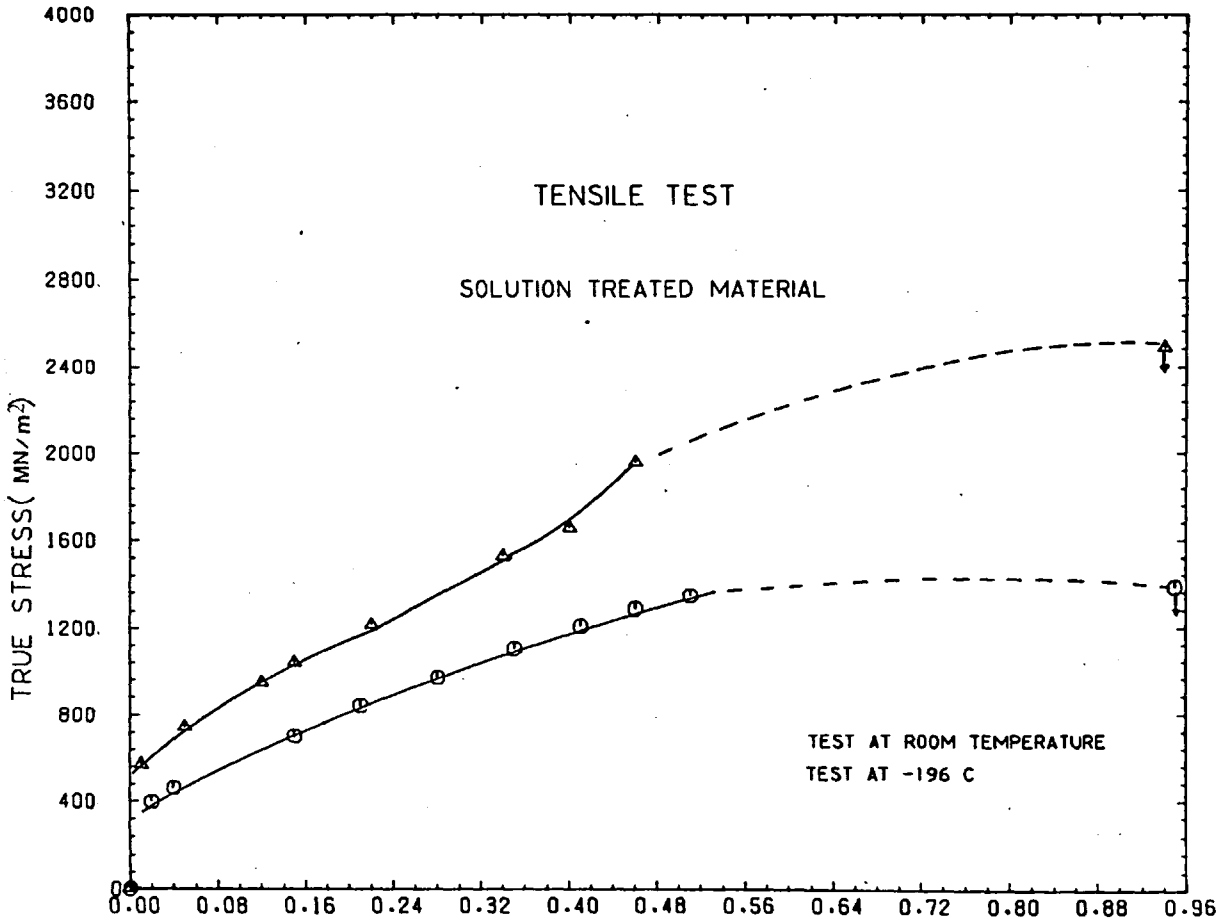
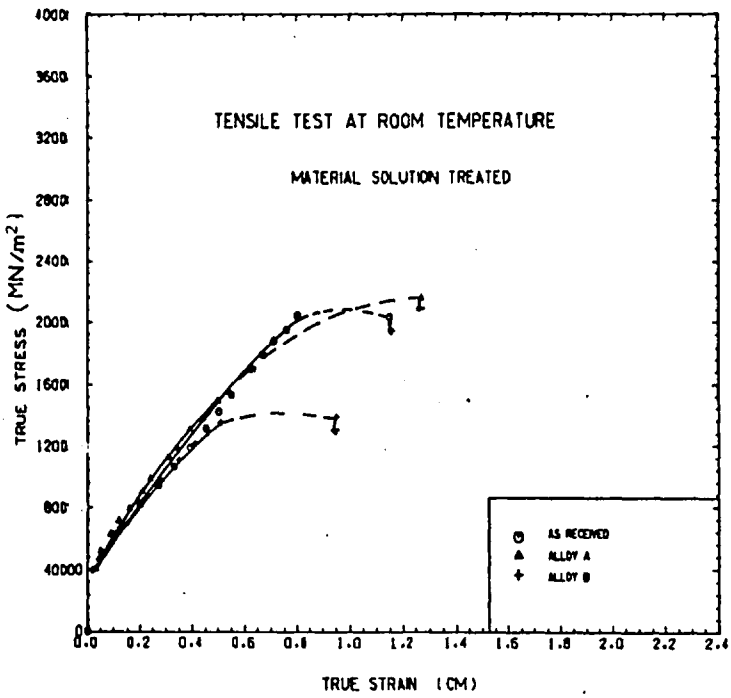


FIG. IV. 52 - TRUE STRESS vs TRUE STRAIN



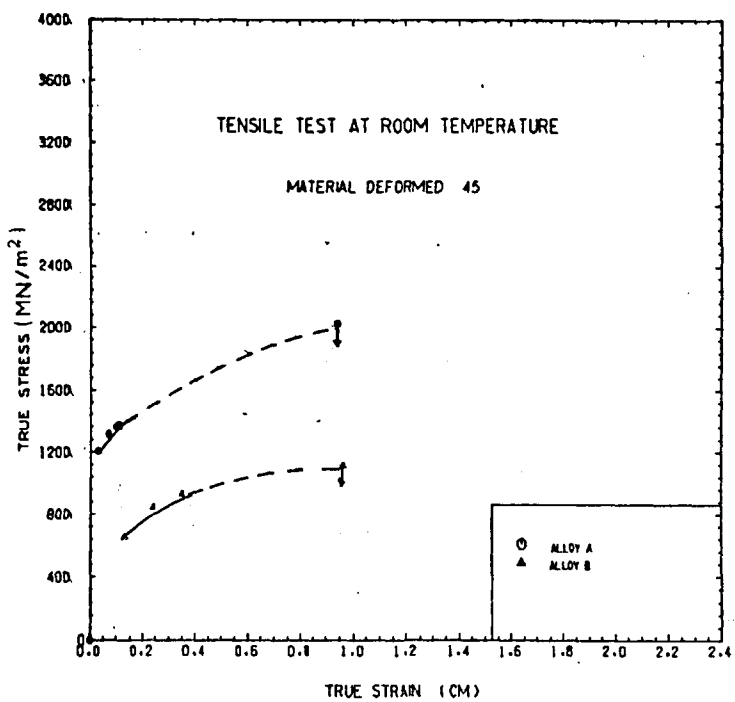
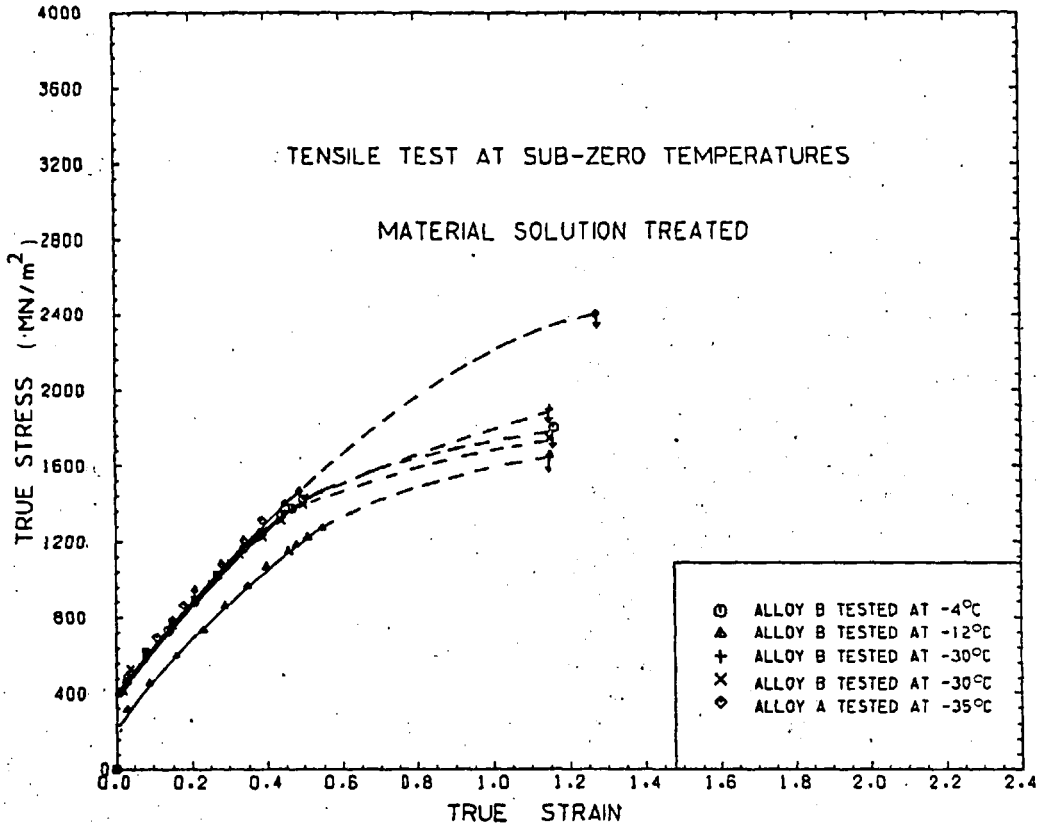


FIG. IV. 53 - TRUE STRESS vs TRUE STRAIN



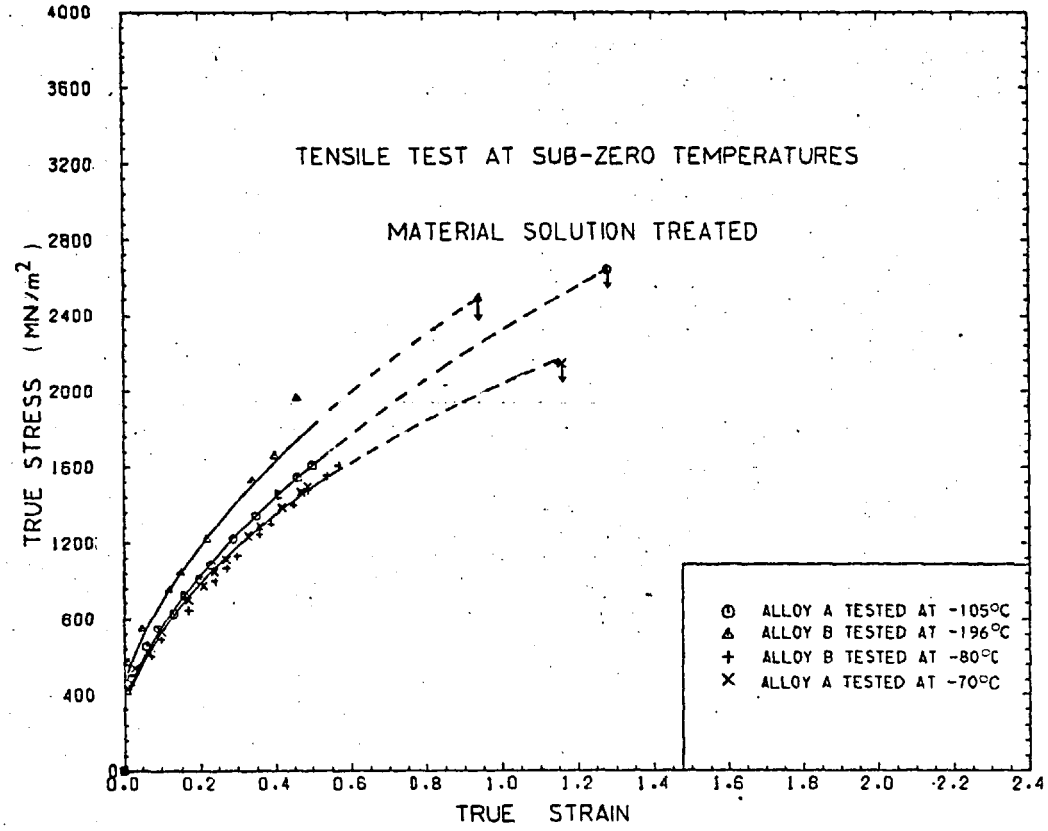
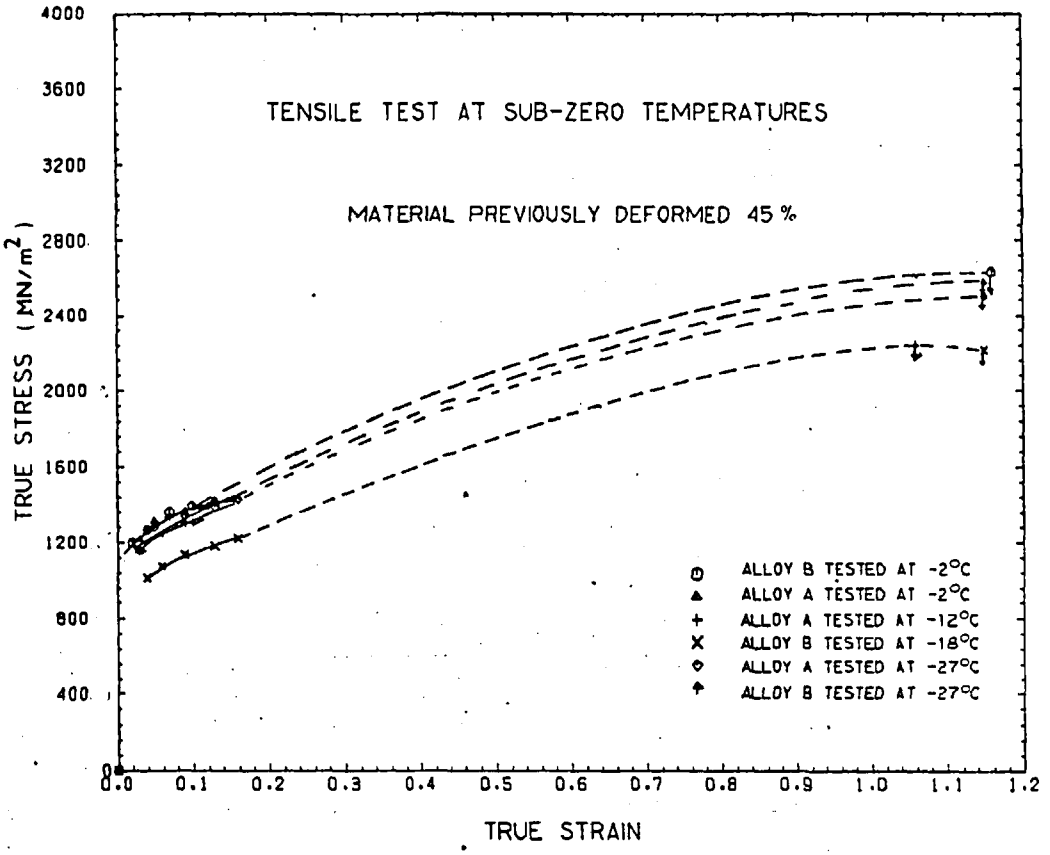


FIG. IV. 54 TRUE STRESS vs TRUE STRAIN



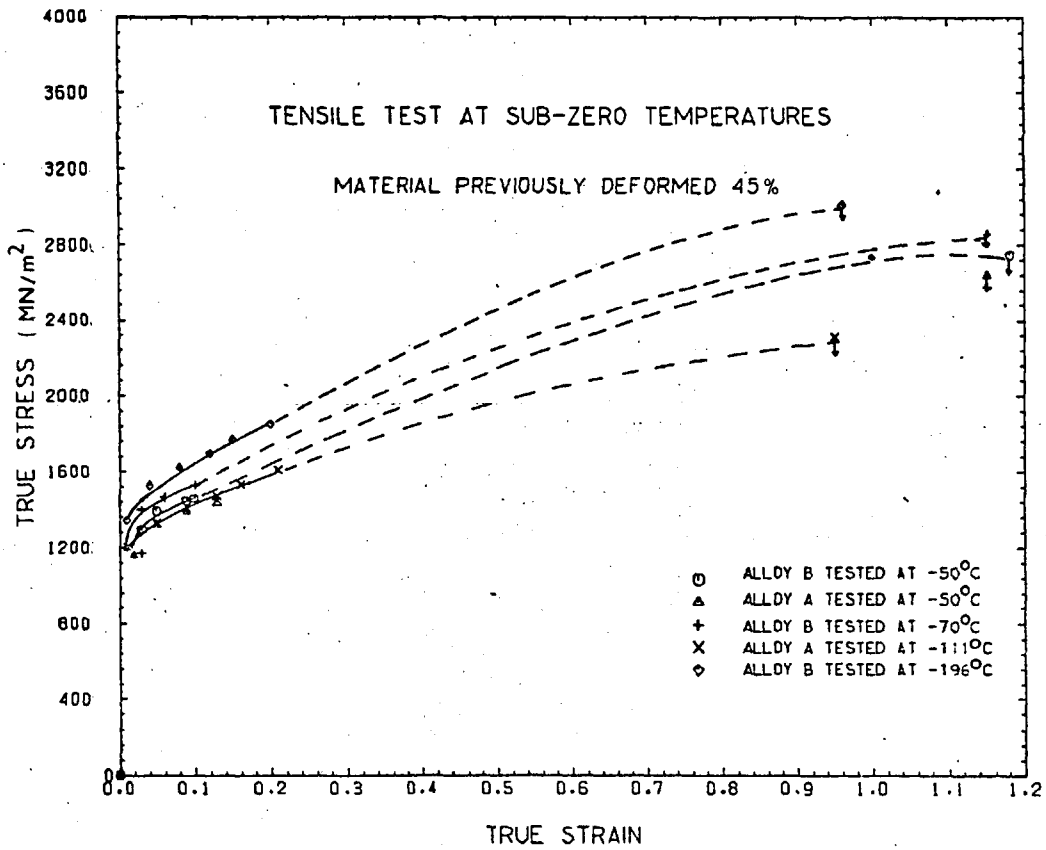
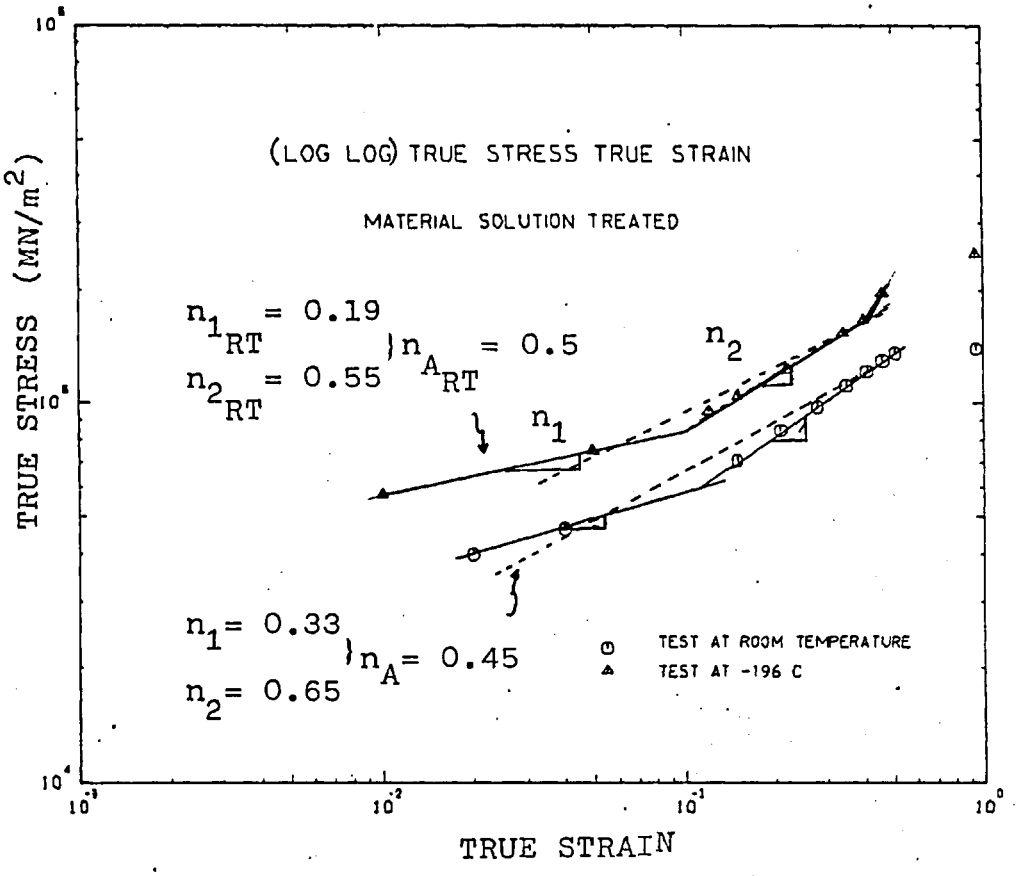


FIG. IV.55 TRUE STRESS vs TRUE STRAIN



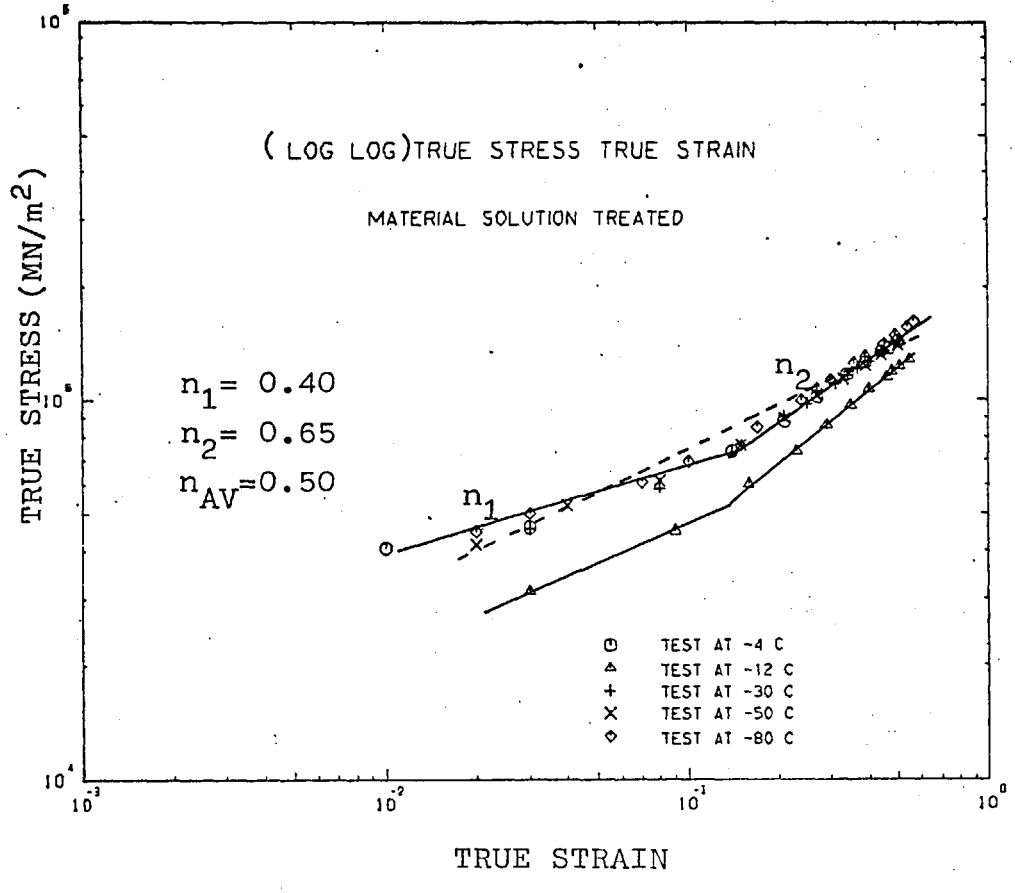


FIG. IV. 56-LOG TRUE STRESS - LOG TRUE STRAIN

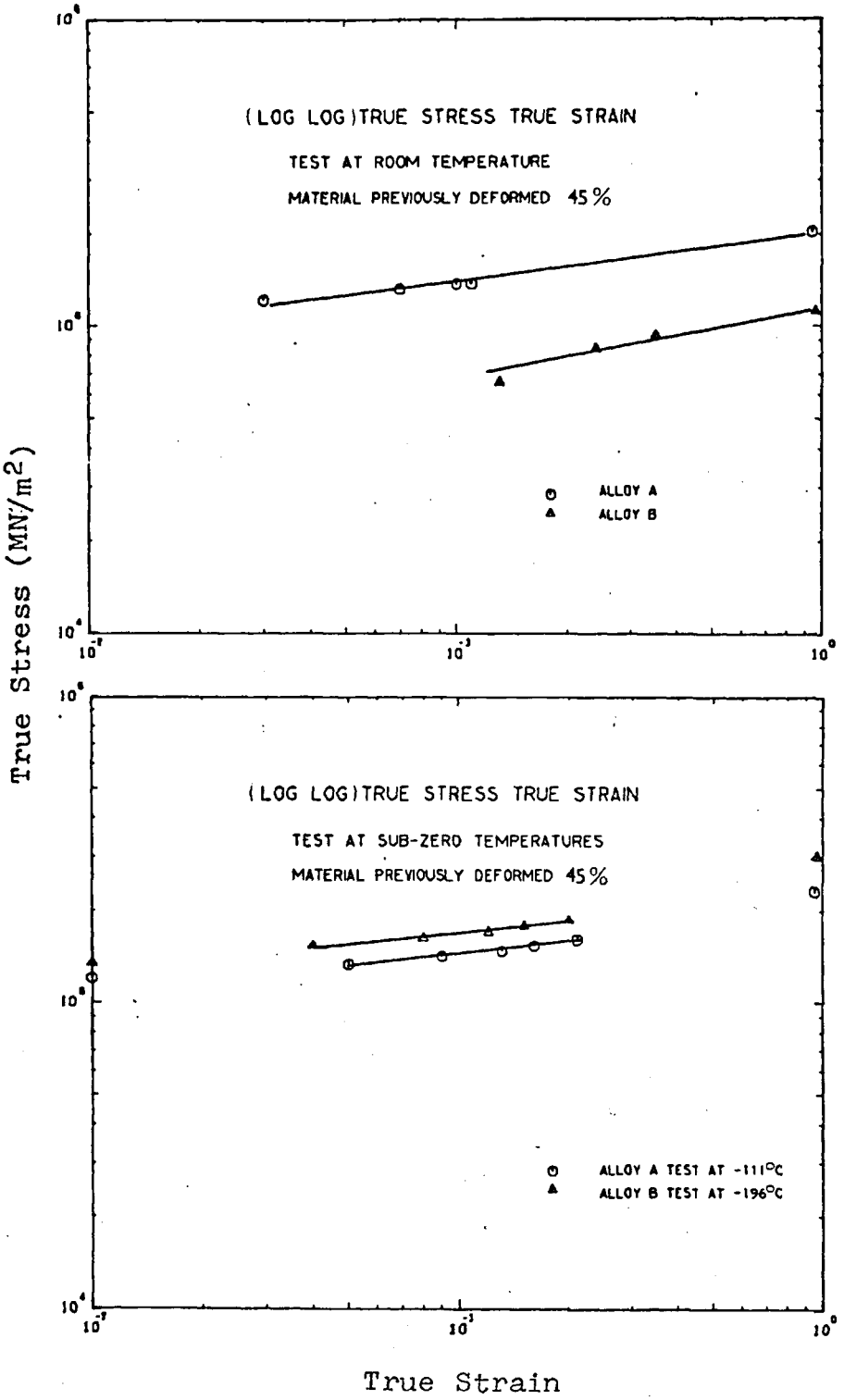


FIG. IV.57 LOG TRUE STRESS - LOG TRUE STRAIN

TABLE IV.11

a. n-Values of strain hardening exponent

Test Temp	Solution Treated		Deformed	
	Alloy A	Alloy B	Alloy A	Alloy B
R T	0.54	0.51	0.11	0.35*
- 4°C	-	0.50	0.13	0.10
- 12°C	-	0.55	0.10	0.16
- 30°C	0.49	0.51	0.16	0.12
- 50°C	-	0.50	0.13	0.10
- 70°C	0.49	0.57	-	0.10
-105°C	0.50	-	0.21	-
-196°C	-	0.46	-	0.20

(n = values of true strain at instability)

b. n Values from graphs log true stress - log true strain

	Solution Treated		Deformed	
	R T	Sub-zero Temperatures	R T	Sub-zero Temperatures
n_A	0.50	0.50	0.12	0.13
n_1	0.19	0.40	-	-
n_2	0.55	0.65	-	-

(both alloys had similar behaviour in this case)

n_1 = slope of the first straight line

n_2 = slope of second straight line

n_A = slope of mean line through all points

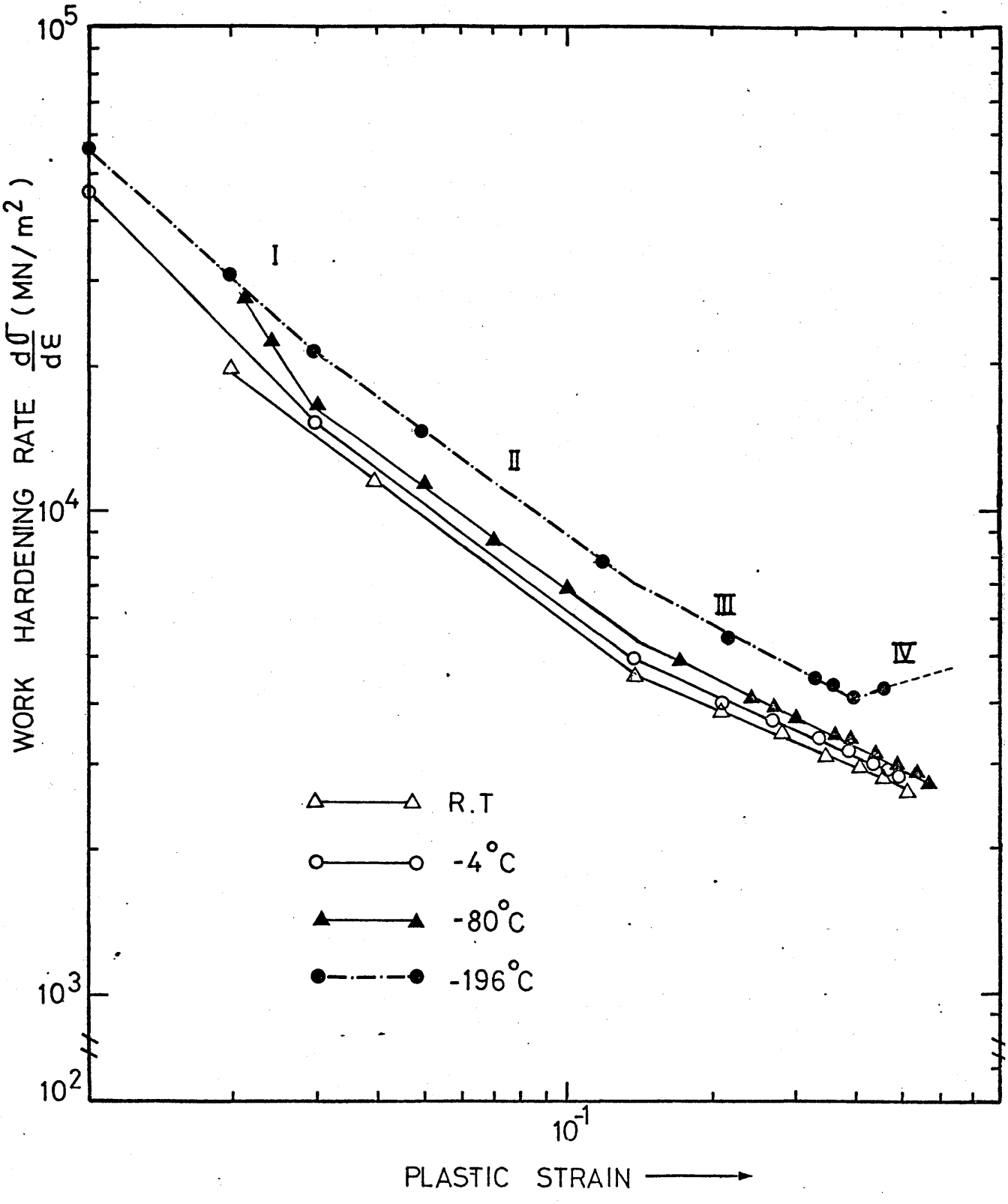


FIG. Ⅳ. 58 Work hardening rate vs. plastic strain.
Solution treated material. (Alloy B).

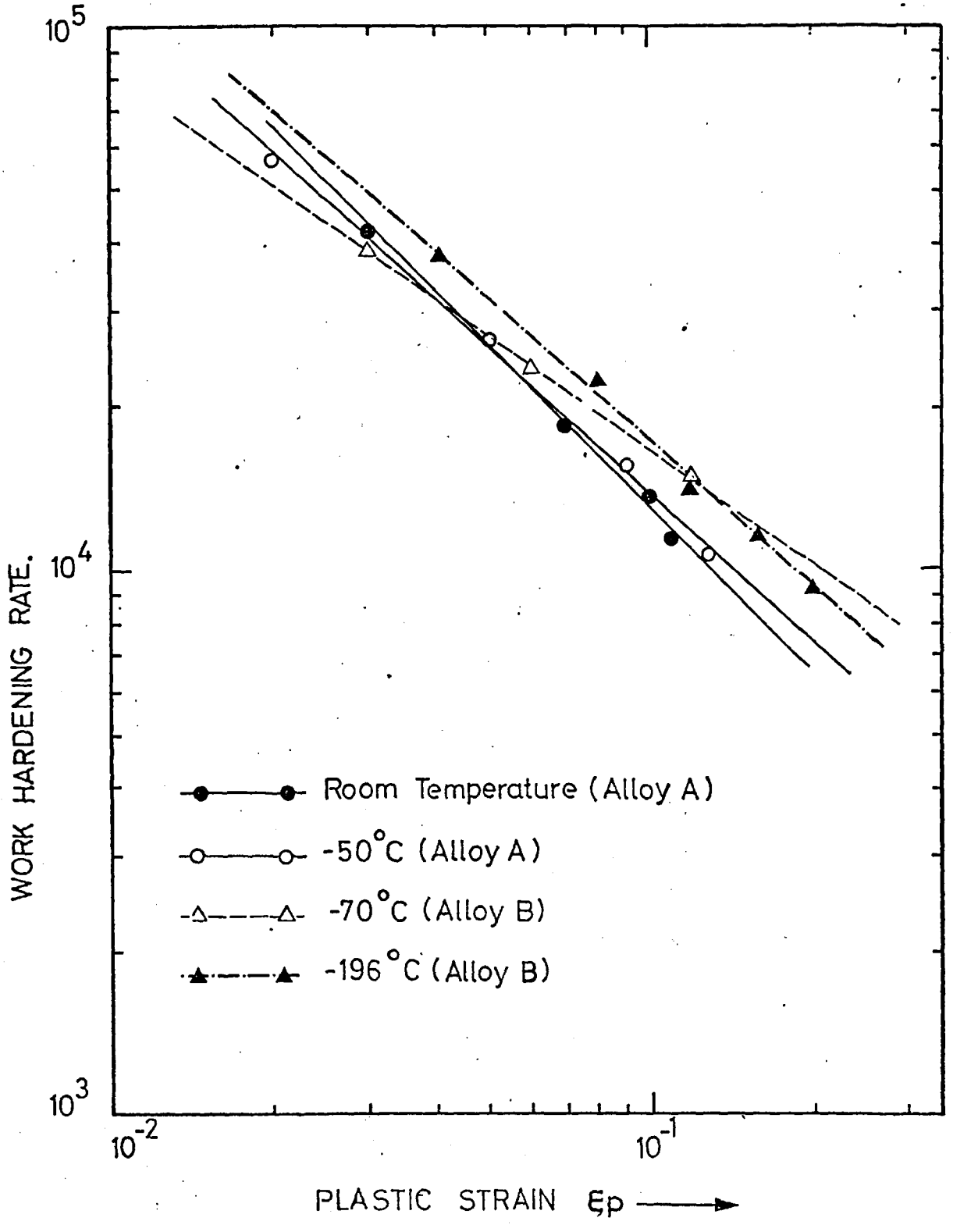


FIG. IV.59 Work hardening rate vs. strain.
Material previously deformed.
Tested at different temperatures.
(Alloys A and B)

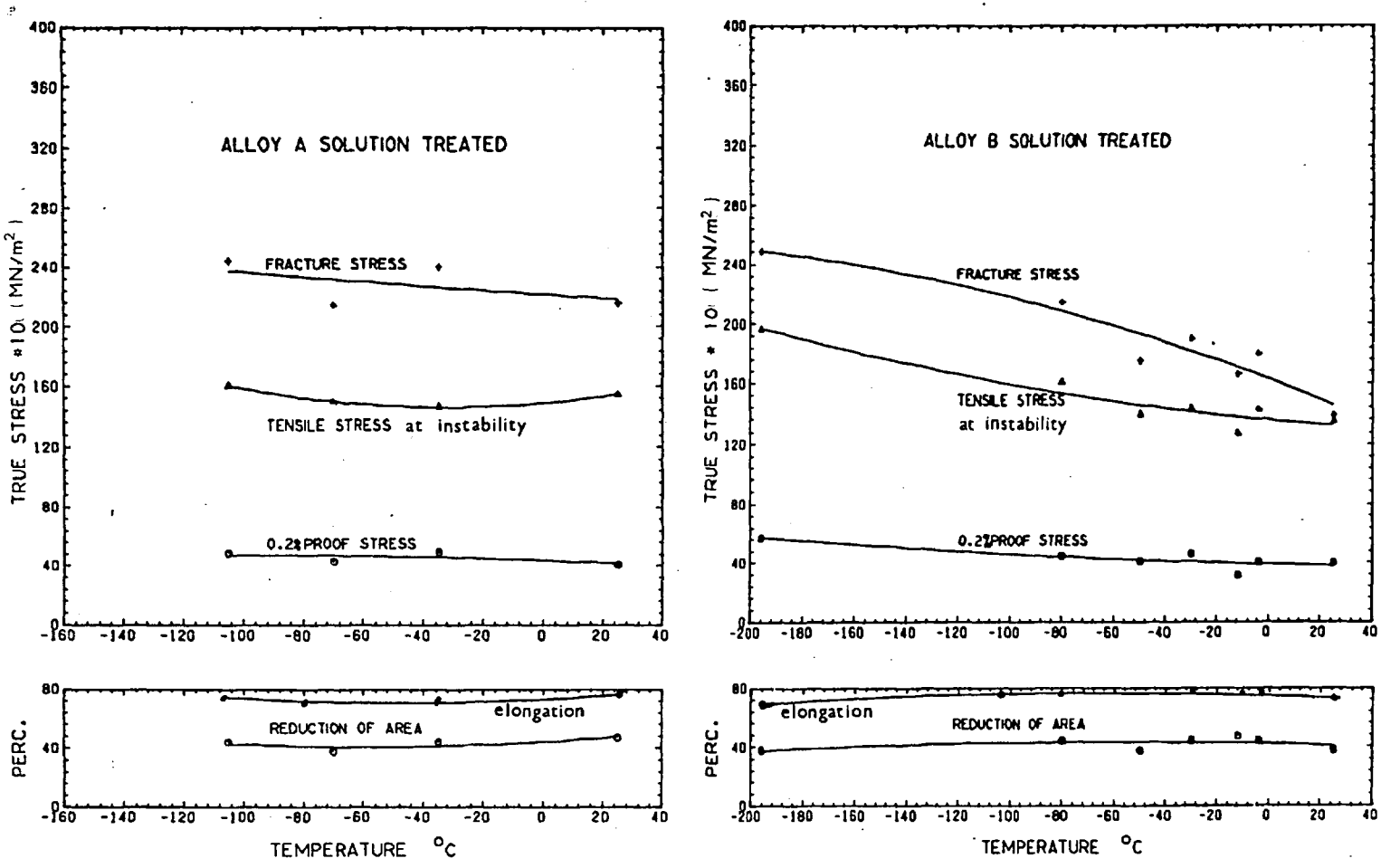

ALLOY A SOLUTION TREATED
ALLOY B SOLUTION TREATED
TRUE STRESS * 10 (MN/m²)
FRACTURE STRESS
TENSILE STRESS at instability
0.2% PROOF STRESS
PERC.
elongation
REDUCTION OF AREA
TEMPERATURE °C

FIG. IV. 60

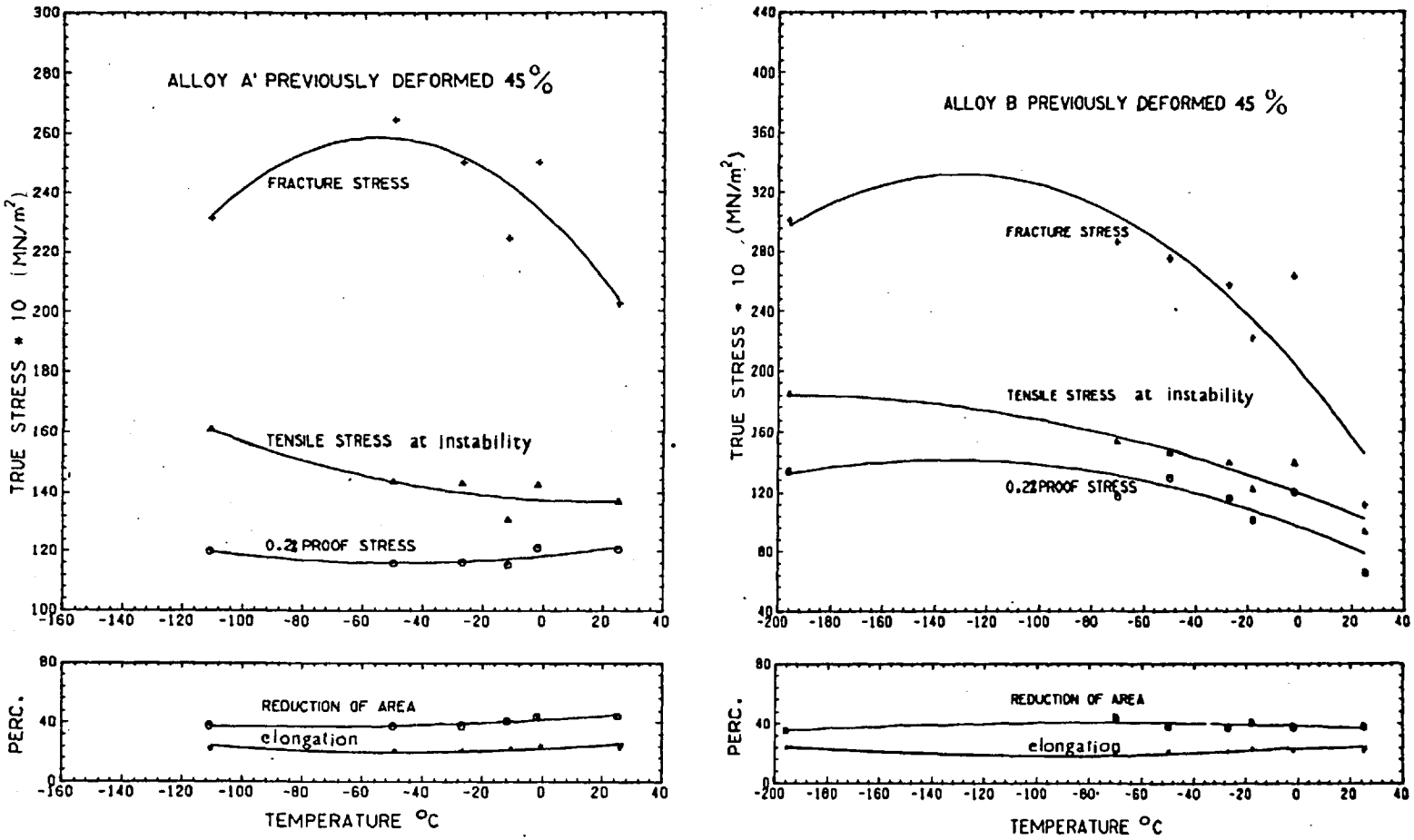

ALLOY A' PREVIOUSLY DEFORMED 45 %
FRACTURE STRESS
TENSILE STRESS at instability
0.2% PROOF STRESS
TRUE STRESS * 10 (MN/m²)
REDUCTION OF AREA
elongation
PERC.
TEMPERATURE °C
ALLOY B PREVIOUSLY DEFORMED 45 %
FRACTURE STRESS
TENSILE STRESS at instability
0.2% PROOF STRESS
TRUE STRESS * 10 (MN/m²)
REDUCTION OF AREA
elongation
PERC.
TEMPERATURE °C

FIG. IV. 61

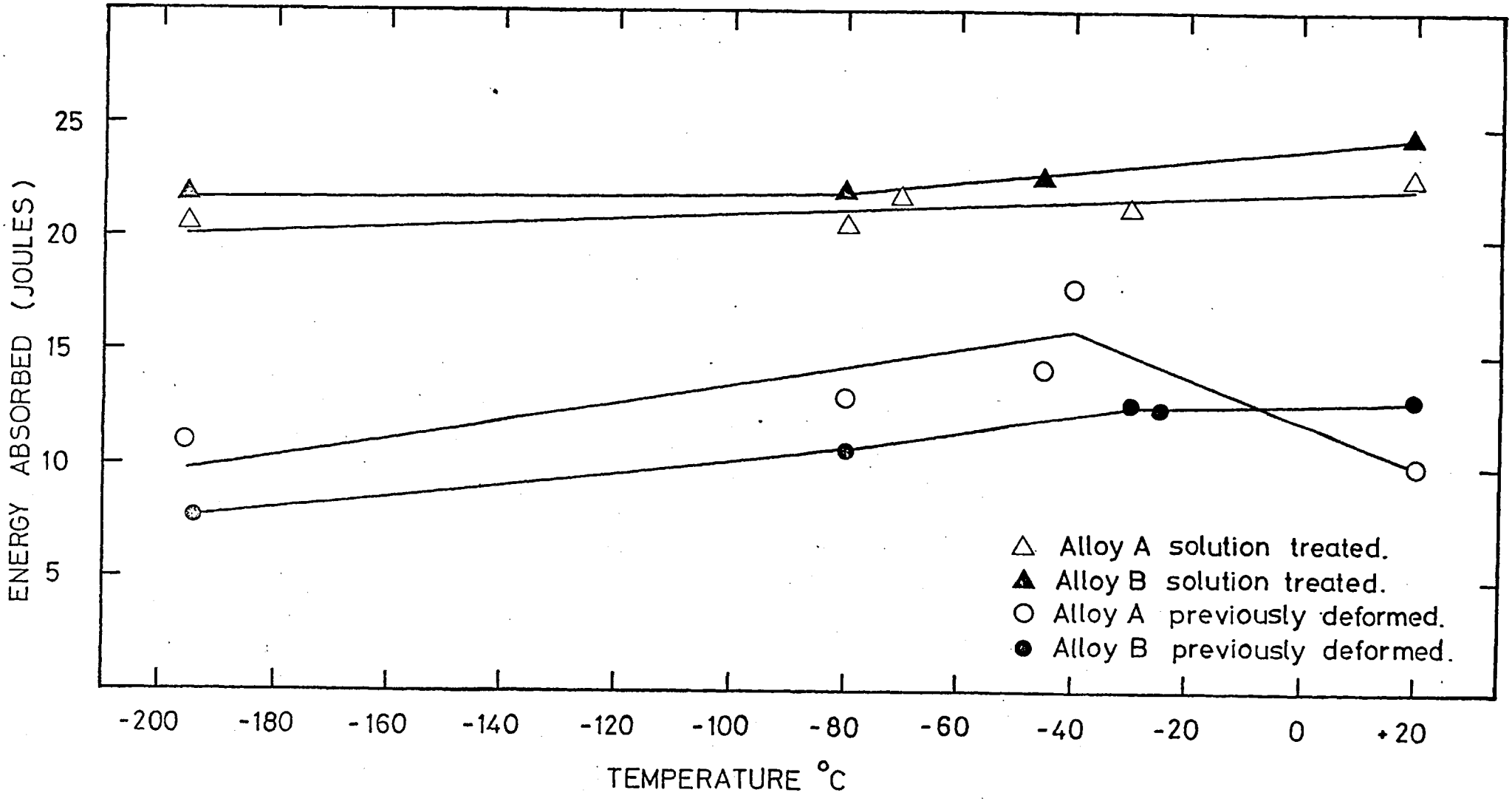


FIG. IV.62 Impact test. Energy absorbed vs. temperature.

slightly with decreasing temperatures. However, alloy A deformed, seems to show a peak at about -40°C and then decreases slightly down to -196°C.

IV.5 Fractographs

The fracture surfaces of both alloys solution treated and deformed material, tested under tension and by impact testing, from room temperature to -196°C were studied by means of scanning electron microscopy. Micrographs showing similarities and/or differences between both alloys, and between the different test temperatures are shown in Figs. IV.71 to IV.90.

Micrographs IV.71 to IV.81 show the tensile fracture surfaces of the solution treated alloys A and B from room temperature to -196°C. Micrographs IV.82 to IV.86 show the deformed material tested under tension from room temperature to -196°C. Figs. IV.87 and IV.88 are low magnification views of the tensile fracture surfaces of the solution treated and deformed material for different test temperatures. Finally micrographs IV.89 to IV.90 are the impact fractures.

IV.5.a Tensile Fracture Results

No difference in fracture mode was observed between alloy A and B. On the contrary they appeared to be very similar as can be observed in the

micrographs, when both alloys are shown at the same test temperature as a matter of comparison. Figs. IV.71 and IV.72 show alloys B and A respectively, in the solution treated condition tested at room temperature, a ductile mode of fracture is observed, with numerous dimples and microvoids, and very few inclusions present. The general appearance of the walls is very wavy. These characteristics are observed in the tensile fracture surfaces from room temperature to -80°C (see Figs. IV.71 to IV.76).

For the test performed at -105°C a different general appearance of the fracture surface is observed, and although there are still a large amount of dimples, the structure presents a rather more flattened appearance (Fig. IV.77.a and b). At -196°C this behaviour is more pronounced, Fig. IV.78 shows the low magnification of the fracture surface, indicating the different areas observed at high magnifications in Figs. IV.79 to IV.81. As can be seen a shear mode is observed in area D. It appears as if a different phase has formed which separates along the boundaries; this is especially clear in area A (Fig. IV.79), some intermetallic particles are also observed which were identified to have high Ti content. Fig. IV.80 which shows a high magnification of area B, shows tearing of this region.

The material in the deformed condition tested from room temperature to -196°C is shown in Figs. IV.82 to IV.85. The test at room temperature did

not show very significant differences from the solution treated condition tested at room temperature, except for the form of the inclusions which looked deformed due to the previous deformation by rolling given to the material; a general ductile mode of fracture with the characteristic dimple appearance is observed. As the test temperature decreases although ductile fracture is still observed down to -70°C, in general the dimples even their conical shape, as can be seen in Fig. IV.84 which shows shallow dimples. At -111°C, although voids can still be observed (Fig. IV.85) the surface has become flat. This effect is more pronounced at -196°C (Fig. IV.86) which is again very similar to the structure of the solution treated material tested at the same temperature; again the phase present separates at the boundaries. However, there is a difference from the solution treated condition which shows intergranular separation which was not observed before (Fig. IV.86.a, b and c). Looking at the micro-mechanisms of fracture at low magnifications (Figs. IV.87 and IV.88), with decreasing temperature, it is observed that down to -35°C, both solution treated and deformed materials are characterized by the formation of a fibrous zone, surrounded by a shear lip zone. Radial marks are observed in the solution treated material tested at -30°C (Fig. IV.87.c) and at -50°C. In the solution treated material tested at -105°C a small fibrous region is present which consists of a series of circumferential ridges (Fig. IV.87.d). The ridges lie

normal to the direction of crack propagation from the origin towards the periphery of the specimen. The previously deformed material tested at -111°C still showed a very small fibrous region also with a large, shear zone and some very coarse radial marks (Fig. IV.88.d). The test at -196°C for both conditions showed predominantly a shear mode of fracture and intergranular separation (Figs. IV.87.e and IV.87.f and Fig. IV.88.g and h).

IV.5.b Impact testing fractographs

Figs. IV.89 to IV.90 show the fracture surfaces of the solution treated and deformed material tested from room temperature to -196°C. Only room temperature and -196°C temperature tests are shown, due to the great similarities for all the conditions and temperatures.

Fig. IV.89 shows the low magnification fracture mechanisms, which as can be seen do not change with decreasing temperature for the solution treated and deformed conditions. It is a ductile mode of fracture and a very extended fibrous zone is observed. At high magnifications Figs. IV.90.1 to IV.90.2 microvoid coalescence is observed at all temperatures for both solution treated and deformed material. The specimen tested at -196°C presents a more rough appearance, and many features are seen in the walls, i.e., microvoids and slip lines (Figs. IV.90.1.c, IV.90.1.d and IV.90.2.b).

IV.6 Compression Testing

In order to describe the different type of serrations observed during the compression testing, the classification given by Brindley and Worthington ([45]) was followed. This has been described in the literature review (Chapter II) and therefore will not be stated here again. However, the definition of each type of serration will be given as they appear during the test.

Figs. IV.63 to IV.66 show schematically the complete compression test procedure, indicating changes of strain rate and relaxation periods for both alloys, in the four different conditions, i.e. solution treated (Fig. IV.63), solution treated and aged (600°C/5hs) (Fig. IV.64), deformed (Fig. IV.65) and deformed and aged (600°C/5hs) (Fig. IV.66); tested from room temperature to 800°C. No significant differences were observed between alloys A and B.

IV.6.a Description of behaviour during compression tests at different temperatures

Room temperature

At room temperature both alloys for all conditions had similar behaviour. The stress increases with an increase in strain rate (at point A); when the strain rate is decreased to its original value ($\dot{\varepsilon}_1$), the stress goes down and then follows the original stress-strain curve at point C. At point D the cross-head is

stopped and the stress starts to decrease as a result of relaxation; at point E the stress is applied again and the curve follows the projection of the original curve, and the whole process is repeated again. However, the deformed and aged material shows a slight drop after relaxation (points I and J) before the projection of the original curve is reached again.

As the temperature increases this behaviour does not follow; and depending on the alloy condition and the temperature different processes take place.

360°C - 450°C

At this temperature the solution treated, and solution treated and aged material show a similar behaviour. When the strain rate is increased at point A, the curve shows a slight increase but immediately drops following the original stress strain curve; in this case there is no increase in stress after increase in strain rate as in room temperature test. When the strain rate is changed to its original value at point C there is a small stress drop but the curve increases again, C D E, followed by serrations up to point F. These serrations are very small; they are type A ([45]) serrations, i.e. they rise above the general level of the stress strain curve and are periodic in nature. At point F the cross-head is stopped and relaxation takes place. In the solution treated and aged material a stress drop is

observed after relaxation, after reapplying stress, H I J, and for the lower strain rate, type A serrations are observed but not for the higher strain rate, this material behaves in a similar way at 450°C.

The deformed and deformed and aged materials behave similarly to one another at 360°C. Up to the second change in strain rate (point B) they show a similar behaviour to the solution treated material. However, when the strain rate is set to its original value $\dot{\varepsilon}_1$, the stress increases to a value higher than the projection of the original σ-ε curve. A stress drop is observed at point C until again the curve slowly recovers to the smooth shape, up to point E where the cross head is stopped for relaxation; after which the curve comes back following the smooth σ-ε curve; for the deformed material, a stress drop is observed again after relaxation for each strain rate change. The material deformed behaves similarly at 450°C as at 360°C however, this is not the case in the deformed and aged material in which, after the second strain rate change, the stress comes to the same value as that before the change (i.e. the stress is independent of the strain rate).

550°C

At this temperature both alloys in all conditions present yield point phenomena ([45]) (i.e. a larger stress is required to initiate deformation by slip

than to continue it and this is observed as a drop in load at the start of yielding). The serrations start immediately after the elastic region of the stress strain curve; the solution treated and solution treated and aged material respond similarly to changes of strain rate before and after relaxation but show serrations of different types. The solution treated material presents type A serrations throughout the test, only of larger size after relaxation. The solution treated and aged material presents type B serrations for the lower strain rates; i.e., these type B are serrations which oscillate about the general level of the stress/strain curve and occur in rapid succession. For this particular condition (solution treated and aged) the serrations are large and periodic. Type A serrations are observed for the higher strain rate. After relaxation a stress drop is observed. The deformed and deformed and aged materials behave similarly. They show type B serrations for the higher strain rate and type C serrations for the lower strain rate. Type C are serrations which fall below the general level of the stress strain curve; for these particular conditions they are very large and periodic in nature. For the deformed and deformed and aged conditions the stress falls below the stress-strain curve after the increase in strain rate giving a negative strain rate sensitivity. After relaxation the stress comes back to a high value following the projection of the curve before relaxation but the process is followed by a progressive

decrease in stress; this is not so marked for the deformed and aged material, in which the serrations (type C) are not so large and the decrease in stress is smaller.

650°C - 680°C

At this temperature the solution treated material shows a large yield drop with increase in strain rate. Alloy A shows type B serrations for the higher strain rate, but alloy B does not show serrations. The stress is independent of the strain rate change (Fig.IV.63.e). In the deformed material the stress falls sharply with increase in strain rate and comes back to follow the original projection of the $(\sigma\text{-}\varepsilon)$ curve on returning to the original strain rate value $\dot{\varepsilon}_1$; after relaxation the stress decreases with strain rate increase, and does not go back to follow the stress/strain curve when the strain rate is returned to the original value.

The deformed plus aged material follows the same behaviour, except that type C serrations, extremely large and periodic, are observed for the higher strain rate before relaxation.

700°C

The solution treated material shows type B serrations before relaxation and type C serrations after relaxation with a stress drop when the strain rate is

increased (Fig.IV.63.f).The stress is independent of the strain rate change. The solution treated plus aged material shows similar behaviour except that alloy B shows serrations only after the increase of strain rate and these were type C serrations Fig. IV.64.d).

The deformed material does not show serrations except for alloy B after relaxation for the higher strain rate. For this condition the stress increases with strain rate increase and decreases with strain rate decrease. However, there is a difference from the lower temperatures behaviour (R.T.) since it seems to take more time to reach the smooth stress-strain curve (Fig. IV.65.e). The deformed and aged material showed a very different behaviour to the deformed material, type C serrations are observed for the higher strain rate, with extremely large periodic serrations. The stress decreases with strain rate increase giving negative strain rate sensitivity. After relaxation type C serrations are observed throughout the rest of the process (Fig. IV.66.e).

800°C

At this temperature all the conditions behave similarly. No serrations are observed, and the stress largely increases with strain rate increase and decreases with strain rate decrease.

IV.6.b The temperature dependence of the 0.2% Proof Stress, the strain rate sensitivity, and the relaxation stress

The 0.2% proof stresses, critical strain (i.e., strain at first serration), $\Delta\sigma$, relaxation after 1 min and after 10 min and the strain rate sensitivity values are given in tables IV.12 and IV.13 for both alloys solution treated, solution treated and aged, deformed and deformed and aged, from room temperature to 800°C. The deformed and deformed and aged material showed much higher values of stress than the solution treated and the solution treated and aged materials. Figs. IV.67 to IV.70 show these values graphically. As can be seen from Fig. IV.67 and Tables IV.12 and IV.13, all the conditions showed higher values of stress at about 550°C. However, some scatter was also obtained at this temperature. The solution treated and solution treated and aged materials showed positive values of strain rate sensitivity at room temperature which falls to zero at 360°C and becomes negative at 460°C; it goes to zero again for 550°C and keeps this value up to 700°C. The deformed and the deformed and aged materials showed negative strain rate sensitivity values in the range 450°C - 650°C and 450°C - 700°C, respectively; followed by a sharp increase at higher temperatures (Figs. IV.68 and IV.69). Low relaxation stresses values were observed in the range 360°C - 550°C for all conditions. The smallest was shown at 460°C for the solution treated materials and at 550°C for the

deformed and deformed and aged materials (Fig. IV.70). All the conditions showed serrated yielding at 550°C. The critical strain, i.e., strain at first serration is very small in the temperature range 450° - 550°C, ranging from 0.05 to 0.5, however these values vary depending on the material condition. The values of the activation parameters were calculated for alloy A, for the different conditions and temperatures. Table IV.14 shows the $\left(\frac{\Delta\sigma}{\Delta T}\right)_{\dot{\varepsilon}}$ values, Tables IV.15 and IV.16 show the calculated values for activation enthalpy and activation volume. The 0.2% proof stress values at room temperature for all conditions are in good agreement with the same values from the tensile test at room temperature.

IV.6.c Calculation of Activation Parameters

Calculation of the activation parameters is done on the basis of the equations given by Evans and Rawlings ([47]). The results are shown in Tables IV.15 and IV.16.

Activation volume $V^* = 2KT \left(\frac{\mathrm{Ln}\dot{\varepsilon}}{\Delta\sigma}\right)_T$

Activation enthalpy $\Delta H = KT^2 \left(\frac{\Delta \mathrm{Ln}\,\dot{\varepsilon}}{\Delta\sigma}\right)_T \left(\frac{\Delta\sigma}{\Delta T}\right)_{\dot{\varepsilon}}$

$\left(\frac{\Delta \mathrm{Ln}\dot{\varepsilon}}{\Delta\varepsilon}\right)_T = \frac{1}{\lambda}$ $\qquad K = 1.38062 \times 10^{-23} J/^oK$

$\frac{\Delta\sigma}{\Delta T}$ is calculated from the different values of proof stress at different temperatures. These values are shown, for different temp intervals for alloy A, in Table IV.14.

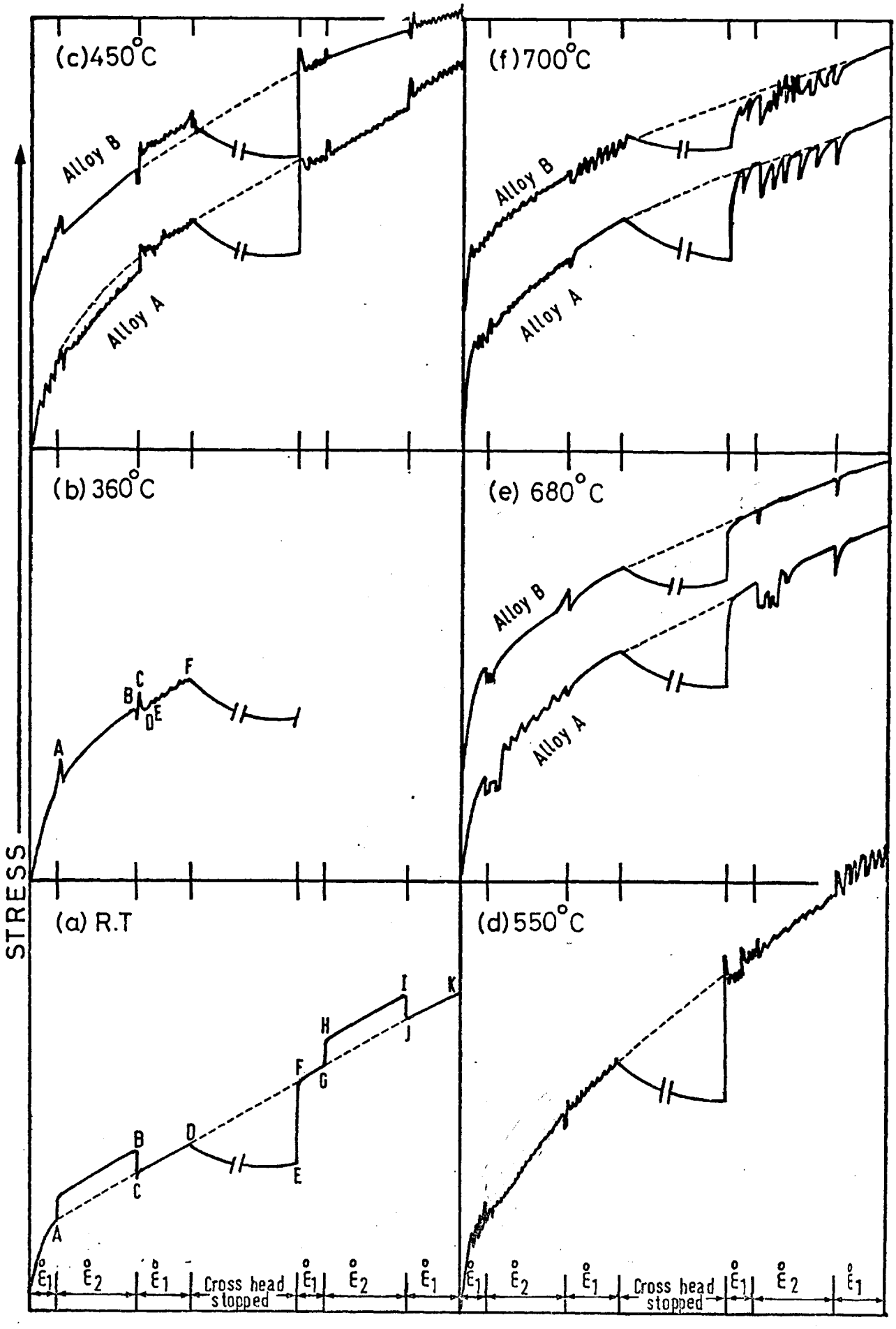


FIG. IV.63 Schematic diagrams of compression test data at various temperatures for the solution treated material. Both alloys showed similar behaviour when not indicated.

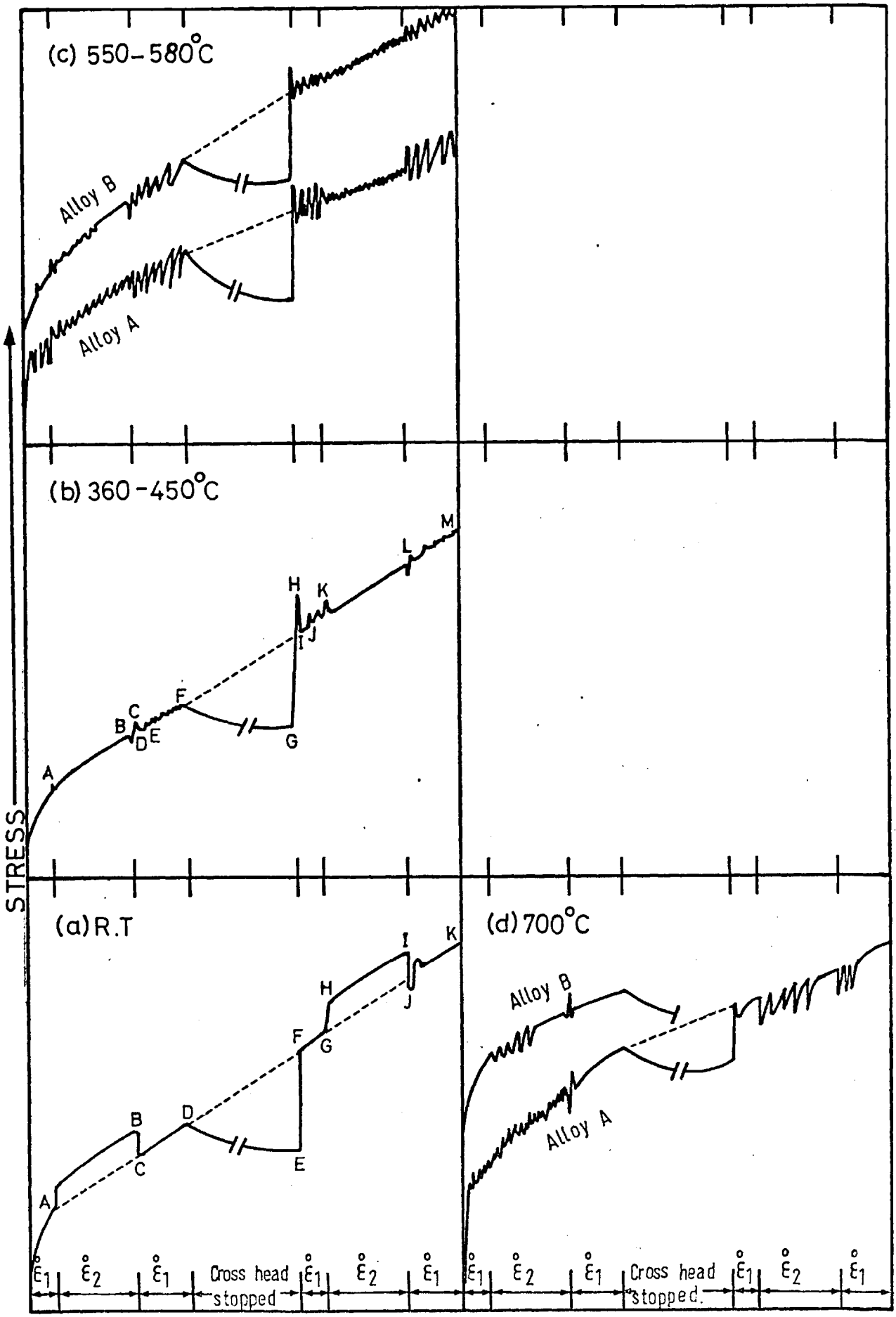


FIG. IV.64 Schematic diagrams of compression test data at various temperatures for the solution treated and aged material. (Both alloys showed similar behaviour when not indicated.)

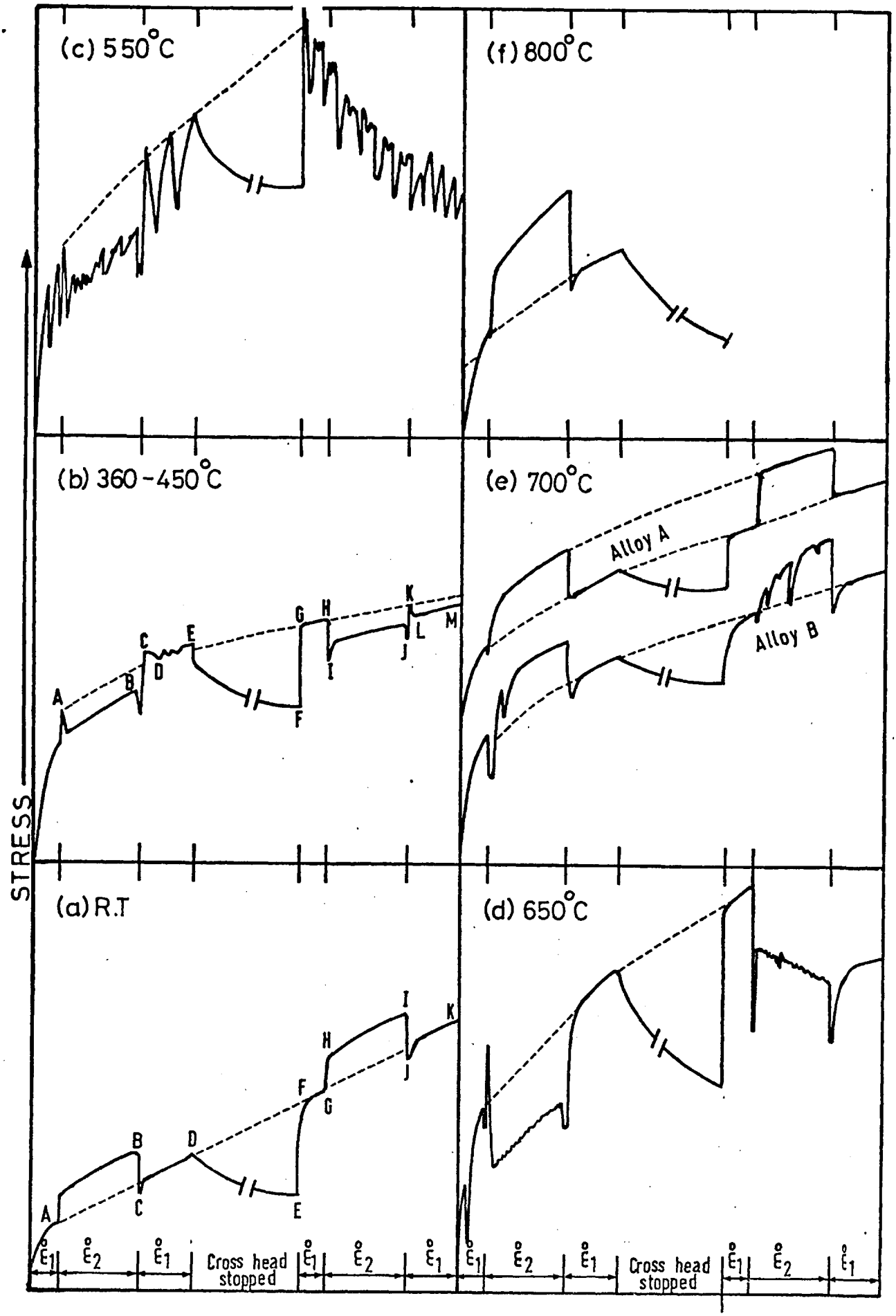


FIG.Ⅳ.65 Schematic diagrams of compression test data at various temperatures for the deformed material. Both alloys showed similar behaviour when not indicated.

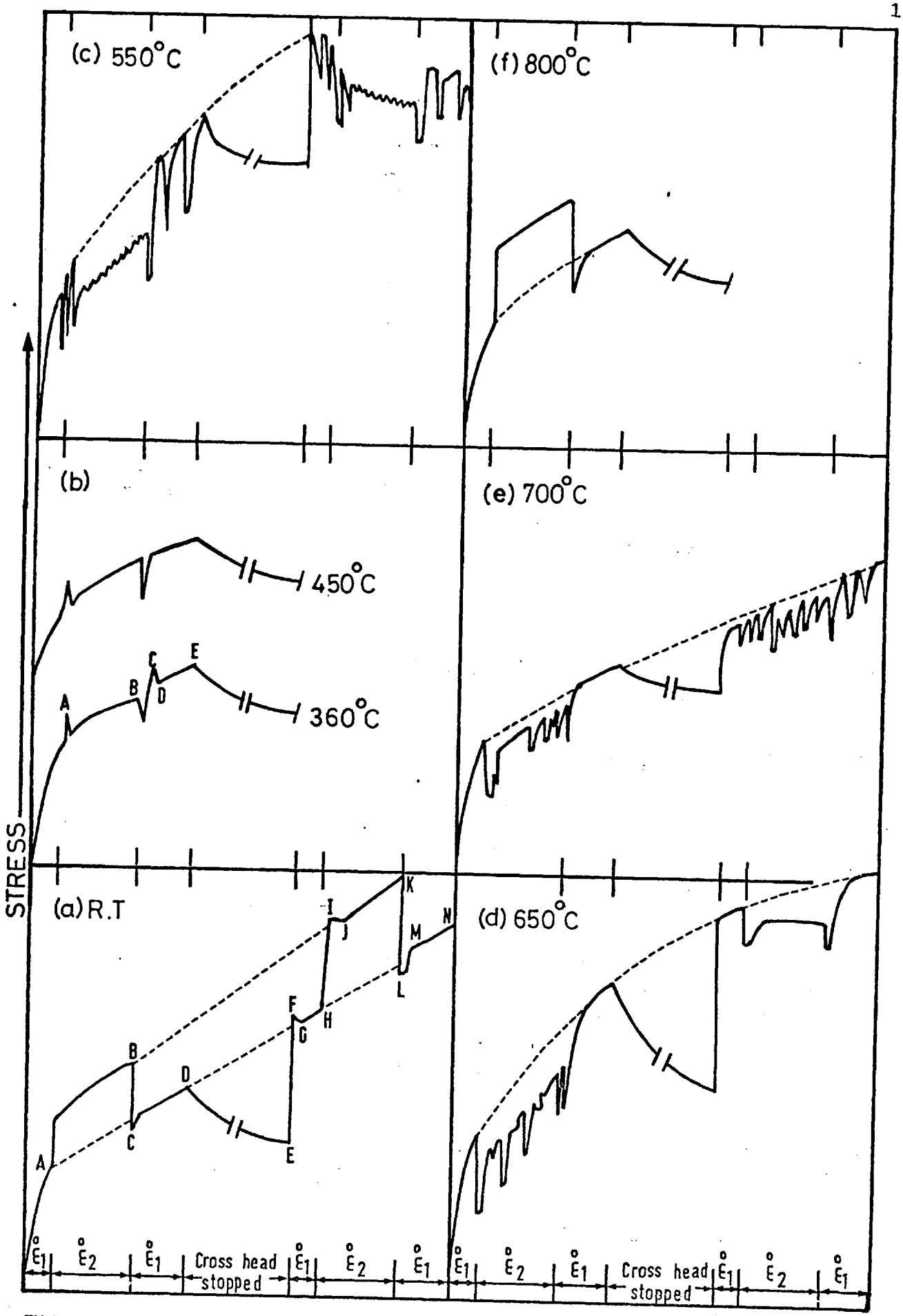


FIG. IV.66 Schematic diagrams of compression test data at various temperatures for the deformed and aged material. Both alloys showed a similar behaviour when not indicated.

TABLE IV.12

TEMPERATURE DEPENDENCE OF 0.2% PROOF STRESS RELAXATION STRESS AND STRAIN RATE SENSITIVITY

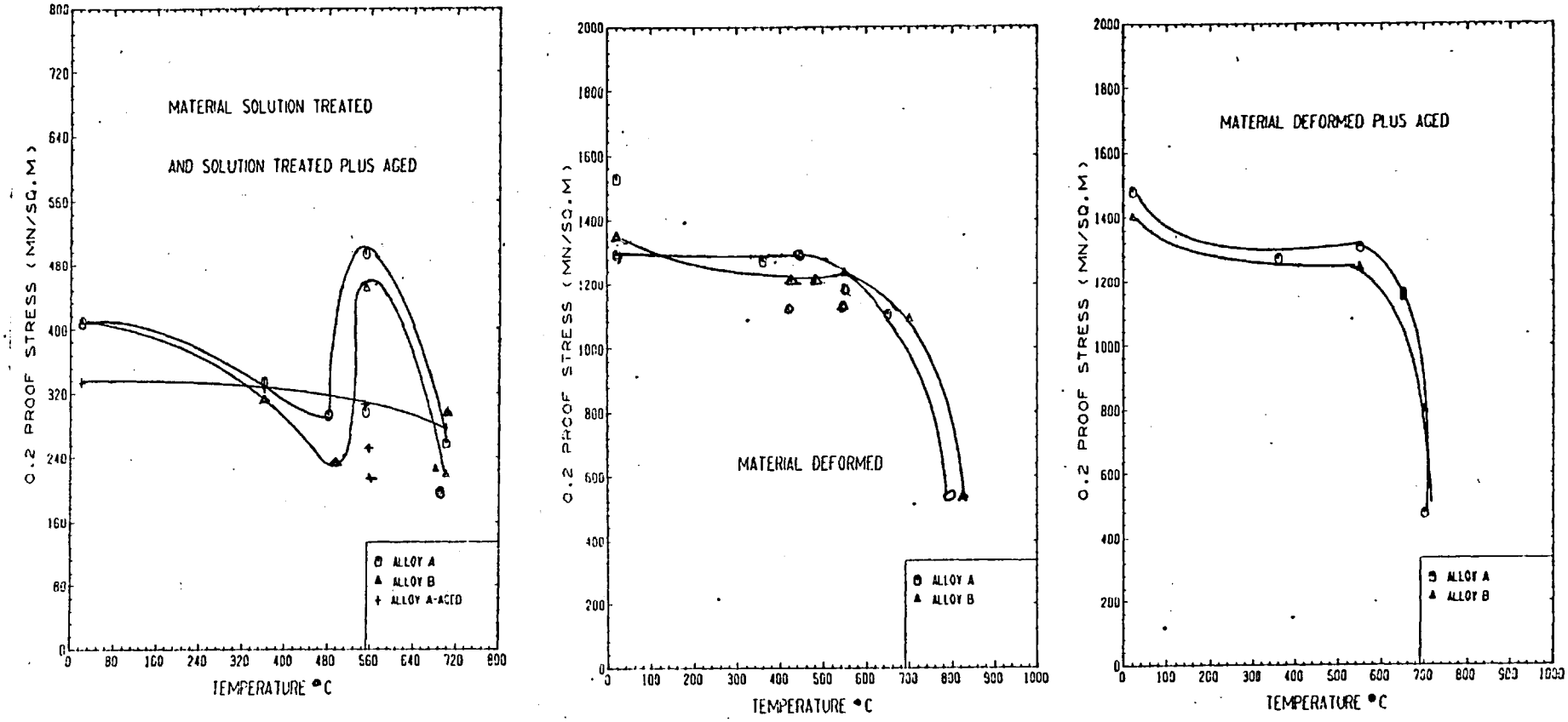
		Material Solution Treated						Material Solution Treated & Aged					
			ε_c (%) Critical Strain		Relaxation		λ		ε_c (%) Critical Strain		Relaxation		λ
Temp. (°C)	Alloy	0.2% Proof Stress (MN/m2)	strain at 1st serration	$\Delta\sigma$ (MN/m2)	1 min R MN/m2	10 min R MN/m2	(MN/m2) strain rate sensitivity	0.2 % Proof stress (MN/m2)	strain at 1st serration	$\Delta\sigma$ (MN/m2)	1 min R MN/m2	10 min R MN/m2	strain rate sensit. MN/m2
R T	A	408.08	-	11.6	11.6	18.9	5.04	334.4	-	+7.27	-	-	3.16
	B	407.08	-	11.6	11.6	18.9	5.04	367.83	-	+7.27	-	-	3.16
360°	A	334.4	-	0	-	-	0	327		0	4.36	8.7	0
	B												
460°	A	313	-	-1.45	4.4	17.5	-0.63						
	B	269	-	-2.9	2.9	19	-1.26						
550°	A	297 494.3	0.08	0	4.36	23	0	312 247 276	0.08	0	2.9	26	0
	B	450.7	0.05	0	4.36	17.4	0	532°/508 565°/276	0.08 0.08	0 0	5.8 7.2	7.2 33.4	0 0
680°	A	225	2.7	0	10.17	36.35	0						
	B	327	-	0	10.17	36.3	0						
700°	A	257	0.05	0	10.17	37.8	0	276	0	0	5.8	10.17	0
	B	218	0.05	0	7.3	29	0	250	2.8	0	-	-	0

TABLE IV.13

TEMPERATURE DEPENDENCE OF 0.2% PROOF STRESS RELAXATION STRESS AND STRAIN RATE SENSITIVITY

		Material Deformed						Material Deformed and Aged					
			ε_c (%) Critical Strain		Relaxation		λ		ε_c (%) Critical Strain		Relaxation		λ
Temp. (°C)	Alloy	0.2% Proof Stress (MN/m2)	strain at 1st serration	$\Delta\sigma$ (MN/m2)	1 min R (MN/m2)	10 min R (MN/m2)	strain rate sensitivity (MN/m2)	0.2% Proof Stress (MN/m2)	strain at 1st serration	$\Delta\sigma$ (MN/m2)	1 min R (MN/m2)	10 min R (MN/m2)	strain rate sensitivity (MN/m2)
R T	A	1294 1527	- -	+13 +11	24.7		+5.7 +6.94	1478.6	-	+16	24.7	40.7	+6.95
	B	1352 1293	- -	+17.4 +13	27.6		+7.6 +5.7	1352 1400	-	+14.5	21.8	36.4	+6.3
360°	A B	1272		0/+11.6*			0/+5*	1378		0/+13*			0/+5.7*
450°	A	440/1090 1243	-	-4.4	10.17		-1.9	952	-	0			0
	B	1218	-	-4.4	10.17	17.5	-1.9	400°/1217	-	0			0
550°	A	1061 1182	0.05	-10	11.6	23	-4.42	1308.5	0.5	-10.2	11.6	20.3	-4.42
	B	1236	0.5	-13	8.7	33.4	-5.65	1243	0.5	-10.2	10.2	19	-4.42
650°	A	1105	0.5	-17.45	40.7	126.5	-7.6	1163	1.5	-17.45	37.8	100	-7.6
	B							1151.5	1	-14.5	23.3	93	-6.3
700°	A	1090	-	+26	68	+212	+11.3	475.4	3.8	-2.9	14.5	33.5	-1.3
	B	1105	-	+29	74	+214	+12.6						
800°	A	531	—	+102			+44.3	509	-	+116			+50.4

* at second strain rate change $\varepsilon_2 \rightarrow \varepsilon_1$



a. b. c.

FIG. IV. 67-0.2% PROOF STRESS vs TEMPERATURE

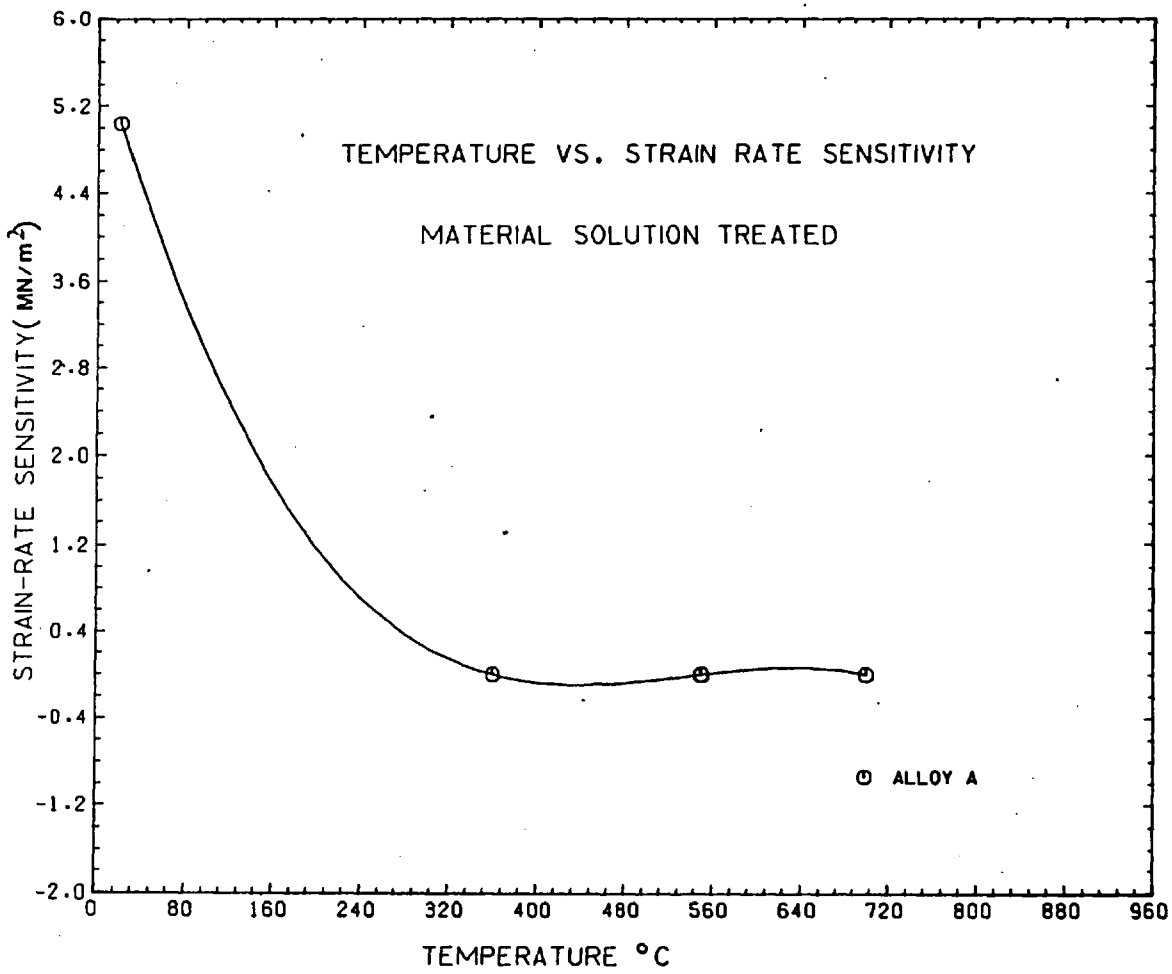


FIG. IV. 68 - STRAIN RATE SENSITIVITY vs TEMPERATURE

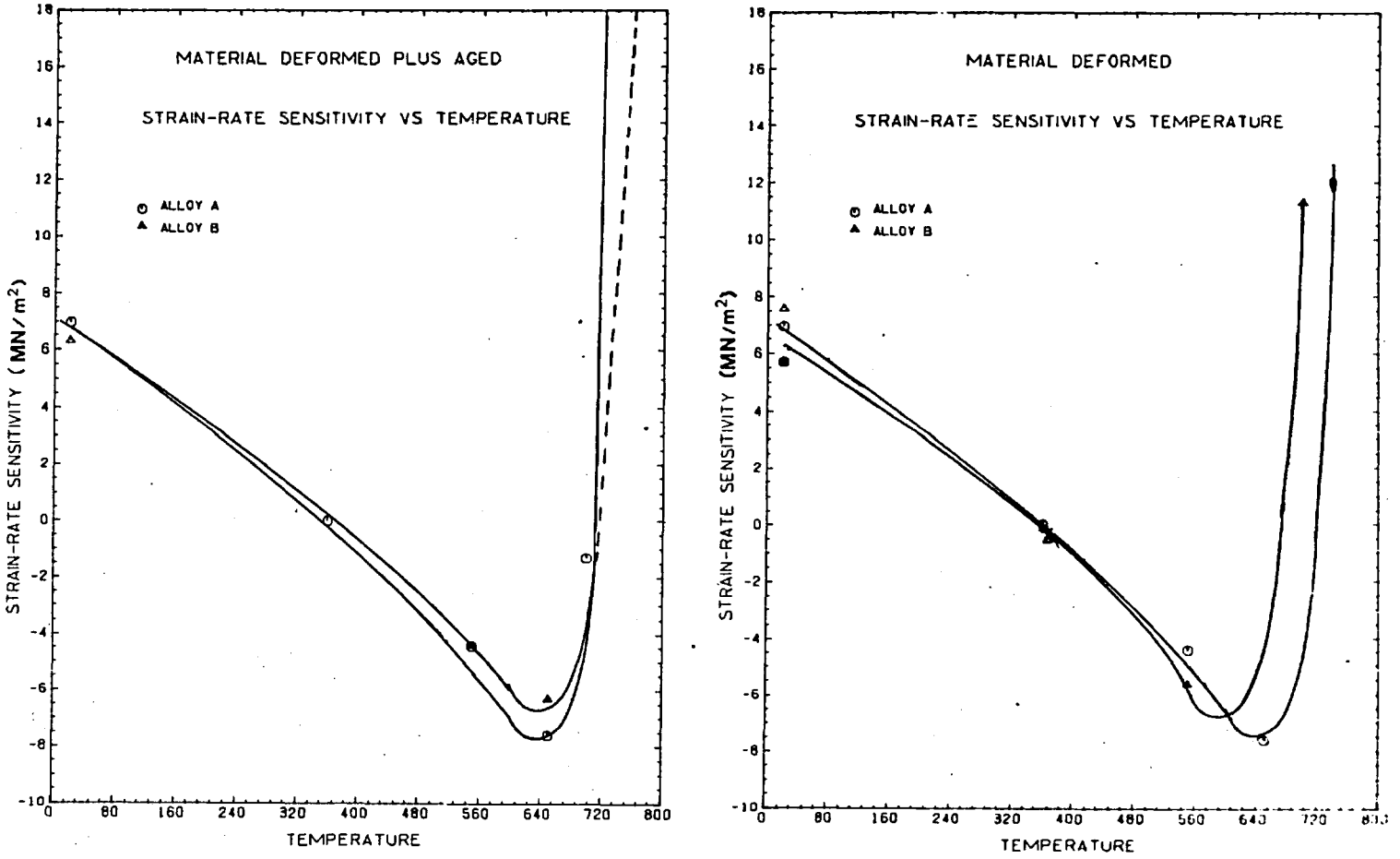


FIG.IV. 69 - STRAIN RATE SENSITIVITY vs TEMPERATURE

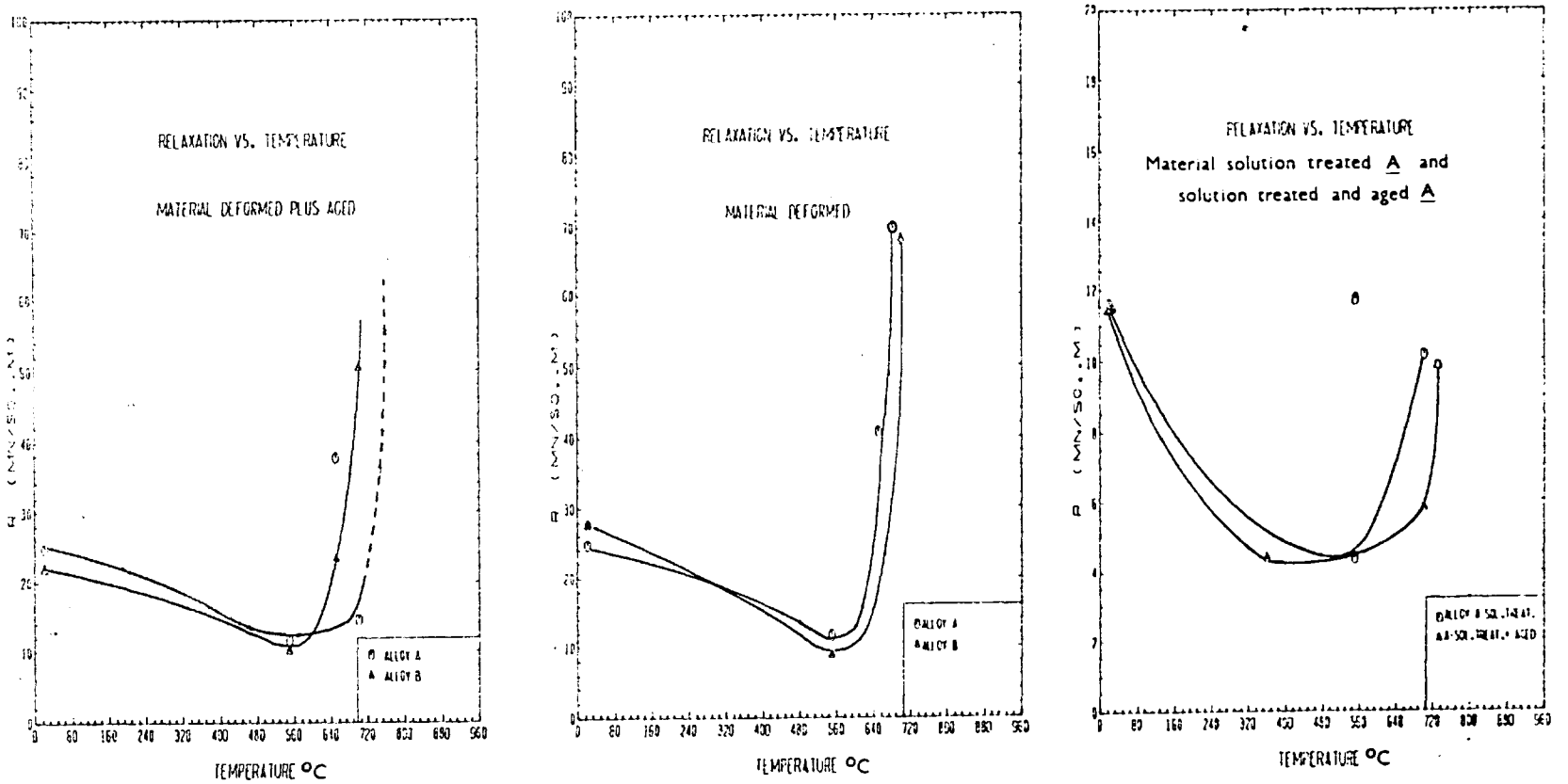


FIG. IV.70 RELAXATION STRESS vs TEMPERATURE

TABLE IV.14

$\Delta\sigma/\Delta T\ \dot{\varepsilon}$ VALUES ($MN/m^2{}^oC$)

(^oC) Temperature	Solution Treated	Sol. Treated and aged	Deformed	Deformed and aged
RT - 360	-4.2	-0.02	-0.06	-0.30
350 - 450	-0.21	-0.05	-0.36	-4.73
460 - 550	+1.81 -0.18	-0.24 (550°C) (700°C)	-0.61	+3.56
550 - 650	-0.55		-0.77	-1.45
650 - 700	+1.6		-0.3	-13.75
700 - 800			-5.59	+0.34

TABLE IV.15

ACTIVATION PARAMETERS MATERIAL SOLUTION TREATED ALLOY A

T (^{o}K)	0.2%Proof Stress (MN/m2)	$\frac{\Delta\sigma}{\Delta T}$ (MN/m^{2} ^{o}C)	KT^{2}	$1/\lambda$	ΔH	V*
293	408	-4.2	713.74	0.198	-71.6	+0.96
633	334	-0.21	3331.3	0	0	0
733	314	-0.18	4467	-1.59	+1278	-19.4
823	297	-0.55	5631	0	0	0
953		+1.6	7551	0	0	0
973	225		7871	0	0	0
1073						

TABLE IV.16

ACTIVATION PARAMETERS

T(°K)	Material Deformed A						Material Deformed plus aged A					
	0.2%P.S.	$\Delta\sigma/\Delta T$ ($MN/m^{2o}C$)	KT^2	$1/\lambda$	ΔH	V*	0.2%P.S.	$\Delta\sigma/\Delta T$ ($MN/m^{2o}C$)	KT^2	$1/\lambda$	ΔH	V*
293	1294	-0.06	713.74	0.175	-7.49	0.85	1479	-0.30	713.74	0.14	-30	0.68
633	1272	-0.36	331.3	0	0	0	1378	-4.73	331.3	0	0	0
723	1243	-0.61	4467	-0.53	+1444	-6.4	952	+3.56	4467	0	0	0
823	1182	-0.77	5631	-0.23	+997	-3.15	1309	-1.45	5631	-0.23	+1878	-3.15
923	1105	-0.3	7083	-0.13	+276	-2.	1163	-13.75	7083	-0.13	+12661	-2.
973	1090	-5.59	7871	+0.09	-3960	+1.5	475	+0.34	7871	-0.76	-2034	-12.3
1073	531	-5.59	9572	+0.02	-1070	+0.4	509	+0.34	9572	+0.02	+65	+0.4

ΔH = activation enthalpy (KJ/mole)

V* = activation volume

k = Boltzmann's Constant

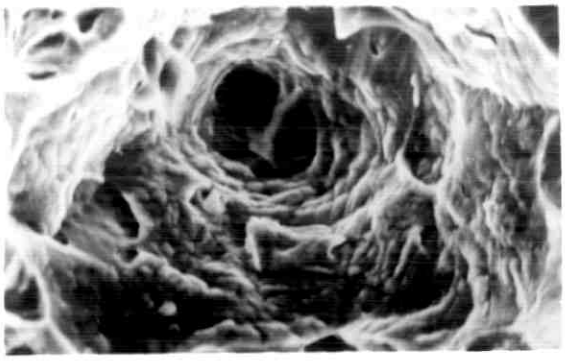


Fig. IV.71 - room temperature test, Alloy A Mag. 5 K

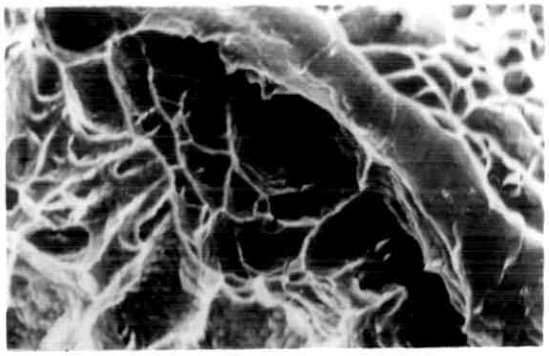


Fig. IV.72 - room temperature test, Alloy B Mag. 2 K

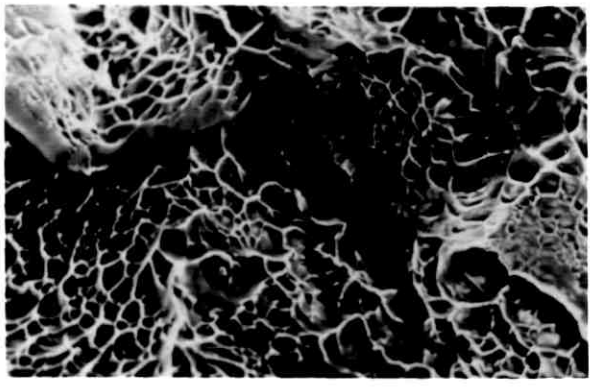


Fig. IV.73 - Alloy B, tested at -12 °C 1 K

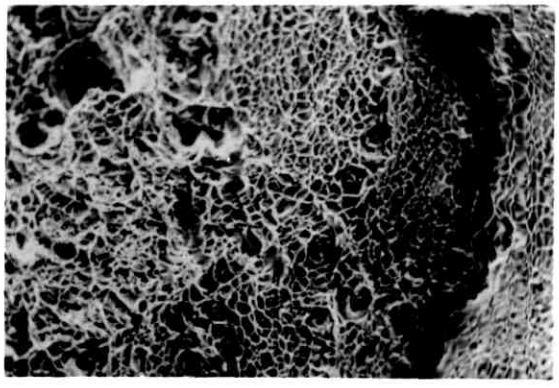


Fig. IV.74 - Alloy A, tested at -35°C X 500

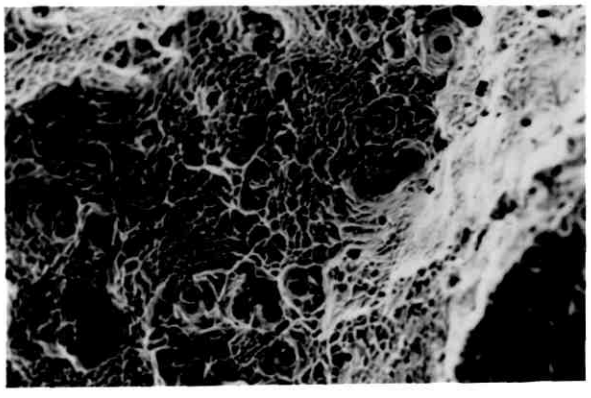


Fig. IV.75 - Alloy A, tested at -50°C X 500

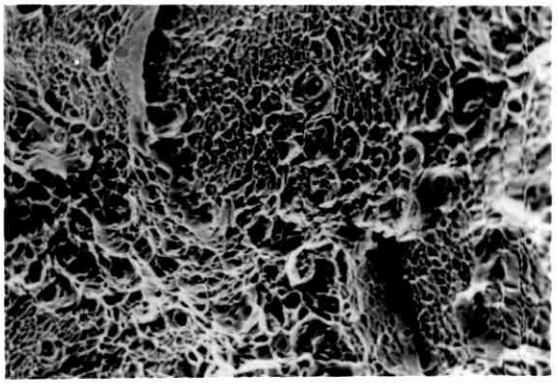


Fig. IV.76 - Alloy B, tested at -50°C X 500

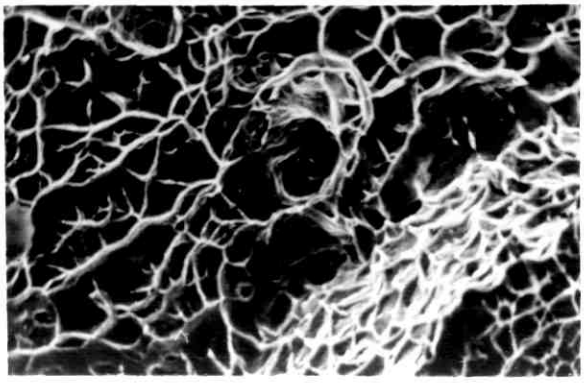


Fig. IV.77a - Alloy A, tested at -105°C 1 K

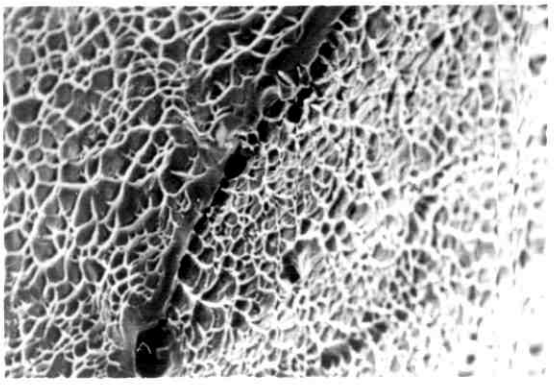


Fig. IV.77b - Alloy A, tested at -105°C × 500



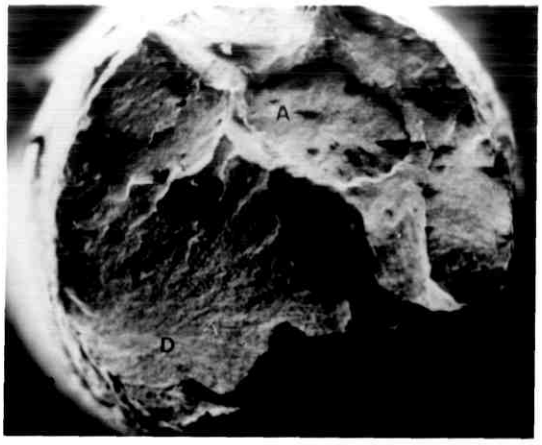


Fig. IV.78 - Two low magnification views of Alloy B, solution treated tested at -196°C X 50

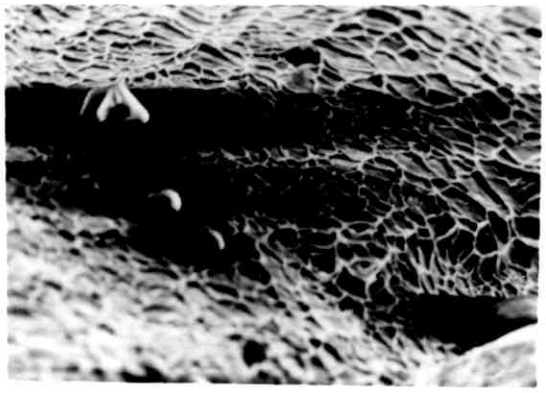


Fig. IV.79.a - 1 K

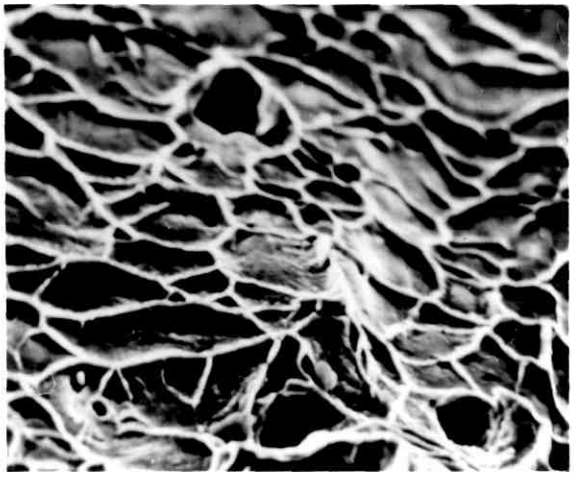


Fig. IV.79.b - 2.7 K

Fig. IV.79 - Higher magnification from area A in IV.78

Fig. IV.80 - Two views of area B in IV.78



Fig. IV.80.a - showing area B and C X 100

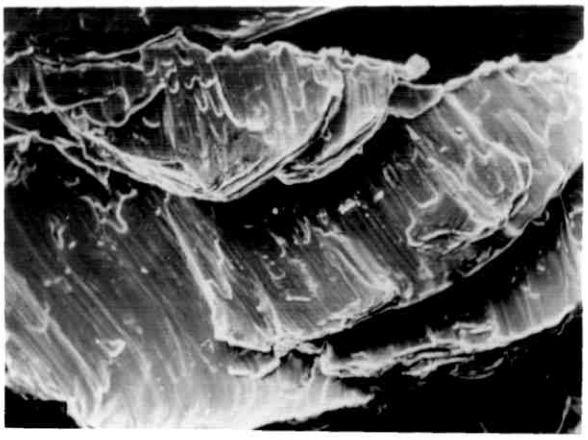


Fig. IV.80.b - area B, showing tear features X 1 K

Fig. IV.81 - Two views of area c in IV.78 and IV.80.a

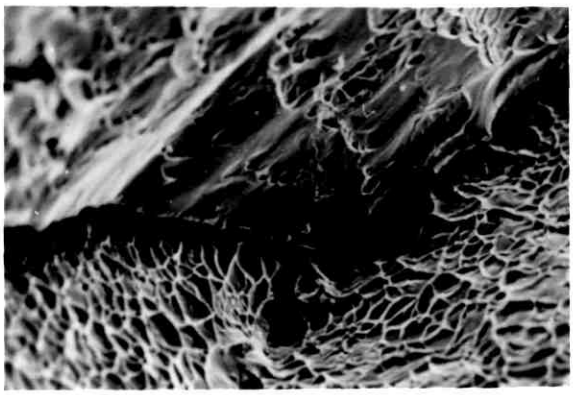


Fig. IV.81.a - X 1 K

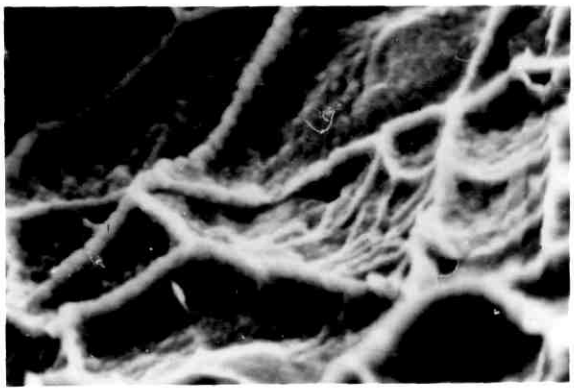


Fig. IV.81.b - X 1.5 K

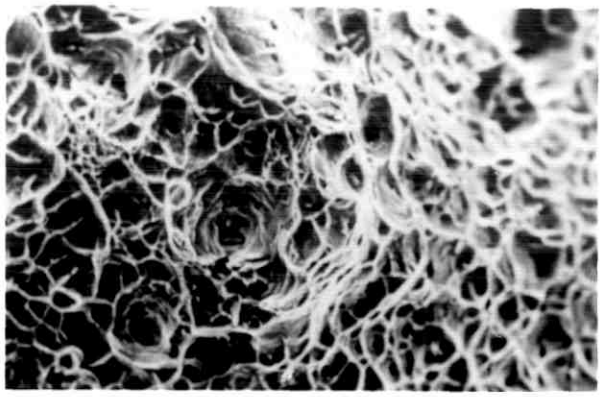


Fig. IV.82.a - Alloy A tested at room temperature 2 K



Fig. IV.82.b - higher mag. same area, showing particle 10 K

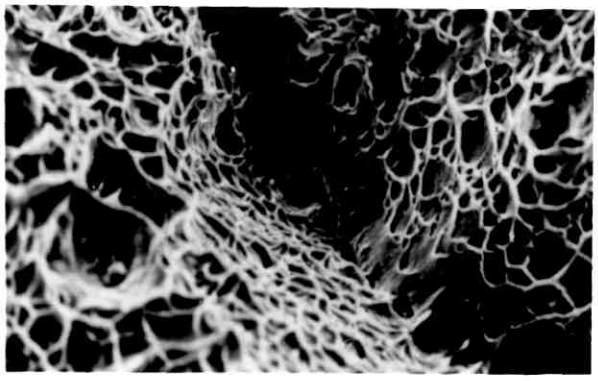


Fig. IV.83.a - Alloy A tested at $-12^{o}C$ showing voids at grain boundary X 2 K

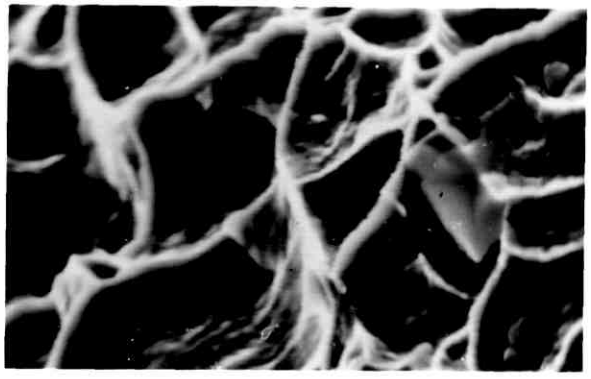


Fig. IV.83.b - closer view, showing particles X 10 K

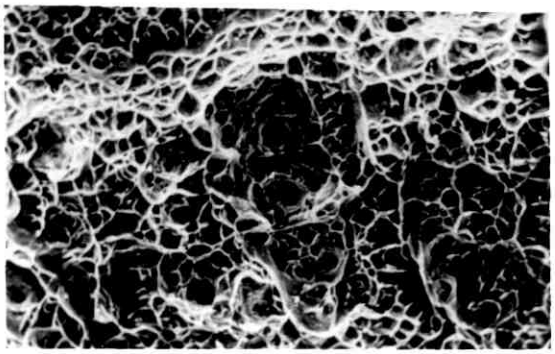


Fig. IV.84 - Alloy A, tested at $-18^{o}C$

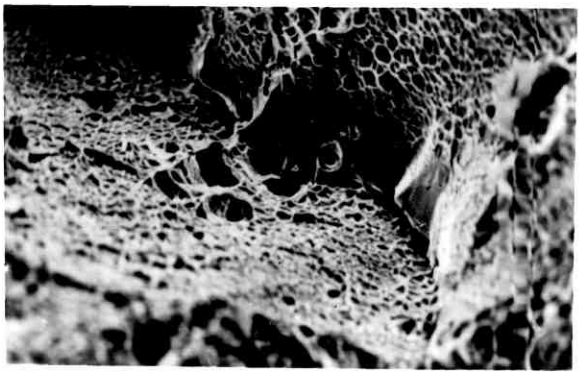


Fig. IV.85 - Alloy A tested at $-111^{o}C$

Fig. IV.82-IV.85 - Material previously deformed by cold rolling 45%. Tensile test at different temperatures

Fig. IV.86 - Alloy B, tested at -196°C showing flattened structure and intergranular separation

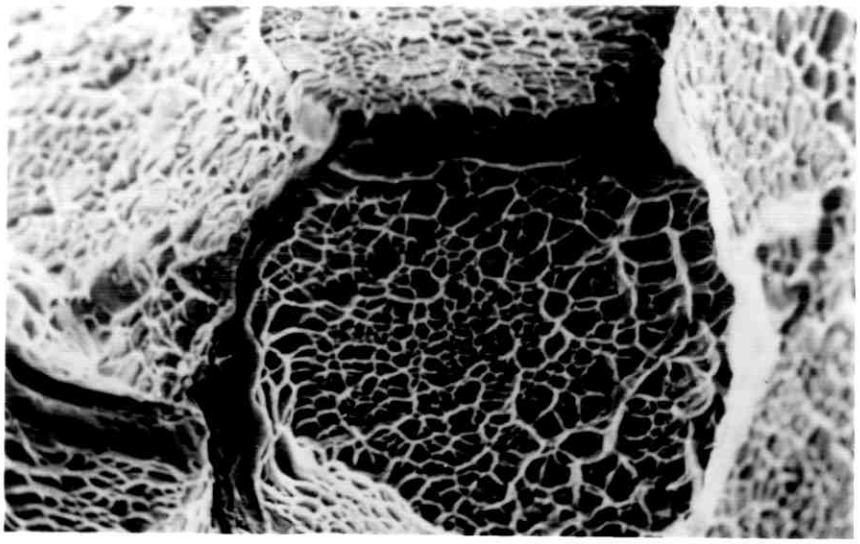


Fig. IV.86.a - X 750

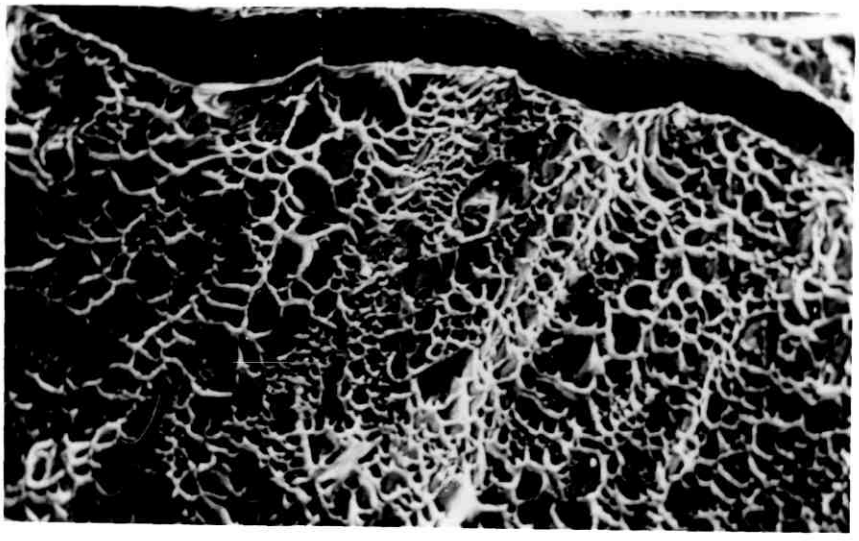


Fig. IV.86.b - 1.5 K

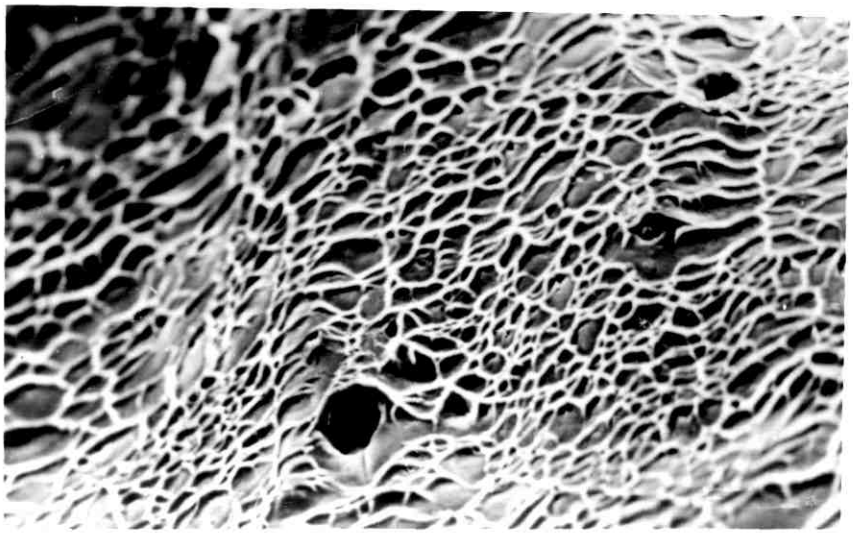


Fig. IV.86.c - 2.7 K



Fig. IV.87.a - R T

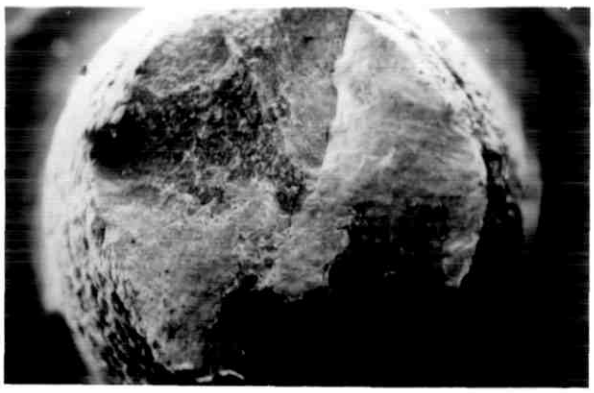


Fig. IV.87.b - -12°C

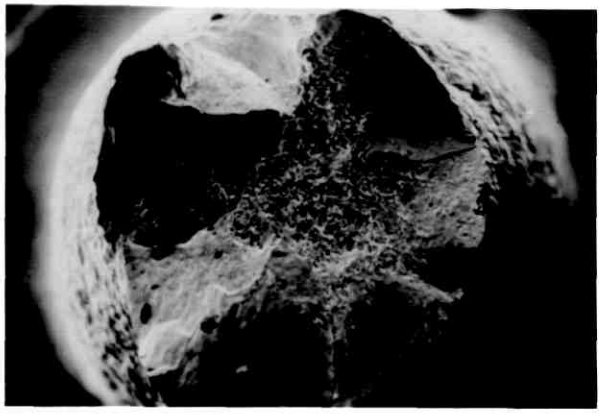


Fig. IV.87.c - -30°C

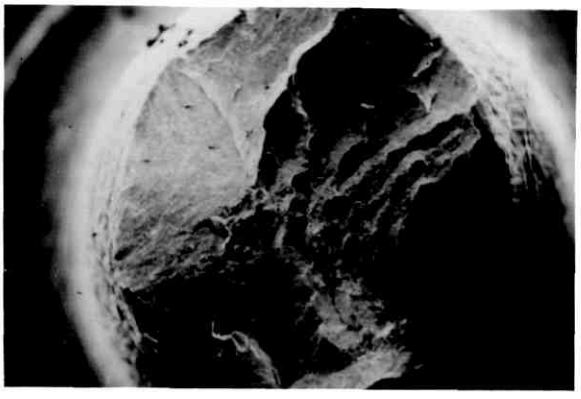


Fig. IV.87.d - -105°C

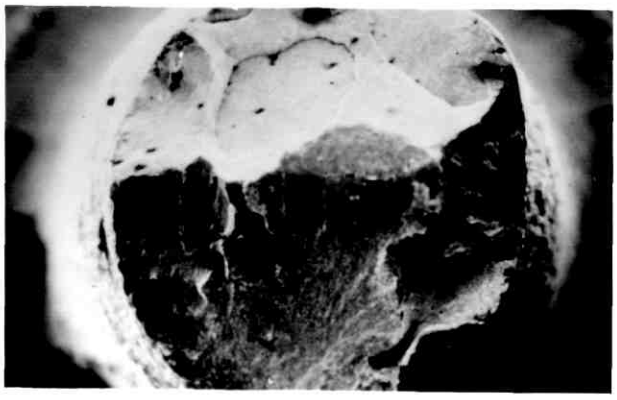


Fig. IV.87.e - -196°C

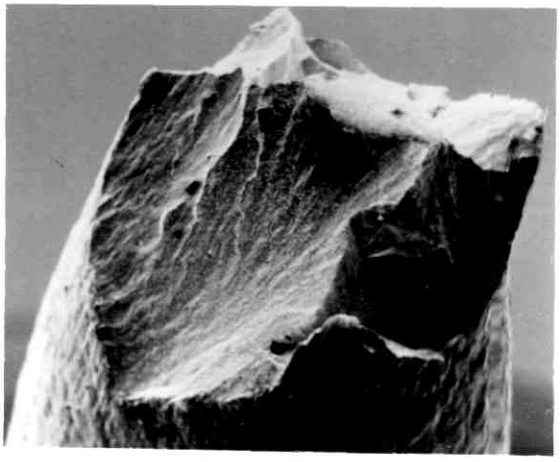


Fig. IV.87.f - -196°C

Fig. IV.87 - Fracture surfaces at low magnification. Material solution treated. Tensile test, different temperatures

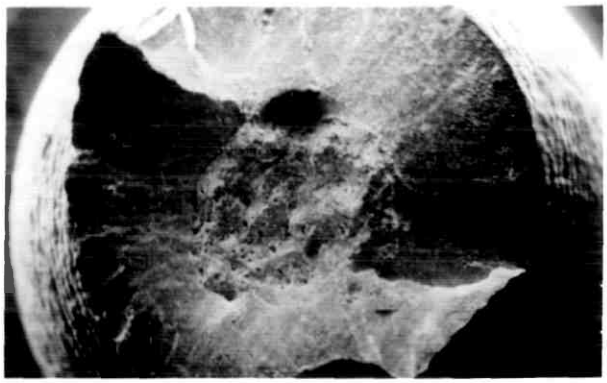


Fig. IV.88.a - room temperature



Fig. IV.88.b - 12°C

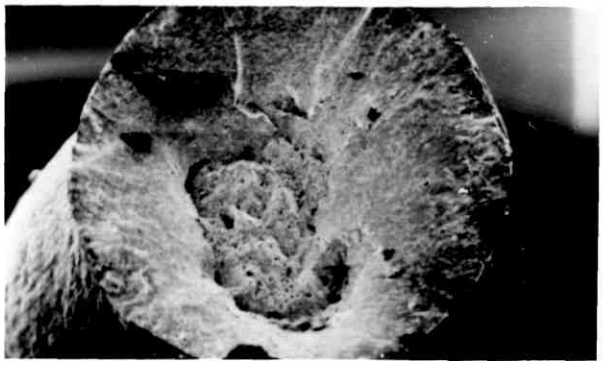


Fig. IV.88.c - 30°C

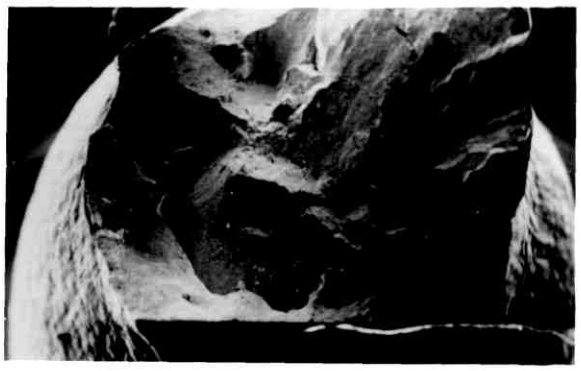


Fig. IV.88.d - 111°C



Fig. IV.88.e - -111°C



Fig. IV.88.f - -196°C

Fig. IV.88 - Fracture Surfaces at low magnification. Material previously deformed. Tensile test at different temperatures. X 50



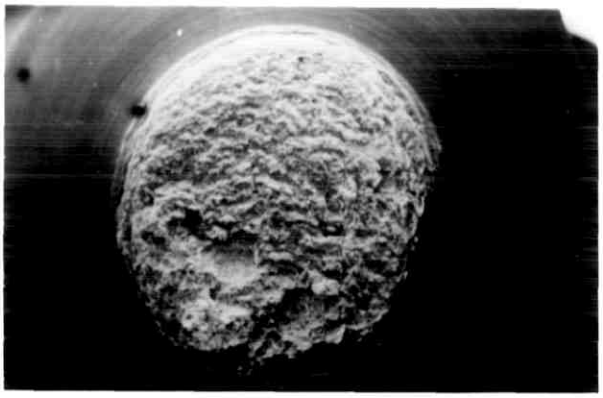


Fig. IV.89.1 - Material solution treated

a) room temperature test

b) test at -196°C

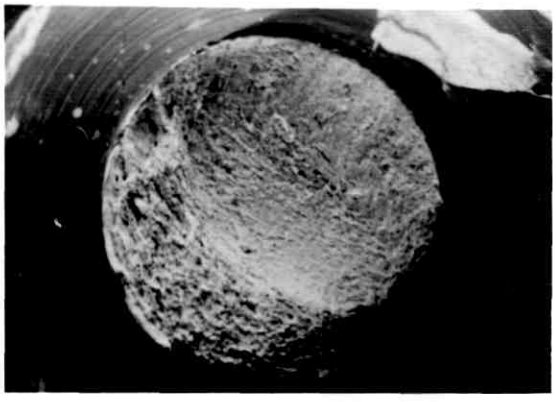




Fig. IV.89.2a- Material previously deformed 45%

a) room temperature test

b) room temperature test

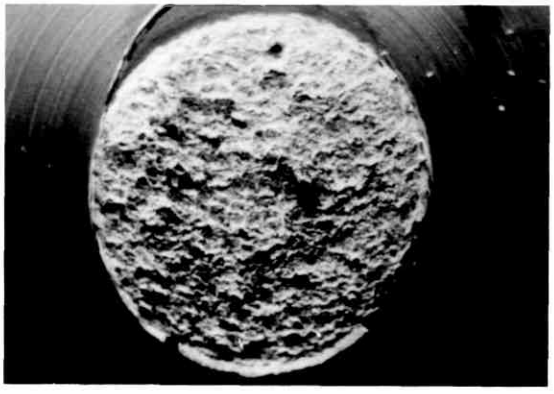




Fig. IV.89.2b- Material previously deformed 45%

c) test at -196°C

d) test at -196°C

Fig. IV.89 - Fracture at low magnification. Impact test at different temperatures X 20

Fig. IV.90 - Impact test higher magnifications

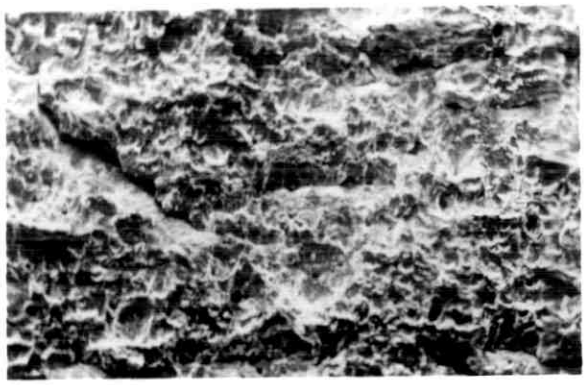


Fig. IV.90.1.a - X 100

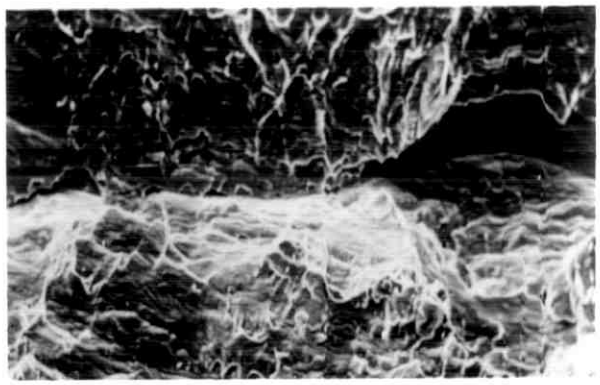


Fig. IV.90.1.b - X 500

Tested at room temperature

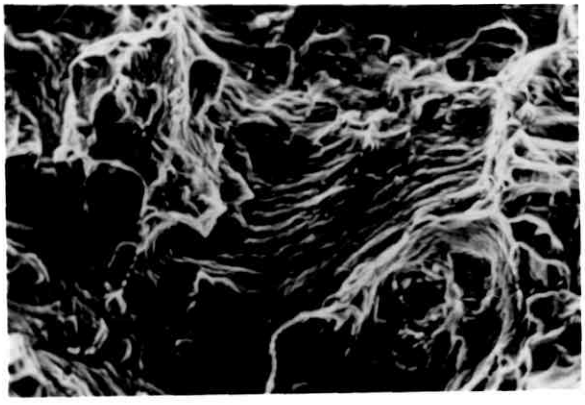


Fig. IV.90.1.c - X 2 K

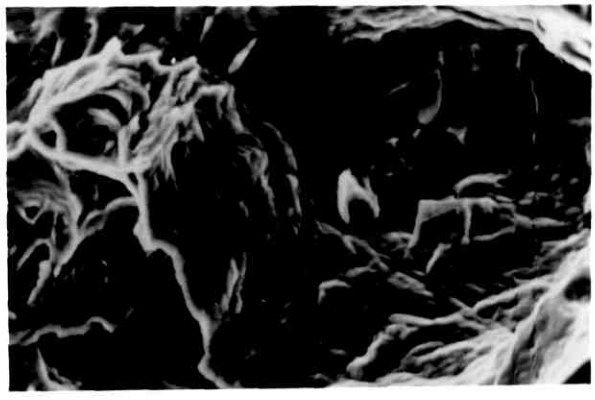


Fig. IV.90.1.d - 5 K

Tested at -196°C

Fig. IV.90.1 - Material solution treated

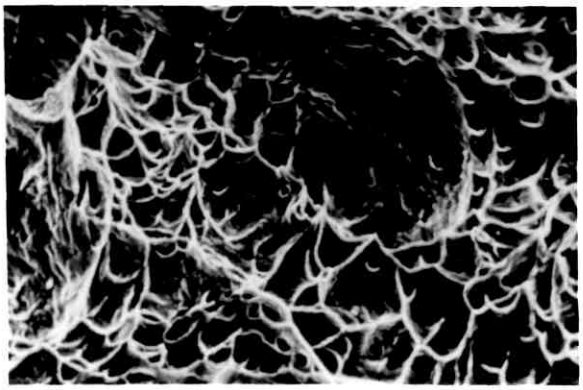


Fig. IV.90.2.a - room temperature X 2 K

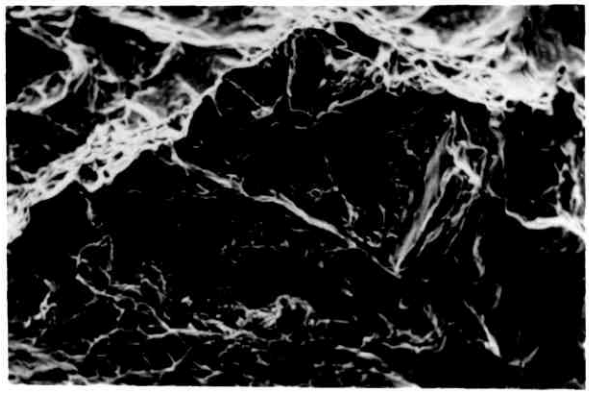


Fig. IV.90.2.b - -196°C X 1 K

Fig. IV.90.2 - Material previously deformed

CHAPTER V

DISCUSSION

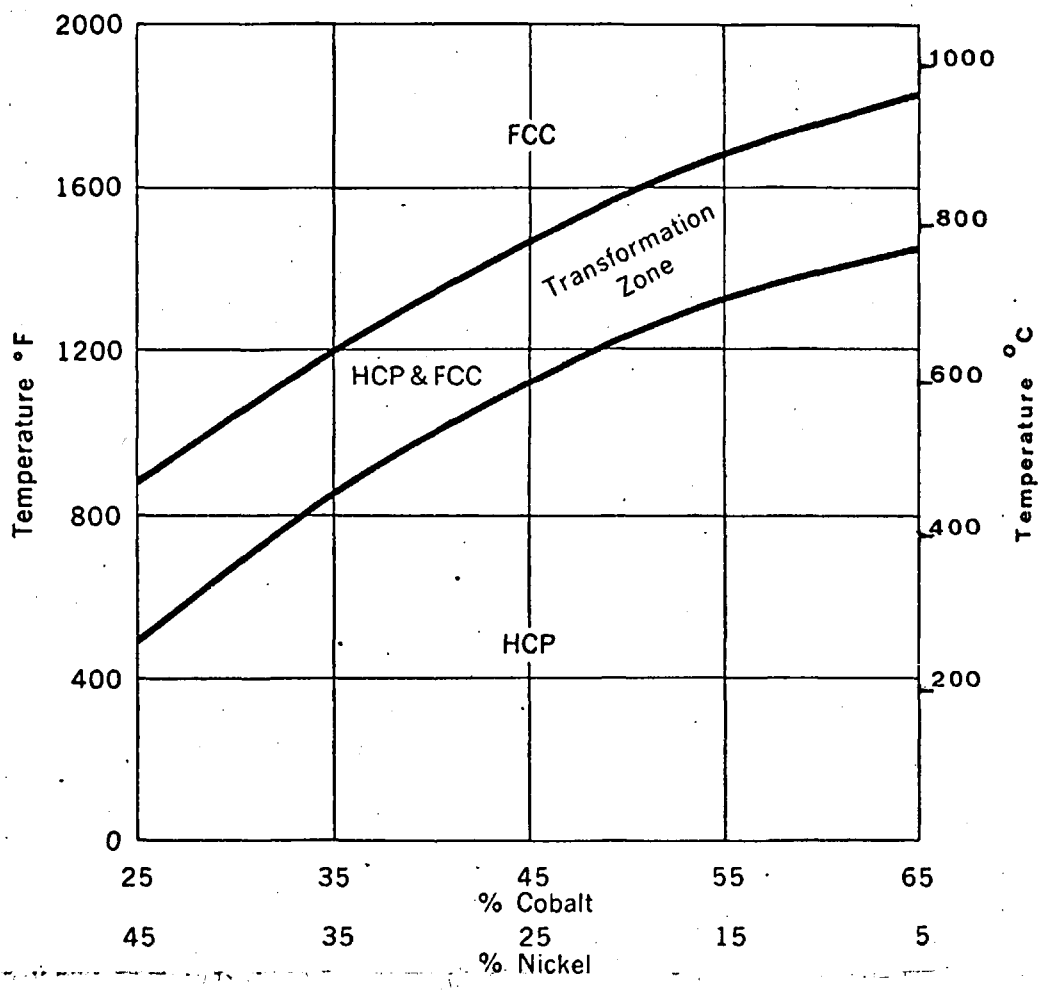
V.1 Deformation Behaviour

V.1.a Work strengthening at room and sub-zero temperature

Introduction

The equilibrium diagram given in Fig. V.1 corresponds to the range of compositions for MULTIPHASE alloys ([43]). In the case of the alloy studied in the present work (which has the same composition as MP35N but with Ti added between(0.5-1%) the fcc structure is stable above 650°C, while the hcp structure is stable below 425°C. However, the fcc → hcp transformation is very sluggish and does not occur by cooling below the lower transformation temperature ([16]) ([18]) ([43]). The fcc structure occurs at room temperature as a metastable phase. In such alloys, in which the Ms lies below room temperature ([5]), deformation of metastable fcc phase may result in the transformation to the hcp ε-phase.

On this basis, some studies have been carried out in the past on the strengthening of MULTIPHASE alloys which has been attributed to the formation of the ε-phase by deformation at room temperature ([16]) ([18]). A more



Structural Diagram for MULTIPHASE Alloys Containing 20% Cr – 10% Mo – 70% Ni + Co.

Figure V-1.

recent study ([20]) has reported that specifically for MP35N (35Co-35Ni-20Cr-10Mo) alloy cold worked 59%, the presence of ε-phase was not detected and the strengthening mechanisms were attributed to increasing dislocation density and formation of deformation twins. A similar result was obtained on an Fe-25Ni-21Co-20Cr-8Mo alloy ([88]) cold drawn up to 75%, with a deformed structure remarkably similar to the iron-free MP35N alloy. Remy ([22]) examined the influence of various deformation modes on Co-Ni, Co-Ni-15Cr and Co-Ni-15Cr-5Mo alloys and reported that low temperature plastic deformation induces the α (fcc) → ε (hcp) martensitic transformation.

At higher temperatures, twinning occurred whereas at still more elevated temperatures, the plastic deformation proceeded only by the propagation of undissociated dislocations.

Mechanical twinning and the formation of an hcp phase have much in common. The difference between a perfect fcc twin and a perfect hcp structure is one of staking sequence. A succession of stacking faults on every (111) plane results in a twin in the fcc structure, while faulting on alternate (111) planes gives a hcp phase. The morphologies of twins and ε phase is very much the same. On the other hand, high deformations make the structure very complicated, giving diffraction patterns in which spots become very elongated (streaking effects) and tend to form rings, which makes very difficult the clear and unambiguous interpretation. All these facts

could explain the contradictions found in the literature on the identification of ε or twins.

In the present work, from transmission electron microscopy observations, no ε phase is present at small deformations (up to 30%). However, ε was observed for much larger deformations (∿ 65% at room temperature and 50% at -196°C). The discussion of the results from X-ray analysis, hardness, optical microscopy and transmission electron microscopy is given below.

X-ray Analysis

X-ray analysis of the deformed material by different amounts did not detect the presence of any new phase, neither were changes of lattice parameters observed. This is in agreement with the observations of Graham and Youngblood ([18]) who reported that for MULTIPHASE alloys with a Co:Ni ratio smaller than about 45:25, the hcp→fcc transformation could not be detected by X-ray diffraction analysis. Peak shifts towards smaller angles were observed as well as broadening especially of the 200 and 311 hkl reflections, with deformation. Patterson ([65]) has shown that stacking faults on the (111) planes of an fcc material produce a line broadening and also a small peak shift. On this basis Warren ([66]) shows a direct determination of the stacking fault probability independent of particle size and distortion broadening. This is directly proportional to relative changes in angular distance between the { 200 }

and {111} diffraction peaks, i.e., $\Delta 2\theta_{200} - \Delta 2\theta_{111} = (2\theta_{200} - 2\theta_{111})^{\text{deformed}} - (2\theta_{200} - 2\theta_{111})^{\text{annealed}}$.

According to this, the values of stacking fault probability calculated for the different amounts of deformation at room temperature and -196°C are given in Table V.1.

TABLE V.1

Deformation	Stacking fault probability
10% (-196°C)	0.10
20% (-196°C)	0.10
30% (-196°C)	0
30% R T	0.20
50% R T	0.15
65% R T	0.10
80% R T	0.10

As more and more faults occur in a fcc material, so there are more and more regions that resemble twins and hexagonal regions; therefore the $(\bar{1}\bar{1}\bar{1})$ and $(\bar{1}11)$ peaks will shift away from the origin to the higher 2θ values of a hexagonal material, but the 200 and $\bar{2}00$ will move toward the origin. The same conclusion was reached by the previous authors ([65]) ([66]); i.e., the effect of stacking faults is to shift (111) outward, i.e. toward higher angles, and (200) inward, i.e. toward smaller angles. This effect is shown diagrammatically in Fig. V.2, where the arrows indicate the direction of

displacement, and the indices indicate the position of the reflection from perfect material. However, this applies only to the ideal case in which each crystal contains only one parallel set of faults.

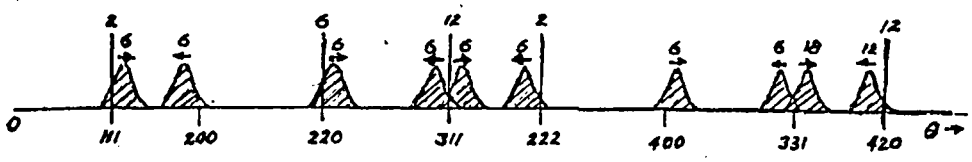


Fig. V.2

Table IV.2 shows the shift directions observed in the present work. Shifts towards smaller angles for all peaks for all deformations were obtained indicating the greater probability of hcp formation with increasing amounts of deformation and decreasing temperature. This is confirmed with the calculations of stacking fault probability, shown in Table V.1. The stacking fault probability decreases with the amount of deformation, and probably more twins and ε are formed. However, from this analysis alone we cannot draw any definitive conclusions.

V.1.b Structural Features

1. Dependence of deformation modes on temperature and amount of deformation

It has been observed, that rolling at room

and sub-zero temperatures resulted in a two-to-three fold increase in the hardness values with deformation and decreasing temperature; this is in agreement with observations in previous work ([16]) ([18]).

The factors affecting strengthening seem to change with increasing deformation and decreasing temperature. For small amounts of deformations up to 5% only dislocations are observed at room temperature (Fig. IV.10) and a few stacking faults are present in the $\sim$ 2% deformed material at -196°C, together with aligned dislocations (Fig. IV.18). For 10% deformation at room temperature, dislocations and a large number of stacking faults lying on the {111} planes are present (Fig. IV.11), while after 10% deformation at -196°C twins are already observed as well as stacking faults (Fig. IV.19). At 20% only twins are observed in this material; however in the material deformed the same amount at room temperature mainly stacking faults are present. For higher reductions up to 50% at room temperature the deformation occurs only by twinning (Fig. IV.13). After about 50% deformation at -196°C there is clear evidence of the presence of hcp phase (Figs. IV.23 and IV.24) which is not so clear in the deformed material at room temperature. After 65% deformation both treatments produce hcp phase and many deformation twins (Figs. IV.14 to IV.17 for R T and Fig. IV.25 L N). Table V.2 gives a summary of the deformation modes found for different amounts of deformation at room temperature and -196°C. From these observations it is inferred that

the strengthening effect cannot be attributed to the presence of ε-phase alone, but deformation twinning seems to be a more important contributing factor to the strengthening mechanism.

Obviously there is a relationship between the deformation modes and the temperature. As the temperature decreases twins occur at smaller applied strains, and for higher deformation, the fcc → hcp transformation occurs at lower temperature; the orientation relationship fcc/hcp is $(111)_\alpha // (0001)_\varepsilon$; $<1\bar{1}0>_\alpha // <11\bar{2}0>_\varepsilon$.

TABLE V.2

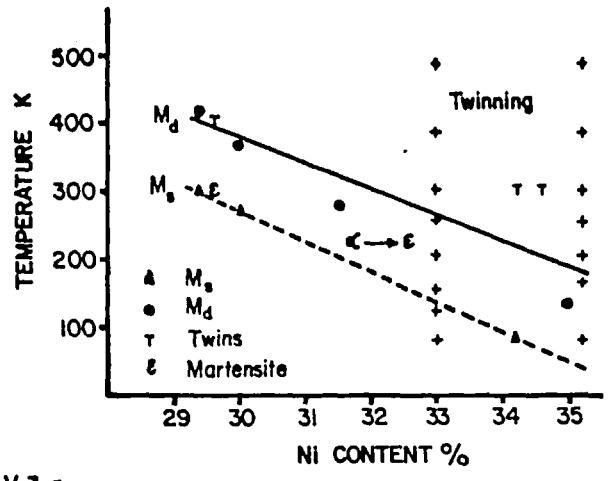
Deformation at room temperature		Deformation at -196°C	
%	Deformation mode	%	Deformation mode
up to 5%	only dislocations	2%	dislocations and a few stacking faults
up to 20%	stacking faults	10% - 20%	twins and stacking faults
30% - 50%	twins	20% - 50%	twins
50%	mainly twins	50%	twins and ε
65%	mainly twins and some ε	65%	increasing twins and ε

Remy ([23]) ([22]) studied the transformation induced structure in binary Co-Ni alloys, ternary Co-Ni-Cr

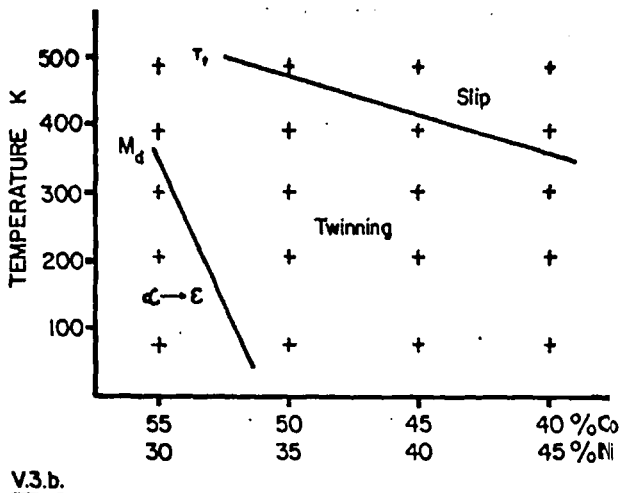
and quatenary Co-Ni-Cr-Mo alloys, (although with higher Co contents than the alloy studied in the present work (Table V.3)), in relation to nickel content, temperature and amount of deformation. Their work is summarised in Figs. V.3 and V.4. At low temperatures ε-martensite and/or twinning operate, while at high temperatures only slip is observed. Below M_d, (maximum temperature at which the $\alpha \rightarrow \varepsilon$ can be induced), ε is observed after small applied strains. Above Md, the alloy deforms by slip and twinning. Around Md, twinning occurs at the beginning of plastic deformation, whilst at higher temperatures it appears at progressively larger applied strains. In the quaternary alloy Co-Ni-15Cr-5Mo these authors reported to have found twins and ε-platelets co-existing in some temperature range below Md such that the domains of twinning and ε-martensite overlapped.

Although in the present work the volume fraction of martensite could not be measured, a similar trend to the Remy et al. results can be observed, in relation to amount of deformation and temperature. These authors establish a relationship between stacking fault energy and deformation modes which is summarised in Fig. V.5.

For stacking fault energy values between 10 and 15 mJ/m^2 the $\gamma \rightarrow \varepsilon$ martensitic transformation is induced by plastic deformation. At about 20 mJ/m^2 twinning occurs as a prevailing deformation mode up to 50 mJ/m^2.



V.3.a



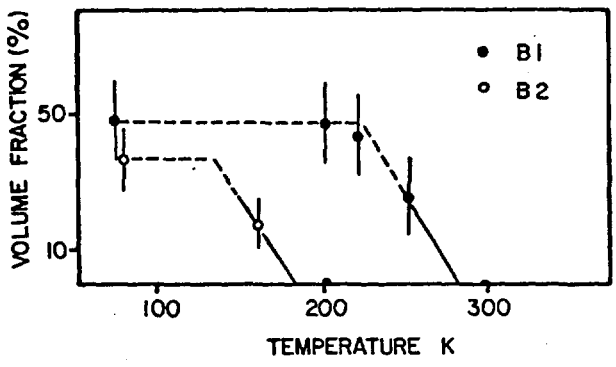
V.3.b.

Fig. V.3. Deformation structures as a function of composition and temperature.(22)
a. Binary Co-Ni alloys. b. CoNi15Cr alloy

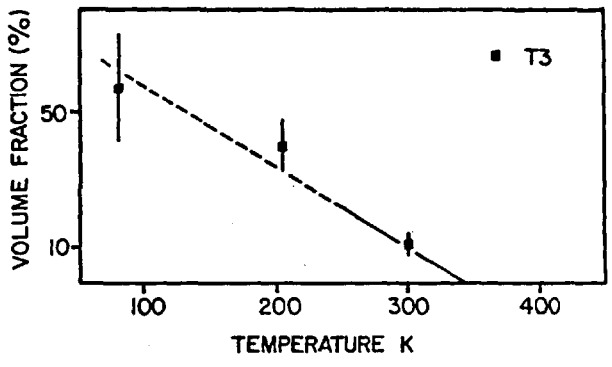
M_s Temperature for the spontaneous $\alpha \rightarrow \varepsilon$ martensitic transformation.

M_d Maximum temperature at which the $\alpha \rightarrow \varepsilon$ can be induced during a tensile test.

T_t Maximum temperature at which twinning is observed.



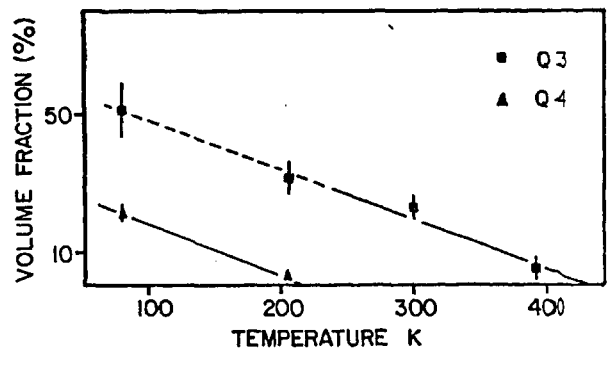
V.4.a.



V.4.b.

Compositions of the alloys (wt.%) and transformation temperatures

Graph	Alloy	Co	Ni	Cr	Mo	M_s °K	Md
a	B1	66.95	33.05	0	0	140	280
	B2	64.8	35.2	0	0	77	185
b	T3	55.6	30.2	14.2	0	77	340
c	Q3	55.0	25.0	14.8	5.2	77	430
	Q4	50.3	30.0	14.2	5.3	77	210



V.4.c.

Fig. V.4. Volume fraction of ε martensite as a function of temperature. Dotted lines
ture failure of the tensile specimen without necking.(22)

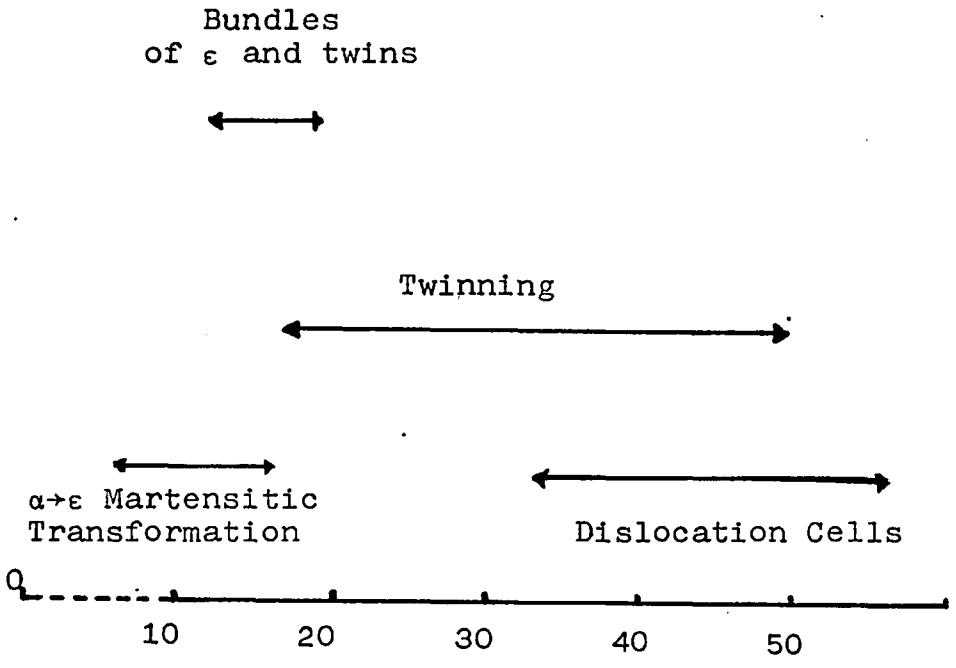


Fig. V.5 ([23]) Deformation structures observed near room temperature as a function of stacking fault energy at room temperature

From about 30 mJ/m^2 twinning occurs together with dislocations. There is a small range of SFE around 15 mJ/m^2 in which both twins and ε martensite are observed; a similar observation has been made in stainless steels ([69]) ([70]) ([71]) ([72]) and in the Co- 6.5Fe System ([73]). The stacking fault energy values at room temperature, calculated by different authors ([16]) ([23]) ([24]) for different Co-Ni alloys are given in Table V.3. The variation of the SFE with temperature in the Co-35Ni-15Cr alloy is illustrated in Fig. V.6 ([23]), and Fig. V.7 ([23]) for the Co-35Ni alloy.

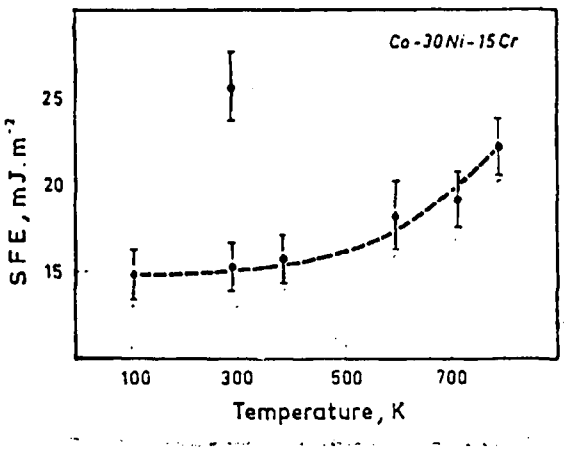


Fig. V.6 - Variation of apparent SFE with temperature for Co-30 wt% Ni-15 wt% Cr alloy (23)

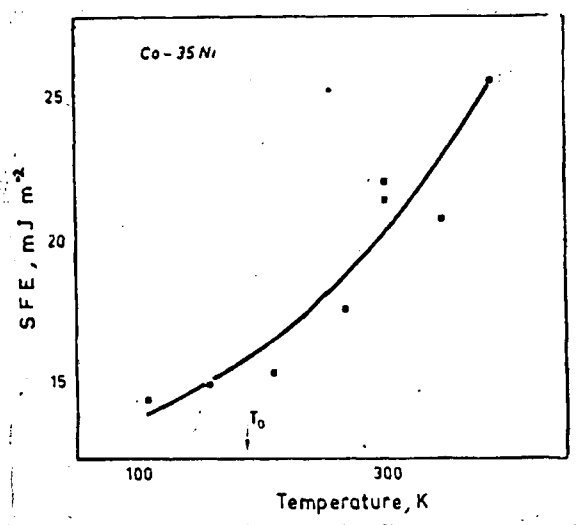


Fig. V.7 - Variation of SFE with temperature for Co-35 at% Ni alloy (23)

TABLE V.3

STACKING FAULT ENERGY VALUES FOR DIFFERENT Co-Ni ALLOYS AT ROOM TEMPERATURE

Alloy Composition	Ref.	(mJ/m^2)
67Co 33Ni	[24]	15
65Co 35Ni	[24]	20.5
56Co 30Ni 14Cr	[23]	15.5
50Co 35Ni 14Cr	[23]	24.7
45Co 40Ni 15Cr	[24]	38
40Co 45Ni 15Cr	[24]	48
55Co 25Ni 15Cr 5Mo	[23]	11.7
50Co 30Ni 15Cr 5Mo	[23]	17.7
35Co 35Ni 20Cr 10Mo	[16]	25

For different binary Co-Ni alloys measurements of the temperature dependence of the SFE are in quite good agreement by different authors [23] [84] and give a value of 0.03-0.05 $mJ/m^2{}^oK$ in the temperature range 100-800°K. Considering these values are applicable to the alloy studied in the present work, since in the quaternary system Cr & Mo decrease the SFE, then γ_{SFE} of $25mJ/m^2$ reported [16] at room temperature reduces to $\sim$ 7-11 mJ/m^2 at -196°C. Therefore in accordance with Fig. V.5 it would be possible to obtain ε at this temperature (-196°C), and twinning would be the prevailing deformation mode at room temperature, which is in good agreement with

the observations made by means of transmission electron microscopy.

Ericsson ([84]) showed the existence of a direct relationship between the fcc → hcp transformation and the decrease in stacking fault energy with temperature, working on a Co-Ni alloy. This investigation relates the stacking fault energy to the Gibbs free energy difference between the hcp and fcc phases, $\Delta G^{fcc \rightarrow hcp}$. For a temperature close to the temperature To $^{fcc \rightarrow hcp}$ at which $\Delta G^{fcc \rightarrow hcp} = 0$ he shows that:

$$\Delta S^{fcc \rightarrow hcp} \sim \frac{1}{2d} \frac{\partial \gamma}{\partial T}$$

where, S = entropy
d = distance between {111} α planes
γ = stacking fault energy

Lecroisey and Pineau ([70]), showed, however, that the opposite is not true, i.e., the existence of an fcc → hcp transformation in steels is not a necessary condition for a strong variation of SFE with temperature.

2. Conditions for twin formation and fcc → hcp

Transformation induced by plastic deformation

Several authors ([74]) ([75]) have shown that deformation twins in fcc are only produced after the application of a critical stress. Venables ([74]) has proposed that the critical stage for the nucleation of

twins is the formation of a semicircular loop of stacking fault, and that the twinning stress is approximately a parabolic function of SFE, given by

$$\eta\sigma = \frac{\gamma}{b_1} + \frac{\mu b_1}{2a_o}$$

η = local stress concentration factor

a_o = radius of the source

μ = shear modulus of the metal

b_1 = is the Burgers vector of a slip dislocation

The dislocation configuration in the neighbourhood of the source is shown schematically in Fig. V.8.

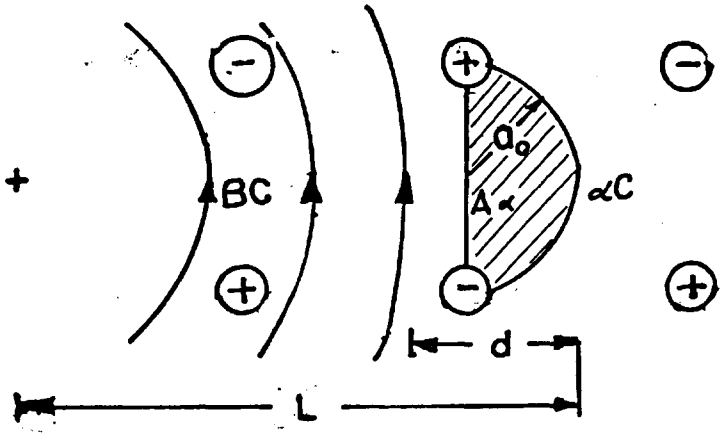


Fig. V.8 Schematic drawing of a dislocation distribution near the twin source. The dislocations BC form a pile-up of length L. The + and - signs indicate forest dislocations crossing the twin plane. The resolved shear stress for slip J, is sufficient to push the leading dislocation of the pile-up to within a distance, d, of the twinning dislocation which is thereby bent to a radius, a_o.

In alloys with low stacking fault energy, ✗, the nucleation of faults is easy, whereas, propagation of twins through the forest dislocations is difficult; the twins grow slowly by breaking down interactions with the

forest dislocations. This approach for twinning formation proposed by Venables ([74]) is shared in a modified way by Cohen and Weertman ([41]) and Hirth ([76]). Cohen and Weertman ([41]) suggested that the glide of Shockley dislocations on the appropriate {111} planes could lead to the formation of overlapping but separated intrinsic stacking faults. Since the process occurs in several regions, it is possible that an ordered staking fault arrangement required for the twin formation may evolve. Mahajan and Chin ([77]), however, working on a Co-Fe alloy, found their results were not compatible with Venables and Cohen-Weertman's models. They proposed ([77]) an alternative dislocation reaction for the nucleation of deformation twins, based on:

(i) a three-layer twin is the basic nucleus

(ii) two co-planar glide dislocations of different Burgers vectors are involved in the nucleation

(iii) thickening occurs by random amalgamation of these basic nuclei

3. Initial stages of $\alpha \rightarrow \varepsilon$ formation

The role of twinning in the $\alpha \rightarrow \varepsilon$ martensitic transformation

The theories of martensitic transformation predict that an additional deformation must accompany the strain which converts the parent structure into the product; this additional deformation has been proposed ([79]) to be twinning on a fine scale. However, it is very difficult to

determine the process of initiation of martensite experimentally, and it is not suggested that the present work has done this; nevertheless, it is clear from the experimental evidence that the deformation process creates dislocations, stacking faults, twins and ε-martensite in that order. Therefore, it appears as a fact that stacking faults and twins intervene in the mechanism of formation of the ε-martensite.

Fujita and Veda ([82]) studying 18-8 stainless steel concluded that the nucleus of ε-phase induced by plastic deformation is formed by overlapping of stacking faults; however, evidence of this initiation was not obtained in the present work from the transmission electron microscopical results, e.g. Figs. IV.11 and IV.21, in which great numbers of groups of stacking faults are present, did not show evidence of hcp reflections. Of course the determination of the initial stages of formation of ε martensite is very difficult considering that the fcc structure with stacking faults in every other {111} is the same as the ε-phase.

From the experimental observations, ε-phase was clearly identified at very high deformations and only after clear evidence of twins had been observed. Other factors are affecting the clear identification of the two phases. First of all the morphology of both is so similar that just by bright field techniques identification is impossible; furthermore electron diffraction patterns exhibited intense streaking of reflections as a

consequence of high stacking fault density and twins and as a result of the parallelism between close-packed planes and close-packed directions in both phases (fcc and hcp); dislocations also influence the shape of diffracted spots, and the spot acquires a disc-type halo perpendicular to the line direction of the dislocation. All these factors made it quite difficult to positively identify the presence of ε in the initial stages of formation, in which, because of the small volume fraction, very few reflections might have been expected. Bollman ([83]) directly observed the behaviour of stacking faults in thin foils of Co and proposed that the ε was formed at fault intersections; of course, the behaviour of pure Co is different than that of a complex alloy.

In the present work, with deformation at -196°C sets of twins intersecting each other were observed before ε formation (Fig. IV.20); perhaps the ε starts to form at these intersections, although no clear evidence for this is established. At room temperature the situation is quite different and it seems as if the twins grow wider with increasing deformation (Fig. IV.15) and the relation to ε formation is not so clear. Therefore, more transformation occurs at lower temperatures, the free energy change favouring the formation of martensite becomes larger at lower temperatures, moreover, the nature of nucleation centres is such that more nucleation events occur at higher driving forces.

Lecroisey and Pineau ([70]) showed that in austenitic alloys containing 18Cr-12Ni, 16Cr-13Ni, 18Cr-14Ni, the tendency to nucleate an ε platelet rather than an austenite twin cannot be rationalized in terms of intrinsic stacking fault energy only. They proposed, based on the work of Cohen and Weertman ([41]) that the value of extrinsic stacking fault energy and of small contractions associated with the fcc → hcp transformation are important in controlling the nucleation process. They made a rough calculation showing that ε nucleation is easier than twin nucleation when

$$\frac{\gamma_o - \gamma(1-x)}{\mu b} > \sqrt{2}\,\xi^2 \pm 2\sqrt{2}\alpha\,\xi\,\frac{\sigma}{\mu} \qquad (1)$$

with

γ_o = intrinsic stacking fault energy at the temperature To $^{fcc \rightarrow hcp}$ where $\Delta G^{fcc - hcp} = 0$

$(1+x)$ = ratio between extrinsic and intrinsic stacking fault energies

b = Burgers vector of a Shockley dislocation

ξ = contraction normal to the (111) α plane during the fcc → hcp transformation

α = parameter of the order of 0.1 to 1, depending on the geometry of the site with respect to the applied stress

σ = applied stress

They establish that this relation can account for the following:

i) the fact that ε platelet nucleation is preferred to twin nucleation at lower temperature, since

SFE increases with temperature,

ii) the coexistence of twins and ε platelets, as the right hand term in eq. (1) is a function of the orientation of the site through α.

Although there is relatively little difference between ε and twin formation in terms of violations of the stacking sequence of the atoms in the { 111 } planes of the fcc lattice, the observations of much more extensive twinning compared to ε , imply that there are fundamental differences in the dislocation mechanisms.

4. Kinetics of strain-induced martensitic transformation and of fcc deformation twinning

The kinetics of the α (fcc) → ε (hcp) strain-induced martensitic transformation in Co alloys are still poorly documented ([85]) ([73]). However, there is extensive literature on steels based on the Fe-Cr-Ni system ([39]) ([40]) ([18]) and also on manganese containing steels ([85]) ([91]).

Remy ([85]) studied this problem for a high manganese steel and proposes a model, which extends to the predeformed condition. This is a most suitable model to apply to the situation found in the present work, since prestrains introduce numerous stacking faults and twins, which act as nuclei for the strain-induced α → ε transformation; however at the same time they act as obstacles which can provide effective barriers to the growth of ε platelets. Unfortunately in the present work

lack of volume fraction data make it impossible to prove the model quantitatively. The model is as follows:

For a strain increase, $d\zeta$, the number of plates formed per unit volume of austenite is proportional to the number of stacking faults present. The probability that a stacking fault could form an ε plate is $pd\zeta$; p is assumed to be independent of the strain ζ and to depend only upon the stacking fault energy, the lower the stacking fault energy the higher the probability $pd\zeta$ for a stacking fault forming an ε plate. The number of martensite plates per unit volume of specimen

$$dNv = (1-f)\ (\ell_o+\ell\zeta)pd\zeta$$

Where

ℓ_o = faults present before deformation = $K\zeta_o^*$

$\ell\zeta$ = faults introduced by strain = $K\zeta$

As the amount of pre-strain ζ_o^*, induces a volume fraction of twins

$$dNv = (1-f_T-f)\ (\zeta_o^*+\zeta)\ Ad\zeta$$

f_T = volume fraction of twins

A = p.K is a decreasing function of the SFE

the volume fraction of platelets is related to the volume fraction of ε-martensite formed $V = Vo\ (1 -K_{fo} -K_f)^2$

After arranging equations, and defining other terms, he finally arrives at the expression obtained after integration:

$$\alpha^1[\zeta^2+2\zeta_o^*\zeta] = \Phi_{k^*}(f^*)$$

$$\Phi_k(f^*) = \frac{1}{(k-1)^2} \log \frac{1-kf^*}{1-f^*} + \frac{k}{k-1} \cdot \frac{f^*}{1-kf^*}$$

Where, $\Phi_K(f^*)$, the volume fraction of the strain-induced martensite is a function of the applied strain and depends upon the constant K and upon three parameters = $(1-f_T)$ volume fraction of untwinned austenite, α^1 which is a decreasing function of the stacking fault energy and ζ_o^* which accounts for the stacking faults introduced by prestrain.

The same author in another work ([86]) on a cobalt-nickel alloy proposed a model for the kinetics of twinning similar to the model previously discussed for the strain-induced ε martensite. In this the twin nuclei evolve from the interaction of perfect slip dislocations and the number of nuclei is taken to be proportional to the overall dislocation density; the reaction is only possible for a suitable critical stress level ζ_c , as discussed by other authors also. Finally, he arrives at the following expression: $\Phi_k(f_T) = \alpha (\zeta^2 - \zeta_c^2)$ this is, the volume fraction of twins f_T is an implicit function of strain, which depends upon the critical strain at the onset of twinning, and α which is a decreasing function of the stacking fault energy and is proportional to the volume fraction of the first twins which form.

V.1.c Low temperature strength

It can be seen in Fig. IV.60 and IV.61 that the strength increases with decreasing temperature. This behaviour was observed for both alloys in both conditions, solution treated and deformed, this effect being much more pronounced in the material previously deformed 45%. The general level of strength was slightly higher in the alloy containing the higher Ti content (alloy A). The reduction of area for the solution treated and for the previously deformed material remains fairly constant with decreasing temperature, decreasing slightly at -196°C for both conditions. The value of reduction of area is very similar for both conditions, being only slightly lower in the deformed material (about 5%) with respect to the solution treated condition. The elongation was higher (about 75%) for the solution treated material remaining fairly constant with decreasing temperatures. For the previously deformed material however the elongation is much lower (about 25%) and also remains fairly constant with decreasing temperature down to about -100°C. From this temperature an increase in elongation (of about 10%) is observed down to -196°C.

There are no data available in the literature for the mechanical properties at low temperatures of the solution treated material.However, there is a report ([88]) on some of the low temperature mechanical properties of the previously 49% c.w. alloy MP35N (without any Ti content) which agrees reasonably well with the results of

the present work.

Work Hardening Behaviour

The stress/strain curves from the tensile tests were analysed based on the Ludwick equation $\sigma = k\varepsilon^n$, which can be made linear by logarithmic transformation $\log \sigma = \log k + n \log \varepsilon$. n is the slope of the resulting straight line and it can be shown that is mathematically equivalent to the true strain at maximum load.

However, for the present results this equation fails to describe the plastic behaviour at lower strains for the solution treated material tested from room temperature to -196°C. The flow curve is concave upwards when plotted on logarithmic coordinates, and lies at higher strains than the extrapolation of the straight line defined by that relation to low strains. This behaviour has been observed ([89]) ([90]) for austenitic stainless steels and fcc metals with low stacking fault energies. Ludwigson ([90]) proposes a modified model of the Ludwick relation which takes account of the initial deviation at low strains and is given by $\sigma = k_1 \varepsilon^{n_1} + e^{k_2} \cdot e^{n_2 \varepsilon}$

where K_1 is the strength factor and n_1 is the strain hardening exponent, (this is the same as in the Ludwick equation)

e^{k_2} = is the true stress value extrapolated to zero true strain. (This is the stress at which plastic flow begins in terms of this model)

n_2 = is the slope of the line given by $\text{Ln } \Delta = k_2 + n_2 \varepsilon$

where Δ is the difference between the observed true stress at low strains and the stress represented by Ludwick relation.

This model can be used to explain the deviation from the straight line observed at low strains in the present work for the solution treated material tested at all temperatures (e.g. Fig. IV.56). However, the deviation from the straight line observed at high strains in the test performed at -196°C can not be accounted for by this model. The deviation at high strains from the extrapolated straight line has been observed in 316 stainless steel ([91]) at low temperatures, and was attributed to the occurrence of the austenite-martensite transformation during plastic deformation. The difference in stress between the experimental curve and the extrapolated line at any value of plastic strain is considered to be the contribution of the martensite formed to the flow stress at that value of strain.

In the present work, the electron microscopy observations of the material deformed by rolling at room temperature and-196°C, provide clear evidence of ε martensite forming at -196°C at high deformations, from 50% onwards. In Fig. IV.56 the deviation from the straight line occurs at about 0.42 plastic strain. This behaviour was not observed in the room temperature test, although some ε was observed by transmission electron microscopy. However, the evidence for ε formation for this temperature was much more difficult to obtain. It was only detected

for higher deformations than those observed at -196°C, and in smaller amounts. Therefore it could be argued that at room temperature the amount of martensite formed is not high enough to make any appreciable contribution to the flow stress.

The previously deformed material did not show this deviation from linearity, either for low or high strains, up to instability. This is due to the deformation already existent in the material prior to testing.

From the fact that it does not show deviation for higher strains up to instability it could be argued that for the amount of previous deformation given (45%), the martensite has already started to form, (as was observed by transmission electron microscopy for 50% deformation), and therefore there is not a certain strain at which the martensite starts to contribute to the flow stress, since it is already contributing from low strain values for this condition.

Looking at the values of work-hardening rate in Appendix III, it is seen that there is a steady increase in work hardening rate (assessed from the slopes of the true stress/true strain curves) with decreasing temperature. This can be explained by the fact that the number of stacking faults and twins increase with decreasing temperature, constituting strong obstacles to dislocations resulting in extra work-hardening. This is consistent with the decrease of stacking fault energy with decreasing temperature.

Lecroisey ([70]) studied the transformations taking place during plastic deformation in the Fe-Ni-Cr-C system, in relation with the stacking fault energy, the conditions for appearance of twinning and of fcc → hcp and fcc → bcc martensitic transformations. The variation of SFE with temperature in relation to the fcc → hcp transformation has been discussed in the previous section (V.1.b). Lecroisey has pointed out that nucleation of both twins and hexagonal platelets is promoted by low values of SFE, but ε platelet nucleation is preferred to twin nucleation at lower temperatures.

The large values of elongation obtained and the fact that it remains almost constant with decreasing temperature and increases from about -100°C (in the previously deformed material) is a characteristic of the phenomenon called transformation-induced-plasticity, TRIP, which has been observed in steels ([53]) having an excellent combination of strength and elongation. They are characterized by a large uniform elongation and suppression of necking, which has been attributed to the formation of martensite. The necked region is hardened more by strain-induced martensite than the rest of the specimen, so incipient necking no longer grows and deformation occurs in the adjacent region.

Guimaraes ([96]) developed a method which allows the tensile necking condition to be correctly predicted in materials which display transformation induced plasticity.

He proposes that the total elongation has two components. One is a uniform strain due to plastic deformation (slip) of the material. The other is due to the (localized) deformation provided by the transformation strain

$$\text{thus, } d\sigma = \sigma(d\varepsilon_u + \Phi_s df)$$

Where Φ_s is effective tensile strain associated with the deformation

ε_u = uniform strain

f = volume fraction of transformed phase at some point in the elongation process

the total engineering strain, e_T , is written

$$e_T = e_u + \Phi_s f\ (1+e_u)$$

and therefore the true strain is

$$\varepsilon = \varepsilon_u + \ln\ (1 + \Phi_s f)$$

Considering that the reaction occurs progressively during deformation, he arrives at the relation:

$$\frac{d\sigma}{d\varepsilon} = \sigma\ \frac{(1+ \Phi_s^2 f\ df/d\varepsilon)}{1 + \Phi_s f}$$

and this equation was in agreement with the experimental data for TRIP steels. Although in the present work this model cannot be applied quantitatively, since the volume fraction values could not be measured, it can be inferred from the transmission electron microscopy observations (Figs. IV.16, IV.17, IV.22), that f could be considered not only as the volume fraction of martensite formed, but also the volume fraction of twins formed during deformation plus the volume fraction of martensite. Since the elongation values for the solution treated material did not change

very much with decreasing temperature, the high elongation values are not necessarily dependent only on the total amount of martensite formed, which increases in content with decreasing temperature for equal amounts of deformation.

The results of strain hardening exponent values (equal to the true strain at instability),in the present work, for the solution treated material range between 46-57%, which are in good agreement with the values observed in some TRIP steels ([56]) which range between 40-55%. Tamura et al. ([54]) have shown in Fe-30Ni and in Fe-13Ni-15Cr that with decreasing test temperature the strain hardening exponent decreases slowly down to the temperature at which the maximum elongation is obtained and increases near Ms, then is almost constant below Ms. This is shown in Fig. V.9.

The present results do not agree with these observations. The previously deformed material showed maximum elongation from about -105°C together with an increase in strain hardening exponent. For the solution treated and the deformed material there was a small drop in the strain-hardening exponent at -196°C but no significant increase in elongation was observed. On the contrary, although variations were small, larger elongation values corresponded to larger strain hardening exponent values. This disagreement is difficult to explain, but it is possible that different mechanisms are taking

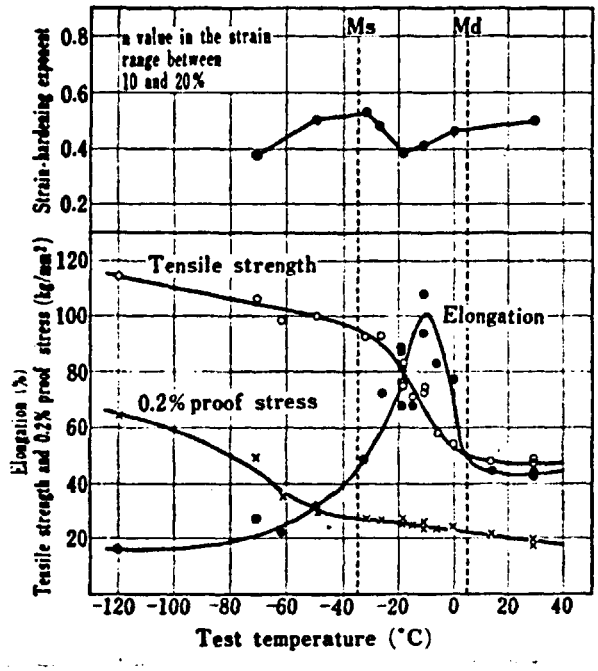


Fig. V.9 - Effect of test temperature on the tensile properties and the strain-hardening exponent in Fe-15%Cr13%Ni alloy (54)

place, since Tamura et al. ([54]) established that the prerequisite for maximum elongation is that deformation of austenite occurs at early stages of deformation without martensitic transformation and then martensite is progressively formed little by little during deformation up to fracture. However, in the present work an increase in elongation was observed in the previously deformed material which already had some martensite present due to the previous deformation treatment.

Tensile Fracture Mode Analysis

During the tensile test the material suffers considerable deformation (elongation and necking) prior to fracture. Cracking in tension originates near the centre of the specimen and propagates towards the surface, ending with a conical shear lip (Figs. IV.87 and IV.88). A typical ductile mode of fracture was observed for both conditions of the material from room temperature down to -111°C. The fracture mechanism was characterized by slow crack growth at the centre creating a fibrous zone and the shear lip around this zone (Figs. IV.87 and IV.88). As the test temperature was decreased the fibrous zone became smaller. At -30°C a radial zone was observed emanating from the periphery of the fibrous zone, indicating a change from slow crack growth to rapid unstable crack propagation which coincides with the general direction of crack extension. At lower temperatures (-111°C) the radial marks are very coarse, similar to those

found in the fractures of medium-strength steels with martensitic structures when broken at or near room temperature ([100]). These coarse radial marks are shear elements, which may be caused by high normal tensile strength resulting from the separation of the radial surfaces along the plane of maximum shear (45°). A closer look at all the fracture surfaces down to this temperature shows microvoid coalescence. Microvoids are initiated at interfaces between matrix and particles such as carbides, precipitates and inclusions, and also at imperfections such as microporosity and microcracks. They grow under the triaxial stress conditions ahead of the crack tip and expand until they coalesce to leave behind on the fracture surface the familiar hemispheroidal cavities, known as dimples (Figs. IV.71 to IV.77 and IV.82 to IV.85). As the test temperature decreases the shear zone becomes larger and a flattening of the over-all fracture surface is observed. At -196°C the fracture surface appears fairly smooth and has a fine texture with very uniform features, showing a predominant shear mode of fracture. (Fig. IV.78 to IV.81 and IV.86). Intergranular separation was also observed at this temperature in previously deformed material (Fig. IV.86.a).

Concerning crack nucleation it is well established that twinning can nucleate cracks ([97]). Deformation twins cannot propagate across a grain boundary and a large stress concentration will be produced at the boundary. In addition, except for one specific twin-twin

orientation, a twin cannot propagate across another twin and again a large stress concentration is produced. The strain is relieved in a number of ways:

i) nucleation of a new twin on the opposite side of the intersected twin;

ii) slip in matrix and in twin;

iii) crack formation.

Because of the large amount of twinning observed to occur during plastic deformation, in the present work, it is reasonable to infer that twinning is one of the causes of crack initiation. However, the role of twinning in fracture cannot be easily discussed since the situation is not clear for a simple case of brittle fracture in bcc crystals. The case of fcc crystals is much more difficult due to the ductile fracture exhibited.

The intergranular separation observed at very low temperature, especially at -196°C (Fig. IV.86) may be attributed to both ε-martensite forming preferentially at the grain boundaries and to twin impingement on grain boundaries. Thus, grain boundary cracking occurs as relieving the stress concentrations ([112]).

Although -196°C was the test temperature which showed clearly intergranular fracture, plastic intergranular fracture (this is, formation and coalescence of micro-voids along the grain boundaries) was observed from much higher temperatures (Figs. IV.73, IV.74, IV.76, IV.77, IV.83 and IV.86), this effect becoming more pronounced with

decreasing temperature.

In high nickel TRIP steels with varying carbon contents, Maxwell ([52]) found that one of the reasons of failure was decohesion at the interfaces between austenite and strain-induced martensite with subsequent void formation. And also intergranular failure was observed when martensite initiated at grain boundaries.

Fracture Mode During Impact Testing

The energy absorbed during impact testing remains fairly constant with decreasing testing temperatures, as can be seen in Fig. IV.62. This is in good agreement with the fracture surfaces analysed (Figs. IV.89 to IV.90). The fracture mechanism does not change with decreasing temperature being a ductile mode. It can be seen from the low magnification fractographs (Fig. IV.89) that the deformed material, tested at room temperature, shows a conical fracture shape indicating that the fracture occurs through the plane of maximum shear stress at 45°, in a very ductile manner. This is the only noticeable difference between the different tests. It is interesting to notice that the modes of fracture resulting from the tensile testing at -196°C and the impact testing at the same temperature are not the same. While in the impact testing the fracture is very ductile, showing microvoids and slip lines, in tension testing the very fine even structure and intergranular separation show that different mechanisms occur. This may be only a consequence of the much higher

strain rate in the impact tests than in tensile tests. In impact testing with the higher strain rate less ε martensite may form.

V.2 Annealing Behaviour

V.2.a Ageing Induced Strengthening

Ageing at temperatures between 450°C and 650°C causes the hardness to increase, provided the material has been previously cold worked. This has been reported ([16]) ([18]) for several MULTIPHASE alloys. During rapid heating treatments, after deformations greater than 30%, the hardness increases very rapidly (within 2 min) and reaches a maximum at about 15 min and then either decreases or remains fairly constant up to 30 min. For long time ageing treatments (from 5 hrs to 100 hrs) the hardness increases with ageing time for temperatures up to 650°C; however it decreases with ageing time for higher temperatures. These effects can be interpreted in relation to the phase diagram given in Fig. V.1 ([43]). The temperature of 700°C is above the range of the fcc → hcp transformation, therefore the hardness is expected to decrease, because of the complete transformation of the ε phase to fcc and because some recovery is taking place at this temperature (Fig. IV.35). Observing the structural changes brought about by ageing the previously deformed material, in the range $\sim$ 474°C-650°C, which lies within the fcc + hcp region, (Fig. V.1), ε phase was observed

to form even after very short time ageing treatments (15 min) in the very heavily deformed materials (from 50% onwards) (Figs. IV.29 to IV.31). However it was not observed in the undeformed material after holding, in this temperature range, for very long times. Neither was it observed on ageing the material with low previous deformation (up to 20% at room temperature and -196°C). This shows the sluggishness characteristic of the fcc → hcp transformation. However, on ageing for longer times ε was observed more easily at deformations at which ε was very difficult to be detected in the non-aged material. These observations suggest the formation of new ε as a result of annealing. Probably both processes are occurring, i.e., some ε formed during prior deformation persists after annealing and new ε platelets are formed because of annealing.

On the other hand, Drapier ([16]) has shown that the stacking-fault energy, γ, derived from the nodes of dissociated dislocations, observed after ageing the annealed material decreases with ageing temperature (within the transformation range), lying between 10 and 14mJ/m^2. This is shown in Table V.4.

This is in agreement with Ericsson's ([84]) observations on Co and Co-Ni alloys, which are summarized in Fig. V.10.

In the previous section (V.1.a) the relationship between deformation modes and stacking fault energy was discussed and Fig. V.5 showed a summary of this. As

TABLE V.4 ([16])

RESULTS OF STACKING-FAULT ENERGY MEASUREMENTS ON HEAT-TREATED MP35N ALLOY

Heat Treatment	Number of nodes	Mean radius, r	Stacking-fault energy, γ * mJ/m^2	
			Screw nodes	Edge nodes
1050°C - 1 h, A. C. (Annealed)	4	184	26.3	24.3
Annealed + 550°C - 4 h, A. C.	9	410	12.8	10.5
Annealed + 550°C - 100 h, A. C.	3	370	14.1	12.2
Annealed + 600°C - 100 h, A. C.	9	437	12.2	10.3

* The shear modulus of MP35N ($G = 0.886 \times 10^9$ J/ m^2) was derived from the value of Young's modulus, E, using a Poisson's ratio, ν, of 0.30

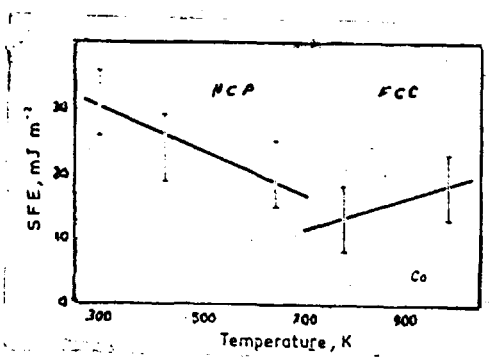


Fig. V.10 - Variation of S.F.E. with temperature for Co and Co-Ni alloys ([84])

could be seen in this fig. the fcc → hcp transformation occurred in the range of stacking fault energy values between 10-15 mJ/m^2, and around 15 mJ/m^2 twins and ε were observed.

Drapier ([16]) shows that ageing in the fcc + hcp regions produces an fcc structure whose stacking fault energy is in the favourable range for ε formation. Several authors ([2]) ([6]) ([9]) have tried to explain the nature and mechanisms of the fcc → hcp transformation in cobalt alloys. The thorough study by Giamei et al. ([9]) of the kinetics of the transformation in the Co-WC and Co-W systems has established that, for the particular compositions and temperatures used, the reaction occurs in three stages:

1. Massive transformation of supersaturated α phase to metastable ε phase.

2. Decomposition of the metastable ε phase by cellular separation

3. Peritectoid formation of the equilibrium hcp ε phase.

This is shown in Fig. V.11.b. Precipitation of Co_3W directly from the fcc α solid solution in a Co-35wt%W alloy would result in a lowering of the free energy from state a to the metastable state c. Final equilibrium would be obtained by a peritectoid reaction between the depleted fcc α phase and the Co_3W to form the equilibrium hcp ε phase. It is also possible for the α matrix to undergo a massive transformation to metastable hcp ε phase (state b)

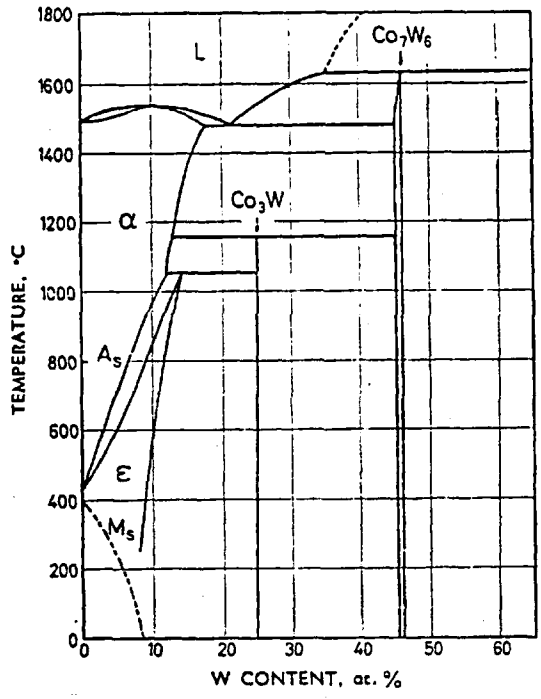
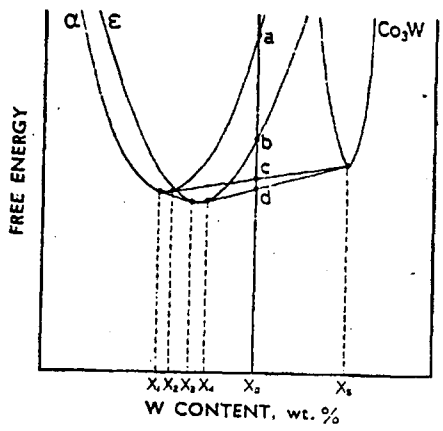


Fig. V.11.a - Equilibrium diagram for Co-W system (7)



Alloy free-energy change		Reaction	Type
A	a→b	$\alpha_o \rightarrow \varepsilon_o$	Massive
B	b→c	$\varepsilon_a \rightarrow \alpha_2 + Co_3W$	Eutectoid
	b d	$\varepsilon_o \rightarrow \alpha_4 + Co_3W$	Precipitatio
C	c→d	$\alpha_2 + Co_3W \rightarrow \varepsilon$	Peritectoid

Fig. V.11.b - Schematic free energy vs composition curves for a Co-35wt%W alloy aged at 800°C after solution treating at 1350°C (9)

without a change in composition.

The equilibrium diagram of the Co-Mo system (Fig. II.4) is very similar to the equilibrium diagram of the Co-W system (Fig. V.11.a). The true equilibrium is represented by $\alpha + Co_3Mo \rightleftharpoons \varepsilon$. Therefore the hypothetical free energy curves could be similar, for both systems. However, the kinetics of the reaction, in the present alloys, seem to be more similar to the Co-Cr system, in which the allotropic transformation occurs very rapidly ([9]). The rapid nature of the allotropic transformation in the Co-Cr system can be demonstrated by comparing the T-T-T curves for the Co-Cr and Co-W systems (Fig. V.12.a and V.12.b, respectively). For the Co-25wt%W alloy (Fig. V.12.b) the maximum rate of transformation occurs somewhere in the region of 700° and 800° and requires an incubation period of approximately 10 min. For the Co-20wt%Cr alloy, below 600°C the reaction begins in less than 6 sec. The rapid increase in hardness observed in the present work, after 2 min, could be explained on the basis of the above observations.

Giamei et al. ([9]) found in the Co-35wt%W alloy a maximum in hardness occurring after very short times (Fig. V.13) corresponding to the onset of the massive transformations. Hcp regions forming at the fcc grain boundaries will be an effective barrier to dislocation motion since slip is limited to one plane in these hcp regions. For long time ageing treatments (between 470°C and 600°C) and deformations above 20%, the hardness

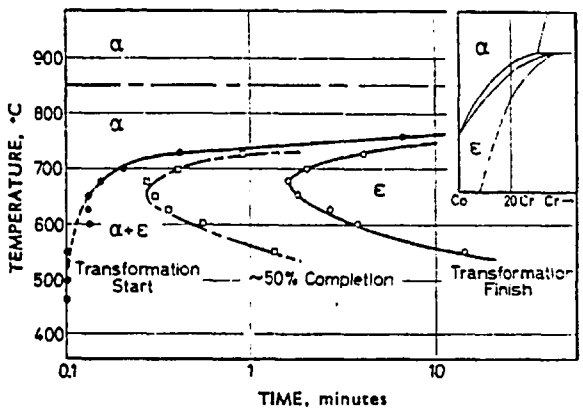


Fig. V.12.a - T-T-T curve for a Co-20wt%Cr alloy obtained from quenching-dilatometer studies (9)

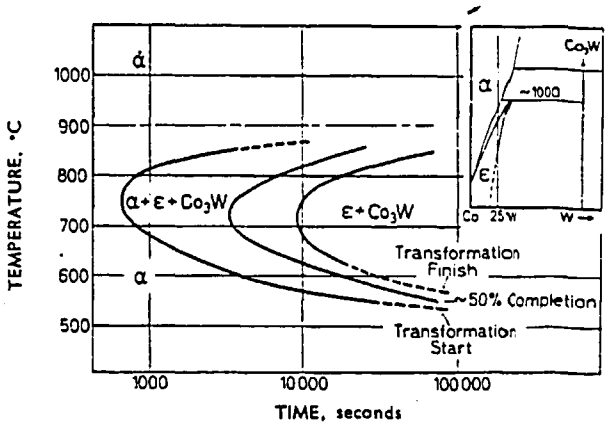


Fig. V.12.b - T-T-T curve for a Co-25wt%W alloy (9)

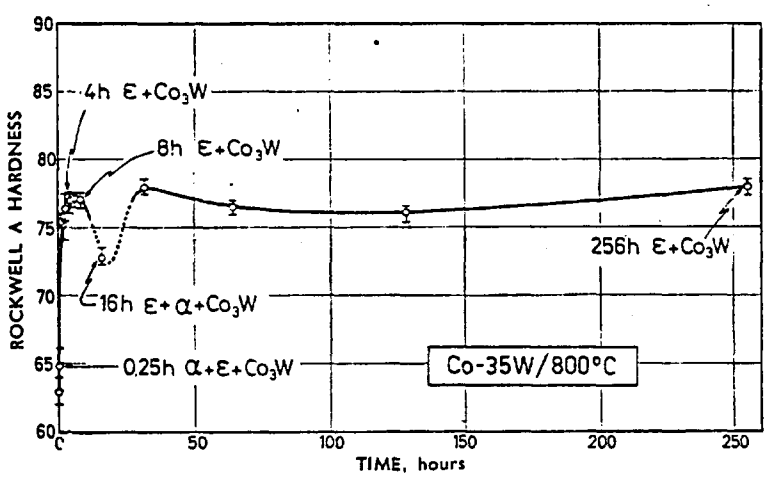


Fig. V.13 - Rockwell hardness vs ageing time for a Co-35wt%W alloy aged at 800°C solution treating at 1350°C (9)

increases with ageing time as has been pointed out before, (Figs.IV.41 and IV.42), and more ε phase was observed by T.E.M. X-ray analysis could not detect the presence of hcp phase for any of the ageing treatments. This has been a problem in the past ([18]) for MULTIPHASE alloys with Co:Ni ratios less than 45:25. However, a decrease in lattice parameter with ageing treatment was observed (Table IV.9). It has been suggested ([16]) that this is due to segregation of chromium and molybdenum atoms on stacking faults, which being ε-stabilizing elements ([5]) contribute to the ε formation and also to the decrease in stacking fault energy observed ([16]) with ageing. Giamei et al. ([9]) also report a decrease in lattice parameter in the Co-WC system with ageing time, which they atribute to the α phase parameter decreasing towards that of pure cobalt while the parameter of the ε phase would increase since this phase is predicted to increase in W and C content with increasing ageing time, in that case.

Concerning the observations that the solution treated undeformed material did not show any significant increase in hardness, this could be explained on the basis that since only a few stacking faults are present for this condition (and no ε phase), segregation which is restricted to the stacking faults is too small to cause any appreciable strengthening.

On ageing at high temperatures (700°C) some recovery was observed with the expected decrease of hardness; hcp phase was not observed at this temperature, but the

matrix still showed many stacking faults and twins (Figs. IV.48 and IV.49) which account for the relatively high values of hardness at this temperature. On holding at 700°C for longer times (100 hrs) the presence of a precipitate was observed (Fig. IV.37), however from X-ray analysis there was some doubt as to the exact nature (Table IV.8), since the d values fitted several possible precipitates. Drapier et al. ([16]) identified this precipitates as Co_3Mo. The presence of some carbides was also detected by X-rays and transmission electron microscopy; these were M_6C or $M_{23}C_6$ carbides, both being possible phases in cobalt alloys.

Some recrystallized grains were observed at 700°C after ageing for 100 hrs. However recrystallization was only complete at 850°C (Fig. IV.38 and Fig. IV.50). The larger the previous deformation given to the material, the smaller the recrystallized grain size obtained. On ageing at 950°C for 2 hrs a grain growth process is observed.

V.3 High Temperature Strength

The general behaviour during compression testing from room temperature to 800°C, for the two alloys A and B, for the four different conditions, i.e., solution treated, solution treated and aged (600°C/5 hrs), 45% deformed (at room temperature), 45% deformed and aged (600°C/5 hrs), is discussed below for the different test temperatures ranges, based on the shape of the stress-strain

curves (Figs. IV.63 to IV.66) and on the strain ageing theory for substitutional alloys. The temperature dependence of the 0.2% proof stress, the strain rate sensitivity and the relaxation stress is discussed later.

V.3.1 General Compressive Deformation Behaviour

V.3.1.a Room Temperature

At point A (Figs. IV.63.a to IV.66.a), the strain rate is increased, which results in an increase in the applied stress. This is in accordance with the equation $\dot{\varepsilon} = \rho b v$ (103); when the strain rate increases, the dislocation velocity v must increase to accommodate the applied strain rate and, since the dislocation velocity can be expressed as a function of the stress by $v=(\sigma/\sigma_o)^n$, therefore the applied stress increases (A-B). At point B, the strain rate is reduced to its original value, $\dot{\varepsilon}_1$, and a reverse process takes place. At point D the cross-head is stopped and the stress starts to fall as a result of relaxation of dislocations. At point E the original strain rate, $\dot{\varepsilon}_1$, is applied and the stress goes up reaching point F, which is the projection of the original stress-strain curve.

It is interesting to note that in the deformed and aged material, at every change of strain rate, after relaxation, the stress overshoots (Fig. IV.66.a); this is due to the very sharp change in dislocation velocity. If the strain rate is suddenly increased, most of

the dislocations are retarded by their atmospheres and the stress must increase in order that the available dislocations can move fast enough to accommodate the applied strain rate. When the stress reaches a critical value, (F or I in Fig. IV.66.a), either the pinned dislocations break free from their atmospheres (unpinning) or there is creation and multiplication of dislocations and deformation continues by the motion of free dislocations and therefore at a lower stress (G-H and J-K). On reducing the strain rate to its original value, the mobile dislocations are still free and the applied stress falls (to C and L, Fig. IV.66.a) because of a reduced dislocation velocity. Fresh atmospheres are formed rapidly and they impede further dislocation motion with a corresponding rise in the stress returning to the smooth stress-strain curve. This explanation is valid at any temperature for those small stress drops observed at every change of strain rate. The fact that this effect is more pronounced in the deformed and aged material, indicates that there are more "atmospheres" present in this condition which impede the movement of dislocations. Probably this is due to the ε phase, formed during the previous ageing treatment (5 hrs at 600°C), which would act as obstacles for dislocation movement.

V.3.1.b Elevated Temperatures

V.3.1.b.1 Introduction

The response at higher temperatures is more

complicated, since serrations appear and it is deduced that dynamic strain ageing is occurring. The mobility of atoms increases with temperature and therefore the solute responsible moves fast enough to slow down freely moving dislocations by forming an atmosphere around them. The solute atmospheres exert maximum drag on the dislocations when they move at some critical speed v_c ([45]), given by

$$Vc = \frac{4D}{h}$$

D = diffusion coefficient of the solute

h = is the effective radius of the solute atmosphere

Thus, there is a critical strain rate given by

$$\dot{\varepsilon}_c = b\rho v_c = \left(\frac{4b\rho}{h}\right) D$$

b = Burger's vector

ρ = mobile dislocation density

This subject has been reviewed in the literature ([45]) and a summary was given in Chapter II (Literature Survey). Therefore further details here would be redundant.

The solute responsible for the pinning of dislocations is believed to be molybdenum; which segregates towards the defects ([16]). This is discussed further in the next section.

The stronger D.S.A. effects were observed in the range 450°C-550°C for the solution treated and solution treated and aged materials (Table IV.12 and Figs.IV.63 and

IV.64) and 550°C-650°C for the deformed and deformed and aged materials (Table IV.13 and Figs. IV.65 and IV.66), i.e. negative strain rate sensitivity, largest drops of stress ($\Delta\sigma$) with increase in strain rate, smallest relaxation stresses and strongest serration effects, were shown in these ranges of temperatures. Within these temperature ranges the main differences between the four material conditions and between both alloys were the shape of the serrations.

The interpretation of the shape of serrations is important in relation to dislocation movements, temperature, strain rate and composition. On this basis a classification (given in Chapter II) and analysis of serrations has been made by Worthington ([104]) ([45]) and Solar-Gomez and Tegar ([105]), in substitutional fcc alloys. A brief summary of the general characteristics and conditions for their appearance is given below.

Type A serrations occur at lower strains and low temperatures. The stress rises above the general level of the stress/strain curve because the diffusion rate is such that some solute atoms can migrate to the moving dislocations and cause a small amount of locking, therefore the mobile dislocation density is reduced and a higher stress is required to maintain the applied strain rate. During this rise in stress, new dislocations are continually being produced and at some critical stress dislocation movement occurs causing the "breakout" of slip

across the whole specimen and a drop in stress.

Type B serrations occur at higher strain than type A serrations or at smaller strains as the temperature is increased. They are associated with a higher rate of diffusion than type A. When the "breakout" of slip occurs the dislocations in the deformation bands are locked before they have completed their movement through the specimen. A new deformation band has to be formed to continue deformation, giving rise to a rapid succession of fine serrations.

Type C serrations occur at higher strain than type B for the same temperature. As the temperature is increased they commence at smaller strains. This behaviour was not always observed in the present work; nonetheless, discussion of these observations is given in the next section.

Type C serrations are explained in terms of dislocation unlocking. When the temperature is high enough for solute atoms to migrate with dislocations at the start of deformation, stress concentrations within the material may result in parts of the specimen deforming at a higher rate than the overall strain rate, and serrations can occur in these regions with an enhanced rate of deformation and large drops in stress.

In the present work the three types of serrations were observed in both alloys for different temperatures and strains. (Figs. IV.63 to IV.66). The

discussion of these observations is given below.

V.3.1.b.2 Discussion of observations at elevated temperature

360°C - 450°C

Figs. IV.63.b and c, IV.64.b, IV.65.b and IV.66.b show the changes occurring at these temperatures for both alloys in the different conditions (S.T., S.T. & aged, deformed, deformed and aged, respectively).

The solution treated and the solution treated and aged materials showed similar behaviour at 360°C. The stress is independent of the applied strain rate which is a characteristic of dynamic strain ageing, (the curve from A to B is a smooth curve) and deformation occurs by creation and multiplication of dislocations with the usual work hardening taking place. When the strain rate is changed to its original lower value $\dot{\varepsilon}_1^o$, at point B, the dislocation velocity is slower and the dislocations are more easily pinned and therefore solute atmospheres are formed; therefore the stress should increase to maintain the applied strain until it is high enough for unpinning the pinned dislocations or multiplication of moving dislocations and this is how serrations are formed.

At this temperatures (360°C) both interstitial and substitutional solutes would be able to take part in the strain ageing process, although the carbon and silicon contents are very small (Alloy B - 0.026C/0.066Si; Alloy

A - 0.01C/0.05Si) these two elements could act as interstitial and substitutional D.S.A. agents respectively, at this temperature. The pair carbon-silicon may act as a D.S.A. agent, since the combination carbon-silicon ([11]) is unique in pairing the small and always interstitial C atom with a much larger but homologous and also quadrivalent Si atom; no study has been found on the effect of this particular pair on D.S.A. However the strongest effect is probably due to the segregation of molybdenum atoms at this temperature. Drapier ([6]) has deduced that segregation of Mo is quite strong at 300°C in the solution treated material, and at 550°C in the deformed material.

The deformed and the deformed and aged materials showed similar behaviour to the solution treated material up to point B (Figs. IV.65.b and IV.66.b), when the strain rate is changed to its original value $\dot{\varepsilon}_1^{\circ}$. However, on decreasing the strain rate the stress increases above the projection of the original σ-ε curve. The explanation would be the same as for the solution treated material, although the pinning effect in this case is stronger, probably due to the deformation previous to testing already existent in the material, which provides a higher density of dislocations and therefore more probability of atmosphere formation. Therefore higher stresses are required for the unpinning or multiplication of dislocations.

At 450°C the deformed material and the solution treated and aged behaved similarly as for 360°C. The deformed and aged material showed a reasonably smooth

stress-strain curve throughout the test (Fig. IV.66.b) with flow stress independent of the strain rate. The solution treated material showed a stronger D.S.A. than at 360°C (Fig. IV.63.c). Type A serrations were observed throughout the σ-ε curve and started immediately after the elastic region for alloy A; negative strain rate sensitivity was observed before relaxation. Alloy A and alloy B showed slight differences in the shape of the serrations (Fig. IV.63.c); especially for the higher strain rate alloy B did not show serrations and showed slightly larger negative strain rate sensitivity and slightly smaller relaxation stresses.

550°C - 650°C

As the test temperature is raised the mobility of atoms increases and therefore the probability of atmosphere formation increases.

At 550°C test temperature the strongest dynamic strain ageing effects are observed for both alloys for all conditions; i.e., negative strain rate sensitivity, low relaxation stresses and very strong serrations occur throughout the stress-strain curve.

Serrations started almost immediately after the elastic region of the stress/strain curve, at this temperature for all conditions. The solution treated material showed type A serrations throughout the stress/strain curve, and the stress was strain rate independent. A yield point phenomena was observed after relaxation

after strain was applied; that is, a larger stress is required to re-initiate deformation than to continue it, therefore, a large increase in stress is observed followed by a stress drop until the normal stress/strain curve takes over again. The solution treated and aged material showed in general the same behaviour, only the shapes of the serrations were different and they were strain rate dependent. The alloys showed different types of serrations with respect to one another (Fig. IV.64.c). Alloy B did not show serrations up to point A; with increase of strain rate very fine type B serrations appear, which become larger with decreasing strain rate ($\dot{\varepsilon}_2 \rightarrow \dot{\varepsilon}_1$); this could be due to the higher solute level of alloy B. At high solute levels the diffusion distance to effect pinning is decreased, so those serrations begin at a higher strain rate ([46]). On decreasing the strain rate the dislocation velocity is decreased and therefore pinning of dislocations is easier; at the same time a larger stress is required for the unpinning or creation and multiplication of dislocations for the deformation to continue by the motion of a higher density of free dislocations. The usual rate of work hardening is intensified by this creation and multiplication mechanism. Alloy A shows type C serrations for the lower strain rates and large type B serrations for the higher strain rate. This behaviour is rather peculiar since it is expected to find type C serrations at higher strain rates ([45]). However, this could be due to higher stress concentrations within this material. The deformed and the

deformed and aged materials showed extremely large type C serrations throughout the test, indicating the presence of very large stress concentrations, probably due to deformation and ageing treatments prior to testing. At this temperature the segregation of molybdenum atoms towards the material defects has been shown ([16]) to be greater than for lower temperatures in the deformed material; therefore there is more probability of atmosphere formation and dislocation movement is more difficult. Higher stresses are required to free the dislocations and when the critical stress is reached at which formation follows by creation and multiplication of dislocation large drops in stress are observed.

Molybdenum atoms have a very strong pinning effect in view of the fact that the atomic diameter of molybdenum is distinctly greater than that of cobalt, nickel and chromium, i.e. Mo 2.81Å, Cr 2.58Å, Co 2.51 Å, Ni 2.50Å. It has been suggested ([111]) that D.S.A. was the consequence of interaction between dislocations and solute atoms due to the elastic misfit of the solute and the lattice atoms.

After relaxation the deformed and the deformed and aged materials showed a continuous decrease of stress with strain (Figs. IV.65.c & IV.66.c) indicating that the solute atoms are so mobile that the atmospheres are able to move with the dislocations and no significant drag can be exerted on the dislocations.

At 650°C the deformed and the deformed and aged materials showed the largest negative strain rate sensitivity. However no serrations were shown by the deformed material, and only serrations for the higher strain rates were observed in the deformed and aged material.

650°C is approximately the temperature at which the ε present should fully transform to fcc (Fig. V.1). Therefore there is less pinning effect to act against the movement dislocations. This is inferred also from the large relaxation stresses observed at this temperature (Table IV.13) and from the decrease in stress for the higher strain rate after relaxation.

700°C

Dynamic strain ageing effects are still observed at this high temperature. The solution treated and the solution treated and aged materials showed similar behaviour, i.e., stress independence of strain rate and serrations throughout the test (Figs. IV.63.f and IV.64.d). Large relaxation stresses are observed at this temperature, indicating that the dislocations are not pinned as the dislocation velocity falls during the relaxation period, therefore indicating the absence of certain obstacles that were acting at lower temperatures. This "absence" could be that the initial ε phase has completely transformed to fcc phase and this effect seems to be greater in the deformed (not aged) material in which there is very little

D.S.A. effect (Fig. IV.65.e) present. On the other hand the deformed and aged material still shows strong D.S.A. effects (negative strain rate sensitivity and serrations). The remarkable difference in behaviour for these two material conditions is probably due to the greater initial content of ε in the deformed and aged material. Possibly some ε remains at 700°C during the period of the test and segregation of Mo to ε may retard the $\varepsilon \rightarrow \alpha$ transformation.

Drapier ([16]) observed serrated yielding in tensile testing at 500°C in a specimen aged for 4 hours at 550°C, however serrated yielding was not observed at 550°C in material previously deformed 47.5% by cold drawing. This is in disagreement with the results from the present work, since at 550°C the strongest D.S.A. effects were observed for all conditions.

Serrations had been observed ([106]) in Ni-Co-C alloys, Fig.V.14, and they were attributed to the presence of carbon causing pinning by elastic interactions between solute atoms and dislocations. Richmand and Bollin ([107]) studied the dynamic responses of Fe-Ni-C, and assumed the similarity of austenite transformation to mechanical twinning, postulating that martensite is indeed a problem for dislocation motion; they related the martensite transformation to serrated yielding and established this effect had been misinterpreted as dynamic strain ageing arising through carbon interaction with dislocations. It is not suggested here that the same approach could be

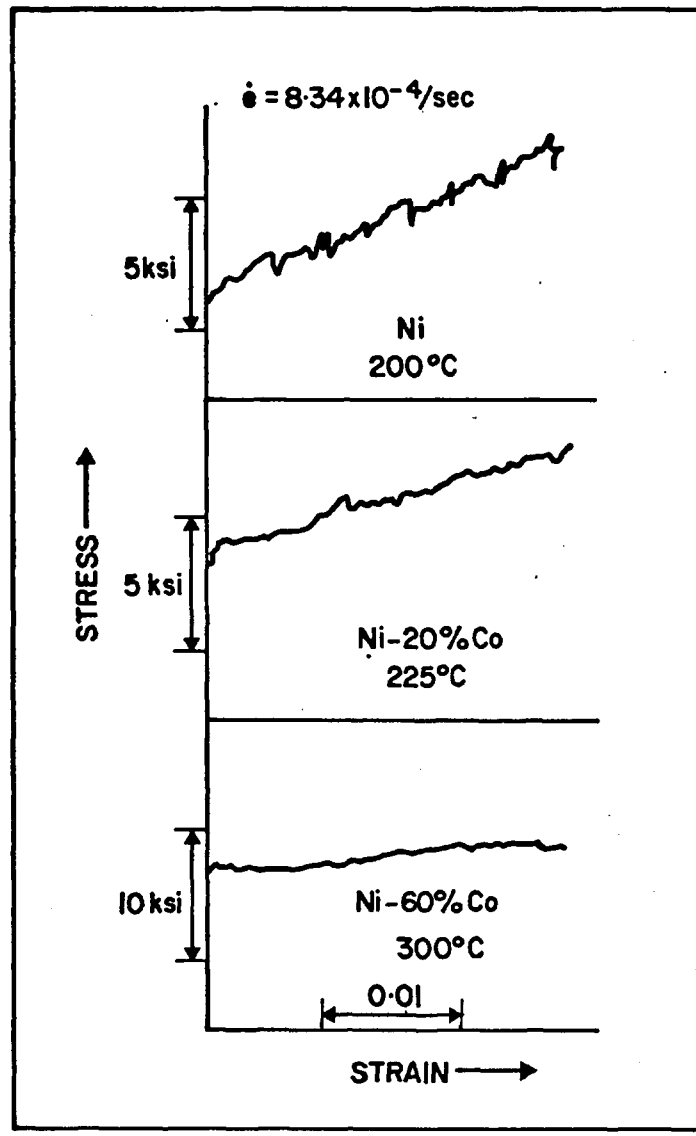


Fig. V. 14 (6). Serrated flow shown on sections of flow curves of nickel and nickel-cobalt alloys.

taken but there may be the probability of an overlapping of ε martensite formation and solute segregation occurring.

V.3.2 The temperature dependence of the 0.2% proof stress, the strain rate sensitivity and the relaxation stress

Figs. IV.67 to IV.70 show the temperature dependence data for both alloys for all conditions tested. It can be seen in Figs. IV.67.a,b,c and Tables IV.12 and IV.13 that the stress shows a small decrease with increase in temperature up to 360°C for all the conditions, showing a small plateau between 360°-450°C and a peak at 550°C followed by a sharp stress decrease for the higher temperatures (700°C-800°C). In the range of temperatures in which the plateau and peak stresses were observed the strain rate sensitivity became zero or negative (Figs. IV.68 and IV.69) accompanied by a fall in the relaxation stresses (Fig. IV.70). At higher temperatures (~680°C-800°C) the strain rate sensitivity became positive (for the deformed and the deformed and aged materials) and very large relaxation stresses were observed. The temperature sensitivity of the proof stress below 360°C and above 650°C (for the solution treated conditions) and 700°C (for the deformed conditions) suggests that the deformation is a thermally activated process in these ranges of temperature.

It was not possible to calculate meaningful values of activation parameters to analyse the thermally

activated deformation. However an attempt was made assuming that all the theoretical requirements ([101]) were met. Tables IV.15 and IV.16 show these results. As can be seen the calculated activation enthalpy, and activation volume values are meaningless, since they are either negative, zero, or very large numbers. In fact, if thermal activation analysis is to be carried out certain conditions must be fulfilled. From the experimental results it is noted that work hardening occurs during the relaxation periods for all test temperatures (this is manifested by an increase in the flow stress after the relaxation period, compared to the flow stress before relaxation).

As can be seen from Figs. IV.63 to IV.66 the stresses after relaxation follow the projection of the original stress/strain curve, and this contributes to the athermal component of the flow stress. The density of dislocations and dislocation substructures may change due to the fcc → hcp transformation occurring at low temperatures and hcp → fcc transformation and some recovery processes taking place at high temperatures. Therefore it can be concluded that in the present work the stress relaxation test results are not valid for the thermal activation analysis.

However, the variation of the proof stress with temperature can be explained as follows. In the range of temperature up to $\sim 360^{o}C$, only interstitial atom barriers are probably present which do not represent very

strong obstacles, at these temperatures. Therefore dislocations move freely and the stress decreases with increase in temperature. Between approximately 360°C and 650°C, the segregation of molybdenum atoms and the transformation hcp → fcc (taking place in the range 425°C-650°C) play a part in making difficult the moving of dislocations; the appearance of D.S.A. processes contributes to the athermal component of the flow stress, which may be responsible for the observed decrease in the temperature sensitivity of the proof stress as the temperature is raised. The very sharp fall in the strain rate sensitivity vs temperature and the relaxation stresses vs temperature, support this suggestion, i.e. barriers are opposing dislocation motion and these barriers become stronger as the temperature is raised. The sharp fall in the proof stress for high temperatures (700°-800°C) indicates that these barriers to dislocation movement have become weaker or have almost completely disappear. Probably the molybdenum atoms move so fast at these temperatures that they do not exert any appreciable drag on the dislocations. Also these temperatures are above the hcp → fcc transformation range for the present alloy (Fig. V.1). Therefore, there is no ε phase which could act as an obstacle for dislocations. This is supported by the large relaxation stresses observed in this range of temperature.

CHAPTER VI

CONCLUSIONS AND SUGGESTIONS FOR FUTURE WORKS

1. Conclusions

1. In agreement with other works ([16]) ([18]), deformation of the material at room temperature and at sub-zero temperatures results in a large increase in strength.

2. This deformation-induced strengthening does not originate entirely from the allotropic transformation fcc → hcp of the initial solid solution, but deformation twinning also plays a very important part. In fact, both ε phase formed during deformation, (higher content at -196°), and deformation twinning are responsible for the strengthening observed.

3. Ageing of the previously deformed material at temperatures between 474°C and 650°C, within the fcc + hcp region of the equilibrium diagram, even for very short times, causes further strengthening; the higher the previous deformation the higher the strengthening obtained. This was attributed to the rapid nature of the allotropic transformation on annealing after heavy deformation.

On ageing for longer times (up to 100 hrs) the hardness slightly increases and this was attributed to

formation of new ε phase and to diffusion of Mo atoms to the ε platelets.

4. On ageing at higher temperatures the previously deformed material, some recovery takes place at 700°C and precipitation occurs after holding for longer times (100 hrs) at this temperature; the main precipitate was a cobalt-molybdenum compound, probably Co_3Mo, and some carbides were also present.

5. Recrystallization takes place on ageing at 850°C the material previously deformed 30% upwards. Grain growth occurs on ageing at 950°C for 2 hrs.

6. The solution treated material showed very high elongation values (70% - 80%) on tensile testing from room temperature to -196°C. There was also a large difference between the 0.2% proof stress (∿ 400-500 MN/m2) and the tensile stress at instability (∿ 1300-1900 MN/m2) revealing a high work-hardening coefficient. Deviation from linearity in the log true stress - log true strain plot at high strains, observed in the solution treated material tested at -196°C was attributed to ε martensite formation.

7. The previously deformed material (45% at room temperature) showed much higher values of 0.2% proof stress (∿ 1200-1340 MN/m2) than the solution treated material on testing from room temperature to -196°C, but smaller values of elongation (20%-35%).

8. The highest elongation values were shown

between -100°C and -196°C and this was believed to result from ε formation taking place at these temperatures. From this stand point the MULTIPHASE alloys can be compared to the TRIP steels.

9. A very ductile mode of fracture in tension was observed from room temperature to about -111°C. Intergranular separation was observed at -196°C, which may be attributed to both ε martensite forming, preferentially at the grain boundaries, and to twin impingement on grain boundaries.

10. The energy absorbed during impact testing remained fairly constant with decreasing temperature. A ductile mode of fracture was observed from room temperature to -196°C.

11. On testing at elevated temperatures dynamic strain ageing was observed within the range of temperatures 360°C-700°C. The strongest D.S.A. effect was observed at 550°C for all the conditions, manifested by the strongest serrations, negative strain rate sensitivity and low relaxation stresses.

12. In the temperature range in which D.S.A. was observed a plateau and a small peak (at ∿ 550°C) occurred in the temperature dependence of the flow stress.

13. The dynamic strain ageing effects were attributed mainly to segregation of substitutional molybdenum atoms.

14. The differences between the alloy with higher titanium content (0.745) and the alloy with lower titanium content (0.15) were very small. They were mainly manifested by slightly higher values of proof stress, tensile stress at instability and elongation, for the alloy with the higher Ti content.

2. Suggestions for further work

1. Measurement of the volume fraction of twins and martensite formed during deformation and ageing would be interesting to make in order to test the quantitative validity of the models considered for the kinetics of ε and twin formation. However, this seems to be a rather difficult task since X-ray analysis is unable to detect the presence of hcp phase for this particular alloy. Probably a finer grain size material could be used and different X-ray techniques. Perhaps a radiation with a longer wavelength like $CrK\alpha$ may improve the accuracy of d-spacings measurements for the low index reflections.

2. The exact nature of the flattening of the fracture surfaces in tensile testing at $-196^{o}C$ was not clear. Further transmission electron microscopy from the fracture surfaces of specimens tested at this temperature should be made.

3. Dynamic strain ageing in tension should be interesting to perform in the range of temperatures

425°C to 700°C, to examine the microstructure by transmission electron microscopy to obtain a better understanding of the processes taking place.

APPENDIX I

X-ray analysis were made by using the Bragg Law and applying the corresponding equations[61] for face centre cubic crystals and for hexagonal closed packed crystals, respectively.

i.e.,

Bragg Law $\lambda = 2d \sin \theta$

for Cubic Crystals $\sin^2\theta = \frac{\lambda^2}{4a^2} (h^2 + k^2 + l^2)$

for hexagonal closed packed crystals

$$\sin^2\theta = \frac{\lambda^3}{3} \cdot \frac{h^2 + h\,k + k^2}{a^2} + \frac{l^2}{c^2}$$

The calculated 2θ values for these crystal structures are given in Table A.I.

Cobalt and Copper radiations were used.

The wave lengths for these radiations are:

$CoK\alpha = 1.79021$ Å

$CuK\alpha = 1.542$ Å

The line positions shown in Table A.I were:

TABLE A.1

FCC			HCP		
hkl	2θ (λcu)	2θ (λco)	hk.l	2θ (λcu)	2θ λ (co)
111	43.75	51.2	10.0	41	48
200	50.97	59.93	10.1	50.06	56.18
			00.2	56.58	56.58
			10.2	72.24	77.3
*220	74.96	89.88	*11.0	74.76	89.6
311	91.04	111.85	20.0	89	108.9
			10.3	104.86	110
222	96.35	119.8	20.1	95.46	115.9
			11.2	100.74	116.3
			00.4	142.83	142.83

* overlapping

Calculated with lattice parameter values taken from the literature: afcc = 3.584 Å

ahcp = 2.54 Å

chcp = 4.22 Å

APPENDIX II

Indexing Diffraction Patterns:

The classical orientations relations between fcc matrix and hcp ε martensite are:

$$\langle 1\bar{1}0\rangle \;//\; \langle 11\bar{2}0\rangle \quad \text{or} \quad \langle 0\bar{1}1\rangle \;//\; \langle 0\bar{1}\bar{1}0\rangle$$

$$(111) \;//\; (0001)$$

from the literature the values of the lattice parameters for 35Ni-35Co-20Cr-10Mo, are:

$$a_{fcc} = 3.585\text{Å}$$

$$a_{hcp} = 3.54\text{Å} \qquad c/a = 1.67\text{Å}$$

$$c_{hcp} = 4.22\text{Å}$$

the average camera constant value was

$$2\lambda L = 5.19$$

From the data d values were calculated and its equivalent in cm, knowing that

for fcc $$d = \frac{a}{\sqrt{h^2 + k^2 + l^2}}$$ and

$$d = \frac{2\lambda L}{R}, \quad D = 2R$$

These values are shown in Table A.II.1

TABLE A.II.1

F.C.C. CRYSTAL STRUCTURE

hkl	N	d Å	D (cm)
111	3	2.07	2.5
200	4	1.79	2.899
220	8	1.268	4.09
311	11	1.08	4.80
222	12	1.03	5.03
400	16	0.89	5.83
331	19	0.82	6.338
420	20	0.8024	6.468
422	24	0.7317	7.093
424	36	0.5975	8.65

For the hcp system

$$\frac{1}{d^2} = \frac{4}{3a^2}(h^2 + hk + k^2) + \frac{1}{c^2}l^2$$

angle between planes $(h_1k_1l_1)$ and $(h_2k_2l_2)$

$$\cos \phi = \frac{\frac{1}{a^2}h_1h_2 + \frac{1}{b^2}k_1k_2 + \frac{1}{c^2}l_1l_2}{\left\{\left(\frac{1}{a^2}h_1^2 + \frac{1}{b^2}k_1^2 + \frac{1}{c^2}l_1^2\right)\left(\frac{1}{a^2}h_2^2 + \frac{1}{b^2}k_2^2 + \frac{1}{c^2}l_2^2\right)\right\}^{1/2}}$$

$h_1k_1i_1l_1$	$h_2k_2i_2l_2$	Angle(°)	d	D (cm)
0001	$10\bar{1}8$	14		
	$10\bar{1}7$	15		
	$10\bar{1}6$	18		
	$10\bar{1}5$	21		
	$\bar{1}105$	21	0.7879	6.6
	$1\bar{1}05$	159		
	$\bar{1}104$	26		
	$10\bar{1}4$	26	0.951	5.468
	$1\bar{1}0\bar{4}$	154		
	$\bar{1}103$	33	1.185	4.398
	$1\bar{1}03$	147		
	$\bar{2}205$	38		
	$20\bar{2}5$	38	0.669	7.757
	$2\bar{2}0\bar{5}$	142		
	$\bar{1}102$	44	1.52	3.414
	$1\bar{1}02$	136		
	$\bar{2}203$	52		
	$20\bar{2}3$	52	0.865	6
	$2\bar{2}0\bar{3}$	128		
	$10\bar{1}1$	63		
	$\bar{1}101$	63	1.95	2.654
	$1\bar{1}0\bar{1}$	117		
	$20\bar{1}1$	74		
	$\bar{2}201$	74	1.06	4.896
	$2\bar{1}0\bar{1}$	106		
	$10\bar{1}0$	90	2.20	2.359
	$\bar{1}100, 1\bar{1}00$			
	0002	0	2.11	2.459
	$000\bar{2}$	180		
$10\bar{1}0$	$21\bar{3}0$	19		
	$11\bar{2}0$	30		
	$01\bar{1}0$	60		
$\bar{1}2\bar{1}0$	$\bar{1}2\bar{1}0$	0	1.27	4.086
	$1\bar{2}10$	180		
	$\bar{1}32\bar{1}$	16	0.815	6.368
	$2\bar{3}11$	164		
	$02\bar{2}1$	33	1.06	4.896
	$2\bar{2}01$	147		

$h_1k_1i_1l_1$	$h_2k_2i_2l_2$	Angle(°)	d	D (cm)
	$01\bar{1}1$	40	1.95	2.654
	$1\bar{1}01$	140		
	$12\bar{3}2$	52	0.772	6.722
	$3\bar{2}\bar{1}2$	128		
	$11\bar{2}2$	62	1.09	4.76
	$2\bar{1}\bar{1}2$	115		
	$20\bar{2}3$	90	0.865	6

b. Twinning systems in an fcc structure under tension

		Stress	Axis	
(K_1)	n_1	[001]	[111]	[011]
$(1\bar{1}1)$	$[121]$	x	x	
$(1\bar{1}1)$	$[\bar{2}\bar{1}1]$	x		
$(\bar{1}\bar{1}1)$	$[\bar{1}21]$	x		
$(\bar{1}\bar{1}1)$	$[2\bar{1}1]$	x		
$(\bar{1}11)$	$[211]$	x	x	x
$(\bar{1}11)$	$[\bar{1}\bar{2}1]$	x		
(111)	$[\bar{2}11]$	x		x
(111)	$[1\bar{2}1]$	x		
$(11\bar{1})$	$[112]$		x	

TABLE A.III.1

WORK HARDENING RATE ($d\sigma/d\varepsilon_p$ MN/m^2) vs STRAIN FOR THE SOLUTION TREATED MATERIAL

ALLOY B								ALLOY A			
RT		-4°C		-80°C		LN		-70°C		-105°C	
$d\varepsilon_p$	$d\sigma/d\varepsilon_p$	$d\varepsilon_p$	$d\sigma/d\varepsilon_p$	$d\varepsilon_p$	$d\sigma/d\varepsilon_p$	$d\varepsilon_p$	$d\sigma/d\varepsilon_p$	$d\varepsilon_p$	$d\sigma/d\varepsilon_p$	$d\varepsilon_p$	$d\sigma/d\varepsilon_p$
0.02	19971	0.01	40736	0.02	22451	0.01	57198	0.01	429673	0.02	24360
0.04	11620	0.03	15371	0.03	16710	0.05	14930	0.03	17825	0.06	10846
0.15	4683	0.14	5227	0.07	8637	0.12	7907	0.07	9203	0.09	8316
0.21	4017	0.21	4185	0.10	6895	0.15	6945	0.10	7299	0.13	6358
0.28	3471	0.27	3771	0.17	4978	0.22	5541	0.17	5266	0.16	5727
0.35	3163	0.34	3421	0.24	4151	0.34	4498	0.21	4636	0.20	5034
0.41	2954	0.39	3206	0.27	3944	0.40	4152	0.24	4367	0.23	4705
0.46	2807	0.44	3040	0.30	3761	0.46	4267	0.27	4115	0.29	4205
0.51	2651	0.47	2922	0.36	3458	0.94	2646^F	0.33	3742	0.35	3834
0.95	146^F	0.50	2846	0.39	3326			0.36	3576	0.41	3545
		1.16	155^F	0.45	3118			0.42	3302	0.46	3357
				0.49	3019			0.47	3121	0.50	3213
				0.54	2877			0.49	3048	1.28	2064^F
				0.57	2818			1.16	1847^F		
				1.15	1863^F						

^{F} = Value at fracture, the previous value to this, corresponds to the work hardening rate at instability

TABLE AIII.2

WORK HARDENING RATE ($d\sigma/d\varepsilon p MN/m^2$) vs STRAIN FOR THE PREVIOUSLY DEFORMED MATERIAL

ALLOY A						ALLOY B					
RT		-50°C		-111°C		-50°C		-70°C		-196°C	
$d\varepsilon p$	$d\sigma/d\varepsilon p$	$d\varepsilon p$	$d\sigma/d\varepsilon p$	$d\varepsilon p$	$d\sigma/d\varepsilon p$	$d\varepsilon p$	$d\sigma/d\varepsilon p$	$d\varepsilon p$	$d\sigma/d\varepsilon p$	$d\varepsilon p$	$d\sigma/d\varepsilon p$
0.03	40213	57881	0.02	0.01	119955	43119	0.03	0.03	39052	0.01	133066
0.07	18711	26408	0.05	0.05	26553	27773	0.05	0.05	36700	0.04	38130
0.10	13593	15374	0.09	0.09	15672	16042	0.09	0.06	24396	0.08	20233
0.11	12425	11042	0.13	0.13	11301	14575	0.10	0.10	15266	0.12	14132
0.94	2154[F]	2298[F]	1.15	0.16	9566	2330[F]	1.18	1.15	2484[F]	0.15	11796
				0.21	7650					0.20	9249
				0.95	2436[F]					0.96	3136[F]

F = Value at fracture, the previous value corresponds to the instability

```
old,plot *DEL*
old,plotss
READY.
list
```

APPENDIX IV

```
 81/06/12. 19.19.58.
PROGRAM   PLOTSS
      PROGRAM PLOTSS(OUTPUT,TAPE6=OUTPUT,DATA,TAPE5=DATA,INPUT,TAPE7=IN
     +PUT,     STORE=131B,TAPE20=STORE)
C       THIS PROGRAM WILL GIVE TWO ARRAYS:TRUE STRESS(TSTRES)VS.
C     ***TRUE STRAIN(TSTRAIN), READY TO BE USED FOR PLOTTING
C     ***INPUT IS GIVEN VIA DIGITIZER FROM THE ELONG.VS.LOAD GRAPH
C     ***INPUT TO THIS PROGRAM HAS THE FORMAT:
C     ***CHART SPEED(CS), CROSS HEAD SPEED(XS), SCALE OF E/L GRAPH(SCALE)
C     ***INIT.DIAM.OF GAUGE(DI), FIN.DIAM.OF GAUGE(DF), GAUGE LENGTH(GL)
        REAL MEMAX,L,M,ME,LC,LPS
        LOGICAL FLAG
C     ***MEMAX=MAXIMUM MACHINE ERROR
C     ***L     =LOAD,AS READ FROM GRAPH FOR EVERY ELONGATION
C     ***M     =SLOPE OF CURVE AT ANY POINT
C     ***ME    =MACHINE ERROR
        DIMENSION D(100),L(100),CD(100),M(100)
        DIMENSION TSTRES(100),TSTRAIN(100)
        DIMENSION HEAD(12)
        PRINT 600
  600 FORMAT(***ENTER ANY HEADING IF REQUIRED***)
        READ(7,1000)(HEAD(J),J=1,12)
        WRITE(6,1000)(HEAD(J),J=1,12)
 1000 FORMAT(12A6)
C     ***LPS=LOAD(PROOF STRESS); DPS=DISTANCE(ELONGATION PROOF STRESS)
        LPS=DPS=M(1)=CD(1)=ME=0.0
C     ***INITIALIZE ARRAYS:TSTRESS,TSTRAIN
        DO 12 I=1,100
        TSTRES(I)=TSTRAIN(I)=0.0
   12 CONTINUE
C     ***SET COUNTERS & FLAG
        N=0
        I=1
        FLAG=.FALSE.
C     ***READ :CHART SPEED(CS),CROSS HEAD SPEED(XS),SCALE OF E/L GRAPH(
C     ***       INITIAL DIAMETER SAMPLE(DI),FINAL DIAMETER(DF),GAUGE LENGT
        READ(5,*)CS,XS,SCALE
        READ(5,*)DI,DF,GL,INT
        PI=4.*ATAN(1.)
C     ***CALCULATE INITIAL AND FINAL AREAS
        A0=(DI**2*PI)/4
        AF=DF**2.*PI/4
C     ***CALCULATE THE .2 OF TOLERANCE
        PERC=(0.002*CS*GL)/XS
        CALL DEBUG1
C    ***HERE BEGINS LOOP***
        DO 9 J=1,100
C     ***READ NEXT POINT
        READ(5,*)L(J),D(J)
        IF(J.GT.2) GO TO 2
        IF(J.EQ.1) GO TO 1
        LC=SCALE/1000.
        IF(L(2).LT.1000.) GO TO 3
        MEMAX=(D(2)-D(1))/CS
        L(1)=L(2)=D(1)=D(2)=CD(1)=CD(2)=0
        I=1
        GO TO 1
    3 MEMAX=1
        PRINT 200
  200 FORMAT(***NO MACHINE ERROR ENTERED***)
        PRINT 300
```

```
      NO=I
      GO TO 13
    1 CONTINUE
      CALL DEBUG2(J,I,L(I),D(I),CD(I),ME,LPS,DPS,M(I),TSTRES(I-N),TSTRA
     +IN(I-N))
    9 CONTINUE
   13 CONTINUE
      CALL OUT1(CS,XS,SCALE,ME,DI,AO,DF,AF,GL,NO,N,HEAD,L,D,CD,LPS,
     + TSTRES,TSTRAIN,Q)
      STOP
      END
      SUBROUTINE DEBUG1
      WRITE(6,800)
  800 FORMAT(1X,3(/),4X,1HJ,3X,1HI,4X,4HL(I),3X,4HD(I),2X,5HCD(I),3X,2HM
     +E    5X,3HLPS,2X,3HDPS,4X,4HM(I),1X,9HTSTRES(N),1X,10HTSTRAIN(N))
      RETURN
      END
      SUBROUTINE DEBUG2(J,I,L,D,CD,ME,LPS,DPS,M,TSTRES,TSTRAIN)
      REAL L,M,ME,LPS
      WRITE(6,900)J,I,L,D,CD,ME,LPS,DPS,M,TSTRES,TSTRAIN
  900 FORMAT(1X,I4,I4,F8.2,F7.2,F7.2,F5.2,F8.2,F5.2,F7.2,F10.2,F6.3)
      RETURN
      END
      SUBROUTINE FIT1(PI,I,X,Y,SLOPE,CONST)
      DIMENSION X(30),Y(30)
      SW2=SWX2=SWY2=SWXY2=SWX22=0.0
      DO 7 N=1,I
      IF(I.LT.2)GO TO 7
      W2=1.0
      SW2=SW2+W2
      SWX2=SWX2+W2*X(I+1-N)
      SWY2=SWY2+W2*Y(I+1-N)
      SWXY2=SWXY2+W2*X(I+1-N)*Y(I+1-N)
      SWX22=SWX22+W2*(X(I+1-N)**2)
    7 CONTINUE
      SLOPE=(SWXY2*SW2-SWX2*SWY2)/(SWX22*SW2-(SWX2**2))
      CONST=(SWXY2*SWX2-SWY2*SWX22)/((SWX2**2)-SW2*SWX22)
      RETURN
      END
      SUBROUTINE OUT1(CS,XS,SCALE,ME,DI,AO,DF,AF,GL,NO,N,HEAD,L,D,CD,
     + LPS,TSTRES,TSTRAIN,Q)
      REAL ME,L,LPS
      DIMENSION HEAD(12),L(100),D(100),CD(100),TSTRES(100),TSTRAIN(100)
      WRITE(6,1000) (HEAD(J),J=1,12)
 1000 FORMAT(12A6)
      WRITE(6,100)
  100 FORMAT('MACHINE CONSTANTS')
      WRITE(6,200)CS,XS,SCALE,ME
  200 FORMAT(1X,2(/),'CHART SPEED = ',F14.0,2X,'CM/MIN'/
     +'CROSS HEAD SPEED = ',F9.2,2X,'CM/MIN'/
     +'SCALE = ',F20.2,2X,'KGS'/
     +'MACHINE ERROR AT MAXIMUN LOAD = ',F4.2,2X,'CM'///)
      WRITE(6,300)
  300 FORMAT('GAUGE CONSTANTS')
      WRITE(6,400)DI,AO,DF,AF,GL
  400 FORMAT(1X,3(/),'INITIAL DIAMETER=',F4.2,'CM',1X,'INITIAL AREA=',
     +F7.3,2X,'SQ.CM'/  'FINAL DIAMETER= ',F7.3,2X,'CM' ,12X,
     +'FINAL AREA= ',F7.3,'SQ.CM'//' GAUGE LENGTH = ' ,F7.3,'CM'///)
      WRITE(6,500)
  500 FORMAT('GRAPH L/D')
      WRITE(6,102)
  102  FORMAT(14X,'   LOAD    ',9X,'DISTANCE ',9X,'CORRECT ')
      DO 91 I=1,NO
      WRITE(6,103)L(I),D(I),CD(I)
  103  FORMAT(11X,3(F12.3,4X))
   91  CONTINUE
```

```
300 FORMAT(***MACHINE ERROR ASSUMED=10MM/1000KGS***)
    PRINT 400
400 FORMAT(***DO YOU WANT TO ALTER VALUE? Y OR N.? ***)
    READ(7,700)RESP
700 FORMAT(A2)
    IF(RESP.NE.1HY)GO TO 8
    PRINT 500
500 FORMAT(***MACHINE ERROR IN MM/1000KGS=*)
    READ(7,*)MEMAX
    MEMAX=MEMAX*SCALE/1000
  8 CONTINUE
    I=J-1
    L(1)=L(1)*LC
    CD(1)=D(1)
    CALL DEBUG1
  2 I=I+1
    L(I)=L(J)*LC
    ME=(MEMAX/SCALE)*L(I)
    D(I)=D(J)
    CD(I)=(D(I))-ME
    IF(L(I).LT.L(I-1)*0.8)GO TO 6
    IF(INT.EQ.0)GO TO 4
    IF(CD(I))10,10,11
 10 CD(I)=0
    M(I)=0
    GO TO 1
 11 IF(LPS.NE.0)GO TO 4
    IF(DPS.NE.0) GO TO 5
 15 M(I)=(L(I)-L(I-1))/(CD(I)-CD(I-1))
    IF(M(I).GE.M(I-1)) GO TO 1
    IF(M(I-1).GE.M(I-2)) GO TO 1
    IF(M(I).GT.0.9*M(I-1)) GO TO 1
    CALL FIT1(PI,I,L,CD,SLOPE,CONST1)
    WRITE(6,1200)SLOPE,CONST1
1200 FORMAT(1X,3(/),10X,'SLOPE = ',F8.3,10X,'CONST1 = ',F8.3)
  5 DPS=PERC+L(I)*SLOPE
    IF(DPS.LT.CD(I)) GO TO 14
    IF(FLAG)GO TO 15
    FLAG=.TRUE.
    GO TO 1
 14 IF(FLAG)GO TO 17
    I=I-1
    GO TO 5
 17 II=I-1
    CALL FIT1(PI,2,L(II),CD(II),RAMP,CONST2)
    WRITE(6,1201)RAMP,CONST2
1201 FORMAT(1X,'RAMP =',F8.3/'CONST 2 =',F8.3)
    LPS=(PERC-CONST2)/(RAMP-SLOPE)
    DPS=PERC+LPS*SLOPE
    I=I+1
    L(I)=LPS
    CD(I)=DPS
    D(I)=D(I-1)
    N=I-1
  4 E=(CD(I)*XS)/(CS*GL)
    S=1+E
    TSTRAIN(I-N)=ALOG(S)
    TSTRES(I-N)=(L(I)*9.08665*S)/A0
    GO TO 1
  6 WRITE(6,801)L(I),(I-N)
801 FORMAT('LOAD AT FRACT.= ',F10.2,10X,'(I-N) =',I3)
    TSTRES(I-N)=(L(I)*9.08665)/AF
    TSTRAIN(I-N)=2*ALOG(DI/DF)
    WRITE(6,802)TSTRES(I-N),TSTRAIN(I-N)
802 FORMAT('FRACT. STRESS =',F10.2/'TRUE FRACT. STRAIN =',F10.2)
    Q=(A0-AF)/A0
```

```
      NO1=NO-N
       WRITE(6,700)
  700 FORMAT('RESULTS')
       WRITE(6,101)TSTRES(1),Q
  101 FORMAT(1X,'.2 PROOF STRESS=',F9.2,15X,'(N/SQ.CM)'/1X,
     +'DUCTILITY = ',F7.3)
       PRINT 800
  800  FORMAT(2X,'I',8X,'TRUE STRESS (N/SQ.CM)',8X,'TRUE STRAIN(CM)')
       WRITE(6,900)(I,TSTRES(I),TSTRAIN(I),I=1,NO1)
       WRITE(20,900)(I,TSTRES(I),TSTRAIN(I),I=1,NO1)
  900  FORMAT(1X,I3,8X,F10.2,18X,F10.2)
       RETURN
       END
READY.




bye

UMCJ067   LOG OFF.  19.24.01.
UMCJ067   CP        0.007 SEC.
```

REFERENCES

(1) Cobalt Monograph: Centre d'information du cobalt 1960

(2) HOUSKA, C.R., AVERBACH, B.L. and COHEN, M., Acta. Met., Vol. 8, Feb. 1960

(3) BIBBY, B.A. and GORDON PARR, J. G. Cobalt, 20, Sept. 1963

(4) SEBILLEAU, F. and BIBRING, H., Symposium on the Mechanism of Phase Transformations in Metals, Institute of Metals Monograph and Report, Series No. 18, London, 1956

(5) GIAMEI, A.F., BURMA, J., and FREISE, E.J., Cobalt, Vol. 39, 1968, p.88

(6) DE LAMOTTE, E. and ALTSTETTER, C., The mechanisms of phase transformation in crystalline solids, Institute of Metals, Monograph No. 33, 1968

(7) HANSEN, M., Constitution of binary alloys, Metal and Metallurgical series, 2nd. ed., McGraw Hill, 1958

(8) RUSS, J., Inorganic Chemistry (English), Vol. 6, 1961, p.827

(9) GIAMEI, A.F., BURMA, J., RABIN, S., CHENG, M., and FREISE, E.J., Cobalt, Vol. 40, 1968, p. 140

(10) AFML-TR-65-2, Part V - Compendium of phase diagram data, June 1969

(11) MANLY, W.D. and BECK, P.A., NACA, Tech. Note 2602, Feb. 1952

(12) RIDEOUT, S.P., MANLY, W.D., KAMEN, E.L., LEMENT, B. S., BECK, P.A., Trans. Amer. Inst. Min. Met. Eng., Vol. 191, 1951

(13) DARBY, J.B. and BECK, P.A., Trans. Amer. Inst. Min. Met. Eng., Vol. 203, 1953

(14) SHELDON, P., and BECK, P.A., NACA Report 1122, 1953

(15) SIMS, C.J., Journal of Metals, 1966, 1119-1130

(16) DRAPIER, J.M., VIATOUR, P., COUTSOURADIS, D., and HABRAKEN, L.,
Cobalt 49, Dec. 1970, p. 171-186

(17) SMITH, G.D. and YATES, D.H.,
Metal Progress, 93, 3, March 1968

(18) GRAHAM, A.H., and YOUNGBLOOD, J.L.,
Met. Trans., Vol. 1, Feb. 1970, p. 423-30

(19) GRAHAM, A.H.,
Trans. A.S.M., Vol. 62, 1969

(20) BAGHAVAN, M., BERKOWITZ, B.J. and KANE, R.D.,
Met. Trans. A., Vol. 11A, Jan. 1980, p. 203

(21) VIATOUR, P. and GOUZOU, J.,
International Conference on the strength of metals and alloys, Asilomar., Calif., paper 130, 1972

(22) REMY, L., and PINEAU, A.,
Mat. Sc. and Eng., Vol. 26, 1976, p. 123-32

(23) HOWIE, A., and SWANN, D.R.,
1961, Phil, Mag., Vol. 6, p. 1215

(24) KOSTER, E.H., THOLEN, A.R., and HOWIE, A.,
1964, Phil, Mag., Vol. 10, p. 1093

(25) DRAPIER, J.M., COUTSOURADIS, D. and HABRAKEN, L.,
1967, Acta Met., Vol. 15, p. 673

(26) REMY L.,
PhD Thesis, Univ. Orsay (1975)

(27) Mechanical-Property Data: MP35N, Data Sheet,
Battelle Memorial Institute, Columbus, Ohio, Sep.1970

(28) SIMMONS, W.F.,
D.M.I.C. Memo 255, June 1971

(29) HICKERSON, J.P. and HERTZBERG, R.W.,
Met. Trans. 3, 1972

(30) BENSON, R.B. and KHAN, K.,
Fall meeting of the Met. Soc. of A.I.M.E., Detroit, Michigan, October 18-21, 1971

(31) MORIZOT, C. and VIGNES,
Mem. Sc. Rev. Met. Vol. 70, 1973

(32) SPS Laboratories, Report No. 5817, 1976

(33) SPS Laboratories, Report No. 5533, Feb. 1974

(34) SEMLITSCH, M., NIEDERER, P.G., WANE, D.O., DEPUY, DePoy Tech. Bulletin, Report No. 7601, July 1976

(35) HIRCHFELD, D. and MULLER, M., Lecture 118, 'Tagung der Vereinigung Nordwest-deutscher Chirurgen' in Hamburg, Dec. 1976

(36) BLISS, V., Climax Molybdenum Co. Report J-4277-01, July 1977

(37) Climax Molybdenum Co. Report J-4386, 1977

(38) SPS aerospace and precision products, MP159 Bolting high strength, corrosion resistant fast for use from 320°F to 1100°F, Form 3780

(39) LORENZ, M., SEMLITSCH, M., PANIC, B., WEBER, H., and WILLERT, H.G, Sulzer Tech. Review 1, 1978

(40) MONTANO, J.W., NASA Tech. Memorandum, May 10, 1971

(41) COHEN, J.B. and WEERTMAN, J., Acta Met. 11, 997 (1963)

(42) DE LAMOTTE, E., PhD., 1968, University of Illinois

(43) PUGLIESE, L.A, STROOP, J.P., Cobalt 43, June 1969, p.80-6

(44) CARTER, G., FLOWER, H., PENNOCK, G., and WEST, D.R.F. J. Mat. Sc. 12 (1977), p. 2149-53

(45) BRINDLEY, B.J. and WORTHINGTON, P.J., Met. Rev. 15, Rev. 145, p.101 (1970)

(46) BAIRD, J.D., Met. Rev. 16, Rev. 149 (1971), p.1

(47) EVANS, A.G. and RAWLINGS, R.D., Phys. stat. sol. 34,9, (1969), p. 9-31

(48) LIEBOWITZ, H., Fracture. Ac. Press, 1968

(49) TAPLIN, D.M.R., Advances in Research on the strength and fracture of materials (4 th Int. Conf. on Fract.), 1977, Univ. of Waterloo, Canada, Perg. Press

(50) BROEK, D., Eng. Fract. Mech. 1973, Vol. 5, p. 55-66

(51) ISHERWOOD, D.P. and WILLIAMS, J.G., Eng. Fract. Mech. 1970, Vol. 2, p. 19-35

(52) MAXWELL, P.C.,
Metallography, 9, 1976, 9

(53) ZACKAY, V.F., PARKER, E.R., FAHR, D. and BUSCH, R.,
Trans. ASM 60, 252 (1967), p. 252-59

(54) TAMURA, I., MAKI, T., and HATO, H.,
Trans. ISIJ 10, 163, (1970)

(55) TAMURA, I., MAKI, T., HATO, H., and ABURAI, K.,
J. Ipn. Inst. Met. 33, 1383, (1969)

(56) BLACK, H.L., and LHERBIER, L.W.,
Met. Prog. 1965, Vol. 87, p. 62

(57) PINEAU, A.G. and PELLOUX, R.M.,
Met. Trans., 5, 1974, p.1103

(58) MONTEIRO S., and FONSECA, H.,
Fracture, Vol. 2, 1977, ICF4, Waterloo, Canada,
p. 135-38

(59) KESTENBACH, H.J.,
Metallography 10, 189-199 (1977)

(60) CROSSARD, C. and JAOUL, B.,
Rev. Met. 47 (1950) 589

(61) CULLITY, B.D.,
Elements of X-ray diffraction

(62) SHELDON, P.R. and BECK, A.,
NACA Report 1122, (1953)

(63) RIDEOUT and BECK,
U.S. N.A.C.A., T.N. 2683 (1952)

(64) WARREN, B.E.,
Progress in Metal Physics, Eds. Chalmers & Kirlg,
Vol. 8, p. 178, Pergamon Press, N.Y. 1959

(65) PATERSON, M.S.,
J. Appl. Phys., 1952, Vol. 23, p. 805-11

(66) WARREN, B.E. & WAREKOIS, E.P.,
Act. Met., Vol. 3, Sept. 1955

(67) SCHWARTZ, L.H., and COHEN, J.B.,
Diffraction from Materials Ac. Press, 1977

(68) HESS, J.B. and BARRETT, C.S.,
Trans. AIME, J. of Met., June 1952, p. 645-47

(69) MANGONON, L., and THOMAS G.,
Met. Trans. Vol. 1, June 1970, p. 1577-86

(70) LECROISEY, F. and PINEAU, A.,
Met. Trans. Vol. 3, Feb. 1972, p.387-96

(71) KESTENBACH, H.J.,
ABM Met., Vol. 32, No. 220, March 1976, p. 181-186

(72) BOWKETT, M.W. and HARRIS, D.R.,
AERE Report R9093 (1978)

(73) MAHAJAN, S., GREEN, M.L., and BRASEN, D.,
Met. Trans. A., Vol. 8A, Feb. 1977, p. 283-93

(74) VENABLES, J.A.,
Deformation Twinning, Proc. of Conf. AIME (1964)
pub. Gordon & Breach; p. 77

(75) CHIN, G.Y.,
et al., Proc. R. Soc. 1309, 433 (1969)

(76) HIRTH, J.P.,
Deformation Twinning, Proc. Of Conf. AIME (1964)
pub. Gordon & Breach, p. 112

(77) MAHAJAN, S., and CHIN, G.Y.,
Act. Met. Vol. 21, Oct. 73, p.1353-63

(78) WASILEWSKI, R.J.,
Met. Trans. A., Vol. 8A, March 1977, p. 391-96

(79) CROCKER, A.G.,
Deformation Twinning, Proc. of Conf. AIME (1964),
pub. Gordon & Breach, p. 272

(80) CHRISTIAN, J.W.,
The theory of transformations in metals and alloys,
1965, Pergamon Press

(81) GAUNT, P., and CHRISTIAN, J.W.,
(1959a) Acta Met. 7, 529, (1959b) Ibid 7, 534

(82) FUJITA, H. and UEDA, S.,
Acta Metall. 20, 759 (1972)

(83) BOLLMAN, W.,
Acta Met. 9, 1972 (1961)

(84) ERICSSON, T.,
Acta Met., 1966, Vol. 14, p. 853

(85) REMY, L.,
Met. Trans. A., Vol. 8A, Feb. 1977, p. 253

(86) REMY, L.,
Act. Met. Vol. 26, p. 443-51 (1978)

(87) DE LAMOTTE, E.,
PhD Thesis, University of Illinois, 1968

(88) MICHELS, H.T. and FORBES JONES, R.M.,
Met. Trans. Vol5, 1974, p. 847

(89) NISHIYAMA, Z.,
Martensitic Transformation, Mat. Sc. Series
Ac. Press, 1978

(90) PRADHAN, R. and ANSELL, G.S.,
Met. Trans. A., Vol. 9A, 1978, p.793

(91) KELLY, P.M.,
Act Met. Vol. 13, June 1965, p.635

(92) MONTANO, J.W.,
NASA TM X-64591

(93) LOW, J.R. and GAROFALO, F.,
Proc. Soc. Stress Anal., 1947, Vol. 4, p.16

(94) LUDWIGSON, D.C.,
Met. Trans. Vol. 2, 1971, p.2825

(95) SEETHARAMAN, V. and KRISHNAN, R.,
J. of Mat. Sc., 16, (1981), 523-30

(96) GUAIMARAES, R.C. and DE ANGELIS, R.J.,
Mat. Sc. Eng., 13 (1974), 109-11

(97) HULL, D.,
Fracture, John Wiley and Son N.Y. 1963

(98) ROSON, A., JAGO, R., and KJER, T.,
Mat. Sc., 7, 1972, 870

(99) PINEAU, A.G. and PELLOUX, R.M.,
Met. Trans., 5, 1974, 1103

(100) Metals Handbook, Vol. 9, American Society for Metals

(101) REMY, L.,
Acta Metall., 25 (1977) 173

(102) SHUNK, F.,
Constitution of binary alloys, McGraw Hill, 1979

(103) COTTRELL, A.H.,
Dislocations and Plastic flow in crystals, Oxford,
1953

(104) WORTHINGTON, P.J.,
1962, Ph.D. Thesis, University of Sheffield

(105) SOLAR-GOMEZ, A.J.R., and TEGART, W.J.,
Mc G. 1969, Phil. Mag., 20, 495

(106) SONON, D.E.,
PhD Thesis, 1967, Cornell University

(107) RICHMAN, R.H. and BOLLING, G.F.,
Met. Trans. Vol. 2, 1971, p.2451

(108) ASSADI, A.T.K.,
PhD Thesis 1977, Imperial College, London

(109) WINSTONE, M.R.,
PhD Thesis 1970, Imperial College, London

(110) GOLDSCHMIDT, H.J.,
Interstitial alloys, Butterworths, (1967)

(111) WINSTONE, M.R. and RAWLINGS, R.D.,
Phys. stat. sol. (a), 8, 79 (1971)

(112) REMY, L.,
Met. Trans. A, Vol. 12A, 1981, p.387

(113) LORENZ, M., SEMLITSCH, M., PANIC, B., WEBER, H., and WILLERT, H.G.,
Sulzer Tech. Rev. 1, 1978